

RÉPUBLIQUE DU CAMEROUN

Paix-Travail-Patrie

UNIVERSITÉ DE YAOUNDÉ I

FACULTÉ DES SCIENCES

CENTRE DE RECHERCHE ET DE
FORMATION DOCTORALE EN
SCIENCES TECHNOLOGIE ET
GÉOSCIENCES

UNITÉ DE RECHERCHE ET DE
FORMATION DOCTORALE EN
PHYSIQUE ET APPLICATIONS

BP: 812 Yaoundé

Email: crfd@uy1.uninet.cm

REPUBLIC OF CAMEROON

Peace-Work-Fatherland

UNIVERSITY OF YAOUNDE I

FACULTY OF SCIENCE

POSTGRADUATE SCHOOL OF
SCIENCE TECHNOLOGY
AND
GEOLOGICAL SCIENCES

RESEARCH AND POSTGRADUATE
TRAINING UNIT FOR PHYSICS
AND APPLICATIONS

P.O. Box: 812 Yaounde

Web Site: www.uy1researchstg.cm



Laboratoire de Physique de l'Environnement Terrestre

Laboratory of Earth's Environment Physics

Central Africa rainfall and associated mechanisms as represented in General Circulation Models (GCMs): Case study of the MetUM outputs

Thesis submitted in partial fulfillment of the requirements for the degree of Doctor/PhD in physics

Option: Atmospheric Sciences

by

TAGUELA NDETATSIN Thierry

Registration number: 06W520

Master degree in Physics

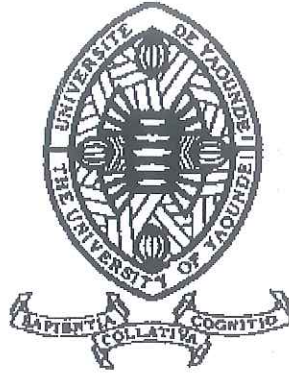
Under the supervision of

POKAM MBA Wilfried
Senior Lecturer
University of Yaoundé 1

Richard WASHINGTON
Professor
University of Oxford



Academic Year 2022/2023



DÉPARTEMENT DE PHYSIQUE
DEPARTMENT OF PHYSICS

ATTESTATION DE CORRECTION DE LA THÈSE DE DOCTORAT/Ph.D

Nous, Professeur TCHAWOUA Clément et Professeur ZEKENG Serge Sylvain, respectivement Examineur et Président du jury de la Thèse de Doctorat/Ph.D de Monsieur TAGUELA NDETATSIN Thierry, Matricule 06W520, préparée sous la direction de Docteur POKAM MBA Wilfried et du Professeur Richard WASHINGTON, intitulée : « Central Africa rainfall and associated mechanisms as represented in General Circulation Models (GCMs): Case study of the MetUM outputs », soutenue le Lundi, 19 Juin 2023, en vue de l'obtention du grade de Docteur/Ph.D en Physique, Spécialité **Physique de l'Environnement Terrestre**, Option **Sciences de l'Atmosphère**, attestons que toutes les corrections demandées par le jury de soutenance ont été effectuées.

En foi de quoi, la présente attestation lui est délivrée pour servir et valoir ce que de droit.

Fait à Yaoundé le 30 JUN 2023

Examineur

Pr TCHAWOUA
Clément

Le Président du jury

Pr ZEKENG Serge
Sylvain

Le Chef de Département de Physique



Pr NDJAKA Jean-Marie
Bienvenu

Central Africa rainfall and associated mechanisms as
represented in General Circulation Models (GCMs):

Case study of the MetUM outputs

Taguela Ndetatsin Thierry

Dedication

To My Kids

Nelson and Maeva

Acknowledgements

This thesis would not have been possible without the guidance and the help of several individuals who in one way or another contributed in the preparation and completion of this work.

- Foremost, I would like to thank the Almighty God for giving me strength throughout my thesis, to Him be the glory. Without Him nothing is possible.
- My utmost gratitude to my advisors Dr Wilfried Pokam and Pr Richard Washington for their guidance, listening, unselfish and unfailing support, their patience, immense knowledge and steadfast encouragement to complete this study. I could not wish having better and friendlier advisors for my PhD study.
- I extend my gratitude to all my esteemed lecturers of the Department of Physics of the University of Yaounde 1, especially Pr Vondou Derbetini, for endowing me with knowledge.
- I would also like to appreciate all researchers of the Laboratory of Environmental Modelling and Atmospheric Physics (LEMAP) at University of Yaounde 1 for wide range discussions on atmospheric Science.
- Thank you to my dad Ndetatsin David, my mum Kadje Madeleine and my brothers and sisters for their multiform contribution to my evolution. I apology that I could not mention all of them personally one by one.
- I am infinitely grateful to my beloved wife, Domleu Yolande, for encouraging me to work hard on this thesis, as well as for her love and understanding. I am not sure it would have been possible without her by my side. She was a great support during my PhD years.

- My thanks also go to all offices, institutions, personalities and projects who provided the needed data for my research, some financial support to attend conferences, workshops and summer schools during this research work. Among others, I can mention the Climate Research Laboratory led by Pr Richard Washington at the University of Oxford, the UK Met Office, the IMPALA and the LaunchPAD projects.
- Finally, because you are too many, I may have forgotten some of you. However, I want to thank all those who in some way contributed to the realization and amelioration of this thesis. May each of you receive an expression of my profound gratitude.

Contents

List of figures	vii
List of tables	xv
List of abbreviations and acronyms	xvi
Abstract	xviii
Résumé	xx
General introduction	1
1 Literature Review and Research questions	4
1.1 Central Africa (CA) rainfall variability	4
1.1.1 The hydrological cycle in CA	4
1.1.2 Seasonal spatial rainfall distribution	5
1.2 Atmospheric features associated with CA rainfall variability	7
1.2.1 Low-level westerlies (LLWs)	7
1.2.2 Regional atmospheric jets	9
1.2.2.1 African Easterly Jets (AEJs)	9
1.2.2.2 Tropical Easterly Jet (TEJ)	10
1.2.3 Congo basin cell	11
1.2.4 Neighbouring Oceans and associated circulations	12
1.2.4.1 Atlantic Ocean and its Atlantic-Congo Walker like circulation	12
1.2.4.2 Indian Ocean and its overturning circulation	14
1.3 General circulation model (GCMs)	15
1.3.1 Coupled General Circulation Models (CGCMs)	16
1.3.2 Coupled Model Intercomparison Project (CMIP)	17

1.4	Climate model evaluation	18
1.4.1	Perfomance-based evaluation	18
1.4.2	Process-oriented assessment	19
1.5	Process-oriented assessment in CA and research questions	20
1.6	Conclusion	21
2	Study area, Data used and Methodology	22
2.1	Study area	22
2.1.1	Location and topography	22
2.1.2	Vegetation	23
2.2	Data used	24
2.2.1	Observed and reanalyses data	24
2.2.1.1	Observed data: GPCP, UDEL, CHIRPS and HadISST	24
2.2.1.2	Reanalyses data: MERRA2 and ERA5	25
2.2.2	Simulated data	26
2.2.2.1	CMIP5 models	26
2.2.2.2	CMIP6 models	27
2.2.2.3	Governing Equations in Climate models	28
2.3	Methods	30
2.3.1	Approach to understand models biases	31
2.3.2	Metrics used for our investigations	31
2.3.2.1	Vertically Integrated Moisture flux convergence	31
2.3.2.2	Mass weighted stream function	33
2.3.2.3	Indian Ocean Dipole (IOD) index	34
2.3.2.4	Ageostrophic wind computation	35
2.4	Conclusion	35
3	Results and discussions	36
3.1	Rainfall Climatology in CMIP5 and CMIP6 models over CA	36
3.1.1	Annual cycle	36
3.1.2	Seasonal spatial mean climatology	37
3.1.3	Quantification of total rainfall pattern similarities	40
3.2	Simulated circulation and rainfall biases	40

3.2.1	Moisture flux convergence	40
3.2.1.1	Zonal moisture flux convergence	41
3.2.1.2	Meridional moisture flux convergence	43
3.2.1.3	Total moisture flux convergence	43
3.2.2	Role of Low-level westelies (LLWs)	44
3.2.3	Simulated Convection over Central Africa	50
3.3	Focus on the Met Office Unified Model (MetUM)	53
3.3.1	Pattern of rainfall biases and link with surrounding oceans	55
3.3.2	Large-scale features associated with rainfall biases	57
3.3.2.1	Sea Surface Temperature teleconnection	57
3.3.2.2	Tropical large-scale circulations	59
	a) Congo basin Walker like circulation	61
	b) Indian Ocean overturning circulation	65
3.3.3	Regional mechanisms associated with rainfall biases	67
3.3.3.1	Low level tropospheric circulations	67
3.3.3.2	Mid-tropospheric circulation	70
3.4	Conclusion	75
	General conclusion and outlooks	76
	References	79
	List of publications	91

List of Figures

Figure 1	Rainfall climatological annual cycle in Central Africa from GPCP, UDEL and CHIRPS. Rainfall is averaged between 10°S–10°N and 10°E–30°E.	5
Figure 2	Spatial distribution of the long term (1981-2015) seasonal mean rainfall (mm.day ⁻¹) in Central Africa from GPCP. The red box shows the main CA domain (10°S–10°N; 10°E–30°E.	6
Figure 3	Schematic showing key features of the Central Africa climate. Locations are approximate. The study area is shown by the green box. AEJ-N = African easterly jet north and AEJ-S = African easterly jet south (Creese and Washington, 2016).	7
Figure 4	Long term (1980-2010) monthly mean zonal wind speed (m.s ⁻¹), averaged between 10°E and 30°E. Povitive (negative) values represent westerly (easterly) winds.	8
Figure 5	Annual cycle of the mean zonal wind speed (m.s ⁻¹), averaged over the longitude band 10°-30°E. Red, Blue and Green points display respectively the mean position of TEJ, AEJ-N and AEJ-S cores (Tamoffo, 2020).	10
Figure 6	Schematic diagram of the zonal large-scale circulation over central Africa and its surrounding oceans as proposed in Longandjo and Rouault (2020). The Congo basin cell acts a small heat engine, transporting latent and sensible heat from the warm central Africa landmass to the cold equatorial Atlantic, reminiscent of a mixed Carnot–steam cycle.	12

Figure 7	Monthly streamline cross sections constructed from the divergent component of the zonal wind (m.s^{-1}) and the vertical-p velocity ($10^{-2}.\text{Pa.s}^{-1}$) averaged between 3°S and 3°N from the ERAI climatology (1979–2014) (Cook and Vizu, 2016).	13
Figure 8	Conceptual diagram of how a numerical model works (Fig.2 in Edwards, 2011).	16
Figure 9	CMIP evolution. CMIP will evolve but the DECK will provide continuity across phases (Eyring et al., 2016).	17
Figure 10	The Central Africa region (red boxes). (left) topography (in meter) based on GTOPO30 Digital Elevation Model; (right) high vegetation cover index, from ERA5 reanalysis data.	23
Figure 11	Schematic of the CMIP/CMIP6 experiment design. The inner ring and surrounding white text involve standardized functions of all CMIP DECK experiments and the CMIP6 historical simulation. The middle ring shows science topics related specifically to CMIP6 that are addressed by the CMIP6-Endorsed MIPs, with MIP topics shown in the outer ring (Eyring et al., 2016).	29
Figure 12	Indian Ocean Sea Surface Temperature (SST) areas (red boxes) used to compute IOD.	34
Figure 13	Rainfall (mm.day^{-1}) climatological annual cycle over Central Africa (10°S – 10°N and 10°E – 30°E) from observations and reanalyses (lines with markers), CMIP5 (solid lines) and CMIP6 models (dashed lines). The blue band represents observational uncertainty (envelope of the standard deviation generated from the mean of the observed and reanalyses data).	37
Figure 14	Spatial representation of the March-May (MAM) long term rainfall mean (mm.day^{-1}) over Central Africa (blackbox) from (a-c) observations, (d-k) CMIP5 models biases and (l-s) CMIP6 models biases. The biases are computed with respect to GPCP	38

Figure 15	Spatial representation of the September–November (SON) long term rainfall mean ($\text{mm}\cdot\text{day}^{-1}$) over Central Africa (blackbox) from (a–c) observations, (d–k) CMIP5 models biases and (l–s) CMIP6 models biases. The biases are computed with respect to GPCP	39
Figure 16	Taylor diagrams displaying the statistics based on the seasonal (DJF, MAM, JJA and SON) mean rainfall. The CMIP5 and CMIP6 models are compared against GPCP (reference field) and rainfall is averaged over the CA region (10°S – 10°N and 10°E – 30°E).	41
Figure 17	Time–height section of Net zonal moisture flux (in $\text{g}/\text{kg}\cdot\text{m}/\text{s}$) in (a–b) reanalyses, (c–j) CMIP5 models and (k–r) CMIP6 models. This is the summing of moisture flux at West–East (West (10°E) minus East (30°E)) frontiers into CA. Negative values indicated moisture divergence and positive values convergence.	42
Figure 18	Time–height section of Net meridional moisture flux (in $\text{g}/\text{kg}\cdot\text{m}/\text{s}$) in (a–b) reanalyses, (c–j) CMIP5 models and (k–r) CMIP6 models. This is the summing of moisture flux at South–North (South (10°S) minus North (10°N)) frontiers into CA. Negative values indicated moisture divergence and positive values convergence.	44
Figure 19	Time–height section of the Total moisture flux (in $\text{g}/\text{kg}\cdot\text{m}/\text{s}$) in (a–b) reanalyses, (c–j) CMIP5 models and (k–r) CMIP6 models. This is the summing of Net zonal moisture flux and the Net meridional moisture flux into CA. Negative values indicated moisture divergence and positive values convergence.	45
Figure 20	March–May long term seasonal mean of zonal wind (m/s) averaged between 10° and 15°E for (a–b) reanalyses, (c–j) CMIP5 and (k–r) CMIP6 models. Positive values correspond to westerly winds and negative values to easterly winds.	46
Figure 21	September–November long term seasonal mean of zonal wind (m/s) averaged between 10° and 15°E for (a–b) reanalyses, (c–j) CMIP5 and (k–r) CMIP6 models. Positive values correspond to westerly winds and negative values to easterly winds.	47

- Figure 22** Long term seasonal mean of March–May 925 hPa total wind (vectors: m/s) and zonal wind (shading: m/s) for (a–b) reanalyses, (c–j) CMIP5 models biases with respect to ERA5 and (k–r) CMIP6 models biases with respect to ERA5. The black box is the study region, and the interest is on the inflow at the region’s western boundary. 49
- Figure 23** Long term seasonal mean of September–November 925 hPa total wind (vectors: m/s) and zonal wind (shading: m/s) for (a–b) reanalyses, (c–j) CMIP5 models biases with respect to ERA5 and (k–r) CMIP6 models biases with respect to ERA5. The black box is the study region, and the interest is on the inflow at the region’s western boundary. 51
- Figure 24** Seasonal cycle of 925 hPa total, divergent and rotational zonal wind averaged between 10°S–10°N and 10°–15°E for (a–c) reanalyses and CIMIP5 models, (d–f) reanalyses and CMIP6 models. (g–i) Uncertainty ranges in total, divergent and rotational zonal wind from reanalyses (red), CMIP5 (blue) and CMIP6 (green) models. Note that westerly winds are positive while easterly are negative. 52
- Figure 25** Latitude–height cross section averaged between 10°E and 30°E of vertical velocity (10^{-3}Pa/s : shading), zonal wind with a speed equal or greater than 6m/s (contours), vertical motion of meridional wind and omega (vectors) and rainfall (mm.day^{-1} : red line) in MAM (March–May) season from (a–b) reanalyses, (c–j) CMIP5 models and (k–r) CMIP6 models. Negative values of vertical velocity represent ascent motion, while positive values represent descent motion. 53

- Figure 26** Latitude–height cross section averaged between 10°E and 30°E of vertical velocity (10^{-3}Pa/s : shading), zonal wind (m/s : contours), vertical motion of meridional wind and omega (vectors) and rainfall ($\text{mm}\cdot\text{day}^{-1}$: red line) in SON (September–November) season from (a–b) reanalyses, (c–j) CMIP5 models and (k–r) CMIP6 models. Negative values of vertical velocity represent ascent motion, while positive values represent descent motion. 54
- Figure 27** September–November spatial rainfall (mm/day) climatology for (a–e) GPCP, UDEL, CHIRPS, ERA5 and MERRA2 absolute values (1981–2015), (f–g) atmosphere-only and (h–i) coupled models biases with respect to GPCP. The box in (a–i) indicates the Central Africa domain used in this study and superimposed dots in (f–i) indicate the areas where the differences are statistically significant at the 95% confidence level using the t-test. 56
- Figure 28** (a) Correlations of observed SON rainfall from GPCP, averaged over eastern Central Africa (the box: 10°S–10°N, 20°–30°E), against observed SON SST from HadISST for the period 1980–2010. (b–e) biases of correlations computed as in (a) for each model with respect to (a). 58
- Figure 29** (a) Correlations of observed SON rainfall from GPCP, averaged over western Central Africa (the box: 10°S–10°N, 10°–20°E), against observed SON SST from HadISST, for the period 1981–2015. (b–e) biases of correlations computed as in (a) for each model with respect to (a). 60
- Figure 30** Longitude–height cross-section of the September–November mean climatology of vertical wind ($10^{-2}\cdot\text{Pa}\cdot\text{S}^{-1}$: Shaded) and streamline constructed from the divergent component of the zonal wind ($\text{m}\cdot\text{s}^{-1}$) and the vertical wind ($10^{-3}\cdot\text{Pa}\cdot\text{S}^{-1}$) averaged between 5°S and 5°N for (a and b) reanalyses, (c–d) atmosphere-only models and (e–f) coupled models. 61

- Figure 31** September–November climatology of (a) absolute values of SST ($^{\circ}\text{C}$: Shaded) from HadISST and 850 hPa wind (m.s^{-1} : Vectors) from ERA5; (b–c) AGCMs 850 hPa wind (m s^{-1} : Vectors) biases with respect to ERA5; (d–e) CGCMs SST ($^{\circ}\text{C}$: Shaded) and 850 hPa wind (m.s^{-1} : Vectors) biases with respect to HadISST and ERA5 respectively. 62
- Figure 32** September–November climatological 850 hPa geopotential height (m: shaded) and moisture transport ($\text{g.kg}^{-1}.\text{m.s}^{-1}$: vectors). a–b) Absolute values of ERA5 and MERRA2 respectively. c–f) Models biases of 850 hPa geopotential height and moisture transport with respect to ERA5. The red box is the Central Africa region. 63
- Figure 33** (a) September–November (SON) meridional average (5°S – 5°N) of 850 hPa geopotential height (m) minus spatial mean (5°S – 5°N ; 25°W – 25°E) of 850 hPa geopotential height for reanalyses, coupled and atmosphere-only models. (b) 850 hPa land-ocean thermal difference between the Central African landmass (5°S – 5°N ; 15° – 30°E) and the coastal Atlantic Ocean (5°S – 5°N ; 5°W – 5°E) for reanalyses, coupled and atmosphere-only models. 64
- Figure 34** Composite anomaly of SON vertical integrated (1,000–100 hPa) zonal moisture transport ($\text{kg.m}^{-1}.\text{s}^{-1}$: Shading) and total moisture transport ($\text{kg.m}^{-1}.\text{s}^{-1}$: Vectors) for positive IOD years. The strongest positive IOD years minus the mean state in (a and b) each reanalysis, (cd) atmosphere-only models and (e–f) coupled models. The box in (a–f) indicates the CA domain used in this study. 66

- Figure 35** September–November (SON) climatological mean of the zonal mass-weighted stream function (contours: $10^{11} \text{ kg.s}^{-1}$) computed with 5°S – 5°N averaged zonal wind for (a and b) ERA5 and MERRA2, (c–d) Atmosphereonly models (GA6 and GA7), and (e–f) coupled models (GC2 and GC3). Solid and dashed contours represent positive and negative values of mass-weighted stream functions respectively, separated with the zero value of mass-weighted stream (thicker contour). Contour intervals are 10 between positive contours and 4 between negative contours. The vertical lines are the zonal boundaries of the CA region. 68
- Figure 36** Vertical profile of zonal wind (m.s^{-1} : vectors) constructed with vertical velocity ($4 \cdot 10^{-2} \text{ Pa.s}^{-1}$) and averaged between 10°S and 10°N . Gray shade represents the orography in (a–b) each reanalysis, (c–d) atmosphere-only models and (e–f) coupled models. 70
- Figure 37** September–November long-term mean meridional potential temperature gradient (10^6 K.m^{-1} ; shaded) at 850 hPa and zonal easterly wind averaged between 700 and 600 hPa with speed $\geq 6 \text{ m.s}^{-1}$ (contours) for (a–b) reanalysis, (cd) atmosphere-only models and (e–f) coupled models. 71
- Figure 38** Latitude-height cross-section of September–November long term mean of (a and b) net zonal moisture flux (shaded: $\text{kg.m}^{-1} \cdot \text{s}^{-1}$) calculated from west boundary (20°E) minus east boundary (30°E) and vertical wind (vectors: $4 \cdot 10^{-2} \text{ Pa.s}^{-1}$) averaged between 20 and 30°E in reanalyses. (c–f) Same as in (a and b) minus ERA5 for atmosphere-only (c–d) and coupled (e–f) models. Solid contours (a–f) represent AEJ components (U m.s^{-1}) at 20°E in reanalyses, atmosphere-only and coupled models. 20 – 30°E is the zonal extent of the wet bias in models. 73

Figure 39 Vertical profile of long term mean September-November wind divergence ($10^{-6} \cdot s^{-1}$; shaded) and ageostrophic component of meridional wind ($m \cdot s^{-1}$; vectors) averaged between $15^{\circ}E$ and $25^{\circ}E$ for (a-b) reanalysis, (cd) atmosphere-only models and (e-f) coupled models. Around the Equator (between $1^{\circ}S$ and $1^{\circ}N$) the coriolis force used to calculate the meridional ageostrophic wind is replaced by $1^{\circ}S$ – $1.5^{\circ}S$ and $1^{\circ}N$ – $1.5^{\circ}N$ nearest values of coriolis force. 75

List of tables

Table 1	Details of CMIP5 and CMIP6 models used in the study. Horizontal resolution (grids) and vertical levels are included.	27
----------------	--	----

List of abbreviations and acronyms

AEJ:	African Easterly Jet
AEW:	African Easterly wave
AGCM:	Atmospheric General Circulation Models
AOGCM:	Atmosphere-Ocean General Circulation Models
CA:	Central Africa
CB:	Congo Basin
CGCM:	Coupled General Circulation Models
CHIRPS:	Climate Hazards group Infrared Precipitation with Stations
CMIP:	Coupled Model Intercomparison Project
CORDEX:	COordinated Regional climate Downscaling EXperiment
DECK:	Diagnostic, Evaluation and Characterization of Klima
DJF:	December-January-February
DMI:	Dipole Mode Index
ECMWF:	European Centre for Medium Range Weather Forecasts
ESGF:	Earth System Grid Federation
GCM:	Global Climate Model
GPCP:	Global Precipitation Climatology Project
IMPALA:	Improving Model Processes for African Climate
IOD:	Indian Ocean Dipole
IOWC:	Indian Ocean Walker Circulation
IPCC:	International Panel on Climate Change
ITCZ:	Inter-Tropical Convergence Zone
JJA:	June-July-August
LEMAP:	Laboratory of Environmental Modelling and Atmospheric Physics
LLW:	Low Level Westerly
MAM:	March-April-May
MERRA:	(Modern-Era Retrospective Analysis for Research and Applications
MetUM:	Met Office Unified Model
MSE:	Mean Square Error

NASA:	National Aeronautics and Space Administration
NSD:	Normalized Standard Deviation
OGCM:	Oceanic General Circulation Models
RDC:	République Démocratique du Congo
RMSE:	Root Mean Square Error
SAH:	South Atlantic High
SON:	September-October-November
SST:	Sea Surface Temperature
SSTAs:	Sea Surface Temperature Anomalies
TEJ:	Tropical Easterly Jet
UDEL:	University of Delaware
WAM:	West African Monsoon
WCRP:	World Climate Research program
WGCM:	Working Group on Coupled Modelling

Abstract

Although climate models are important for making projections of future climate, little attention has been devoted to model simulation of the complex climate of Central Africa (CA). This study investigates, through processes over CA, the rainfall biases in eight (8) climate models from Phase 6 of the Coupled Model Intercomparison Project (CMIP6) and the corresponding eight previous models from CMIP5 with the focus on the Met Office Unified Model (MetUM). In association with an unrealistic moisture flux convergence, models such as the BCC-CSM model overestimate rainfall in both version while other, such as the GISS-E2 model underestimate. As far as the MetUM model is concerned, the study shows that the two versions of the model depict a wet (dry) bias over the eastern (coastal western) CA in the September–November season, with the wet (dry) bias stronger in coupled (atmosphere-only) models. Here, we explore potential regional to large-scale causes of these biases. Results reveal that the overestimation of the simulated sinking branch of the Atlantic-Congo zonal overturning cell is associated with a strong near-surface temperature and pressure gradient between CA and the eastern Atlantic Ocean. This leads to strong low-level westerlies (LLWs) which dry the coastal western CA and strengthen the intensity of the Congo basin cell. Over eastern CA, the wet bias is partially due to the misrepresentation in the strength of both African easterly jet components that shift the mid-tropospheric moisture flux convergence southward, favouring more convection south of the equator. Furthermore, the overestimation in the simulated width and intensity of the Congo basin cell is associated with a strong low-level moisture convergence over eastern CA, which contributes to more precipitation. Remote contributions to the wet bias come from both the Atlantic and the Indian Oceans. The simulated Atlantic-Congo zonal overturning circulation dries the coast through its overestimated lower branch (LLWs) which moves further into the continent and advects more moisture to the eastern CA. In the meantime, during positive Indian Ocean Dipole

years, the advected moisture from the Indian Ocean to the CA region is overestimated in models, much more in coupled models and contributes to the eastern CA wet bias.

Key words:

Central Africa; MetUM; Rainfall Bias; Walker type circulation; Indian Ocean dipole; African Easterly Jet

Résumé

Bien que les modèles climatiques soient importants pour faire des projections du climat futur, jusqu'à présent, peu d'attention a été consacrée à la simulation par ces modèles du climat complexe de l'Afrique centrale (AC). Cette étude examine, à l'aide des processus atmosphériques qui gouvernent le climat de l'AC, les biais de précipitations dans huit (8) modèles climatiques de la phase 6 du projet d'intercomparaison des modèles couplés (CMIP6) ainsi que leurs prédecesseurs de la phase 5, en se concentrant sur le modèle unifié du Met Office (MetUM). En association avec une convergence irréaliste du flux d'humidité, des modèles tels que le modèle BCC-CSM surestiment les précipitations dans les deux versions, tandis que d'autres, comme le modèle GISS-E2, les sous-estiment. Pour ce qui est du modèle MetUM, l'étude montre que les deux versions du modèle dépeignent un biais humide (sec) à l'est (ouest côtier) de l'AC pendant la saison septembre-novembre, le biais humide (sec) étant plus fort dans les modèles couplés (atmosphériques). Nous explorons ici les causes potentielles de ces biais, qu'elles soient régionales ou à grande échelle. Les résultats révèlent que la surestimation de la branche descendante simulée de la cellule de retournement zonal de l'Atlantique-Congo est associée à un fort gradient de température et de pression près de la surface entre l'AC et l'océan Atlantique oriental. Ceci conduit à de forts vents d'ouest à basse altitude (LLWs) qui assèchent la côte ouest de l'CA et renforcent l'intensité de la cellule du bassin du Congo. À l'est de l'AC, le biais humide est partiellement dû à la mauvaise représentation de l'intensité des deux composantes du jet d'est africain qui déplacent la convergence du flux d'humidité de la moyenne troposphère vers le sud, favorisant une convection plus importante au sud de l'équateur. En outre, la surestimation de la largeur et de l'intensité simulées de la cellule du bassin du Congo est associée à une forte convergence de l'humidité à basse troposphère sur l'est de l'AC, ce qui contribue à davantage de précipitations. Les contributions à distance au biais humide proviennent à la fois de l'Atlantique et de l'océan

Indien. La circulation zonale de retournement Atlantique-Congo simulée assèche la côte par sa branche inférieure surestimée (LLWs) qui se déplace plus loin dans le continent et advecte plus d'humidité vers l'est de l'AC. En simultanée, pendant les années positifs du dipôle de l'océan Indien, l'humidité advectée de l'océan Indien vers la région de l'AC est surestimée dans les modèles, beaucoup plus dans les modèles couplés, et contribue au biais humide de l'AC oriental.

Mots clés:

Afrique Centrale; MetUM; Biais des précipitations; Circulation de type Walker; Dipôle de l'Océan Indien; Jet d'Est Africain

General introduction

Central Africa (CA) is dominated by the Congo River, the world's second largest river basin in terms of water discharges, abundant water resources, high per capita water availability, inland wetlands and lakes, and the second largest rainforest on Earth covering an area of $1.7 \times 10^6 \text{ km}^2$, that provide a range of socioeconomic benefits to local communities. The role of the Congo Basin in the Earth climate system is undisputed (Washington et al., 2013). The Basin is known as one of the three hot spots of major convective activity in the world (Webster, 1983), experiencing the highest lightning strike frequency of anywhere on the planet (Jackson et al., 2009) and receiving around 1500-2000 mm of rainfall per year (Dezfuli, 2017). This amount can be above 10,000 mm particularly near the coast, the center of the Congo basin, and on the mountain on the Western Rift Valley borders. In addition, its rainforest stores incredible amounts of carbon, preventing it from being emitted into our atmosphere and fueling climate change. At the local scale, through evaporation, tropical forests and woodlands exchange vast amounts of water and energy with the atmosphere, controlling the seasonality of rainfall in the region (Crowhurst et al., 2020). Furthermore, livelihood of populations in CA is strongly related to natural resources and agriculture (rain-fed agriculture, hydroelectric power, forestry resources, livestock, water resources management) and is highly dependent on climate.

Despite its importance, the climate of the region, compared to other regions of the World, has remained critically understudied (Hua et al., 2019) partly due to a lack of observational data (Washington et al., 2013; Creese and Washington, 2018). This creates a gap in the understanding of the global climate system and complicates analysis of its representation in climate models. In addition, based on the urgent need for action to tackle climate change, the Paris agreement has called to limit global warming to well below 2°C above pre-industrial levels and is pursuing efforts to limit the temperature

increase to 1.5°C (Masson-Delmotte, 2018). According to King and Harrington, 2018, for a 0.5°C global warming, equatorial regions, and especially CA, will experience the largest changes in local climate compared to extratropical areas. In the meantime, according to the latest IPCC report (Masson-Delmotte et al., 2021), in the whole Africa in general and Central Africa in particular, increases in heavy precipitation and pluvial flooding is likely to be observed with an increase in global warming. The means of adaptation and resilience are still underdeveloped. This is partly due to the poor knowledge of the regional climate system, and partly due to limited financial resources. However, the population of this part of Africa is already suffering from the consequences of increasingly extreme climatic phenomena, including floods and drought, which are consequences of the climate disruption observed over the past few decades. A better knowledge of the climate can allow to set up warning means and to take adequate measures to reduce the harmful consequences of its alteration. Numerical climate models are, for this purpose, tools that can provide additional information. This underlines the need for accurate projection of the future climate over the region to efficiently build mitigation and adaptation plans in order to reduce potential impact on CA countries where livelihoods mainly depend on climate. Since Global climate models (GCMs) are crucial to developing climate projections (Creese and Washington, 2016), it becomes urgent to better evaluate hindcasts in order to identify strengths, diagnose deficiencies and thereby improve them.

Several studies have assessed models over CA (Nikulin et al., 2012; Haensler et al., 2013; Washington et al., 2013; Saeed et al., 2013; James and Washington, 2013; Aloysius et al., 2016; Vondou and Haensler, 2017; Fotso-Nguemo et al., 2018; Tamoffo et al., 2018; Sonkoué et al., 2019). However, a lack of real progress in the new generation of climate models has been reported (Flato et al., 2013; Whittleston et al., 2017). Early efforts at climate models analysis were mostly restricted to a statistical evaluation. However, scalar metrics in climate model evaluation give information on the degree to which the model is far from the observation but does not yield the reason behind biases. Identification of misrepresentation of physical processes underlying model biases may help to explain why models fail and enable efforts to improve them (James et al., 2018).

Recent studies have started to apply a process-based approach to evaluate climate models over CA (Washington et al., 2013; Creese and Washington, 2016; Dyer et al., 2017; James et al., 2018; Creese and Washington, 2018; Tamoffo et al., 2019). Such studies are

useful for models development because they provide reasons for model errors by tracing processes which are not well simulated. Therefore, they provide to model developers directions for improvement of the next generation of climate models. This study aims to continue efforts on process-based evaluation of models over CA. First of all, investigations are focused on how models from the Coupled Model Intercomparison Project (CMIP) phases 5 and 6 simulate rainfall over CA. Secondly, investigation of simulated rainfall bias will emphasize both regional and large-scale features already identified as key contributors to climate variability over the region.

This dissertation is organised in three chapters: chapter 1 presents a general background of CA climate and poses research questions. In Chapter 2 we describe data used and computation methods applied to assess the model outputs. Chapter 3 shows and discusses findings of the study.

Chapter 1

Literature Review and Research questions

This chapter gives an overview of the Central African climate system. Over the region, features of the rainfall climatology are presented, as well as the drivers associated with rainfall variability. Together with a brief description, the importance of General Circulation Models (GCMs) is also discussed with a highlight of what the Coupled Model Intercomparison Project (CMIP) is. Finally, a brief review of climate model evaluation over Central African region is done follow with some research questions.

1.1 Central Africa (CA) rainfall variability

1.1.1 The hydrological cycle in CA

The CA region experiences the well-known bimodal rainfall distribution (Fig.1). The peaks rainfall are found during the transition seasons of September to November (SON) and March to May (MAM) with the SON season wetter than MAM season. The timing of the rainy seasons was first associated with the north-south displacement of the tropical rainbelt, often broadly referred to as the movement of the Inter Tropical Convergence Zone (ITCZ). Although that former theory has been contradicted, considerable studies have established the connection between the seasonal cycle and amount of precipitation with that of moisture convergence (e.g. Muller et al., 2009; Shi et al., 2014). Recent work (Pokam et al., 2012; Washington et al., 2013; Creese and Washington, 2016; Dyer et al., 2017) have clearly shown that these MAM and SON peak rainfall are linked to peaks of

moisture convergence at these times of year.

In fact, moisture flux, through complex feedback mechanisms, determine the rainfall amount and is linked to dry or wet conditions (Yin et al., 2013). In line with this, findings from Creese and Washington (2016) has demonstrated a strong positive correlation between precipitation and moisture flux convergence at 700 hPa in MAM, and at 850 hPa in June–August (JJA), September–November (SON), and December–February (DJF).

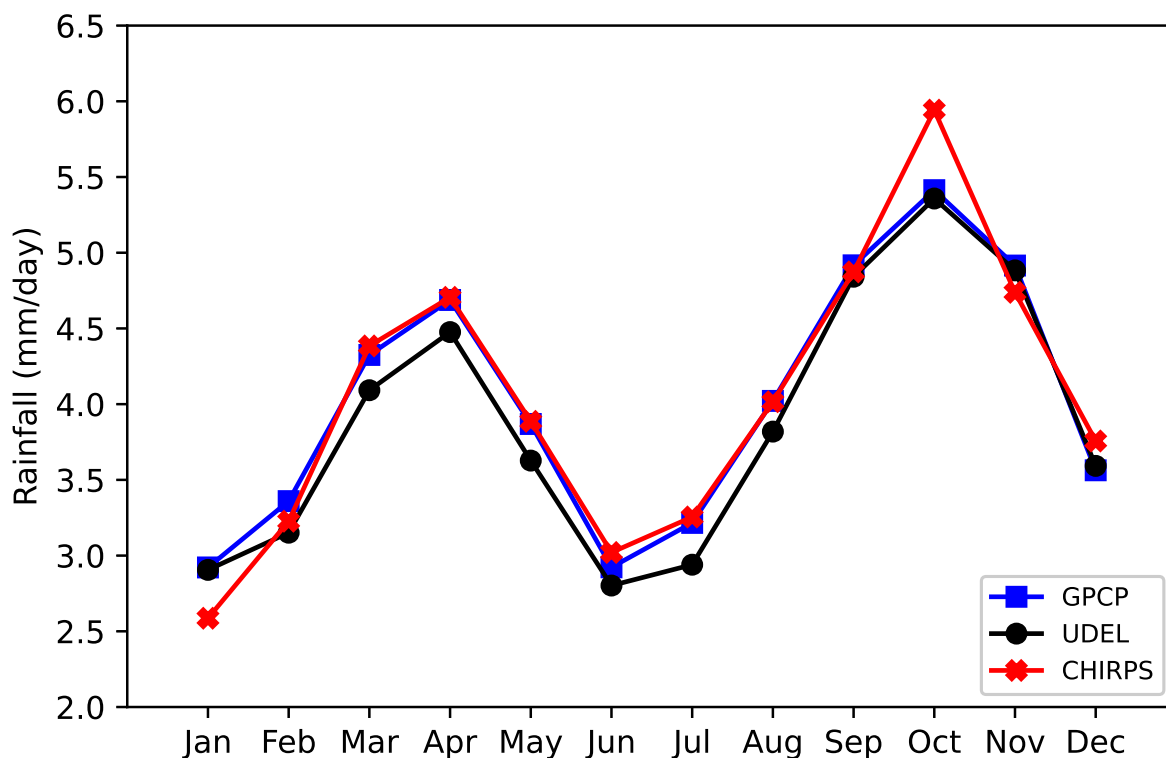


Figure 1: Rainfall climatological annual cycle in Central Africa from GPCP, UDEL and CHIRPS. Rainfall is averaged between 10° S– 10° N and 10° E– 30° E.

1.1.2 Seasonal spatial rainfall distribution

The annual mean rainfall over Central Africa consists of a zone of intense convective activity centered on the equator, which extends southward and covers almost all the Congo forest, making this area one of the three key convective regions on the planet in which the transition seasons dominate global tropical rainfall (Washington et al., 2013). However, there is a strong season-to-season variability in spatial patterns of rainfall (Fig.2).

In CA, rainfall oscillates meridionally, crossing the equator twice a year during the

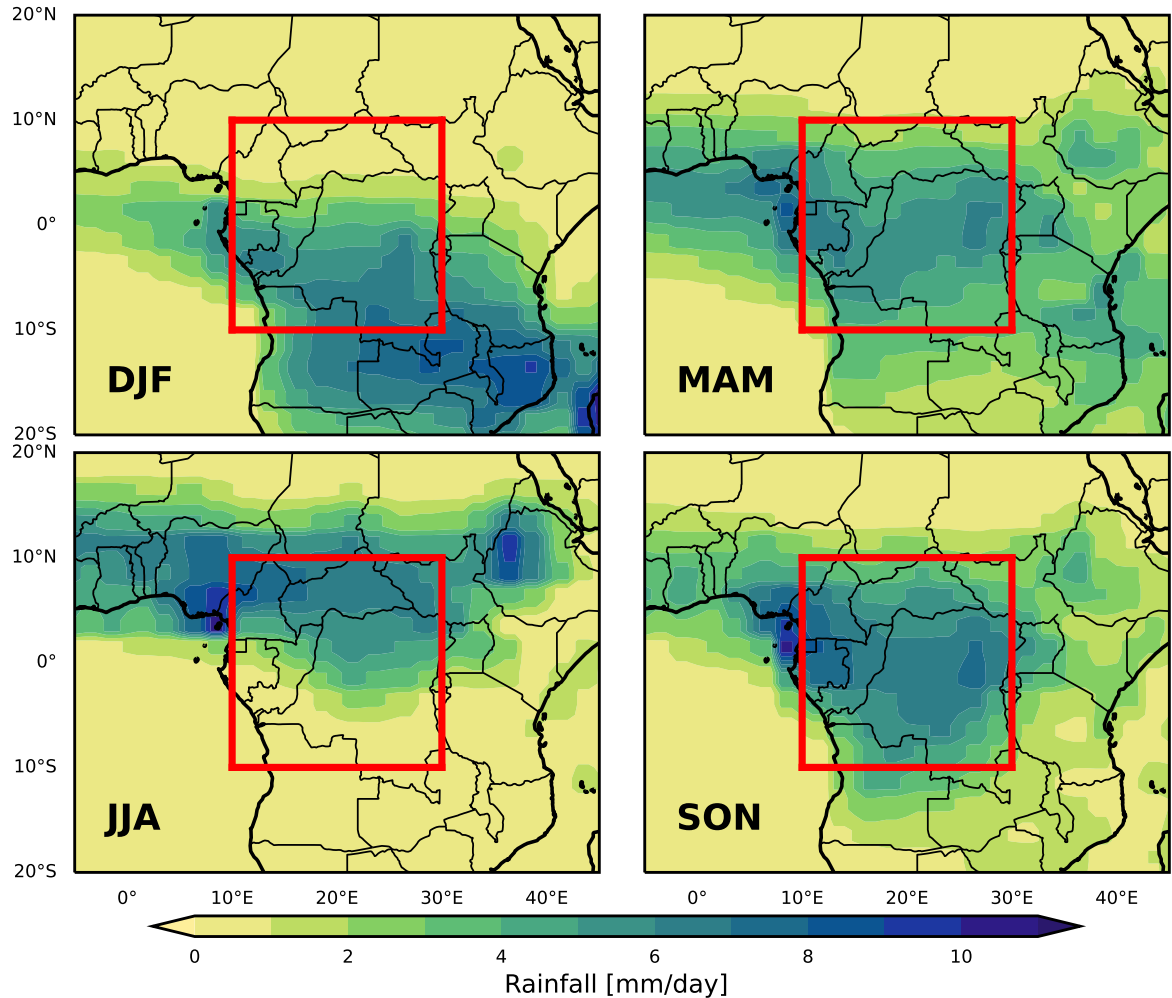


Figure 2: Spatial distribution of the long term (1981-2015) seasonal mean rainfall ($\text{mm}\cdot\text{day}^{-1}$) in Central Africa from GPCP. The red box shows the main CA domain (10°S – 10°N ; 10°E – 30°E .)

transition seasons of March to May (MAM) and September to November (SON), with dry seasons in June to August (JJA) and December to January (DJF). The peak of the rain belt shifts from the north to the south of the equator during November–December and returns to the north during March–April. During the SON (long rains) season, precipitation events tend to be heavier and longer in duration, while the MAM (short rains) season is characterized by less intense precipitation events of shorter duration (Sandjon et al., 2012). Findings from Jackson et al. (2009) have suggested that this is due to enhanced mesoscale convective system activity. The zone of maximum rainfall occurs broadly over the western central African region, covering almost the entirety of the Congo forest (Pokam et al., 2012) and coinciding with a locus of intensive convective activity (Sandjon et al., 2012). During the transition seasons, March to May (MAM) and

September to November (SON), it is the wettest place on earth (Xie and Carton, 2004).

1.2 Atmospheric features associated with CA rainfall variability

Some key features of the CA climate regime such as the low-level westerlies (LLWs) and the African easterly jet (AEJ) components (north and south) are shown in Figure 3. Their description, together with other features is given in the following. Furthermore, details on the role they play in modulating the CA rainfall variability is highlighted.

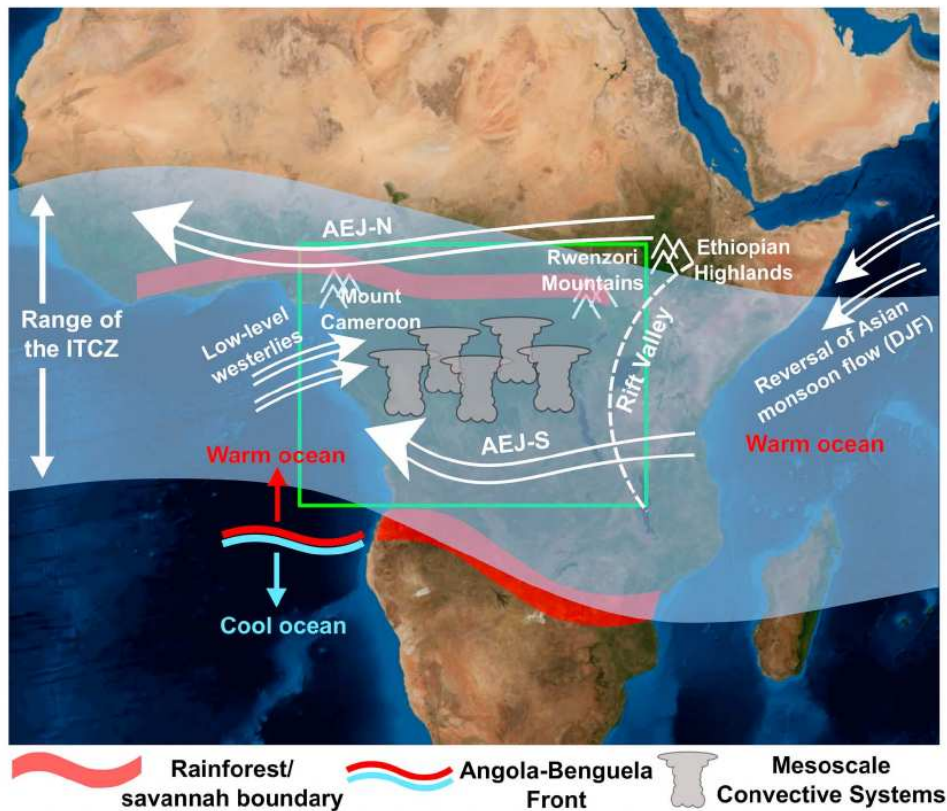


Figure 3: Schematic showing key features of the Congo Basin climate. Locations are approximate. The study area is shown by the green box. AEJ-N = African easterly jet north and AEJ-S = African easterly jet south (Creese and Washington, 2016).

1.2.1 Low-level westerlies (LLWs)

Low-level westerlies (LLWs) are associated with the southeasterly trades on the north-eastern flank of Saint Helena (South Atlantic) high. Due to the Coriolis force, the

southeasterlies recurve and become westerlies when crossing the equator (Pokam et al., 2014). Nicholson and Grist (2003) suggested that the strength of equatorial westerlies is related to the sea level pressure associated with the South Atlantic High (SAH). However, in investigating the drivers of LLWs, Pokam et al. (2014) split the zonal wind into its divergent and rotational component and found that north of 6°N in CEA, LLWs are primarily a rotational flow forming part of the cyclonic circulation driven primarily by the heat low of the West African monsoon system. This northern arm of the LLW is well-developed from June to August. It weakens during September–November, disappears in the December–February season and originates in the March–May season (Fig.4). South of 6°N , the circulation is dominated by the divergent component and the seasonal variability of the LLW is controlled by the zonal land-sea thermal contrast near the equator.

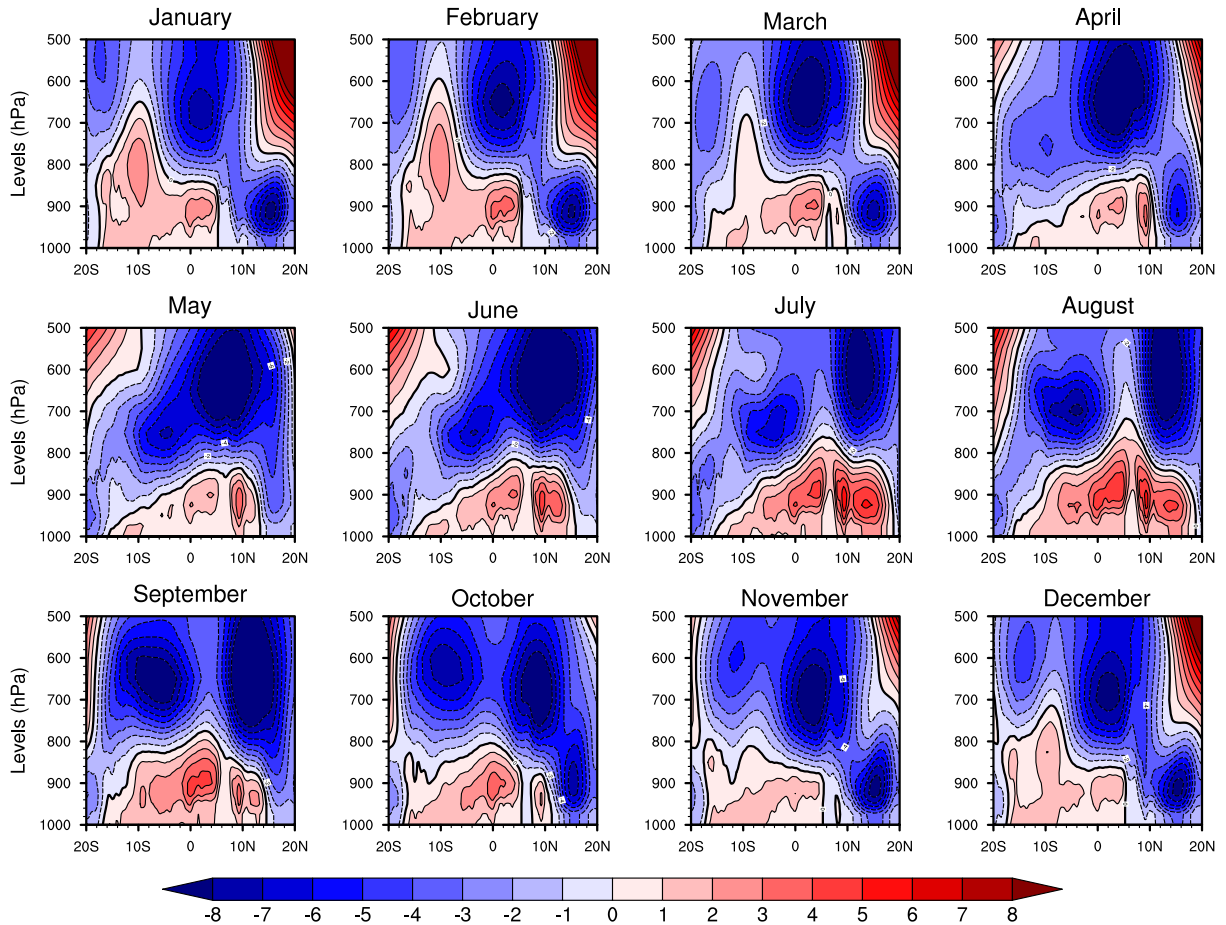


Figure 4: Long term (1980–2010) monthly mean zonal wind speed ($\text{m}\cdot\text{s}^{-1}$), averaged between 10°E and 15°E . Positive (negative) values represent westerly (easterly) winds.

By advecting moisture from the Atlantic ocean to the CEA region, the strength of LLWs is related to rainfall variability in the region where wet years exhibit a distinct

westerly jet during both wet seasons (Dezfuli and Nicholson, 2013; Nicholson and Dezfuli, 2013). This makes LLWs an essential circulation feature in CA.

1.2.2 Regional atmospheric jets

There exist a set of atmospheric jets that exist at various vertical levels and also contributing to the region's climate variability by modulating the moisture transport and vertical motion. These include the upper-level Tropical Easterly Jet (TEJ) and the midlevel African Easterly Jet of the Northern Hemisphere (AEJ-N) and the Southern Hemisphere (AEJ-S) as shown in (Fig.5) from Tamoffo (2020).

1.2.2.1 African Easterly Jets (AEJs)

The Northern African Easterly Jet (AEJ-N), which is perhaps known primarily for its crucial role in generating the African Easterly Waves (AEWs) and organized moist convection in the West African Monsoon (WAM) system, develops in response to the meridional temperature gradient caused by the land–sea contrast between the warm Sahara and the cool Gulf of Guinea (Paradis et al., 1995; Hsieh and Cook, 2005; Hall et al., 2006). The AEJ-N is strongest during June–September, and its core appears at about 600 hPa, between 10 and 15N, with a maximum speed of 10–12 m/s. The AEJ-N is mainly a product of the shallow meridional circulation driven by the Saharan heat low and deep moist convection within the rainbelt, located equatorward of the jet (Thorncroft and Blackburn, 1999). However, other studies have suggested that the meridional gradient in soil moisture and associated land surface properties also exerts significant control on the jet (Cook, 1999; Wu et al., 2009). Although the jet is most active within the WAM region, its tail extends eastward within the longitude of CA, and in some years it is manifested as a separate core from the western sector (Dezfuli and Nicholson, 2011). The AEJ-N is recognizable throughout the year, though it weakens and moves equatorward between October and March, when its core is located between 0 and 5N, and its maximum speed reduces to 8 m/s compared to its peak in summer.

The Southern African Easterly Jet (AEJ-S), however, is best discernible in August–November (Diedhiou et al., 1999; Nicholson and Grist, 2003). Its position varies between 10S and 5S at 600–700 hPa, and its maximum core speed is about 9 m/s in October. Although the AEJ-S is weaker and more zonally confined than the northern

jet, its existence is also a result of the reversal of the surface temperature gradient. The maximum meridional temperature gradient is evident between the semiarid Kalahari to the south and the humid rainforest of CA to the north. Nicholson and Grist (2003) noted that the rainbelt during August–November, when both AEJs are present, is approximately bound by the axes of the two jets. The AEJ-S and its associated secondary circulation also play a role in aerosol transport off the continent (Adebiyi and Zuidema, 2016).

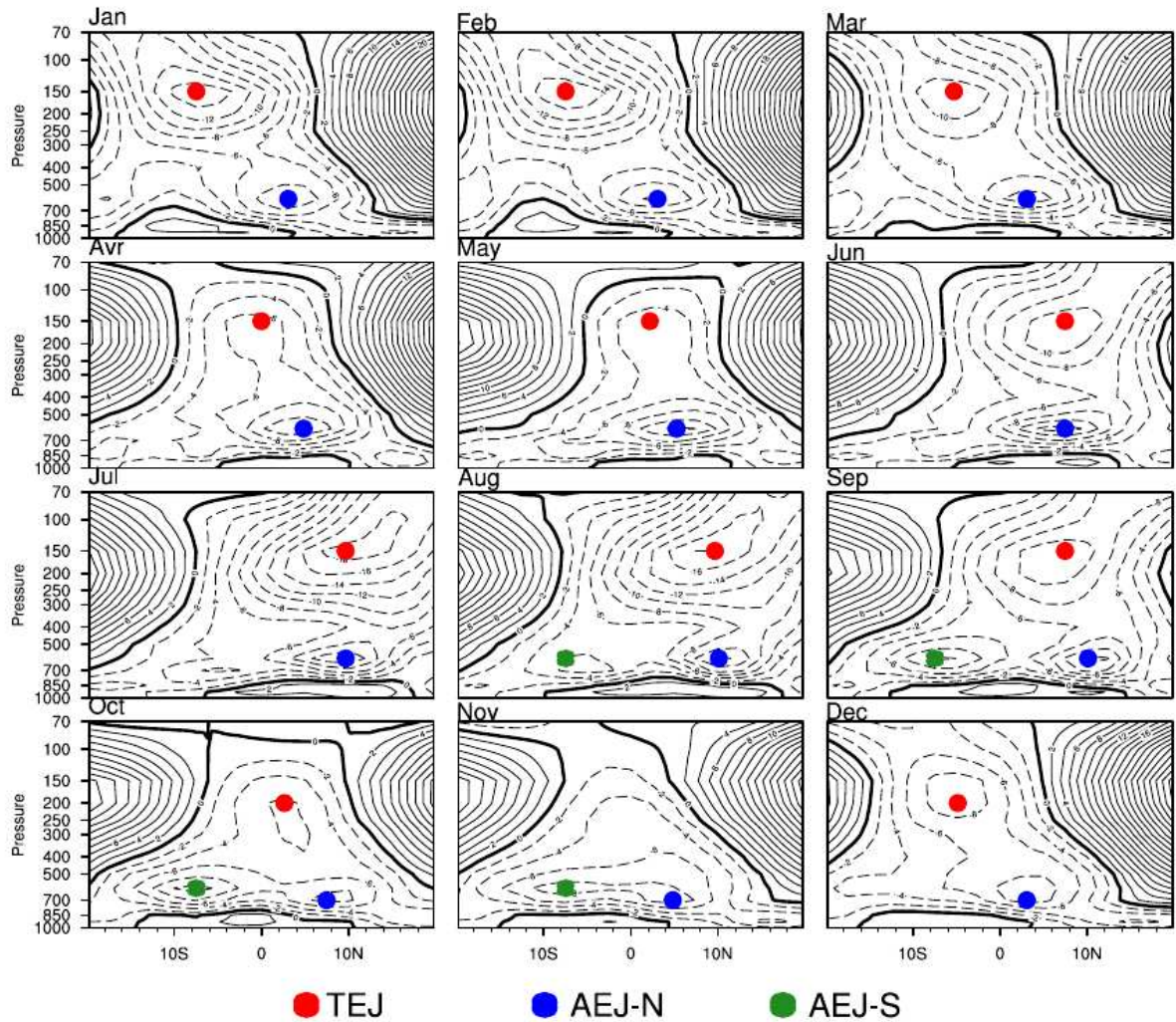


Figure 5: Annual cycle of the mean zonal wind speed ($m.s^{-1}$), averaged over the longitude band 10° - 30° E. Red, Blue and Green points display respectively the mean position of TEJ, AEJ-N and AEJ-S cores (Tamoffo, 2020).

1.2.2.2 Tropical Easterly Jet (TEJ)

Another important feature of the circulation in the region is the TEJ, which develops as a response to the intense meridional temperature gradient between the Himalayan

Plateau and the Indian Ocean during boreal summer and extends to the African continent (Koteswaram, 1958). During the month of August, its maximum speed is about 16 m/s at 200 hPa and 10°N along the western boundaries of CA (Fig.5). The jet's left exit zone is collocated with the northern part of CA and may provide a mechanism of rainfall variability over that region (Nicholson and Grist, 2003). The westward extension of the TEJ over the West African Monsoon (WAM) region seems to be at least partly a result of the Coriolis force acting on the equatorward outflow of deep convection just to the north of the jet (Thorncroft and Blackburn, 1999). The upper-level easterly flow is evident in the equatorial latitudes all year round. However, it is weak during the transition seasons when it crosses the equator, and it exhibits a secondary maximum during January and February when it reaches its southernmost position at around 7°S (Nicholson and Grist, 2003). This secondary maximum speed of the easterly flow is usually not considered part of the TEJ; it is attributed to the equatorward branch of the upper-level flow that is deflected westward by the Coriolis force, a process similar to that suggested by Thorncroft and Blackburn (1999) for the Northern Hemisphere. The upper-level flow in transition seasons, although it is weaker than in boreal winter and summer, contributes strongly to rainfall variability by modulating the vertical motion by altering the upper-level divergence (Dezfuli and Nicholson, 2013; Nicholson and Dezfuli, 2013).

1.2.3 Congo basin cell

Many studies (Pokam et al., 2014; Cook and Vizy, 2016; Neupane, 2016) have suggested the presence of a zonal shallow overturning cell over central Africa. The cell was finally highlighted by Longandjo and Rouault (2020) and they denoted it the Congo basin cell (Fig.6). It is a closed, counterclockwise and shallow zonal overturning cell that is confined at the lower troposphere (between the surface and 800 hPa) and is active throughout the year. LLWs form the lower base of the cell and similar to LLWs, the Congo Basin cell intensity and width are driven by the near-surface temperature warming on both the central African landmass and the eastern equatorial Atlantic. The cell's maximum (minimum) intensity and width are registered in August/September (May). As shown by Longandjo and Rouault (2020) the eastern edge of the cell is associated with the Congo Air Boundary, a convergence zone where the low-level jets from the equatorial Atlantic, having crossed the central African landmass, meet the Indian monsoon system

easterlies to form the ascending branch of the cell. It is a zone of maximum convection and precipitation in the region. The zonal rainfall maximum position in the region is then modulated by the width of the Congo basin cell.

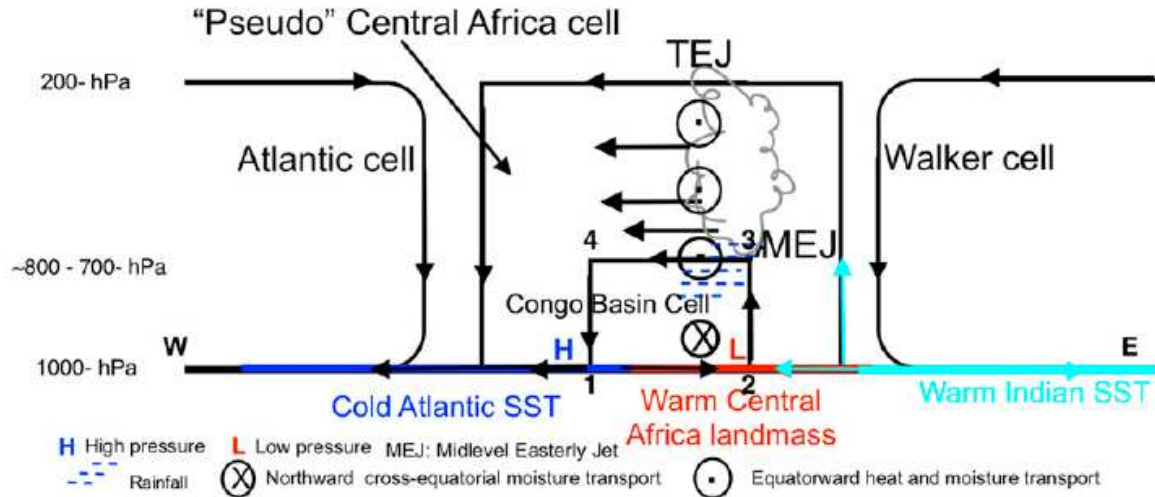


Figure 6: Schematic diagram of the zonal large-scale circulation over central Africa and its surrounding oceans as proposed in Longandjo and Rouault (2020). The Congo basin cell acts a small heat engine, transporting latent and sensible heat from the warm central Africa landmass to the cold equatorial Atlantic, reminiscent of a mixed Carnot–steam cycle.

1.2.4 Neighbouring Oceans and associated circulations

The CA regional climate is modulated and influenced by the adjacent Atlantic and Indian Oceans, where variability in SSTs can influence moisture availability, moisture advection, and the static stability of the lower troposphere (Balas et al., 2007; Pokam et al., 2014; Dyer et al., 2017).

1.2.4.1 Atlantic Ocean and its Atlantic-Congo Walker like circulation

The impact of the sea surface temperature (SST) changes in eastern equatorial Atlantic on rainfall variability of the coastal part of CA has been long recognized (Hastenrath, 1984; Hirst and Hastenrath, 1983; Nicholson and Entekhabi, 1986, 1987; Okumura and Xie, 2006; Dezfuli and Nicholson, 2013; Nicholson and Dezfuli, 2013). Coastal rainfall in CA has been found to be enhanced in years with positive SST anomalies (SSTAs), and suppressed in years with negative SSTAs, in response to both indirect atmospheric

mechanisms and direct local forcings (Nicholson and Entekhabi, 1987; Nicholson and Dezfuli, 2013) such as the thermodynamics consequences of the SST pertaining to the

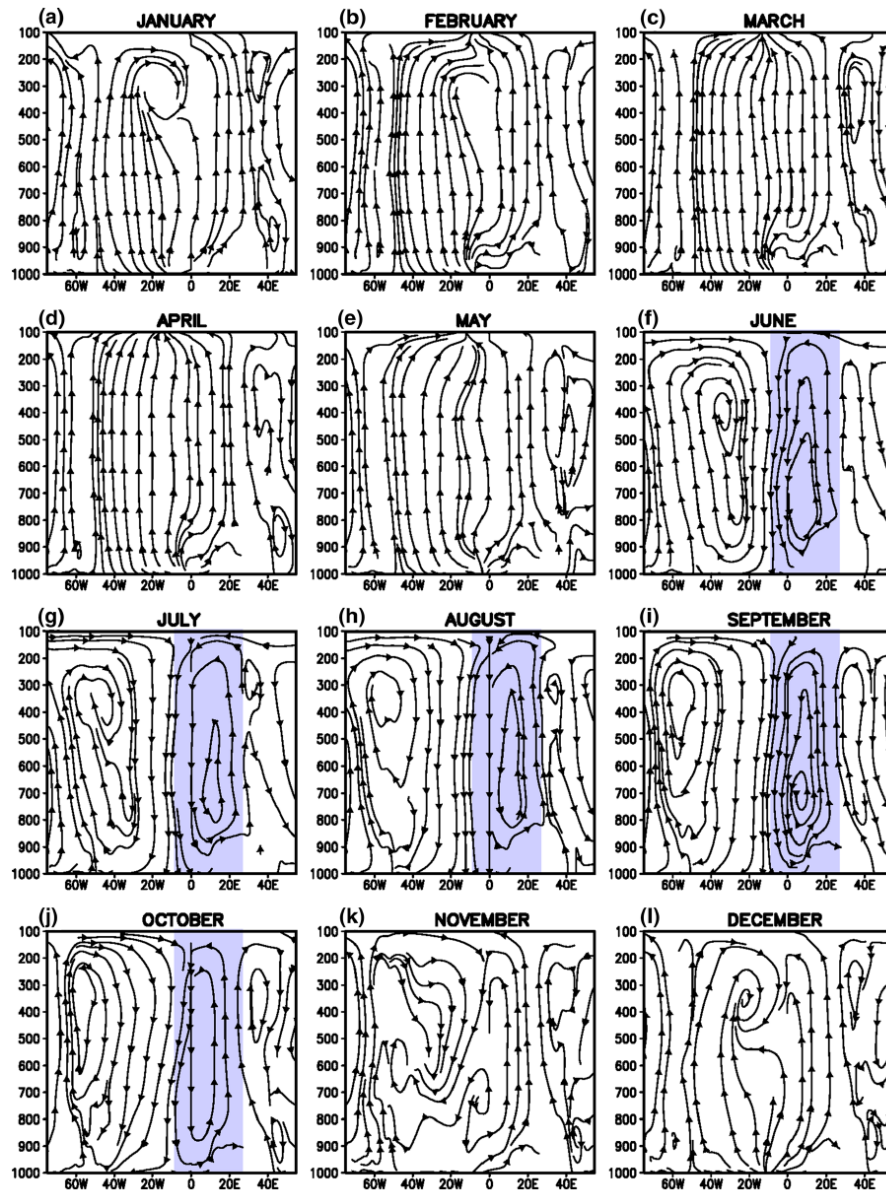


Figure 7: Monthly streamline cross sections constructed from the divergent component of the zonal wind ($m.s^{-1}$) and the vertical- p velocity ($10^{-2}.Pa.s^{-1}$) averaged between $3^{\circ}S$ and $3^{\circ}N$ from the ERAI climatology (1979–2014) (Cook and Vizy, 2016).

moisture content and static instability in the lower troposphere. The local SST variability has been attributed to various interrelated components of the tropical Atlantic variability. For example, during an Atlantic Niño, relaxation of the equatorial trade winds in the midbasin is associated with warm SST anomalies in the eastern basin. Climate features in the tropical Atlantic also include the Atlantic cold tongue, and the south Atlantic High (SAH) (Nobre and Shukla, 1996; Xie and Carton, 2004; Okumura and Xie, 2006)

Variability in Atlantic SSTs has also been found to modulate a local Atlantic-Congo Walker circulation (Fig.7), where warm SSTAs result in enhanced evaporation, enhanced low-level onshore flow and enhanced convection over the continent (Cook and Vizzy, 2016; Neupane, 2016). The zonal overturning circulation along the equator connects rising motion in the Congo Basin and sinking in the eastern Atlantic. This zonal overturning circulation over the Congo basin (15° – 25° E, 3° S– 3° N), which is forms only from June to October (Cook and Vizzy, 2016), occurs when the Atlantic cold-tongue sea surface temperature (SST) matures to set up favorable atmospheric conditions for its development (Cook and Vizzy, 2016). The up-branch is located in the Congo basin around 20° E. Mid-tropospheric easterly flows constitute the returning-branch and sinking over the Gulf of Guinea forms the down-branch, which diverges at 2° W near the surface, with winds to the east flowing eastward to complete the circulation. This circulation is driven by surface temperature differences between the eastern Gulf and Congo basin. When cold tongue SSTs are anomalously cool (warm), evaporation from the ocean surface is reduced (enhanced) and the westerly flow advects less (more) moisture into the base of the Congo Basin Walker circulation. This reduces (increases) the release of latent heat in the up branch and weakens (strengthens) the Walker circulation.

1.2.4.2 Indian Ocean and its overturning circulation

The Indian Ocean also influences the climate of the Congo Basin and adjacent regions (Hastenrath, 2000; Black et al., 2003; Ummenhofer et al., 2009; Dyer et al., 2017). Variability in rainfall over the Indian Ocean region is dominated by the monsoon systems, which produce southeasterly flow along the east coast of Africa during boreal summer, and northeasterlies during boreal winter (Schott et al., 1997; Schott and McCreary Jr, 2001). These easterly flows directly affect moisture advection into the region, which in turn is modulated by the East Africa Highlands, which are likely to block some moisture penetrating inland to the Congo Basin (Van der Ent et al., 2010). Dyer et al. (2017), using the Community Earth System Model, identified the Indian Ocean as a dominant oceanic moisture source for the Congo Basin, contributing 21% during the rainy seasons.

Variability in Indian Ocean SSTs has long been linked to variability in East African rainfall (Beltrando and Camberlin, 1993; Goddard and Graham, 1999; Endo and Tozuka, 2016). The Indian Ocean Dipole (IOD), an SST phenomenon which features warm SSTAs

in the west Indian Ocean and cold SSTAs in the east during its positive phase, has been linked to both East and Central African climate variability (Ogallo and JE, 1988; Ummenhofer et al., 2009; Dezfuli and Nicholson, 2013; Moihamette et al., 2022) through the Indian Ocean Walker Circulation (IOWC).

The latter is a mean state zonal overturning cell located over the equatorial Indian Ocean. A strong gradient of SST anomalies in the Indian Ocean during the IOD phenomenon modulates the atmospheric circulation by weakening (strengthening) the Walker cell during positive (negative) IOD events (Black et al., 2003). As highlighted in Moihamette et al. (2022) during extreme positive IOD events (hereafter pIOD), CA experiences enhanced moisture supply from the Indian Ocean that results in increased rainfall while the opposite process is recorded during the negative phase (hereafter nIOD), with the magnitude of pIOD events anomalies stronger than those of nIOD events. Furthermore, the inflow is strongest in the lower troposphere over the ocean while it is strongest in the mid-troposphere over CA because much of the lower-level inflow is blocked by the topography to the east of CA.

1.3 General circulation model (GCMs)

A climate model is a more or less idealized representation of the climate system based on the mathematical equations called primitive equations of the mechanics of the fluids and thermodynamics and on the parameterization of the phenomena of sub-meshes. It is a primary means for scientists to understand how the climate has changed in the past and may change in the future. Thus, to represent the atmospheric processes, we use the discretization of space on the horizontal vertical and temporal planes (Fig.8). The model therefore solves the equations in a three-dimensional space (altitude, latitude, longitude) forming meshes (or grid points).

General circulation models (GCMs) are models that simulate the evolution of climate on a global scale and over the long term. A few years ago, GCMs only included a representation of the atmosphere, the land surface, sometimes the ocean circulation, and a very simplified version of the sea ice. Nowadays, GCMs take more and more components into account, and many new models now also include sophisticated models of the sea ice, the carbon cycle, ice sheet dynamics and even atmospheric chemistry. General circulation models (GCMs) are grouped into three categories: Atmospheric General Circulation

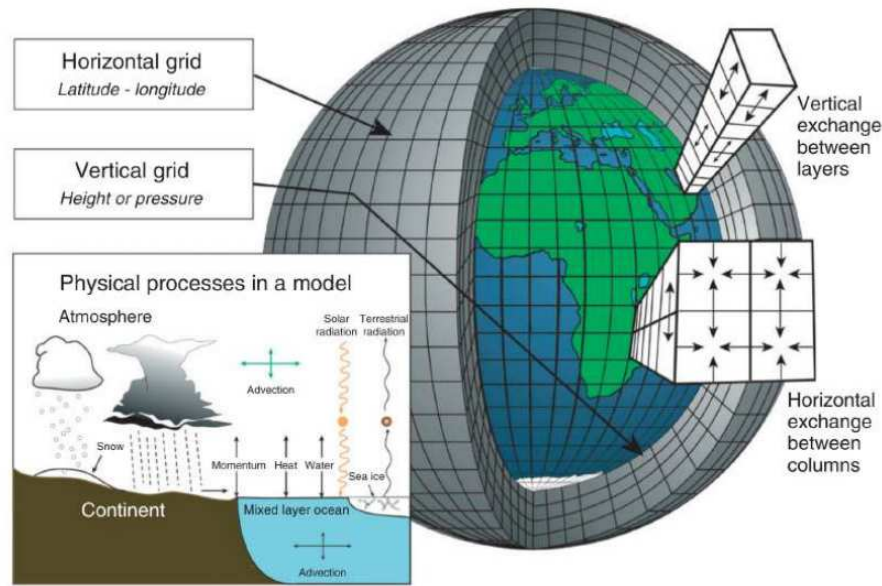


Figure 8: *Conceptual diagram of how a numerical model works (Fig.2 in Edwards (2011)).*

Models (AGCMs), Oceanic General Circulation Models (OGCMs) and Coupled atmosphere-ocean General Circulation Models (CGCMs).

1.3.1 Coupled General Circulation Models (CGCMs)

The most advanced tools that are currently available for simulating the current climate and the climate response to external natural and human-made perturbations are coupled or atmosphere-ocean general circulation models (CGCMs or AOGCMs). A CGCM combine both an Atmospheric General Circulation Models (AGCM) and an Oceanic General Circulation Models (OGCM). It describes all components of the climate system and their interactions in sufficient detail (Soldatenko et al., 2021). In recent decades, the development of AOGCMs has been marked by significant progress due to both advances in the study of the climate system itself and an increase in computing resources, which provide ever greater detail and completeness of the descriptions of climatically significant processes. Present-day developments in computer technology provide the ability to numerically integrate AOGCMs for many hundreds of years. In addition, They have evolved since the 1970s with a considerable improvement in their resolution and a better consideration of new components of the climate system (convection, clouds and precipitation, aerosols, atmospheric chemistry, etc).

1.3.2 Coupled Model Intercomparison Project (CMIP)

The Coupled Model Intercomparison Project (CMIP) is organized under the auspices of the World Climate Research Programme’s (WCRP) Working Group on Coupled Modelling (WGCM). It started 20 years ago as a comparison of a handful of early global coupled climate models performing experiments using atmosphere models coupled to a dynamic ocean, a simple land surface and thermodynamic sea ice (Meehl et al., 1997). In response to a growing need to systematically analyze coupled ocean and atmosphere model outputs from multiple climate modeling centres, it has subsequently grown into a large program to advance model development and scientific understanding of the Earth system. It has since evolved over six phases into a major international multi-model research activity (Meehl et al., 2000, 2007; Taylor et al., 2012) that has not only introduced a new era to climate science research but has also become a central element of national and international assessments of climate change (e.g. IPCC, 2013).

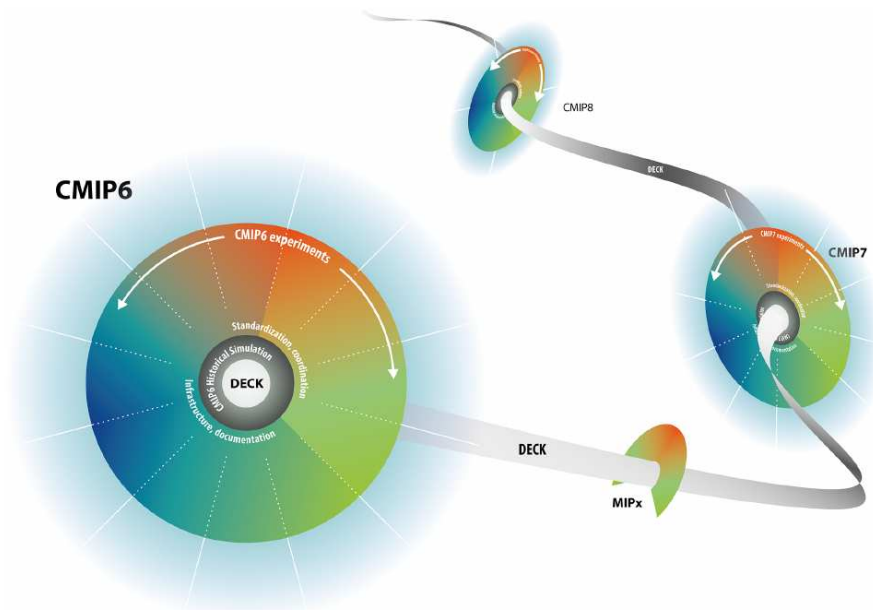


Figure 9: *CMIP evolution. CMIP will evolve but the DECK will provide continuity across phases (Eyring et al., 2016).*

Figure 9 shows the evolution of the CMIP project with a handful of common experiments (DECK: the Diagnostic, Evaluation and Characterization of Klima) involves in forthcoming phases (klima is Greek for “climate”). The objective of CMIP is to better understand past, present, and future climate change arising from natural, unforced variability

lity or in response to changes in radiative forcings in a multi-model context. To meet these new goals, CMIP has developed well-defined climate model experiment protocols, formats, standards, and distribution mechanisms to ensure model output availability to a wide research community. The standardization of the model output in a specified format, and the collection, archival, and access of the model output through the Earth System Grid Federation (ESGF) data replication centres have facilitated multi-model analyses. The IPCC sixth Assessment Report (Masson-Delmotte et al., 2021) openly acknowledged a heavy reliance on CMIP phase 6 (Eyring et al., 2016). Dr David Carlson, Director of WCRP, emphasizes that “it’s really not possible to conceive or sustain the entire international climate research, assessment and negotiation processes without a community effort like CMIP at the heart of it.”

1.4 Climate model evaluation

The African continent is increasingly recognised as a priority for climate model improvement, given its importance for global climate and the comparative lack of attention it has received from the climate science community (James et al., 2018). In this line, climate model evaluation is of importance because it helps to highlight weaknesses of models, which give directions for improvement. Model evaluation approaches are diverse, but they can be divided into two groups: quantification of model performance and analysis of physical processes (James et al., 2018).

1.4.1 Performance-based evaluation

This is the most common method of model evaluation, and it involves comparing the output of individual models in the historical period with observational and reanalysis data in the variables of interest (sometimes known as ‘hindcast validation’) (Boer and Lambert, 2001; Taylor, 2001; Reichler and Kim, 2008). Checking a model’s capacity to replicate known climate is an important part of model evaluation, since it identifies model biases and helps to direct model development efforts (Flato et al., 2013). Regular hindcast validation of progressive model versions also allows for tracking the development of models over time (Reichler and Kim, 2008). To quantify the differences between models and observations, standard statistical tests such as mean square error (MSE), root-mean

square error (RMSE), and correlation are used, and these can be represented in a variety of ways (e.g. Taylor diagrams Taylor, 2001). Models are typically tested for their ability to represent the variable's climatological mean state, but they can also be examined for other properties such as temporal variability. Some research have sought to develop a standardized set of 'performance metrics' that can be used to objectively assess model suites (e.g Gleckler et al., 2008; Baker and Taylor, 2016). Performance-based evaluation methods frequently calculate a 'skill-score' for individual models, which can be used to rank models and to assess models' performance relative to one another (e.g Watterson et al., 2014).

However, despite its importance, the performance-based evaluation method is limited because while comparisons to observations help to identify biases in models, they are on their own unable to demonstrate the causes of biases, or point to possible fixes (Gleckler et al., 2008; James et al., 2018). In other words, scalar metrics in climate model evaluation give information on the degree to which the model is far from the observation but does not yield the reason behind biases.

1.4.2 Process-oriented assessment

In response to the issue outlined at the end of the preceding section, there has been increasing recognition over the last decade that understanding model simulations at a process level is the key to assessing model reliability (Niznik and Lintner, 2013; Guilyardi et al., 2009; Kim et al., 2009; Jiang et al., 2012). Process-based assessments are used primarily in two ways: to investigate the ability of models to represent physical processes which are known to be important to the climatological variable of interest; and to determine the processes which cause model differences and biases. In the context of intercomparison projects, such as CMIP, process-based evaluation often proceeds by examining the differences in the representation of key dynamics, or features, amongst models and compared to some observational reference, commonly reanalysis estimates of circulation. Such an approach to evaluation contains a number of key benefits, including: a more meaningful assessment of model reliability (as opposed to performance-based approaches); demonstration of essential areas for model improvement; and the potential to guide observations and generate hypotheses concerning the functioning of the real climate system.

This is particularly valuable in cases where a model deficiency can be firmly linked to the simulation of a variable of interest. Previous work has shown, for example, that global scale biases in rainfall can be linked to the inadequate representation of orographic drag in models (Berckmans et al., 2013; Pithan et al., 2016; van Niekerk et al., 2016), to cloud biases in the Southern Hemisphere (Hwang and Frierson, 2013) and to biases in the representation of Antarctic sea ice extent (Bracegirdle et al., 2013). Such evaluations can set the priorities for model development because the identification of misrepresentation of physical processes underlying model biases may help to explain why models fail and enable efforts to improve them (James et al., 2018). That is why, in this thesis, a process-based approach to evaluating climate models is adopted.

1.5 Process-oriented assessment in CA and research questions

Recent studies have started to apply a process-based approach to evaluate climate models over CA (Washington et al., 2013; Creese and Washington, 2016; Dyer et al., 2017; James et al., 2018; Creese and Washington, 2018; Tamoffo et al., 2019). Findings from Creese and Washington (2018) show that, over the Atlantic Ocean, models combining larger and more equatorward sea surface temperature (SST) bias, higher evaporation and higher local convection lead to wet bias in the western CA. They also found that underestimation of the simulated strength of northern component of African easterly jet (AEJ-N) leads to wet bias over eastern CA while an overestimation of the strength of AEJ-N may suppress convection and lead to a dry precipitation bias. Furthermore, they have concluded that, overestimation of the simulated Indian Ocean overturning cell may also contribute to an overestimation of both subsidence over the western Indian ocean and convection over the eastern CA. Tamoffo et al. (2019) found that overestimation of the strength of simulated AEJ components favour mid-level moisture divergence which dries mid-tropospheric layers over CA and in turn induces a dry precipitation bias. It has also been established (Washington et al., 2013; Creese and Washington, 2016) that there is a strong relationship between simulated rainfall and moisture flux convergence over CA. Therefore simulated moisture transport is a good candidate for understanding precipitation bias. Findings from Pokam et al. (2014) show that low-level westerlies

(LLWs) from the eastern Atlantic Ocean is an important source of moisture over CA. However, as demonstrated by James et al. (2018), an overestimation on the strength of simulated LLWs in models leads to dry precipitation bias over the coastal region in CA. It clearly appears from these studies that rainfall biases could be reduced by improving simulated SST, both wind convergence and divergence, moisture transport and/or Walker type circulations. Such studies are useful for models development because they provide reasons for model errors by tracing processes which are not well simulated. Therefore, they provide to model developers directions for improvement of the next generation of climate models.

This study aims to continue efforts on process-based evaluation in models over CA. In light of the foregoing, this thesis aims to answer the following questions:

- How is the Central Africa (CA) rainfall represented in CMIP5 and CMIP6 models?
- Is there an improvement in CMIP6 compared to CMIP5 models?
- Do the rainfall associated mechanisms explain changes in models' behaviour?

Attention will be particularly put on the Met Office Unified Model (MetUM) which is currently a particular focus of model development as part of the Improving Model Processes for African Climate (IMPALA) programme.

1.6 Conclusion

This chapter presents the state of knowledge of the climate system over CA. Over the region, features of the rainfall climatology are presented, as well as the drivers associated with rainfall variability. These drivers are the north and south components of the African Easterly Jet, the Tropical Easterly Jet, the lower level westerlies, the Congo basin cell and the overturning circulations located in the Atlantic and Indian oceans. A description and a presentation of different kinds of General Circulation Models (GCMs) is also discussed with a highlight of what the Coupled Model Intercomparison Project (CMIP) is. Finally, a brief review of climate model evaluation over Central African region is done follow with some research questions.

Chapter 2

Study area, Data used and Methodology

This chapter starts in locating and describing the study area. Then, models and observational data used for analyses are outlined. Lastly, the chapter closes in presenting the approach used to understand models biases and the metrics used for investigations.

2.1 Study area

2.1.1 Location and topography

The analysis focuses on CA, a geographic entity consisting of plateaus with complex land cover, river basins, and extending from latitudes 10°S to 10°N and longitudes 10°E to 30°E (Figure 10, red boxes). The region encompasses a number of countries including Gabon, the Republic of Congo, Cameroon, and the Democratic Republic of Congo (DRC), which is by far the largest in the region.

The region is located to the west of the East African highlands, and extends towards the Atlantic coast to the west. The landscapes of Central Africa are most often wide plateaus, which are smooth in the central part and etched at the periphery. The basin contains some marshlands in the region where the Congo, Ubangi, Likouala, and Sangha rivers converge and where Lakes Mai-Ndombe and Tumba are found. Its major part, however, consists of drier surfaces (low plateaus or alluvial terraces). Higher plateaus, which extend through older sedimentary strata around the centre of the Congo basin, reach an elevation of 2,600 to 3,000 feet (790 to 900 metres) north of Brazzaville and

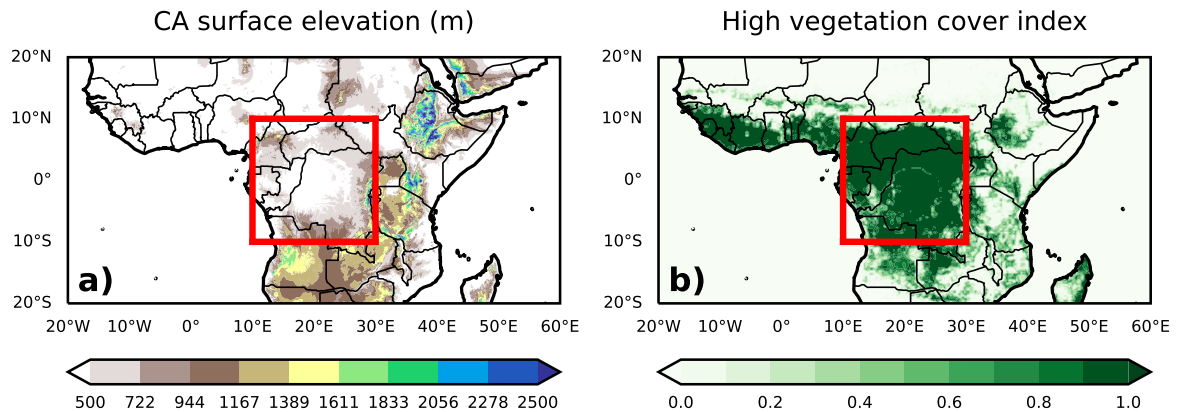


Figure 10: *The Central Africa region (red boxes). (left) topography (in meter) based on GTOPO30 Digital Elevation Model; (right) high vegetation cover index, from ERA5 reanalysis data.*

exceed 3,000 feet near the Angolan border to the south. The highest point in Central Africa, Margherita Peak (16,795 feet [5,119 metres]), whose summit bears residual features of glaciation, is located on the eastern fringe of the Rift Valley on the border of Congo (Kinshasa) and Uganda.

2.1.2 Vegetation

Central Africa is covered by an evergreen forest with an area of almost 1,035,920 square km. This rainforest, an exuberant world of high trees, rich in epiphytes and lianas takes three main forms: permanently wet marshy forests at the confluence of the Ubangi and Congo rivers; gallery forests, which are subject to periodic flooding, along banks and river floodplains; and, most extensive, forests of dry land, either featuring a single dominant species or, more often, harbouring a variety of species (sometimes several hundred per acre). This last type of forest is also found on the eastern slopes of the Congo basin, but it changes to high-altitude life-forms on the highlands of the Western Rift Valley. The rainforest is surrounded by a patchwork of savannas and other forests.

We should note that, the Congo Basin is a dry rainforest compared to its counterparts, such as the Amazon (Malhi et al., 2013). A high percentage of semi-evergreen vegetation means that short-term rain stresses that affect regions such as the Amazon, would not affect the Congo Basin in the same way (Zhou et al., 2014). This does not mean, however, that there is not a threshold beyond which rain stresses could strongly alter the forest

(Zhou et al., 2014).

2.2 Data used

2.2.1 Observed and reanalyses data

Various observationally based datasets have been used in this study to evaluate the models performance, to identify the key systematic errors and to provide a description of rainfall variability and its teleconnections with large scale atmospheric features.

2.2.1.1 Observed data: GPCP, UDEL, CHIRPS and HadISST

This thesis is primarily concerned with evaluating model rainfall. Measuring rainfall is a non-trivial task, with observations having a degree of dependence on the type of raingauge used to make the measurements (Haselow et al., 2019) and the use of manual versus automatic observations (Valík et al., 2021). In general, it is advantageous to combine point measurements of rainfall from stations with remotely sensed data to reduce the influence of interpolation techniques on the rainfall amount (Awange et al., 2016). For the case of this study, monthly time scale resolution observational data covering the period 1980 to 2010 (31 years) are used to evaluated models output. They are:

- **GPCP:** The Global Precipitation Climatology Project version 2.1 (Huffman et al., 2009) available on a 2.5° grid, derived from gauge measurements and satellite estimates.
- **UDEL:** Precipitation from The University of Delaware version 5.01 (Matsuura and Willmott, 2018) with a spatial resolution of 0.5° and derived from gauge measurements.
- **CHIRPS:** The Climate Hazards group Infrared Precipitation with Stations (Funk et al., 2015) at 0.05° grid spacing. This is a high-resolution (0.05°) gridded dataset which combines observed rainfall from raingauges with remotely sensed infrared measurements of cold cloud duration.
- **HadISST:** The satellite estimates and observed sea surface temperatures version 1 (Rayner et al., 2003) with a 1° spatial resolution.

2.2.1.2 Reanalyses data: MERRA2 and ERA5

In the absence of direct observations of key aspects of the atmospheric circulation, it is necessary to use reanalysis data as a proxy for such observations. The assessment of dynamical aspects of the atmosphere (such as convection, subsidence, moisture transport and wind convergence) is done using reanalysis data which is a widespread practice for the region of interest (Nicholson and Dezfuli, 2013; Todd and Washington, 2004; Sandjon et al., 2012; Balas et al., 2007; Dezfuli and Nicholson, 2013; Nicholson and Dezfuli, 2013; Jury et al., 2009; Jackson et al., 2009; Pokam et al., 2012, 2014; Cook and Vizy, 2016; Neupane, 2016; Dommo et al., 2018). Owing to the large variation in precipitation estimates from satellite and reanalysis datasets (Washington et al., 2013; Creese and Washington, 2016; James et al., 2018), two reanalysis datasets at monthly time scale from 1980-2010 are used in this study to assess models output. They are :

- **MERRA2** (Gelaro et al., 2017) the updated version of MERRA (Modern-Era Retrospective Analysis for Research and Applications), is a reanalysis dataset from the National Aeronautics and Space Administration (NASA). It is available on 72 sigma levels at a horizontal resolution of $0.5^\circ \times 0.625^\circ$. It has been suggested to be the most realistic of those currently available at representing tropospheric wind fields over equatorial Africa when compared to quality-controlled observations from radiosondes (Hua et al., 2019).
- **ERA5** (Hersbach et al., 2020), the reanalysis dataset with the highest spatial resolution used in this study, is also produced by the European Centre for Medium-Range Weather Forecast (ECMWF) Integrated Forecast System (IFS Cycle 41r2) to replace their ERA-Interim product. It has a spatial resolution of $0.25^\circ \times 0.25^\circ$ with 137 levels and was reported as performing best in a global-scale assessment of near-surface winds (Ramon et al., 2019).

Some variables used in our investigations are the horizontal wind (both zonal and meridional components), the vertical wind, the specific humidity and the near surface temperature and pressure.

2.2.2 Simulated data

Simulated data used in this study are output from coupled general circulation models' (CGCMs) simulations taking part in the Coupled Model Intercomparison Project Phase 5 (CMIP5; Taylor et al., 2012) and 6 (CMIP6; Eyring et al., 2016). Only one ensemble member for each model is used: the r1i1p1 integration for CMIP5 and r1i1p1f1 for CMIP6 models. We analyse the monthly output of 16 climate models, 8 from CMIP5 and 8 from CMIP6 (see Table 1 for more details). To track any improvement, each CMIP6 model used is the new version of a corresponding CMIP5 model. For this study, models cover a period from 1980-2005 and 1980-2010 for the CMIP5 and CMIP6 output respectively.

2.2.2.1 CMIP5 models

CMIP5 builds on the successes of earlier phases of CMIP (Meehl et al., 2000, 2005). In phase 3, for example, climate model output was for the first time released almost immediately upon completion of the runs so that scientists outside the modeling groups could provide a more timely and comprehensive analysis of the results. This unprecedented openness ushered in a “new era” in climate change research (Meehl et al., 2007). The CMIP3 multimodel dataset provided the basis for hundreds of peer-reviewed papers and played a prominent role in the IPCC’s AR4 assessment of climate variability and climate change. During phase 4 of CMIP (Meehl et al., 2007), additional simulations were performed that could be used to separate anthropogenic and natural influences on twentieth-century climate.

Relative to earlier phases, CMIP5 included more comprehensive models and called for a broader set of experiments that address a wider variety of scientific questions (Taylor et al., 2012). CMIP5 also differs from earlier phases in that generally higher-spatial-resolution models were used and a richer set of output fields archived. There was a better documentation of the models and experiment conditions, and a new strategy for making model output available to researchers. More than 20 modeling groups performed CMIP5 simulations using more than 50 models. However, It was impossible to satisfy all the needs of potential users of model output. So the CMIP5 “requested output” was far from exhaustive.

Table 1: Details of CMIP5 and CMIP6 models used in the study. Horizontal resolution (grids) and vertical levels are included.

Institute Country	Model short name	Model name	Resolution ($lat \times lon, lev$)
Beijing Climate Center, China Meteorological Administration (China)	BCC-CSM	CMIP5: BCC-CSM1.1-m CMIP6: BCC-CSM2-MR	$1.125^\circ \times 1.12^\circ$, L26 $1.125^\circ \times 1.12^\circ$, L46
Centre National de Recherches Météorologiques (France)	CNRM-CM	CMIP5: CNRM-CM5-2 CMIP6: CNRM-CM6-1	$1.4^\circ \times 1.4^\circ$, L31 $1.4^\circ \times 1.4^\circ$, L91
NOAA Geophysical Fluid Dynamics Laboratory (USA)	GFDL-CM	CMIP5: GFDL-CM3 CMIP6: GFDL-CM4	$2.0^\circ \times 2.5^\circ$, L48 $1.0^\circ \times 1.25^\circ$, L48
NASA Goddard Institute for Space Studies (USA)	GISS-E2	CMIP5: GISS-E2-R CMIP6: GISS-E2-1-G	$2.5^\circ \times 2^\circ$, L29 $2.5^\circ \times 2^\circ$, L40
Met Office Hadley Centre (UK)	HadGEM	CMIP5: HadGEM2-ES CMIP6: UKESM1-0-LL	$1.25^\circ \times 1.8^\circ$, L38 $1.25^\circ \times 1.8^\circ$, L38
Met Office Hadley Centre (UK)	MetUM	CMIP5: HadGEM2-CM3 CMIP6: HadGEM3-GC31-LL	$1.25^\circ \times 1.8^\circ$, L38 $1.25^\circ \times 1.8^\circ$, L38
Atmosphere and Ocean Research Institute, The University of Tokyo (Japan)	MIROC	CMIP5: MIROC5 CMIP6: MIROC6	$1.4^\circ \times 1.4^\circ$, L40 $1.4^\circ \times 1.4^\circ$, L81
Meteorological Research Institute (Japan)	MRI-ESM	CMIP5: MRI-ESM1 CMIP6: MRI-ESM2-0	$1.1^\circ \times 1.1^\circ$, L48 $1.1^\circ \times 1.1^\circ$, L48

2.2.2.2 CMIP6 models

The sixth phase of CMIP (i.e. CMIP6) is the latest released of the CMIP project with the need to address an ever-expanding range of scientific questions arising from more and more research communities. After a long and wide community consultation, a new and more federated structure (CMIP6) has been put in place. It consists of three major elements as listed in Eyring et al. (2016): (1) a handful of common experiments, the DECK (Diagnostic, Evaluation and Characterization of Klima) and CMIP historical

simulations (1850–near present) that will maintain continuity and help document basic characteristics of models across different phases of CMIP; (2) common standards, coordination, infrastructure, and documentation that will facilitate the distribution of model outputs and the characterization of the model ensemble; and (3) an ensemble of CMIP-Endorsed Model Intercomparison Projects (MIPs) that will be specific to a particular phase of CMIP (now CMIP6) and that will build on the DECK and CMIP historical simulations to address a large range of specific questions and fill the scientific gaps of the previous CMIP phases.

As far as the goal of filling the scientific gaps of the previous CMIP phases is concerned, CMIP6 aims to address three broad questions which are:

- How does the Earth system respond to forcing?
- What are the origins and consequences of systematic model biases?
- How can we assess future climate changes given internal climate variability, predictability and uncertainties in scenarios?

These questions are summarised in Fig.11 and the present work attempt to address question 2 with the focus on the Central African region.

2.2.2.3 Governing Equations in Climate models

Climate models are based on well-documented physical processes to simulate the transfer of energy and materials through the climate system. General circulation models or GCMs, use mathematical equations to characterize how energy and matter interact in different parts of the ocean, atmosphere, land. Building and running a climate model is complex process of identifying and quantifying Earth system processes, representing them with mathematical equations, setting variables to represent initial conditions and subsequent changes in climate forcing, and repeatedly solving the equations using powerful supercomputers.

The system of equations that is used in GCMs to describe the atmospheric general circulation can be written in spherical coordinates (λ, φ) as the horizontal coordinates (here λ and φ are the longitude and latitude, respectively), and the dimensionless pressure $\sigma = p/p_s$ (here p is the pressure and p_s is the surface pressure) is used as the vertical

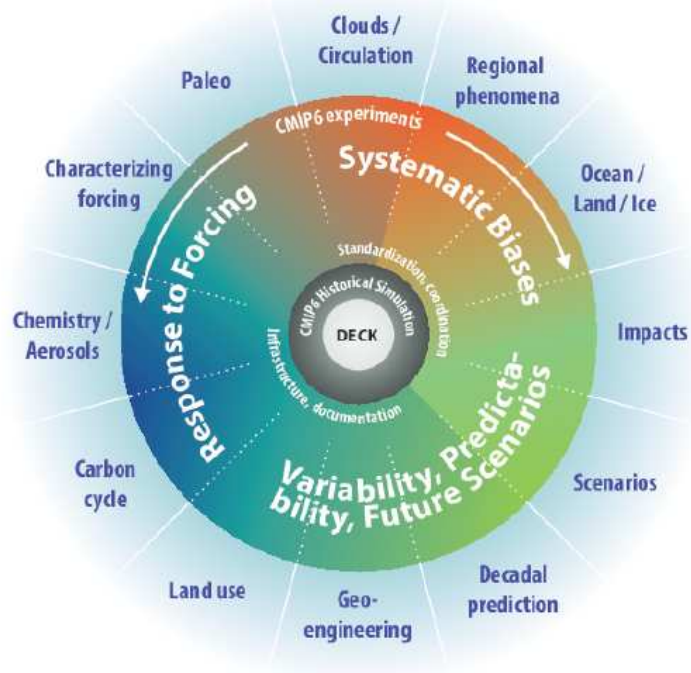


Figure 11: Schematic of the CMIP/CMIP6 experiment design. The inner ring and surrounding white text involve standardized functions of all CMIP DECK experiments and the CMIP6 historical simulation. The middle ring shows science topics related specifically to CMIP6 that are addressed by the CMIP6-Endorsed MIPs, with MIP topics shown in the outer (Eyring et al., 2016).

coordinate. As highlighted in Soldatenko et al. (2021), the system of equations comprises the following:

- **Two momentum equations:**

$$\frac{\partial u}{\partial t} + \frac{1}{a \cos \varphi} \left[-\Omega p_s v \cos \varphi + \frac{\partial}{\partial \lambda} (\Phi + K) + \frac{RT}{p_s} \frac{\partial p_s}{\partial \lambda} + \sigma \frac{\partial u}{\partial \sigma} \right] = F_u \quad (2.1)$$

$$\frac{\partial v}{\partial t} + \Omega p_s u + \frac{1}{a} \left[\frac{\partial}{\partial \varphi} (\Phi + K) + \frac{RT}{p_s} \frac{\partial p_s}{\partial \varphi} + \sigma \frac{\partial v}{\partial \sigma} \right] = F_v \quad (2.2)$$

- **The thermodynamic equation:**

$$\frac{\partial p_s T}{\partial t} + \frac{1}{a \cos \varphi} \left(\frac{\partial u p_s T}{\partial \lambda} + \frac{\partial v p_s \cos \varphi T}{\partial \varphi} \right) + \frac{\partial \sigma p_s T}{\partial \sigma} - \frac{RT}{c_p \sigma} \left[p_s \sigma + \sigma \left(\frac{\partial p_s}{\partial t} + \frac{u}{a \cos \varphi} \frac{\partial p_s}{\partial \lambda} + \frac{v}{a} \frac{\partial p_s}{\partial \varphi} \right) \right] = p_s (F_T + \epsilon) \quad (2.3)$$

- **The equation for specific humidity that describes the hydrological cycle:**

$$\frac{\partial p_s q}{\partial t} + \frac{1}{a \cos \varphi} \left(\frac{\partial u p_s q}{\partial \lambda} + \frac{\partial v \cos \varphi p_s q}{\partial \varphi} \right) + \frac{\partial \sigma p_s q}{\partial \sigma} = p_s [F_q - (C - E)] \quad (2.4)$$

- **The continuity equation:**

$$\frac{\partial p_s}{\partial t} + \frac{1}{a \cos \varphi} \int_0^1 \left(\frac{\partial p_s u}{\partial \lambda} + \frac{\partial p_s v \cos \varphi}{\partial \varphi} \right) d\sigma = 0 \quad (2.5)$$

- **Hydrostatic equation:**

$$\frac{\partial \Phi}{\partial \sigma} = -\frac{RT}{\sigma} \quad (2.6)$$

- **The equation of state:**

$$p = \rho R T_v \quad (2.7)$$

Here u and v are the zonal and meridional wind components; a is the Earth's mean radius; $\sigma = d\sigma/dt$ is the analogue of the vertical velocity in the σ coordinate system; T is the temperature; Φ is the geopotential; $\Omega = \zeta + f$ is the absolute vorticity, where ζ is the relative vorticity; f is the Coriolis parameter; K is the kinetic energy; R is the gas constant for dry air; q is the specific humidity; c_p is the specific heat of dry air at constant pressure; T_v is the virtual temperature; and ρ is the air density. The terms F_u and F_v describe the vertical friction and the horizontal diffusion processes; ϵ is the diabatic heating rate; F_T and F_q describe the vertical and horizontal diffusion of heat and water vapor, respectively; and C and E describe the source and sink processes for water vapor, respectively. The absolute vorticity and kinetic energy are given by:

$$\zeta = \frac{1}{p_s} \left[f + \frac{1}{a \cos \varphi} \left(\frac{\partial v}{\partial \lambda} + \frac{\partial u \cos \varphi}{\partial \varphi} \right) \right], K = \frac{u^2 + v^2}{2}$$

These equations can admit several solutions, justifying the existence of a multitude of climate models. Methods of resolution of these equations are diverse and have motivated a number of studies (Ogura and Phillips, 1962; Tapp and White, 1976; Tanguay et al., 1990; Xu et al., 1992).

2.3 Methods

First of all, to keep uniformity between datasets in terms of spatial resolution and enable comparison, all data used in this study are remapped onto a $1^\circ \times 1^\circ$ spatial grid. Data sets with higher resolution than $1^\circ \times 1^\circ$ are remapped using the first-order conservative remapping method (Jones, 1999) while coarser-resolution datasets are bilinearly interpolated (Nikulin et al., 2012).

2.3.1 Approach to understand models biases

Atmospheric features associated with the CA climate variability were highlighted in chapter 1. Some features, such as the Walker-like circulation and the Indian ocean overturning circulation can be categorised as large scale circulation due to the large area on which they are spread on. Similarly, features such as the AEJ components and the Congo basin cell are categorised as regional scale circulation because of their local impact on the regional climate. In this study, the investigation of simulated rainfall bias will emphasize both regional and large-scale features already identified as key contributors to climate variability over the region. The goal here is to highlight the contribution of each circulation to the simulated rainfall biases.

2.3.2 Metrics used for our investigations

2.3.2.1 Vertically Integrated Moisture flux convergence

The vertically integrated moisture flux \vec{Q} , is obtained by integrating over the depth of the atmosphere. The moisture budget indicates that precipitation, evaporation, and net moisture transport into and out of an atmospheric column through its lateral boundary are in balance at the seasonal time-scale (Brubaker et al., 1993). Following Peixoto and Oort (1992), the atmospheric water budget in pressure coordinates is expressed as follows:

$$\frac{\partial \bar{W}}{\partial t} + \nabla \bullet \bar{Q} = \bar{E} - \bar{P} \quad (2.8)$$

In Eq. (2.8), W is precipitable water, E is evaporation, P precipitation, and $\nabla \bullet Q$ is the divergence field of moisture flux, which represents the net moisture transport. The overbars denote the seasonally varying climatological mean. From a climatological perspective, the long-term accumulation of precipitable water in the atmosphere is negligible ($\frac{\partial \bar{W}}{\partial t} = 0$). Therefore, the mean moisture budget is a balance between moisture flux divergence and the water source/sink. Thus, Eq. (2.8) can be written as:

$$\nabla \bullet \bar{Q} = \bar{E} - \bar{P} \quad (2.9)$$

and

$$\vec{Q} = \frac{1}{g} \int_{P_{surf}}^{P_{top}} \vec{V} q dp \quad (2.10)$$

where \vec{V} is the horizontal wind vector, q the specific humidity (in $g.kg^{-1}$), g the gravitational acceleration (in $N.kg^{-1}$), P_{top} the pressure at the top of the atmosphere, and P_{surf} the surface pressure (in $N.m^{-2}$). Using the zonal (u) and meridional (v) components of the horizontal wind (in $m.s^{-1}$), the zonal and meridional transport of \vec{Q} can be separately obtained by the following equations.

$$\vec{Q}_\lambda = \frac{1}{g} \int_{P_{surf}}^{P_{top}} \vec{u} q dp \quad (2.11)$$

and

$$\vec{Q}_\phi = \frac{1}{g} \int_{P_{surf}}^{P_{top}} \vec{v} q dp \quad (2.12)$$

The integration limit P_{top} is the pressure above which the flux and flux divergence become negligible. In this study, the vertically integrated moisture flux computation was limited to the layer from the surface to 300 hPa. Neglecting the moisture flux above that level does not greatly impact the overall water budget because most of water vapor is concentrated in the lower troposphere.

The net moisture flux convergence (divergence) is the total inflow to (outflow from) the region, scaled by the surface area. On the time serie, it's obtained in applying the Zheng and Eltahir (1998) method: in a given rectangular ($L \times H$) region which the atmospheric water vapor inflows and outflows, the inflow comes from the contribution of the *East – West* ($Q_\lambda(y, t)$ in $kg.s^{-1}$) and *North – South* ($Q_\phi(x, t)$ in $kg.s^{-1}$) boundaries. By using Gauss's theorem, the total zonal and meridional moisture flux convergence or divergence are obtained as follows:

$$Q_\lambda(y, t) = \frac{Q_{West}(y, t) - Q_{East}(y, t)}{S} \quad (2.13)$$

and

$$Q_\phi(x, t) = \frac{Q_{South}(x, t) - Q_{North}(x, t)}{S} \quad (2.14)$$

S (in m^2) is the surface area of the region calculated as:

$$S = R^2 \Delta\lambda (\sin\phi_2 - \sin\phi_1) \quad (2.15)$$

$\Delta\lambda = \lambda_2 - \lambda_1$, where λ_1 and λ_2 are respectively western (10°E) and eastern (30°E) boundary longitudes, ϕ_1 and ϕ_2 are respectively southern (10°S) and northern (10°N) boundary latitudes (all converted in radians) and R (in m) is the earth's radius.

2.3.2.2 Mass weighted stream function

At the local or regional scale, the zonal mass-weighted stream function as computed in Longandjo and Rouault (2020) is used to explore the Congo basin cell. To better understand the regional-scale zonal circulation over central Africa, we used the mass-weighted streamfunction because it is commonly used for its counterpart Hadley circulation (Oort and Yienger, 1996; Stachnik and Schumacher, 2011; Donohoe et al., 2013). The primary reason is that the mass-weighted streamfunction helps to objectively define indices that describe the regional-scale circulation over central Africa in terms of intensity and width on various time scales.

Following Cook (2003), the conservation of mass, in vertical coordinates, must satisfy the equation

$$\frac{1}{R\cos\theta} \frac{\partial u}{\partial\phi} + \frac{1}{R\cos\theta} \frac{\partial(v\cos\theta)}{\partial\theta} + \frac{\partial w}{\partial p} = 0 \quad (2.16)$$

where u and v are the zonal and meridional wind components, w is the vertical velocity, R is Earth's radius, ϕ is the longitude, θ is the latitude, and p is the pressure level. When Eq.(2.16) is averaged over latitude, the second term on the left-hand side of the equation is zero. Therefore, Eq. (2.16) can be written, with square brackets denoting the meridional average, as:

$$\frac{1}{R\cos\theta} \frac{\partial[u]}{\partial\phi} + \frac{\partial[w]}{\partial p} = 0 \quad (2.17)$$

From Eq. (2.17), one could state that if one component ($[u]$ or $[w]$) is known, the other can be identified. This means that one variable can be used to fully determine the two-dimensional flow. The continuity and hydrostatic equations allow us to express the combined circulation $[u]$ and $[w]$ in terms of mass-weighted (or Stokes) streamfunctions ψ , which define the total eastward mass flux above a given pressure level and longitude:

$$[u] = \frac{g}{2\pi R} \frac{\partial\psi}{\partial p} \quad (2.18)$$

and

$$[w] = -\frac{g}{2\pi R^2} \frac{\partial\psi}{\partial p} \quad (2.19)$$

with $g = 9.8m/s^2$ being the gravitational constant.

By solving for ψ , we found the following solution representing the zonal stream function ψ , satisfying the meridional mean continuity equation in spherical coordinates that can be calculated at each pressure p and latitude ϕ as:

$$\psi(p, \phi) = \frac{2\pi R(\phi)}{g} \int_{P_{surf}}^P [u] dp \quad (2.20)$$

The zonal mass-weighted streamfunction will be applied to characterize the Walker-like circulation over central Africa. We use following convention: when the mass-weighted streamfunction is positive, it corresponds to clockwise circulation, whereas counterclockwise circulation corresponds to the negative mass-weighted streamfunction. The unit of the mass-weighted streamfunction is Sverdrups ($1Sv = 10^9 kg.s^{-1}$). This definition is also equivalent to $10^6 m^3.s^{-1}$, corresponding to the mass flux produced by a 1-Sv flow of water of $10^3 kg.m^{-3}$ of density. The zonal wind is averaged meridionally between $5^\circ N$ and $5^\circ S$, before computing the mass-weighted streamfunctions.

2.3.2.3 Indian Ocean Dipole (IOD) index

The large-scale forcing such as the influence of Indian Ocean SST on CA rainfall is investigated through the Indian Ocean Dipole (IOD). Also called Dipole Mode Index (DMI: Saji et al., 1999), the IOD index is defined as the SST difference between the western equatorial Ocean ($10^\circ S-10^\circ N$, $50^\circ-70^\circ E$) and the southeastern Ocean ($10^\circ S-0^\circ N$, $90^\circ-110^\circ E$). Those areas are highlighted in Fig.12 (red boxes). Composites of strongest (lowest) IOD years are selected to investigate the role of IOD on Central African precipitation.

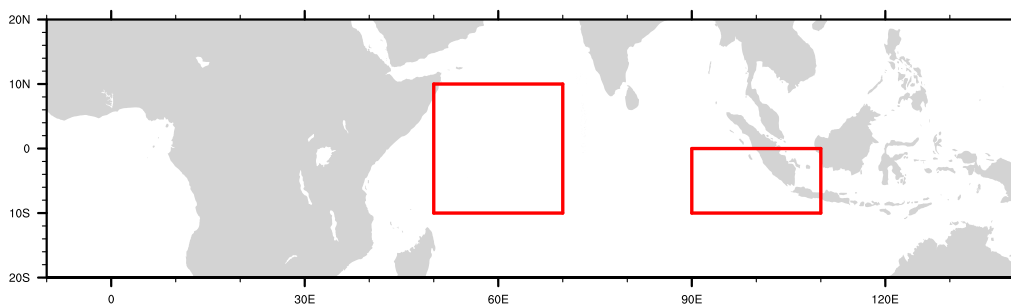


Figure 12: Indian Ocean Sea Surface Temperature (SST) areas (red boxes) used to compute IOD.

2.3.2.4 Ageostrophic wind computation

The ageostrophic wind (V_{ag}), representing friction and other effects is responsible for surface wind crossing isobars rather than following them. It is used here to investigate transverse ageostrophic circulation related to the jets and is defined as the vector difference between the real (or observed) wind (V) and the geostrophic wind (V_g) as follow:

$$V_{ag} = V - V_g \quad (2.21)$$

with

$$V_g = -\frac{1}{f} \frac{\partial \Phi}{\partial n} \quad (2.22)$$

Where $f = 2\Omega \sin\phi$ is the Coriolis parameter, n is the direction normal to the isobars (or geopotential height contours) and Φ represents the geopotential. The terms Ω and ϕ in the expression of the Coriolis parameter represent respectively the angular rotation rate of the earth ($7.292 \times 10^{-5} \text{ s}^{-1}$) and the latitude.

Between 1°S and 1°N the value of Coriolis parameter used to calculate the meridional ageostrophic wind is replaced with the Coriolis value applicable to 1°S – 1.5°S and 1°N – 1.5°N so as to allow computation of winds at and surrounding the equator.

2.4 Conclusion

This part has presented the study area, and has briefly described topography and land-vegetation cover features. It also includes descriptions of the simulated, observed and reanalyses datasets used in analyses. Details of methods and computation processes applied to obtain findings are likewise conveyed.

Chapter 3

Results and discussions

This chapter summarises findings of this work, subdivided into three main parts: the first part highlights the performance of both CMIP5 and CMIP6 models to replicate observed and reanalyses data. The second part discusses the models assessment based on atmospheric processes (moisture transport, moisture convergence/divergence, AEJs) and the changes from CMIP5 to CMIP6 models. The last part focuses on the MetUM outputs with the highlight of the contribution of the large and the regional scale circulations to the simulated rainfall biases.

3.1 Rainfall Climatology in CMIP5 and CMIP6 models over CA

In this section, the skills of the models in simulating the mean climatology of rainfall over CA during the period 1980–2010 are presented.

3.1.1 Annual cycle

Figure 13 shows the annual cycle of rainfall averaged between 10°S–10°N and 10°E–30°E over CA from observations, reanalyses, CMIP5 and CMIP6 models with the blue band representing uncertainty between observations and reanalyses data.

From the Figure, MERRA2 overestimates rainfall throughout the year as compared to other reference data. However, both observed and reanalyses data agree relatively well with peaks found in MAM and SON seasons. As far as the models are concerned, in general, the timing of the peaks is well captured but considerable differences in terms

of intensity are depicted. From CMIP5 to CMIP6, some models show an improvement while others do not. For instance, the BCC-CSM1-1-m model is generally found within the uncertainty range of observational data, but its CMIP6 version (BCC-CSM2-MR) significantly overestimates rainfall throughout the year by up to 1 mm/day. Conversely,

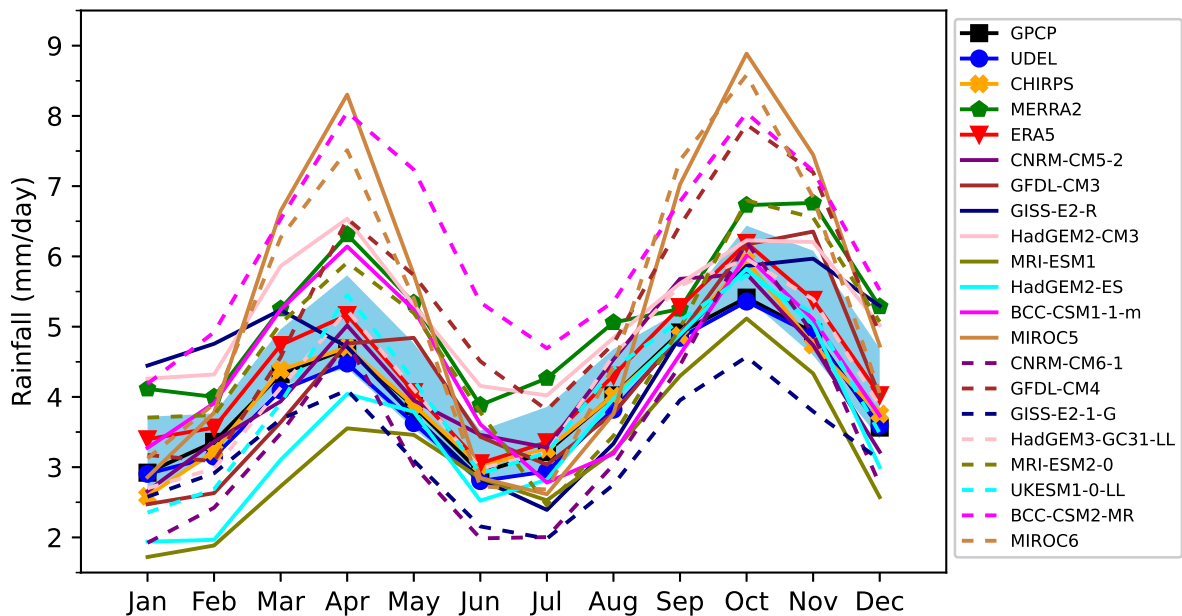


Figure 13: Rainfall ($\text{mm}\cdot\text{day}^{-1}$) climatological annual cycle over Central Africa (10°S – 10°N and 10°E – 30°E) from observations and reanalyses (lines with markers), CMIP5 (solid lines) and CMIP6 models (dashed lines). The blue band represents observational uncertainty (envelope of the standard deviation generated from the mean of the observed and reanalyses data).

CNRM-CM6-1 and GISS-E2-1-G underestimate rainfall in most months while their CMIP5 version (CNRM-CM5-2 and GISS-E2-R) are found within the uncertainty range in most months. However, a model such as the MIROC model overestimate rainfall peaks in both version although there is a slight improvement in the CMIP6 version. In term of spatial distribution, models' ability to represent the spatial pattern of rainfall over CA during the two transition seasons (March-May: MAM and September-November: SON) is discussed next.

3.1.2 Seasonal spatial mean climatology

Figures 14 and 15 show for MAM and SON seasons respectively, the seasonal mean climatology of rainfall from observations (Fig.14a-c and Fig.15a-c). Biases relative to GPCP are also shown for CMIP5 and CMIP6 models (Fig.14d-s and Fig.15d-s). The CA

domain used in this study is 10°S–10°N and 10°E–30°E (black box: Fig.14 and 15).

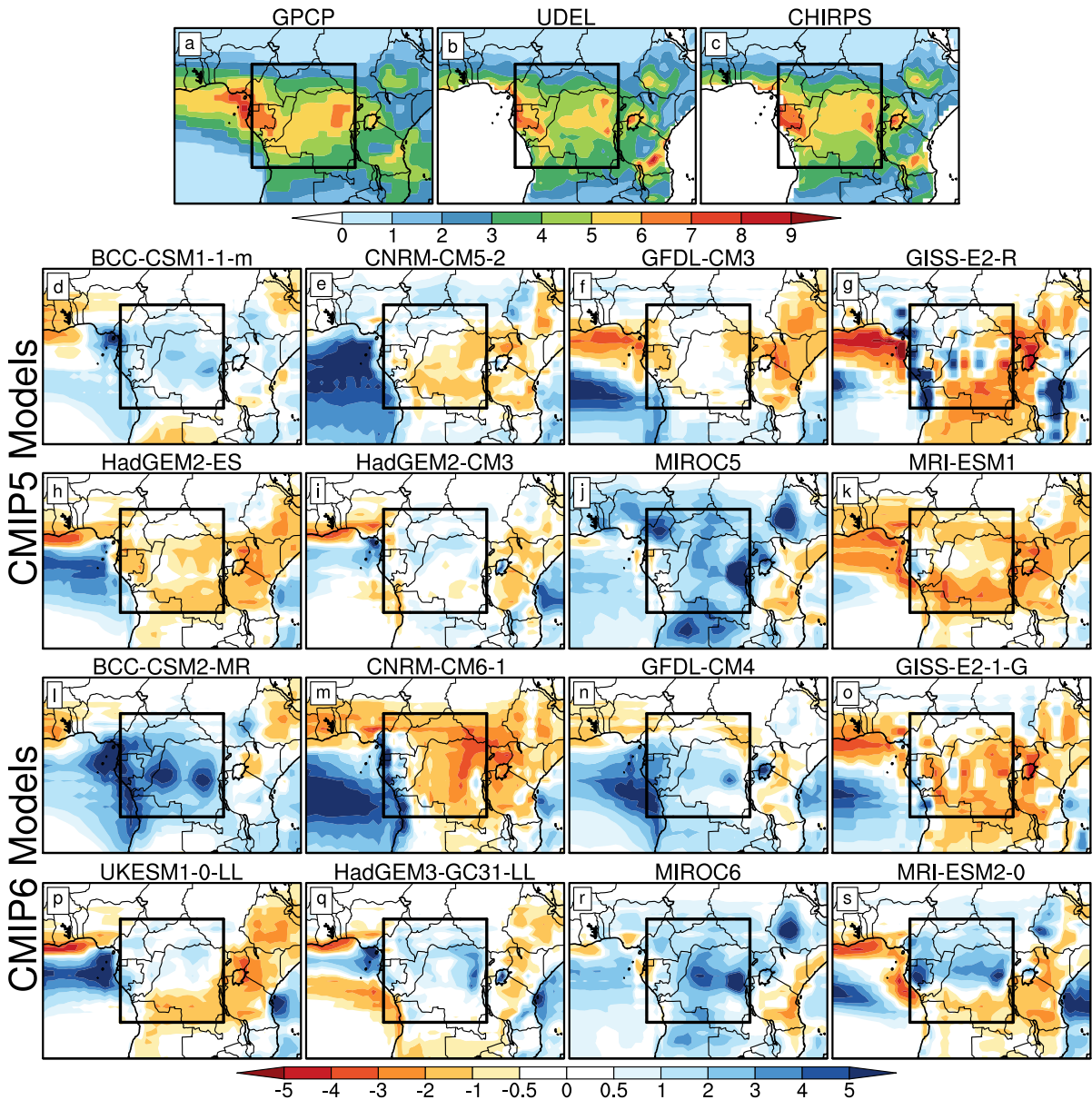


Figure 14: Spatial representation of the March-May (MAM) long term rainfall mean over Central Africa (blackbox) from (a-c) observations, (d-k) CMIP5 models biases and (l-s) CMIP6 models biases. The biases are computed with respect to GPCP

In observations, the SON season is wetter than the MAM season with an agreement with maximum rainfall found at the eastern and western boundaries in both seasons. As far as models are concerned, in MAM season (Fig.14), the CMIP5 version of the BCC-CSM (CNRM-CM) model depicts a wet (dry) bias over the study region, and the latter is stronger in the CMIP6 version of the model. However, an improvement is observed from the CMIP5 to the CMIP6 version of the HadGEM (MIROC) model with a mitigation

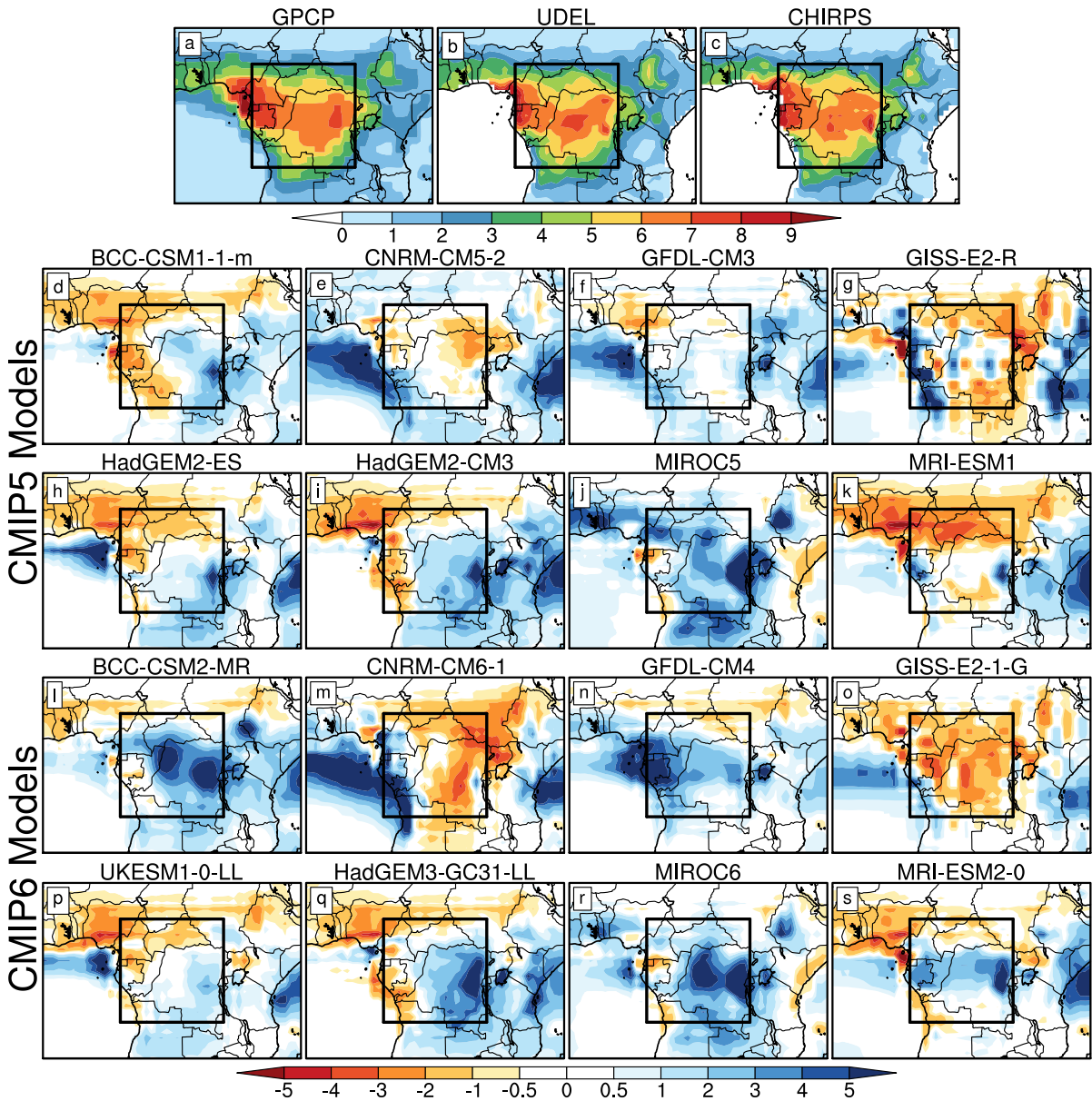


Figure 15: Spatial representation of the September-November (SON) long term rainfall mean over Central Africa (blackbox) from (a-c) observations, (d-k) CMIP5 models biases and (l-s) CMIP6 models biases. The biases are computed with respect to GPCP

of the dry (wet) bias. In SON season (Fig.15), the CMIP5 version of the GFDL model depicts very low biases over the study region showing that the simulated rainfall is close to observation. On the other hand, its CMIP6 version overestimates rainfall in agreement with the seasonal cycle (Fig.13). For the MetUM model, it depicts a wet bias (dry bias) over the eastern (western) CA in both version and the eastern CA wet bias strengthens while the coastal western CA dry bias weakens in the CMIP6 version.

3.1.3 Quantification of total rainfall pattern similarities

The Taylor diagram, described by Taylor (2001), is a diagram used to quantify the statistical relationship between two fields, a “test” field (often representing a field simulated by a model) and a “reference” field (usually representing “truth,” based on observations). It is used here (Fig.16) to summarize the similarity between GCMs and observations in simulating precipitation patterns over CA using seasonal means of DJF, MAM, JJA, and SON. Model outputs are compared against GPCP using Root-Mean-Square Error (RMSE), Pearson’s Correlation coefficient and Normalized Standard Deviation (NSD) metrics.

Both CMIP5 and CMIP6 models depict lower correlations and higher RMSE and NSD in MAM (Fig.16b) and SON (Fig.16d) seasons compared to DJF (Fig.16a) and JJA (Fig.16c) seasons. This shows that models struggle most to reproduce the seasonal variability during transition seasons. The highest value of the NSD depicted by the CMIP6 version of the BCC-CSM model is in agreement with its overestimated annual cycle. However, in term of correlation and whatever the season, CMIP6 models generally outperform their corresponding CMIP5 versions indicating an improvement in the CMIP5 models.

In the following section, investigations are done to understand simulated rainfall biases through mechanisms associated to rainfall such as moisture flux convergence and convection over Central Africa.

3.2 Simulated circulation and rainfall biases

3.2.1 Moisture flux convergence

In order to understand causes of modeled biases over the CA region, we have first focused our attention on the simulated upstream moisture flux convergence. The moisture flux dynamic and its contribution to the CA rainfall has already been analyzed by some studies (Van der Ent et al., 2010; Pokam et al., 2012, 2014; Washington et al., 2013; Creese and Washington, 2016; Dyer et al., 2017). They have helped to establish that the credibility of a model to simulate rainfall is positively correlated to its ability to reproduce correctly moisture flux climatology, especially for tropical regions where moisture flux

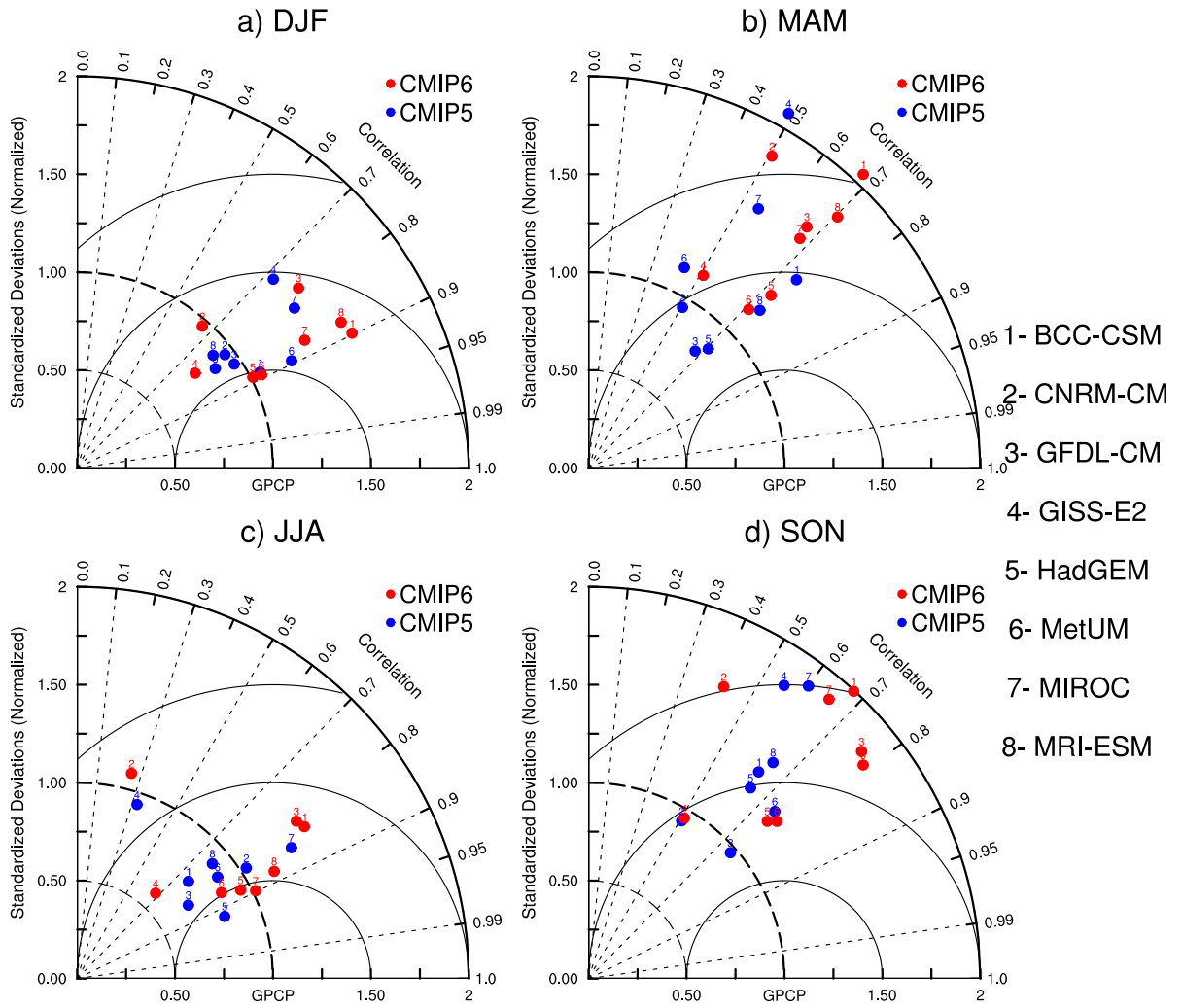


Figure 16: Taylor diagrams displaying the statistics based on the seasonal (DJF, MAM, JJA and SON) mean rainfall. Here, the CMIP5 and CMIP6 models are compared against GPCP (reference field) and rainfall is averaged over the CA region ($10^{\circ}S-10^{\circ}N$ and $10^{\circ}E-30^{\circ}E$).

convergence strongly modulates the hydrological cycle (Pokam et al., 2012).

3.2.1.1 Zonal moisture flux convergence

The intra-seasonal variability of the net zonal moisture flux convergence across atmospheric layers is shown in Figure 17 for reanalyses (Fig.17a-b), CMIP5 models (Fig.17c-j) and CMIP6 models (Fig.17k-r). This is the summing of moisture flux at West–East (West ($10^{\circ}E$) minus East ($30^{\circ}E$)) frontiers into CA. Negative values indicated moisture divergence and positive values convergence.

In reanalyses, throughout the year, moisture flux convergence is observed at lower troposphere between 1000 hPa and 800 hPa while the divergence moisture flux is found

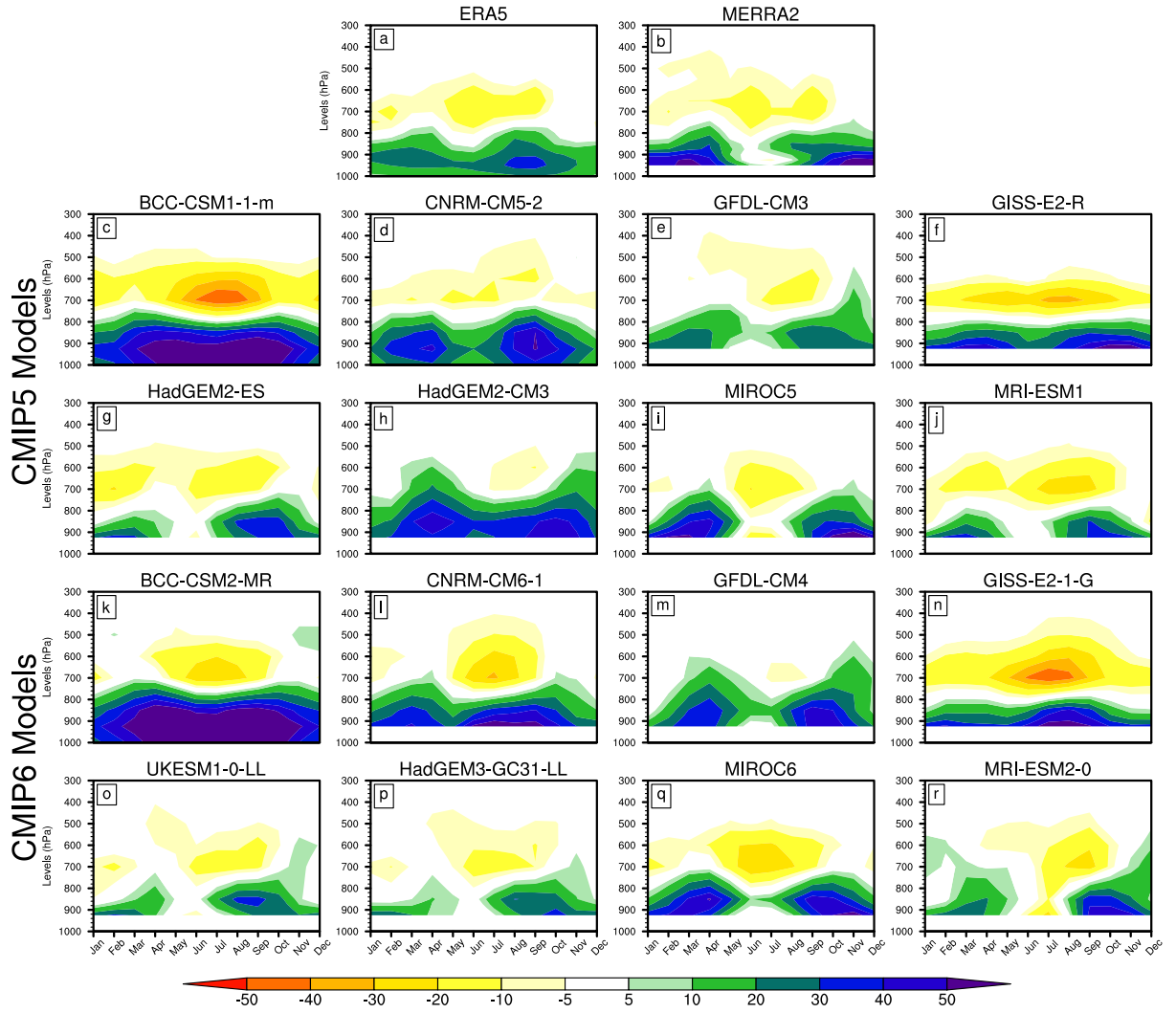


Figure 17: Time–height section of Net zonal moisture flux (in $g/kg.m/s$) in (a-b) reanalyses, (c-j) CMIP5 models and (k-r) CMIP6 models. This is the summing of moisture flux at West–East (West ($10^{\circ}E$) minus East ($30^{\circ}E$)) frontiers into CA. Negative values indicated moisture divergence and positive values convergence.

in the mid-tropospheric layer (800–600 hPa). Moreover, the rate of low level moisture flux advection is stronger in MAM and SON seasons. Although basic climatology features (mode of seasonal and intra-seasonal variability) of model outputs of moisture fluxes are captured well, it is found that rainfall biases of CA region are associated to an unrealistic simulated moisture amount. For instance, the BCC-CSM model overestimates the rate of advected low level moisture in its CMIP5 version (Fig.17c) and this overestimation is more pronounced in its CMIP6 version (Fig.17k) which is associated with an increase in the wet bias when going from CMIP5 to CMIP6 version (Fig.13). In the other hand, the strengthening of dry bias in CMIP6 version of the GISS-E2 model is likely associated to

the reinforcement of the mid-tropospheric moisture flux divergence.

3.2.1.2 Meridional moisture flux convergence

The meridional component of the moisture flux convergence across atmospheric layers is shown in Figure 18. In reanalyses (Fig.18a-b), the meridional advected moisture is more upward than the zonal advected moisture (Fig.17a-b) and its rate is also stronger in MAM and SON seasons. Reanalyses also agree with a low level moisture flux divergence between May and July, stronger and more widespread in ERA5 than in MERRA2. The simulated mid-tropospheric meridional moisture flux convergence is overestimated in both versions of the BCC-CSM (Fig.18c and Fig.18k) but underestimated in the CMIP5 version of the CNRM-CM model (Fig.18d), an underestimation which is more pronounced in its CMIP6 version (Fig.18l). Although the simulated mid-tropospheric meridional moisture flux convergence is underestimated in both versions of the GISS-E2 model (Fig.18f and Fig.18n), an improvement is observed in its CMIP6 version (Fig.18o).

3.2.1.3 Total moisture flux convergence

The total moisture flux across atmospheric layers is shown in Figure 19. It represents the summing of Net zonal moisture flux (Fig.17) and the Net meridional moisture flux (Fig.18) into CA. Reanalyses (Fig.19a-b) show that the shape of the total moisture is rather close to that of the zonal component. These results were also reported by Pokam et al. (2012). The opposite sign of upper and lower layer moisture fluxes is generally assigned to the presence in the region of Hadley and Walker type circulations (Washington et al., 2013; Cook and Vizu, 2016).

In most models, rainfall biases are definitely associated with moisture flux convergence and/or divergence. For instance, the wet bias in both versions of the BCC-CMS model is actually the result of the overestimated simulated moisture flux convergence stronger in its CMIP6 version. This could be attributed to an overestimation in the strength of LLWs advecting more moisture in the CA region from the Atlantic ocean. In a model such as the GISS-E2 model, the dry bias in both versions of the model is associated with a mid-tropospheric moisture flux divergence, stronger in its CMIP6 version in agreement with the stronger dry bias. The mid-tropospheric moisture flux divergence could be associated to an overestimated AEJ components. More investigations are required to support this

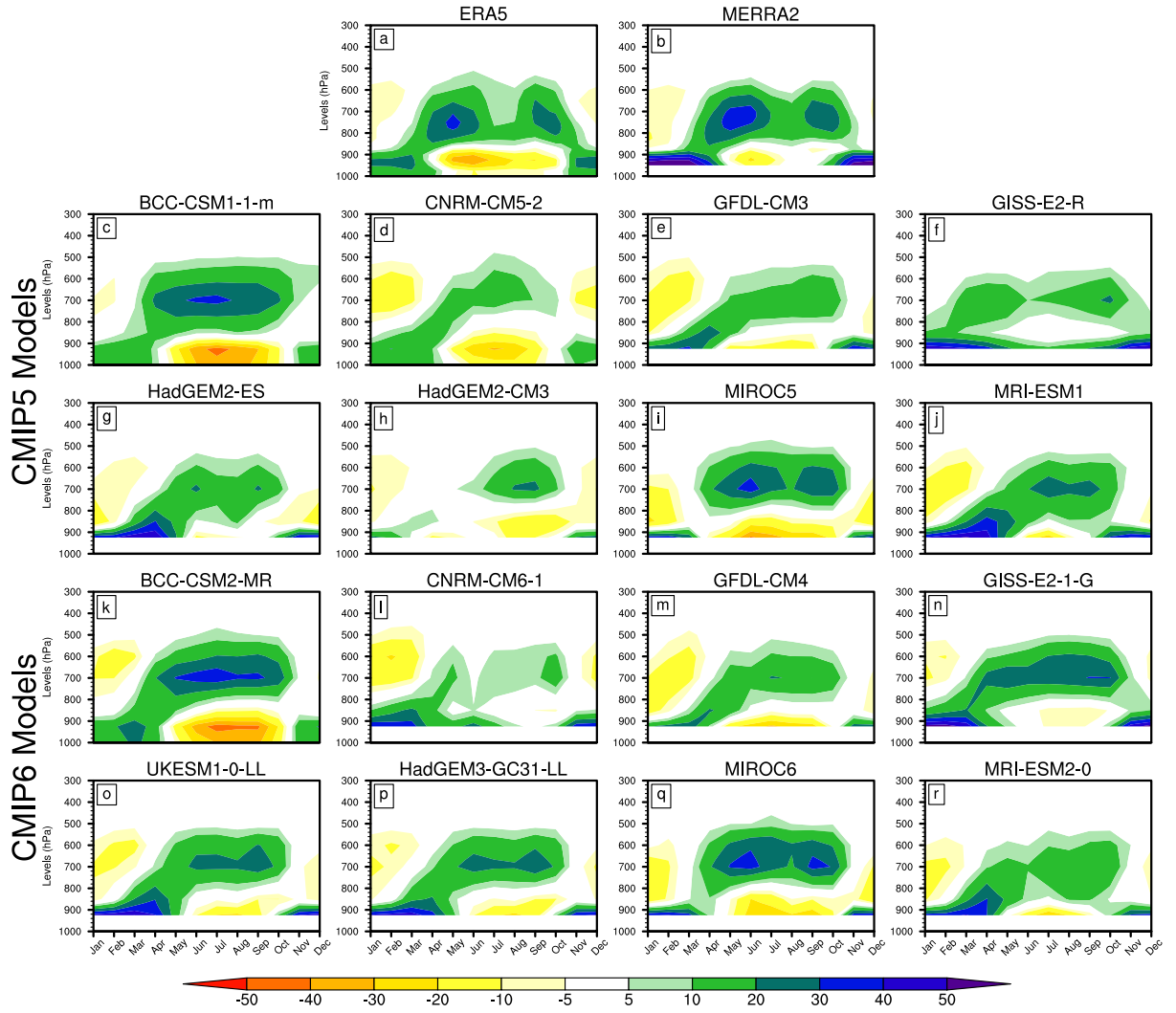


Figure 18: Time–height section of Net meridional moisture flux (in $g/kg.m/s$) in (a–b) reanalyses, (c–j) CMIP5 models and (k–r) CMIP6 models. This is the summing of moisture flux at South–North (South ($10^{\circ}S$) minus North ($10^{\circ}N$)) frontiers into CA. Negative values indicated moisture divergence and positive values convergence.

hypothesis.

3.2.2 Role of Low-level westelies (LLWs)

With the core speed of the LLWs in CEA located along the coastal region between 10° and $15^{\circ}E$ year-round (Pokam et al., 2014), the long term mean of the zonal wind is averaged in that longitude band in all the reanalyses, CMIP5 and CMIP6 models and represented in Figures 20 and 21 for March–May (MAM) and September–November (SON) seasons, respectively. The focus is on the MAM and SON seasons because they are wet seasons that encompass the majority of mechanisms driving the region’s climate

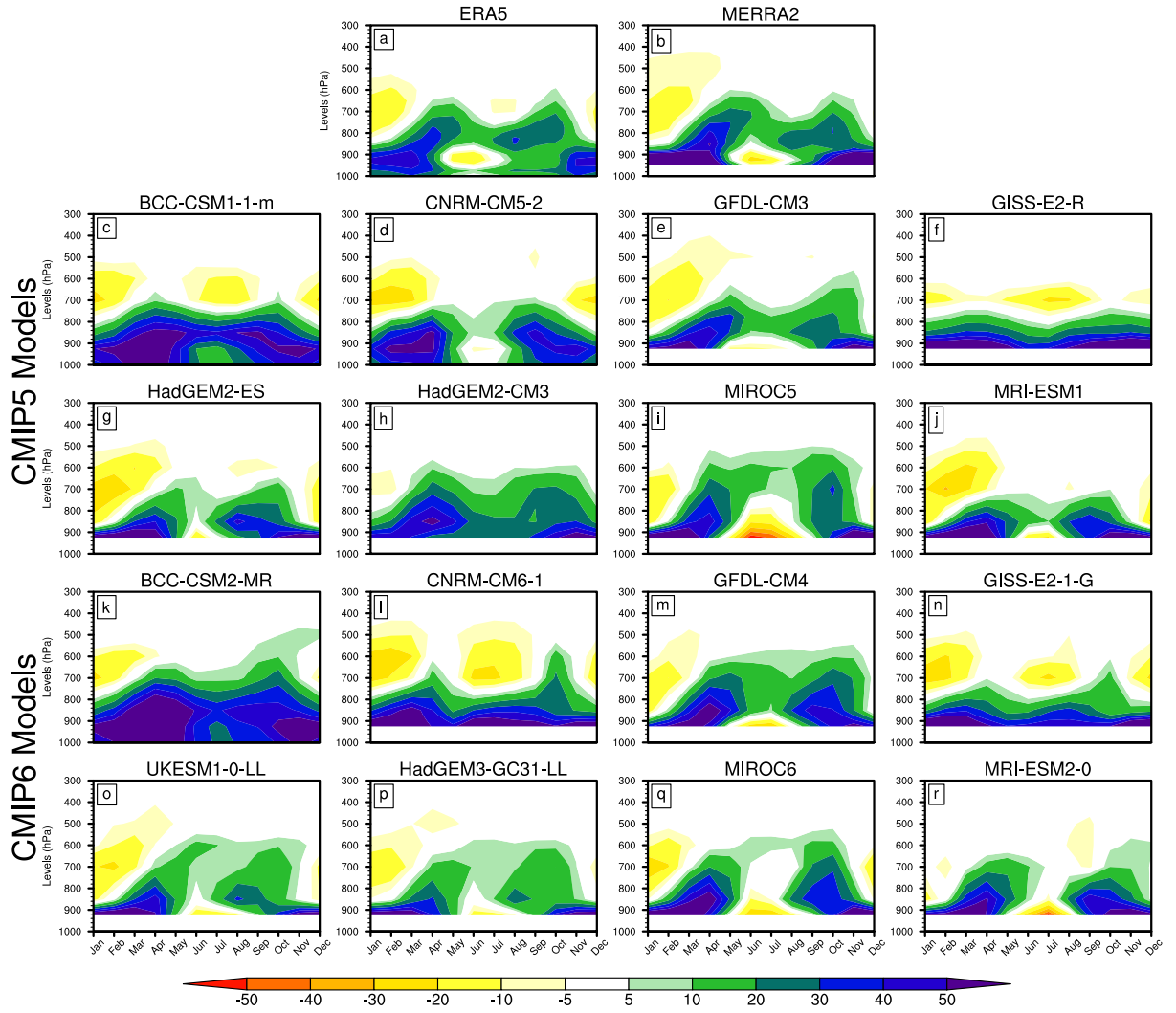


Figure 19: Time–height section of the Total moisture flux (in $\text{g}/\text{kg}\cdot\text{m}/\text{s}$) in (a–b) reanalyses, (c–j) CMIP5 models and (k–r) CMIP6 models. This is the summing of Net zonal moisture flux and the Net meridional moisture flux into CA. Negative values indicated moisture divergence and positive values convergence.

system. It appears in reanalyses that, although the westerlies are weaker in MAM (Fig.20a–b) than in SON (Fig.21a–b) season, there is an agreement (even though not perfect) with the upper boundary of LLWs found around 850 hPa and the core speed located around 925 hPa in both seasons. Furthermore, in reanalyses, the MAM season depicts a distinct arm of westerly winds located north of 6°N which is strengthened (not shown here) in June–August (JJA) and weakened significantly in SON, to disappear (not shown here) in December–February (DJF) as highlighted in Pokam et al. (2014). Although they bear some biases, the above basic features of LLWs are relatively well represented in models. In MAM, HadGEM2-CM3, BCC-CSM1.1-m and MIROC5 (GFDL-

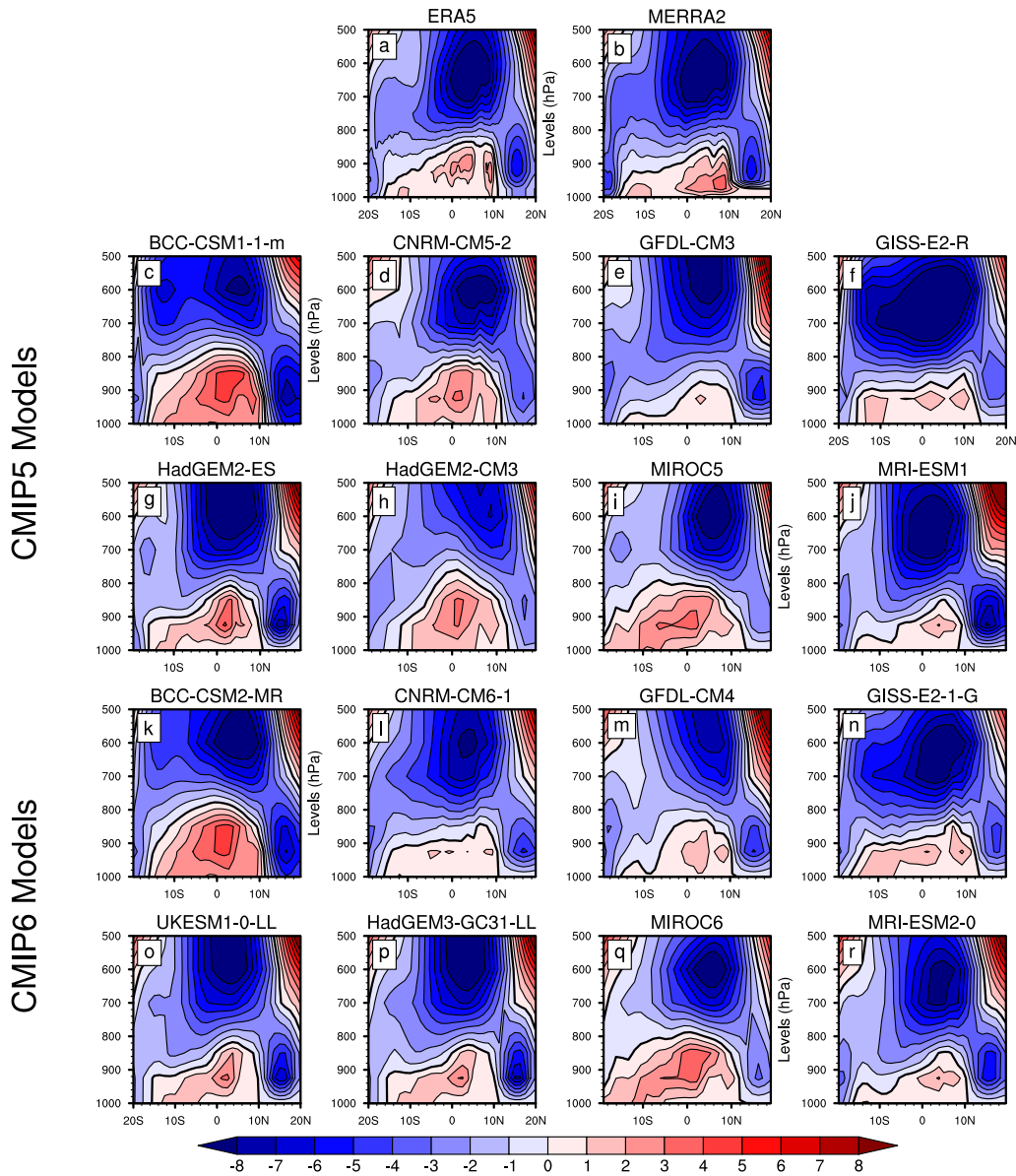


Figure 20: *March–May long term seasonal mean of zonal wind (m/s) averaged between 10° and 15° E for (a–b) reanalyses, (c–j) CMIP5 and (k–r) CMIP6 models. Positive values correspond to westerly winds and negative values to easterly winds.*

CM3, GISS-E2-R and MRI-ESM1) are CMIP5 models overestimating (underestimating) the upper boundary of LLWs found at around 800 hPa (900 hPa). However, this is slightly improved in CMIP6 models except in BCC-CSM2-MR and MIROC6. In addition to the overestimation of the upper boundary of LLWs in HadGEM2-CM3, the modelled westerlies are also extended further south in the SON season, with once more an improvement in its CMIP6 version. In the MAM season, most of the CMIP5 models fail to represent the arm of westerly winds located north of 6° N. There is no improvement observed in that

feature in CMIP6 models. This could be due to the coarse resolution of both CMIP5 and CMIP6 models. However, the focus is on the arm of westerly winds located south of 6°N because that arm is present year-round (Pokam et al. 2014). In both seasons, CMIP5 and CMIP6 models depict well the vertical location of the core speed of LLWs found at around 925 hPa as in reanalyses. Models' ability to represent the intensity and the spatial pattern of the core speed of LLWs at this level (925 hPa) is discussed next.

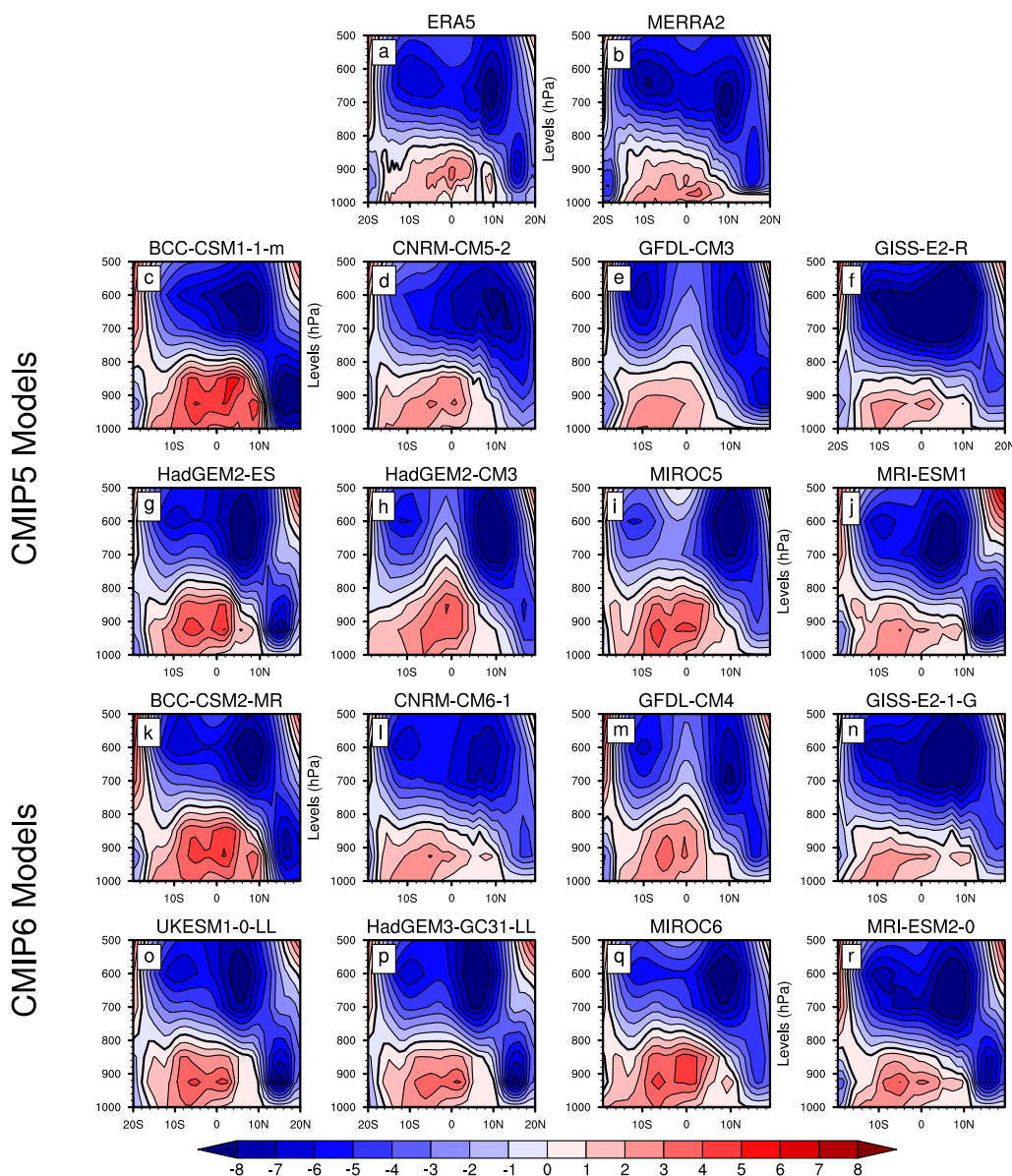


Figure 21: September–November long term seasonal mean of zonal wind (m/s) averaged between 10° and 15°E for (a–b) reanalyses, (c–j) CMIP5 and (k–r) CMIP6 models. Positive values correspond to westerly winds and negative values to easterly winds.

Figures 22 and 23 show for MAM and SON seasons respectively, the 925 hPa seasonal

mean climatology of total circulation (vectors) and zonal wind (shading) speed from all the reanalyses (Figs.22a–b and 23a–b). Biases relative to ERA5 are also shown for CMIP5 and CMIP6 models for MAM and SON seasons (Figs.22c–r and 23c–r). In both seasons, reanalyses depict an inflow of westerly winds in the study region through the western boundary with the inflow stronger in SON than in MAM season. The simulated biases of CMIP5 and CMIP6 models are similar in their spatial pattern but differ in intensity. In both seasons, the positive (negative) bias along the coastal region in HadGEM2-CM3, HadGEM2-ES, BCC-CSM1.1-m and MIROC5 (GFDL-CM3, GISS-E2-R and MRI-ESM1) denotes an excess (a deficient) in the intensity of westerly winds, much more pronounced in BCC-CSM1.1-m (GFDL-CM3). Although the sign of the biases is the same, an improvement in reducing the biases depicted in CMIP5 models is observed in their corresponding CMIP6 models in both seasons. However, in the MAM season, the CNRM-CM5 model and its corresponding CMIP6 version (CNRM-CM6-1) have an opposite bias in the simulated zonal wind along the coast. CNRM-CM5 overestimates while CNRM-CM6-1 underestimates. This is associated with the pronounced dry bias observed in the CNRM-CM6-1 model during the MAM season (Fig.14m).

The 925 hPa zonal wind is split into its divergent and rotational components and averaged between 10°S – 5°N and 10° – 15°E . Their annual cycles are then displayed in Figure 24 for reanalyses, CMIP5 and CMIP6 models (Fig.24a–f). This is done to assess the contribution of each component to the total zonal wind and to determine to what extent they contribute to the models' biases. Reanalyses agree well in the representation of the total zonal wind and its components. Throughout the year, the divergent circulation (Fig.24b and e) is a westerly wind (positive values) while the rotational circulation (Fig.24c and f) is an easterly wind (negative values) in most months. The total zonal wind being also a westerly wind (positive values: Fig.24a and d), it follows that it is mainly divergent in its kinematic character. This is in line with the findings from Pokam et al. (2014). In addition, the reanalyses (Fig.24a–f) show that, the total and divergent zonal wind peaks' are found in February and August while for the rotational circulation, the peaks are found in May and November since it is principally an easterly wind as highlighted above. Although the seasonality of the total zonal circulation and its components is reasonably captured by the CMIP5 and CMIP6 models, considerable differences in terms of intensity are depicted (Fig.24a–f). Most of the CMIP5 models overestimate the strength

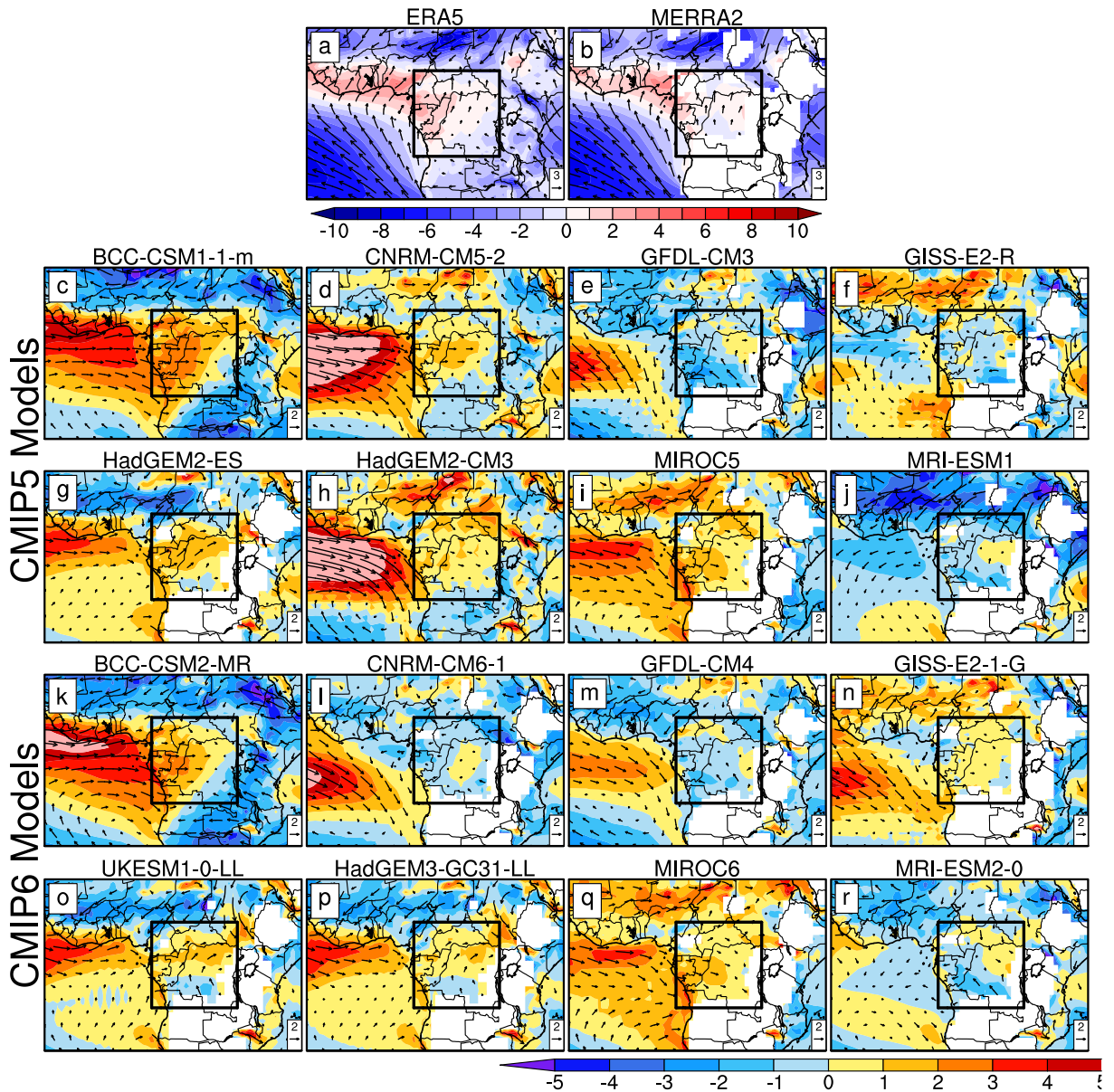


Figure 22: Long term seasonal mean of March–May 925 hPa total wind (vectors: m/s) and zonal wind (shading: m/s) for (a–b) reanalyses, (c–j) CMIP5 models biases with respect to ERA5 and (k–r) CMIP6 models biases with respect to ERA5. The black box is the study region, and the interest is on the inflow at the region’s western boundary.

of the total zonal circulation at the beginning and around the end of the year (Fig.24a). Moreover, in addition to what emerges from Figs. 22 and 23, the BCC-CSM1.1-m model overestimates the total circulation not only in MAM and SON but over the whole year, in contrast with GFDL-CM3 which underestimates the westerly flow in most months (from February to September). Examining the wind components (Fig.24b and c), most models overestimate the westerly component of the rotational circulation throughout the year (Fig.24c), making it a westerly flow that increases its contribution to the total wind.

However, from one model to another, the positive or negative bias in the total zonal circulation (Fig.24a) is generally attributed to the combined biases in both the divergent (Fig.24b) and rotational (Fig.24c) circulation. This is observed in the BCC-CSM1.1-m model that overestimates the total zonal wind as the result of the overestimation of both divergent and rotational components. On the other hand, the overestimated total zonal wind in the HadGEM2-CM3 model is only attributed to the rotational circulation in MAM and SON while from May to August, the deficit of the total wind in the GFDL-CM3 model is mainly due to its underestimated divergent component.

Compared with reanalyses, the rotational circulation (Fig.24f) in the CMIP6 models has led to a stronger underestimated total wind in GFDL-CM4 and MRI-ESM2-0 during June and May (Fig.24d). However, in comparison with the CMIP5 models, smaller biases are generally observed in their corresponding CMIP6 models, highlighting the improvement in the total wind (Fig.24d) which is the result of the improvement in both components (Fig.24e and f). This is well observed in Fig.24g–i displaying the annual cycle of the uncertainty ranges in total, divergent and rotational zonal wind from reanalyses, CMIP5 and CMIP6 models. The uncertainty range here is the spread or the dispersion in a set of data. It is represented with a band and the smaller the bandwidth, the smaller the uncertainty and vice-versa. It appears that, compared to reanalyses, in most months, the spread of the total wind in CMIP6 models is slightly smaller than the one from CMIP5 models due to the improvement in both divergent (Fig.24h) and rotational (Fig.24i) circulation. However, in general, in both CMIP5 and CMIP6 models, the spread of the rotational component (Fig.24i) is larger than the spread of the divergent (Fig.24h) component. This highlights the fact that, in most months, the bias in the rotational circulation contributes most to the bias in the total zonal circulation.

3.2.3 Simulated Convection over Central Africa

To investigate the link between simulated convection and rainfall over CA, Figures 25 and 26 show for reanalyses (Fig.25a-b and Fig.26a-b), CMIP5 models (Fig.25c-j and Fig.26c-j) and CMIP6 models (Fig.25k-r and Fig.26k-r) the Latitude–height cross section averaged between 10°E and 30°E of vertical velocity (shading), zonal wind with a speed equal or greater than 6m/s (contours), vertical motion of meridional wind and omega (vectors) and rainfall (red line) in MAM and SON seasons respectively. Here, zonal

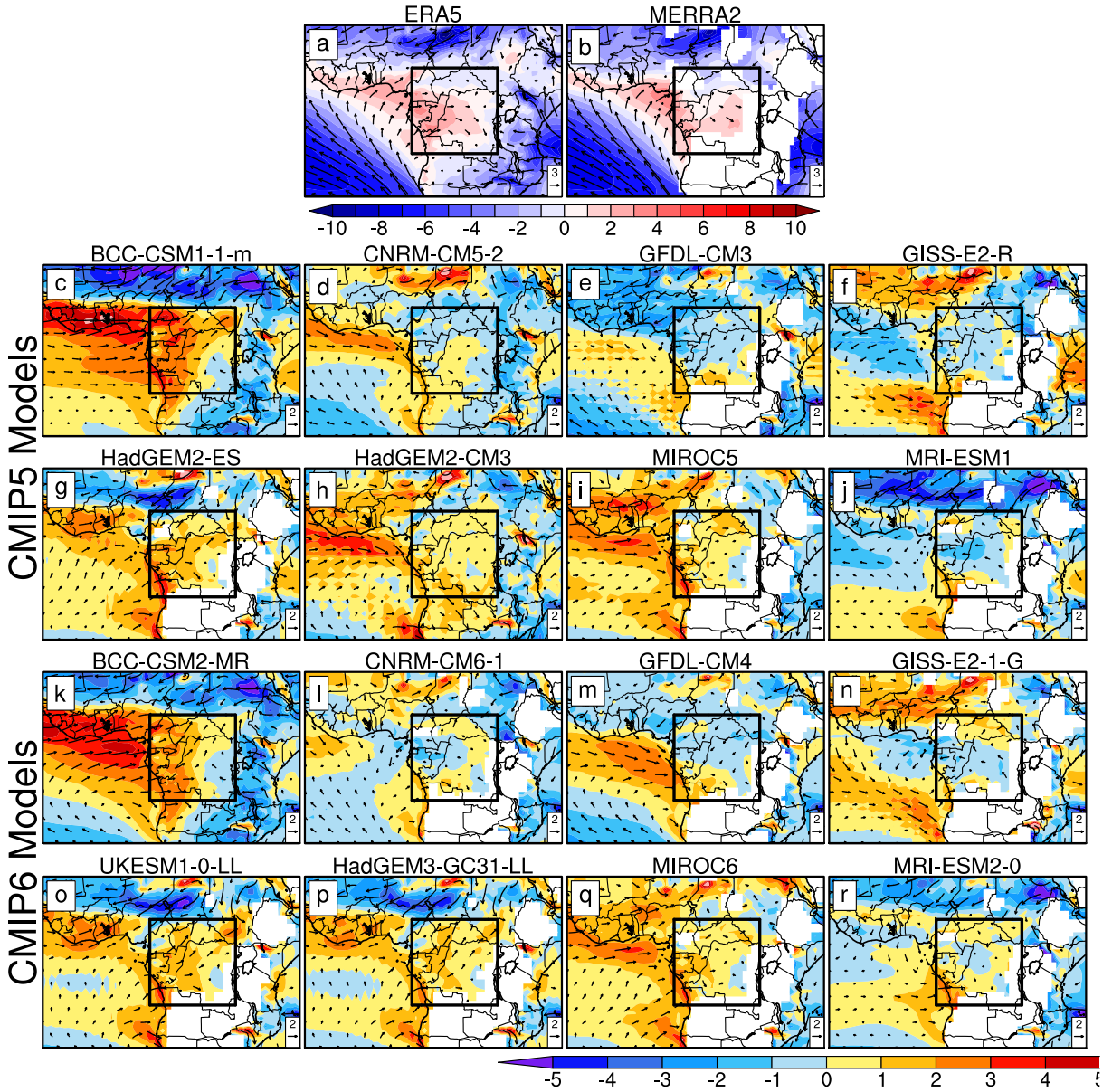


Figure 23: Long term seasonal mean of September–November 925 hPa total wind (vectors: m/s) and zonal wind (shading: m/s) for (a–b) reanalyses, (c–j) CMIP5 models biases with respect to ERA5 and (k–r) CMIP6 models biases with respect to ERA5. The black box is the study region, and the interest is on the inflow at the region's western boundary.

wind with speed equal or greater than 6m/s represent the African Easterly Jet (AEJ) components.

Although its rate is stronger in MERRA2 (Fig.25b and Fig.26b) than in ERA5 (Fig.25a and Fig.26a), convection in reanalyses is centred around the equator in both seasons (MAM: Fig.25a-b and SON: Fig.26a-b) with its intensity stronger in SON season and associated with a higher rainfall amount. In models, the amount of rainfall is associated with the intensity of the simulated convection. In both seasons (Fig.25 and Fig.26),

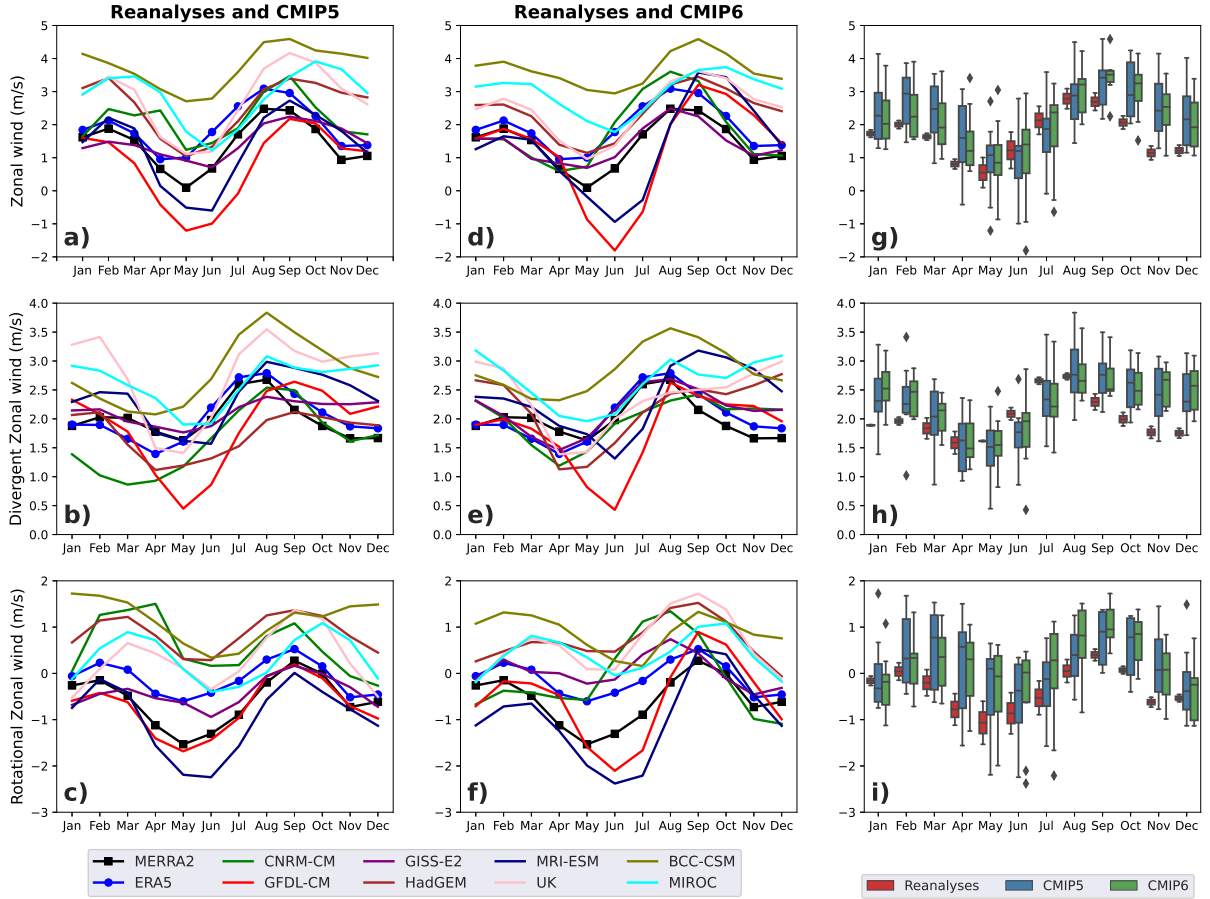


Figure 24: Seasonal cycle of 925 hPa total, divergent and rotational zonal wind averaged between $10^{\circ}S-10^{\circ}N$ and $10^{\circ}-15^{\circ}E$ for (a-c) reanalyses and CIMP5 models, (d-f) reanalyses and CMIP6 models. (g-i) Uncertainty ranges in total, divergent and rotational zonal wind from reanalyses (red), CMIP5 (blue) and CMIP6 (green) models. Note that westerly winds are positive while easterly are negative.

the overestimated rainfall depicted in the BCC-CSM model, especially in its CMIP6 version is associated with stronger convection compared to reanalyses. The surplus of advected moisture in the BCC-CSM model as seen above plays an important role in the understanding of the overestimated rainfall. For the GISS-E2 model (Fig.26f and Fig.26n), underestimated rainfall is associated with the intensity of the simulated weak convection which in turn is associated to the mid-tropospheric moisture flux divergence as seen in the previous section, in agreement with the overestimated intensity of the AEJ which acts as an inhibitor of convection. As far as the MIROC model is concerned, the overestimated rainfall in both version is also associated with a stronger simulated convection in MAM (Fig.25i and Fig.25q) and SON (Fig.26i and Fig.26q) seasons. However, to fully understand simulated rainfall biases in a model, deeper investigation is necessary, and this is done in

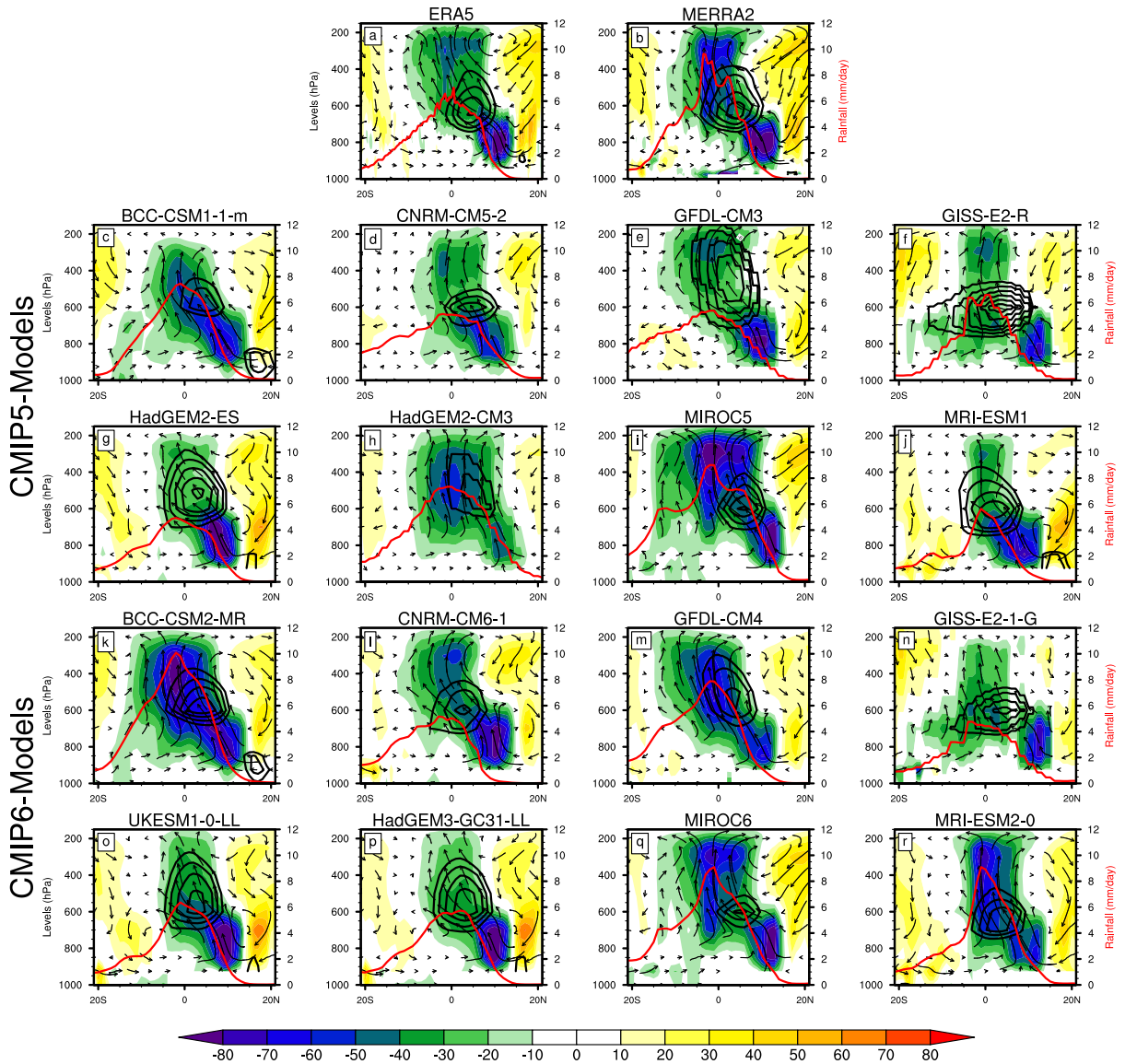


Figure 25: Latitude–height cross section averaged between 10° E and 30° E of vertical velocity (10^{-3} Pa/s: shading), zonal wind with a speed equal or greater than 6m/s (contours), vertical motion of meridional wind and omega (vectors) and rainfall ($\text{mm}\cdot\text{day}^{-1}$: red line) in MAM (March–May) season from (a–b) reanalyses, (c–j) CMIP5 models and (k–r) CMIP6 models. Negative values of vertical velocity represent ascent motion, while positive values represent descent motion.

the following with the MetUM model.

3.3 Focus on the Met Office Unified Model (MetUM)

As seen above, from one model to another, the pattern of rainfall bias is different and the reasons behind each bias also differ from one model to another and could be associated

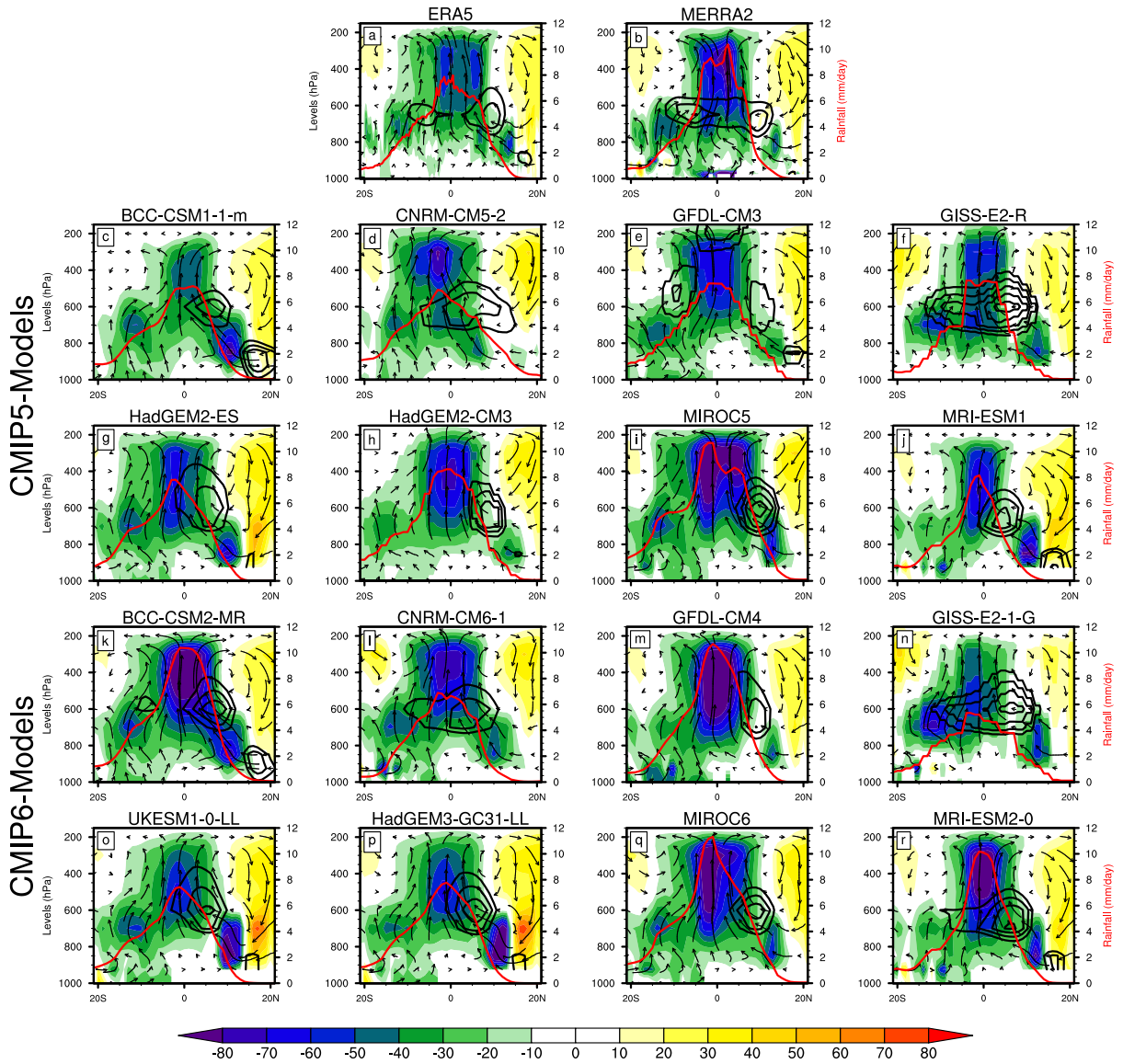


Figure 26: Latitude–height cross section averaged between 10° E and 30° E of vertical velocity (10^{-3} Pa/s : shading), zonal wind (m/s : contours), vertical motion of meridional wind and omega (vectors) and rainfall (mm.day^{-1} : red line) in SON (September–November) season from (a–b) reanalyses, (c–j) CMIP5 models and (k–r) CMIP6 models. Negative values of vertical velocity represent ascent motion, while positive values represent descent motion.

to different atmospheric features going from regional to large scale features. This makes difficult the investigation in all single model. Therefore, to go deeper in the understanding of rainfall biases, the following analyses will focus on the MetUM model which is currently a particular focus of model development over Africa as part of the Improving Model Processes for African Climate (IMPALA) programme. In addition, analysis will be done during the SON season identified in the literature as the main rainy season in the region.

The versions of the MetUM which are considered in this study are those taking part to the CMIP5 and CMIP6 projects denoted respectively as GC2 and GC3 in the following together with their associated atmosphere-only formulations GA6 and GA7. This will help investigate the influence of the atmosphere–ocean coupling by highlighting differences and similarities between the coupled and atmosphere-only formulations of the model over CA.

Let us note that, The most noteworthy modifications in GA7/GC3 compared with GA6/GC2 are to the physical parameterization including a new modal aerosol scheme, an improved treatment of gaseous absorption in the radiation scheme, revisions to the numerics of the convection scheme, introduction of multi-layer sea ice and the introduction of a seamless stochastic physics package in the atmospheric model (Williams et al., 2018; Walters et al., 2019).

3.3.1 Pattern of rainfall biases and link with surrounding oceans

Here, we present (Figure 27) the spatial pattern of the mean September–November rainfall climatology over CA depicted by three observations (GPCP: Fig.27a, UDEL: Fig.27b and CHIRPS: Fig.27c) and two reanalyses (ERA5: Fig.27d and MERRA2: Fig.27e). The models’ (coupled models and their corresponding atmosphere-only version) biases with respect to GPCP are shown in Fig.27f–i. Three observational data sets of precipitation provide a perspective on precipitation uncertainty. The choice of GPCP in bias calculation is due to its availability over oceans. The CA domain used in this study is 10° – 30° E, 10° S– 10° N (box, Fig.27) but Fig.27 covers a larger area including surrounding oceans to provide an overview of the spatial distribution of rainfall biases around CA and to detect possible links with CA rainfall biases.

Observations agree well with the spatial distribution of mean SON rainfall over CA (Fig.27a–c). Two areas of maximum rainfall are located in the northwestern and northeastern parts of CA (Fig.27a–c) although both are higher in CHIRPS (Fig.27c). At the centre of the region, UDEL and CHIRPS show a rainfall maximum that is higher in UDEL and does not appear in GPCP. This highlights uncertainties between observations. According to Maidment et al. (2014), in regions where the gauge network is sparse and unevenly distributed, conversion from point to area averages may be subject to large representativeness errors. This is the case over the Congo Basin where very few gauges exist (Washington et al., 2013). In general, the reanalyses (Fig.27d–e) struggle

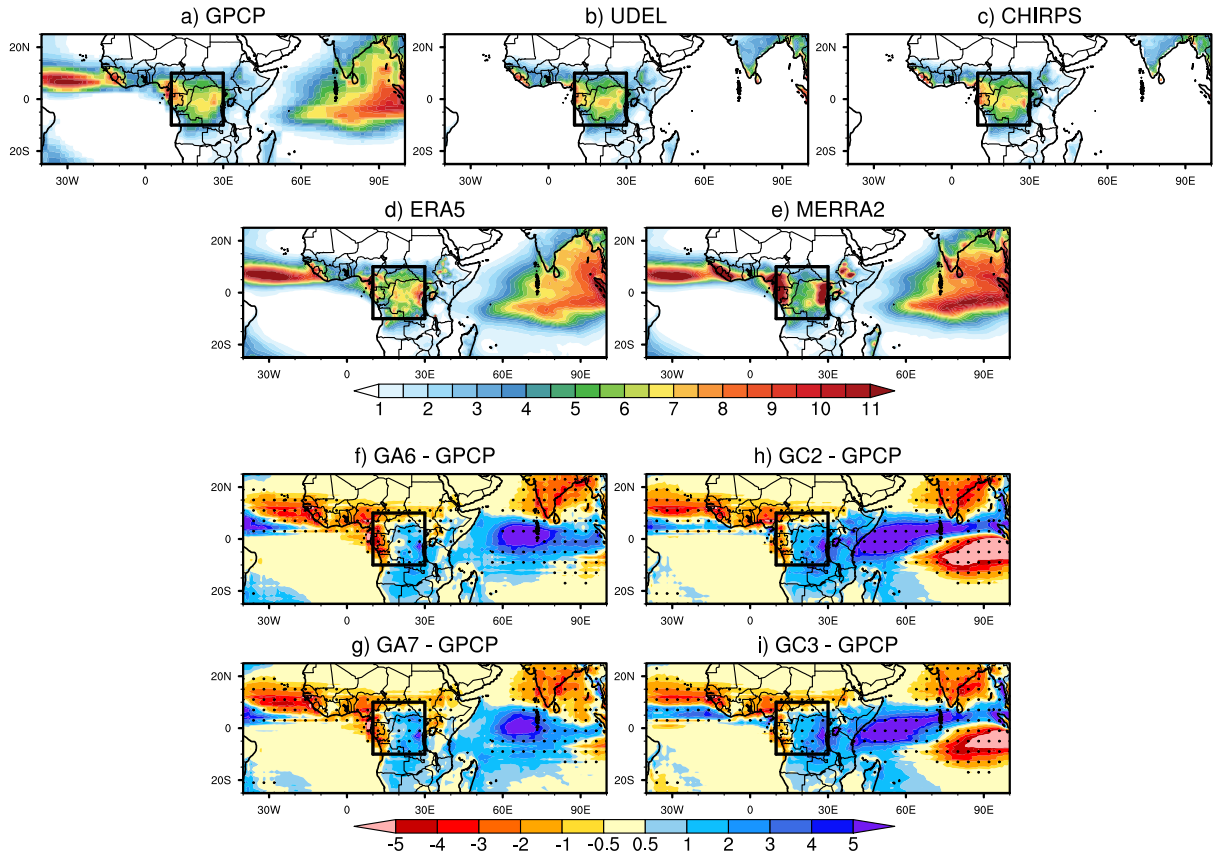


Figure 27: *September–November spatial rainfall (mm/day) climatology for (a–e) GPCP, UDEL, CHIRPS, ERA5 and MERRA2 absolute values (1981–2015), (f–g) atmosphere-only and (h–i) coupled models biases with respect to GPCP. The box in (a–i) indicates the Central Africa domain used in this study and superimposed dots in (f–i) indicate the areas where the differences are statistically significant at the 95% confidence level using the t -test.*

to capture both the spatial pattern and the intensity of rainfall over CA. For instance, the northwestern and the northeastern rainfall maxima are overestimated in the two reanalyses and this is more pronounced in MERRA2 compared to ERA5. In addition, the spatial extent of rainfall maxima in MERRA2 is too large. The disagreement among the reanalyses is likely due to differences in forecast models, data assimilation schemes and available observations (e.g., radiosonde, aircraft and satellite data) (Lin et al., 2014). However, compared to MERRA2 (Fig.27e), ERA5 (Fig.27d) is closest to the mean observed rainfall climatology (GPCP: Fig.27a). Therefore, in dynamical analyses, ERA5 will be considered as the principal reference among reanalyses.

All versions of the MetUM in both coupled and atmosphere-only formulation depict a dipole bias over CA in SON season (Fig.27f–i) with a wet bias (dry bias) over the eastern (western) CA. The dipole pattern is consistent across the model versions whichever

observation is taken as reference (not shown). The wet bias is noticeably larger in coupled models while in atmosphere-only formulations, the dry bias in the western CA is most pronounced. Furthermore, from the older (GA6/GC2) to the recent (GA8/GC4) version in both atmosphere-only and coupled models, the eastern CA wet bias strengthens while the coastal western CA dry bias weakens. This suggests that newer versions of MetUM are wetter over the entire CA compared to previous ones although remaining dry over the coastal region compared to GPCP. Over the Indian Ocean, a wet bias is evident in the central equatorial basin in atmosphere-only models (Fig.27f–g) while in coupled models (Fig.27h–i) the structure of the bias is a dipole with the predominance of dry (wet) bias in the southeastern (western) equatorial Indian Ocean. Let us notice that, the wet bias found in the equatorial Indian Ocean in both atmosphere-only and coupled formulations is much improved in the latest version of the model (GA7/GC3). The improvement could be due to the important convection changes made in GA7/GC3. However, unlike in atmosphere-only models, in coupled models, the Indian Ocean wet bias extends to the east of the African continent to link with the wet bias over eastern CA. The hypothesis here is that a large-scale circulation associated with the Indian Ocean contributes to the eastern CA wet bias in coupled models and may help to explain why they are wetter than their atmosphere-only versions. It should be noted that the wet bias over eastern CA increases in recent versions of the MetUM while over the western Indian Ocean it decreases. This shows that the contribution to the eastern CA wet bias is not limited to the Indian Ocean. As far as the dry bias over the coastal western CA is concerned, in both coupled and atmosphere-only formulations, the bias is not a localized bias too. It extends to the southern coast of Western Africa and could also be the result of the Atlantic Ocean large-scale circulation. Therefore, to understand the models' biases, analyses will first focus on the remote or large-scale drivers such as the atmospheric response to the simulated SST over the Atlantic and Indian Oceans.

3.3.2 Large-scale features associated with rainfall biases

3.3.2.1 Sea Surface Temperature teleconnection

Dezfuli and Nicholson (2013) have highlighted the relationship between rainfall in CA subregions and SST. Their findings reveal that the boreal autumn (October–December) rainfall over eastern (western) CA shows a large spread of positive correlation with

SST over the equatorial Indian Ocean (Benguela coast and the equatorial Atlantic Ocean). Similar findings are shown in Fig.28a (Fig.29a) where observed SON rainfall from GPCP is averaged over eastern (western) CA and correlated with observed SON SST from HadISST for the period 1980–2010. However, in Fig.28a (Fig.29a), the highest positive correlation is found south of Madagascar (southwest of South Africa in the Atlantic Ocean). Fig.28b–e (Fig.29b–e) show biases of correlations computed as in Fig.28a (Fig.29a) for each model with respect to Fig.28a (Fig.29a). The eastern (western) CA area over which rainfall is averaged represents the area of the wet (dry) bias.

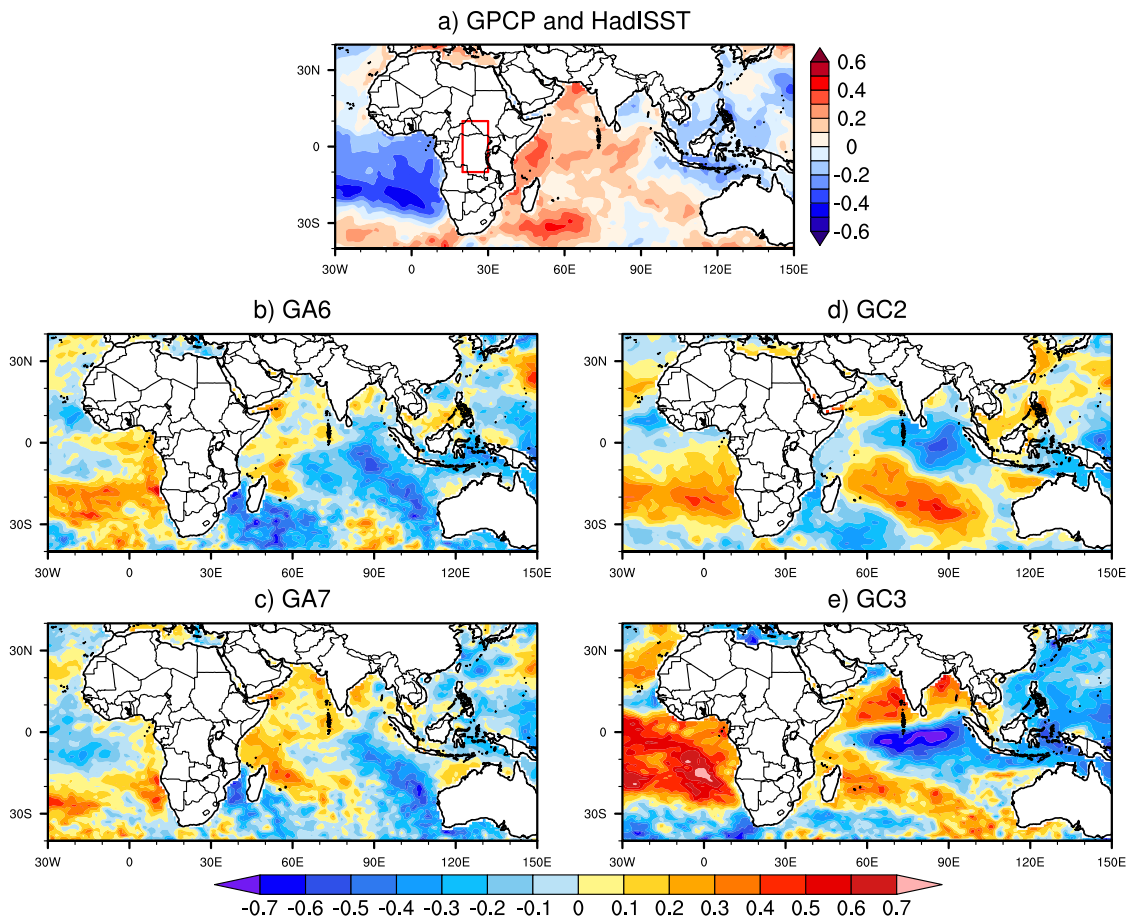


Figure 28: (a) Correlations of observed SON rainfall from GPCP, averaged over eastern Central Africa (the box: 10°S – 10°N , 20° – 30°E), against observed SON SST from HadISST for the period 1980–2010. (b–e) biases of correlations computed as in (a) for each model with respect to (a).

In general, the models struggle to capture the basic features of the teleconnection such as the areas of positive and negative correlation between CA rainfall and SST. In Fig.28b–e, between 0 and 30°S , models generally depict a position correlation bias over the Atlantic Ocean, stronger in coupled than in atmospheric models. This shows that

the relationship between the eastern CA rainfall and SST over the Atlantic Ocean is stronger in models than in observations and the strength of the relationship is more pronounced in coupled models. In the Indian Ocean, a dipole pattern of correlation bias is observed with positive and negative biases in the western and eastern Indian Ocean respectively (although the structure is not well observed in GC2). In addition, the western positive (eastern negative) correlation bias extends southeasterly (westward) in the coupled models. For the relationship between the simulated western CA rainfall and SST (Fig.29b–e), over the Atlantic Ocean, models depict a positive correlation bias stronger than that in Fig.28b–e showing that the western CA rainfall is more associated with the Atlantic Ocean SST variability than the eastern CA rainfall. Furthermore, this positive correlation bias is stronger in coupled (Fig.29d–e) than in atmosphere-only (FFig.29b–c) formulations. In the Indian Ocean basin, west of Australia, a negative correlation bias stronger in AGCM than in CGCM is observed and extends westward along the equatorial region in all CGCM (Fig.29d–e). In sum, in both AGCMs and CGCMs, the deficiencies in the representation of the shared variability between CA rainfall and SST compared to observation are noticed and CGCMs seem to be not superior to AGCMs in this regard. This suggests biases in simulated mechanisms linking Indian and Atlantic Oceans to CA rainfall in both AGCMs and CGCMs.

3.3.2.2 Tropical large-scale circulations

To investigate possible links between the large-scale circulation and precipitation biases, an overview of the zonal circulation along the equator is shown in Fig.30. It represents the longitude-height cross-section of vertical wind and the streamlines constructed from the divergent component of the zonal wind and the vertical wind averaged between 5°S and 5°N. The Atlantic-Congo zonal overturning cell is found between 5°W and 25°E in reanalyses (Fig.30a-b). The cell is described in Longandjo and Rouault (2020) as being a non-closed cell at the base when we assume that the zonal circulation is not thermally driven by the divergent component of the zonal wind. However, its simulated subsiding branch is more intense in the models (Fig.30c–f), particularly in atmospheric versions (Fig.304c–d). Furthermore, the downward branch of the Indian Ocean zonal overturning circulation is almost absent in the three versions of the coupled model (Fig.30e–f). SST biases may help understand this and how rainfall is affected.

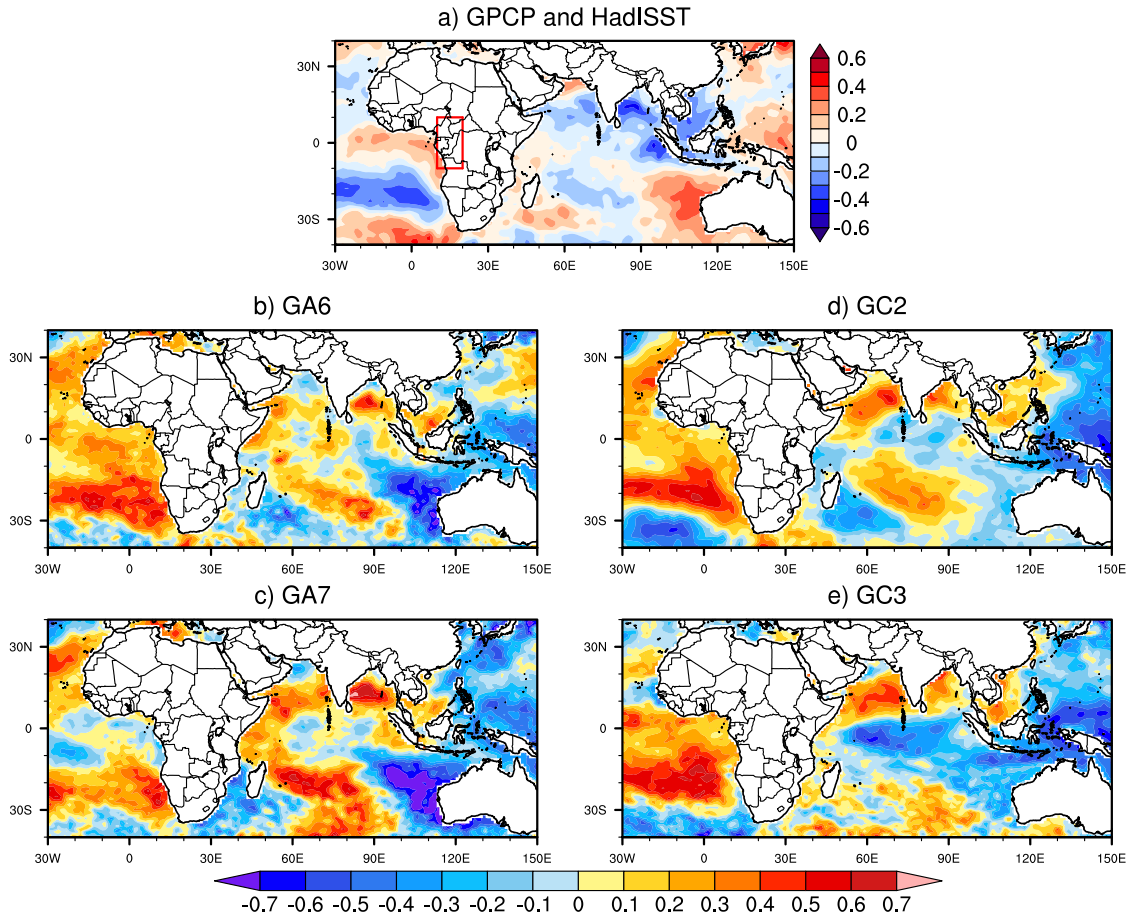


Figure 29: (a) Correlations of observed SON rainfall from GPCP, averaged over western Central Africa (the box: 10°S – 10°N , 10° – 20°E), against observed SON SST from HadISST, for the period 1981–2015. (b–e) biases of correlations computed as in (a) for each model with respect to (a).

The SON climatological SST from HadISST (Fig.31a) and CGCMs SST biases with respect to HadISST (Fig.31d–e) are represented in Figure 31. Given that the AGCMs are prescribed with HadISST, AGCMs SST biases with respect to HadISST are zero and therefore are not represented (Fig.31b–c). Then, it is plausible that the strong subsidence over the Gulf of Guinea (Fig.30) may be attributed to the lack of ocean–atmosphere coupling in the case of the AGCMs. It is also plausible that this response could derive from the anomalously strong upward motion located between 60°E and 90°E over the equatorial Indian Ocean (Fig.30c–f). However, in the coupled models, though the convection over the equatorial Indian Ocean is still pronounced and even more zonally extensive, compared to atmospheric models, a weakening of the subsidence in the Gulf of Guinea is observed (Fig.30e–f). This is associated with the warm SST biases depicted over the Gulf of

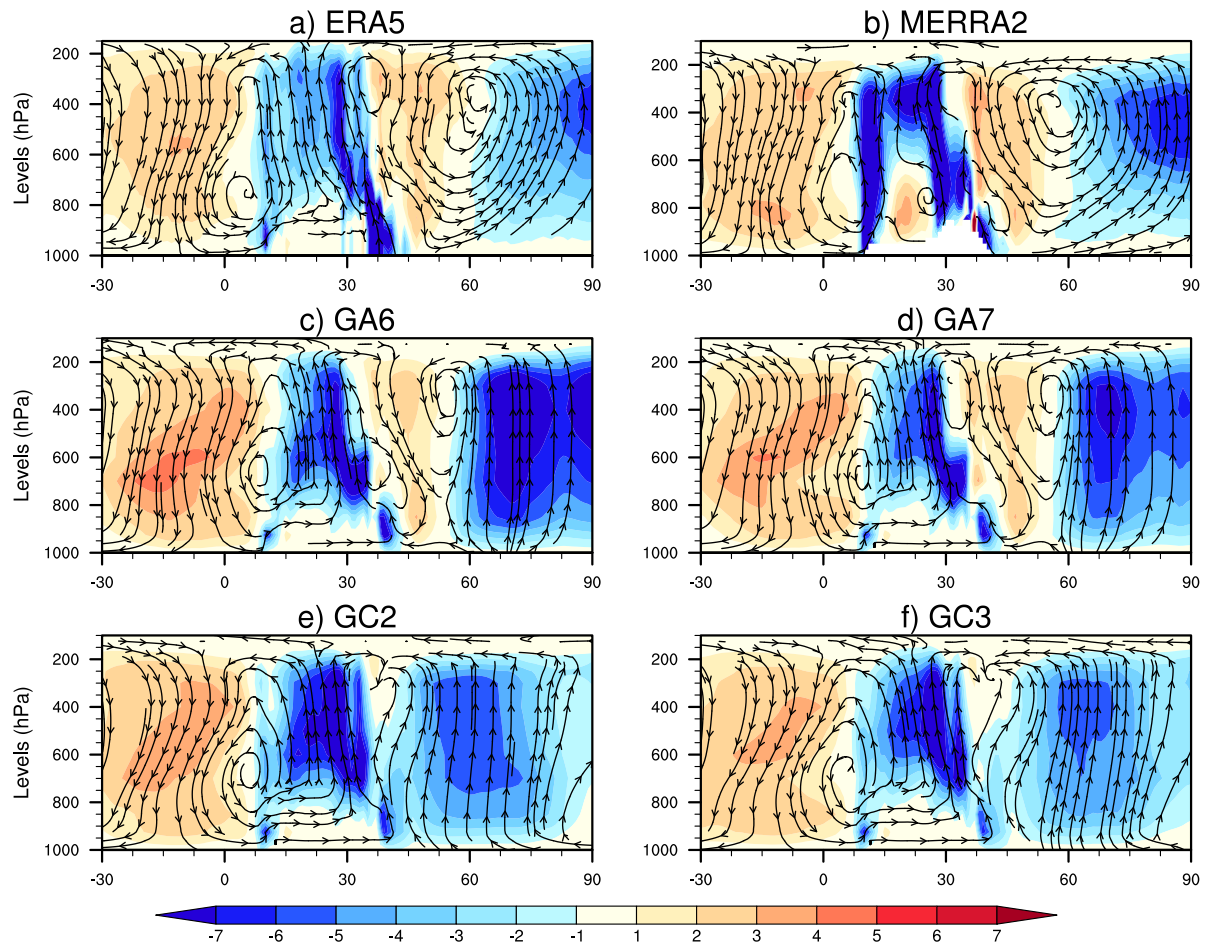


Figure 30: Longitude-height cross-section of the September–November mean climatology of vertical wind ($10^{-2} \text{ Pa} \cdot \text{s}^{-1}$: Shaded) and streamline constructed from the divergent component of the zonal wind ($\text{m} \cdot \text{s}^{-1}$) and the vertical wind ($10^{-3} \text{ Pa} \cdot \text{s}^{-1}$) averaged between 5°S and 5°N for (a and b) reanalyses, (c–d) atmosphere-only models and (e–f) coupled models.

Guinea (Fig.31d–e). Although the strength of the downward branch is less pronounced in the coupled models than in the atmospheric models, it remains stronger than in the reanalyses. Over the western Indian Ocean, coupled models also depict a warm SST bias inhibiting the subsidence branch of the overturning circulation there.

a) Congo basin Walker like circulation Low-level atmospheric circulation with its associated moisture transport from the Atlantic Ocean is known to be primarily driven by the surface temperature difference between the Atlantic Ocean and the Congo basin landmass (Pokam et al., 2014). In this section, in addition to the surface temperature difference, we explore the contribution of the anomalously strong simulated subsidence over the Gulf of Guinea (Fig.30) on low-level moisture transport off the Atlantic Ocean

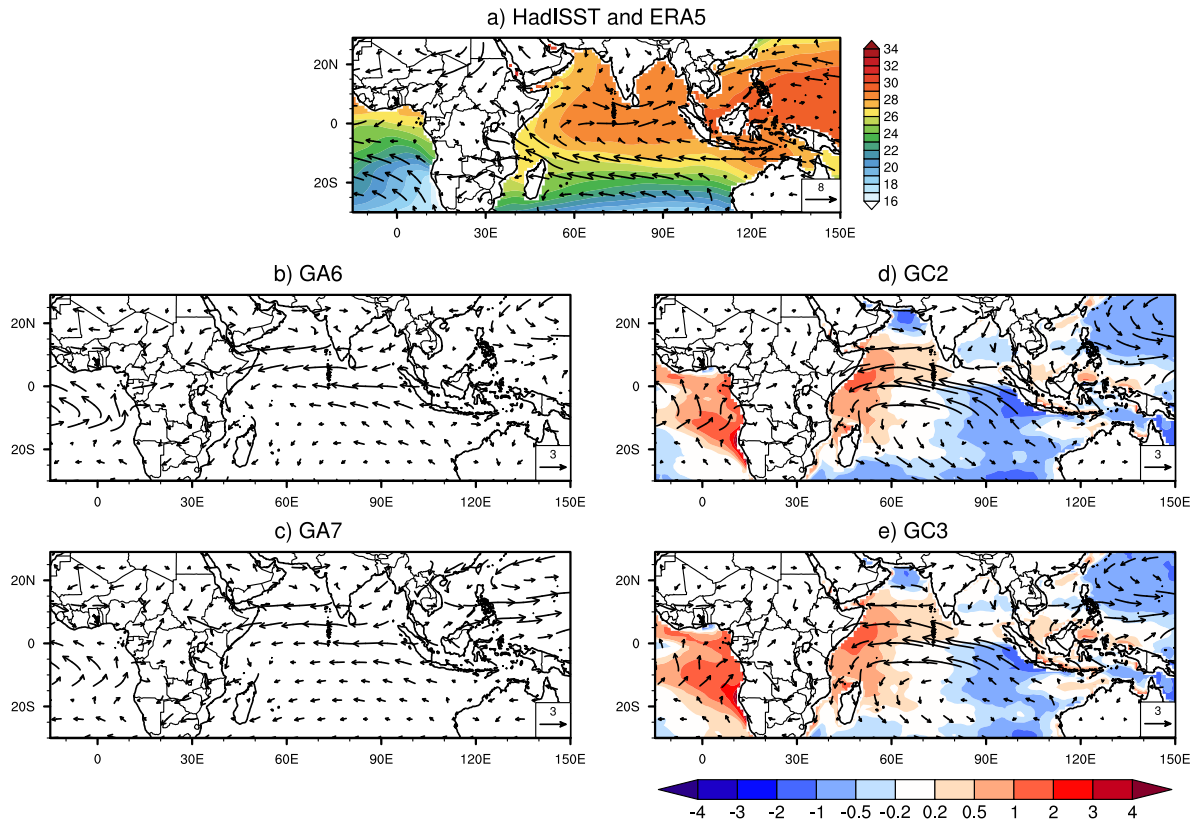


Figure 31: September–November climatology of (a) absolute values of SST ($^{\circ}\text{C}$: Shaded) from HadISST and 850 hPa wind (m.s^{-1} : Vectors) from ERA5; (b–c) AGCMs 850 hPa wind (m s^{-1} : Vectors) biases with respect to ERA5; (d–e) CGCMs SST ($^{\circ}\text{C}$: Shaded) and 850 hPa wind (m.s^{-1} : Vectors) biases with respect to HadISST and ERA5 respectively.

to CA to understand the western CA dry bias.

Figure 32 shows the September–November climatological 850 hPa geopotential height (shaded) and moisture transport (vectors) from reanalyses (Fig.32a–b) and the models’ biases with respect to MERRA2 (Fig.32c–f). In reanalyses (Fig.32a–b) and around the equator (between 5°S and 5°N), the geopotential height decreases progressively eastward from the Atlantic Ocean (Gulf of Guinea) to the continent. This shows a contrast of surface pressure between the ocean and the continent with high (low) pressure over the ocean (continent) bound up with the sinking (rising) branch of the Atlantic-Congo zonal overturning cell. The simulated 850 hPa geopotential height biases (Fig.32c–f) show differences in the models with GA6, GC2 and GC3 depicting in general negative biases while GA7 depicts positive biases. However, despite the differences, in all versions and formulations of the model, the zonal transect of surface pressure exhibits a decrease from

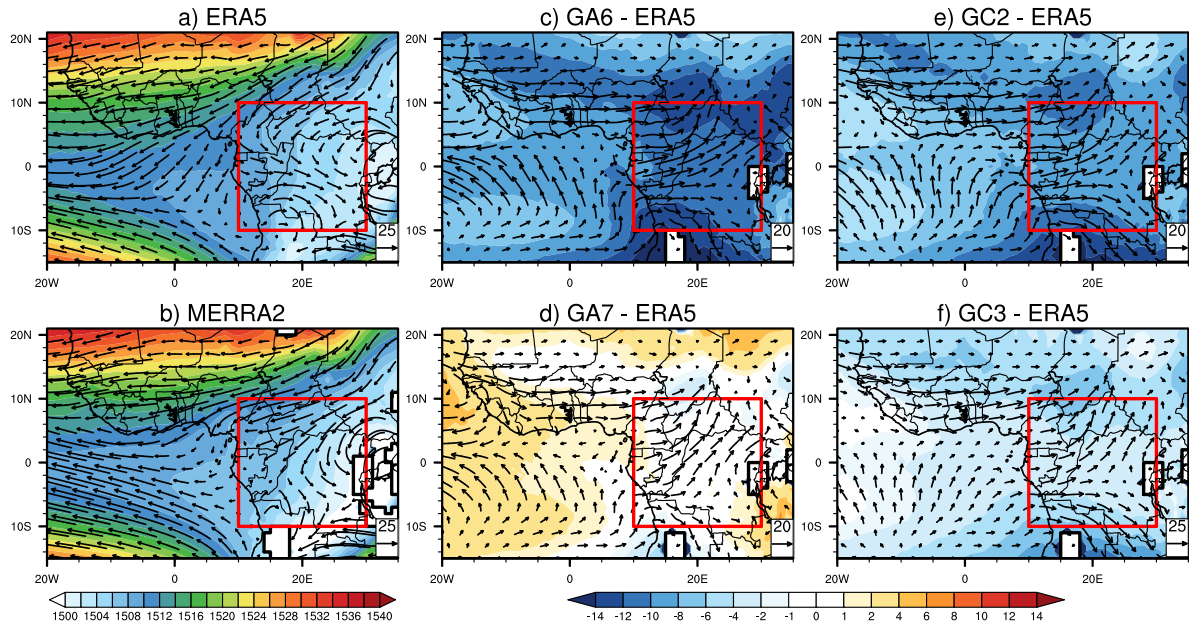


Figure 32: September-November climatological 850 hPa geopotential height (m: shaded) and moisture transport ($\text{g.kg}^{-1}.\text{m.s}^{-1}$: vectors). a-b) Absolute values of ERA5 and MERRA2 respectively. c-f) Models biases of 850 hPa geopotential height and moisture transport with respect to ERA5. The red box is the Central Africa region.

the Atlantic Ocean to the continent, stronger in models than in the reanalyses (Fig.33a). This is particularly well observed in GA7 (Fig.32d) with a higher pressure bias over the ocean and a lower pressure bias over the continent related to the strong simulated sinking branch of the Atlantic-Congo zonal overturning cell (Fig.30). In addition, the stronger simulated land-ocean thermal difference between the Central African landmass and the coastal Atlantic Ocean (Fig.33b) is in agreement with the simulated strength of the zonal surface pressure decrease from the Atlantic Ocean to the continent (Fig.33a). This has an impact on low-level moisture transport.

In reanalyses and over the Atlantic Ocean (Fig.32a-b), moisture transport is predominantly easterly and northeasterly north of the equator and southeasterly south of the equator. However, the strength of the subsidence branch of the Atlantic-Congo zonal overturning cell in the models (Fig.30c-f) is associated with higher pressure over the Gulf of Guinea (Fig.32c-f). This enhances the pressure gradient between the Atlantic Ocean and the Coastal area which increases moisture transport as indicated by the westerly and southwesterly biases over southern West Africa and along the coastal region of CA (Fig.32c-f). The strong moisture transport in the models results in the dry bias at the western CA coast. Therefore, the stronger dry bias in atmospheric models over western

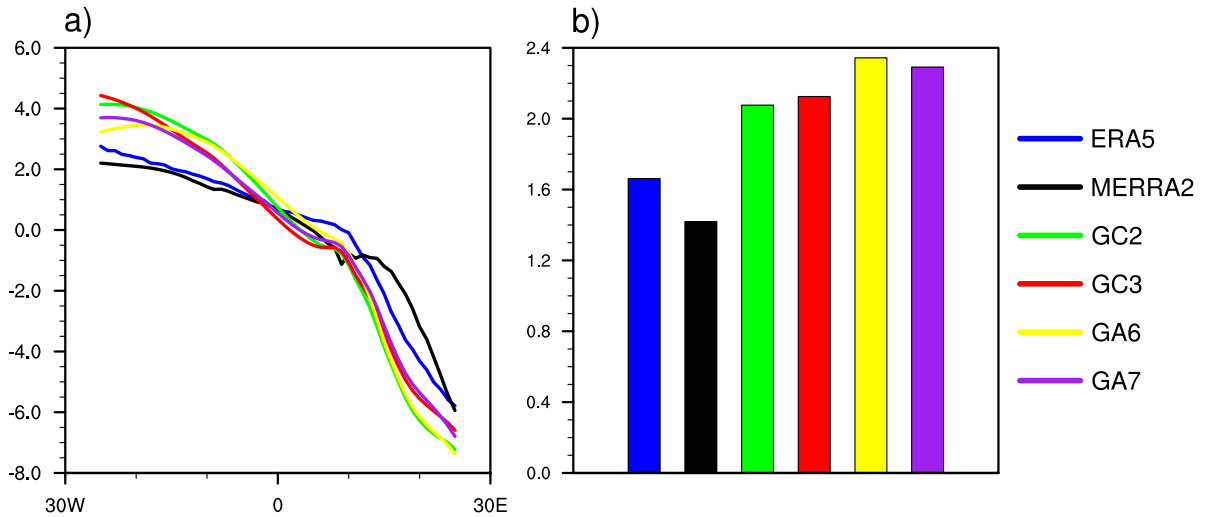


Figure 33: (a) September–November (SON) meridional average (5°S – 5°N) of 850 hPa geopotential height (m) minus spatial mean (5°S – 5°N ; 25°W – 25°E) of 850 hPa geopotential height for reanalyses, coupled and atmosphere-only models. (b) 850 hPa land-ocean thermal difference between the Central African landmass (5°S – 5°N ; 15° – 30°E) and the coastal Atlantic Ocean (5°S – 5°N ; 5°W – 5°E) for reanalyses, coupled and atmosphere-only models.

CA as compared to coupled models is associated with the more pronounced overestimated subsidence over the Gulf of Guinea. Furthermore, although in the most recent version of both coupled and atmospheric models (GC3/GA7) the strength of the downward branch of the Atlantic-Congo zonal overturning circulation is still overestimated with respect to ERA5, an improvement in the strength is observed compared to older version (Fig.30). Its weakening in GC3/GA7 is in agreement with the reduced dry bias over western CA compared to older version (GC2/GA6).

In terms of the contribution from the Atlantic Ocean to the eastern CA wet bias, as shown above, the strength of the simulated subsidence over the Gulf of Guinea is overestimated (Fig.30) and associated with a high ocean-land pressure gradient which strengthens the moisture transport from the Atlantic Ocean to CA (Fig.32). The strength of the moisture transport is then sufficiently strong to dry out the coast and wet the eastern CA. Moisture entering through the western boundary of the CA region is then overestimated in both coupled and atmospheric models. In addition, in all versions of the coupled model, warmer SST in the Gulf of Guinea (Fig.31d–e) is likely to enhance evaporation and therefore, more moisture is available to be advected toward eastern CA. This can explain why eastern CA is wetter in coupled models than in atmospheric models.

b) Indian Ocean overturning circulation To understand the misrepresentation of the Indian Ocean large-scale circulation (Fig.30) and how this could affect CA rainfall, mean SON SST and low-level (850 hPa) wind are explored over the Indian Ocean in Figure 31. Maximum SST are found over the equatorial Indian Ocean (Fig.31a) with warmer SST in the eastern sector of the ocean compared to the western sector. This leads to a prevalence of westerly winds which form the lower branch of the Indian Ocean zonal overturning circulation (Fig.31a). With regard to the coupled models, they depict a mean SST bias in the Indian Ocean with the pattern of the positive IOD with a warm (cold) bias over the western (southeastern) Indian Ocean (Fig.31d–e). This is similar to the findings from Hirons and Turner (2018). In agreement with the dipole pattern of correlation over the Indian Ocean (Fig.28b–e), the simulated 850 hPa equatorial winds in the Indian Ocean exhibit easterly anomalies which are more pronounced in CGCMs than in AGCMs (Fig.31b–e). The easterly anomalies result in weaker westerly winds in AGCM and anomalous easterly winds in CGCM (not shown here). Therefore, the easterly anomalies present in the atmospheric models are intensified in the coupled models due to the positive IOD pattern in the mean state of their SST biases (Fig.31d–e). Indeed, in the coupled models, the positive IOD pattern weakens the downward branch of the Indian Ocean East–West overturning circulation (Fig.30) and strengthens the existing easterly anomalies at the surface (Fig.31). The easterly anomalies are likely to be associated with an anomalous moisture advection from the Indian Ocean to the continent.

To assess the effect of the positive IOD-like pattern on the advected moisture from the Indian Ocean, an examination of the strongest positive IOD years compared to the mean state in both the reanalyses and the models is performed. A composite of years with the strongest positive IOD pattern is constructed following Hirons and Turner (2018). For each dataset, the IOD index is calculated for each year in the SON season and years are ranked from the lowest to the highest value of their IOD index. The top 20% of years is then chosen to build the composite. The SON climatological mean of the vertical integrated zonal moisture flux (shading) and total moisture flux (vectors) is subtracted from the mean of the years corresponding to the composite to form the composite anomaly which is represented in Figure 34 for each dataset. The two reanalyses agree with an inflow of moisture through the eastern boundary of the CA region (Fig.34a–b). In agreement with findings from Moihamette et al. (2022), this highlights the fact that during positive IOD

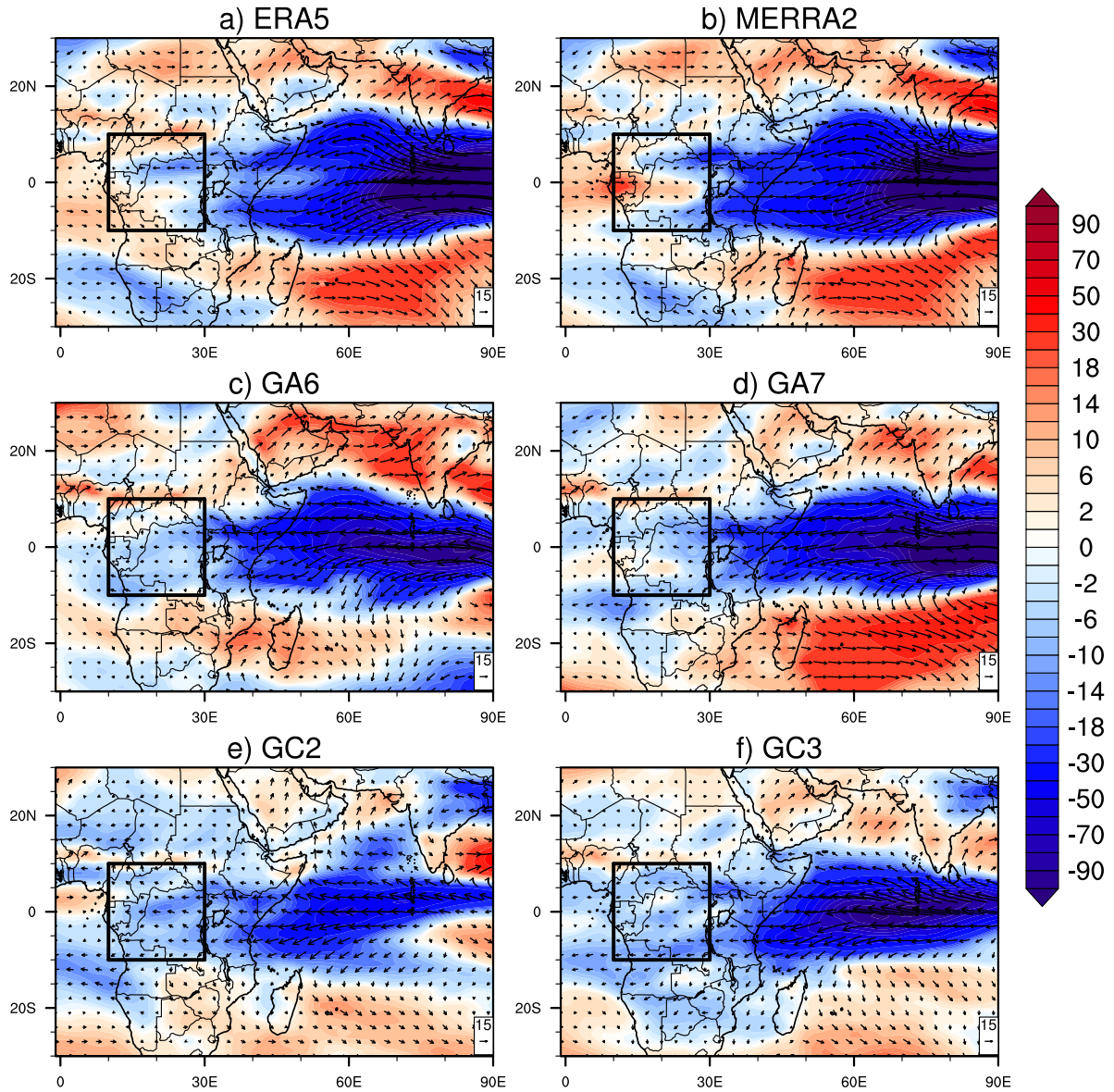


Figure 34: Composite anomaly of SON vertical integrated (1,000-100 hPa) zonal moisture transport ($\text{kg.m}^{-1}.\text{s}^{-1}$: Shading) and total moisture transport ($\text{kg.m}^{-1}.\text{s}^{-1}$: Vectors) for positive IOD years. The strongest positive IOD years minus the mean state in (a and b) each reanalysis, (cd) atmosphere-only models and (e-f) coupled models. The box in (a-f) indicates the CA domain used in this study.

years, easterly winds advect more moisture from the Indian Ocean to CA and contribute to rainfall in the region. Although the moisture is drawn from a much broader area across the IO basin in the reanalyses (Fig.34a-b) compared with a narrower channel of moisture in the models (Fig.34c-f), the inflow of moisture from the Indian Ocean at the eastern boundary of the rectangular box is stronger and extends further west in models.

The westward extension is more pronounced in the coupled than in the atmosphere-only models (Fig.34c–f). In the atmosphere-only models, the mean state easterly winds anomalies (Fig.31b–c) is added to the easterly wind due to a positive IOD pattern in the composite to advect more moisture from the Indian Ocean to the CA region as shown in Fig.34c–d. In the coupled models, the anomalous mean state easterly winds from the atmosphere-only models are reinforced by the positive IOD pattern in the mean state SST biases (Fig.31d–e). This is added to the easterlies of the positive IOD years to advect more moisture from the Indian Ocean to the CA region (Fig.34e–f) compared to the atmosphere-only models. As a result in the MetUM models, biases in large-scale circulation over the Indian Ocean contribute to the wet conditions over eastern CA, in line with the spatial distribution of simulated rainfall biases (Fig.27f–i).

These results show that large-scale circulations from both the Atlantic and the Indian Oceans have a role in the simulated rainfall biases over CA. However, simulated key regional features may also contribute to overestimating or underestimating simulated rainfall over the region.

3.3.3 Regional mechanisms associated with rainfall biases

Past studies (Nicholson and Grist, 2003; Jackson et al., 2009; Dezfuli and Nicholson, 2013; Kuete et al., 2020; Longandjo and Rouault, 2020) have shown that there are dominant features of the local circulation such as the two components of the African Easterly Jet (AEJ-S and AEJ-N) and the Congo basin cell that play an important role in rainfall variability over CA. In this section, these features are investigated in association with the wet and dry biases over eastern and western CA respectively.

3.3.3.1 Low level tropospheric circulations

Longandjo and Rouault (2020) highlights the existence of a lower tropospheric, closed, counterclockwise and shallow zonal overturning cell over CA namely the Congo basin cell discernible throughout the year. The Congo basin cell intensity and width are driven by the near-surface temperature warming on both the central African landmass and the eastern equatorial Atlantic, leading to LLWs which form the lower branch of the cell. Therefore, the width of the cell is linked to the strength of LLWs. The stronger the LLWs, the larger the Congo basin cell.

Figure 35 shows the zonal mass-weighted stream function with the zonal wind averaged over the latitudinal band 5°S – 5°N before computing the zonal mass-weighted stream function. Negative values of the mass-weighted stream function (dashed red contours) depict the Congo basin cell. It appears that the models overestimate the intensity

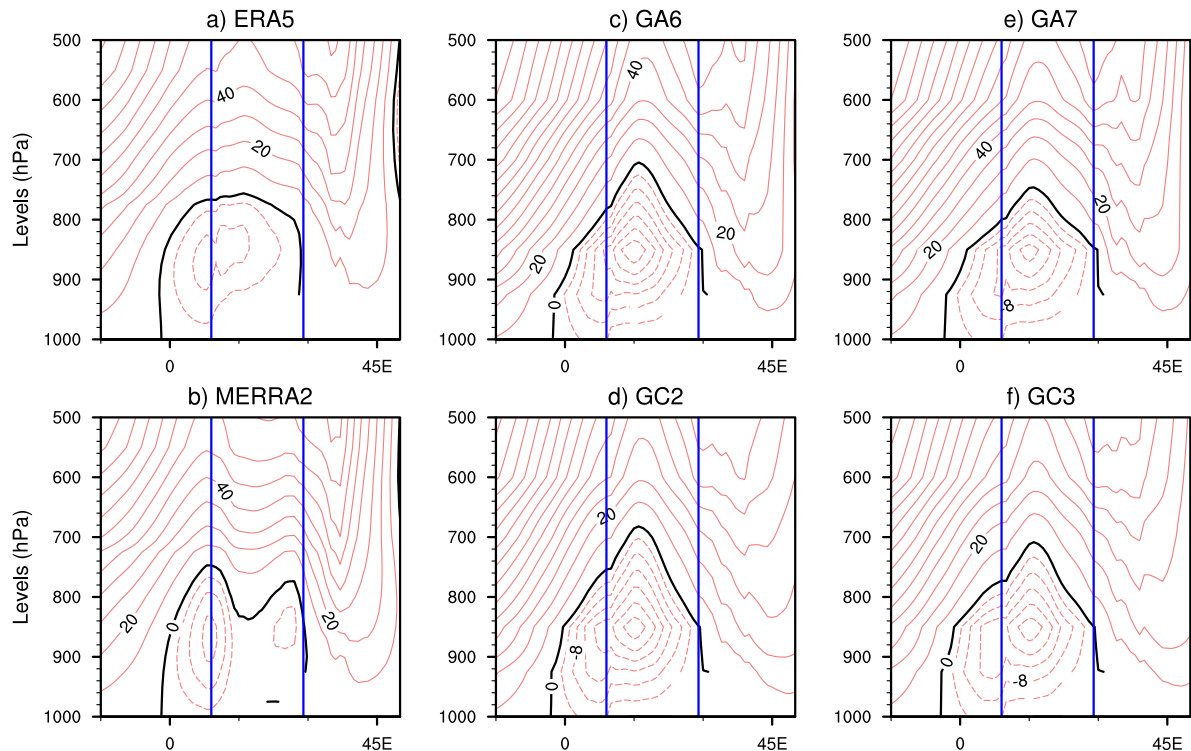


Figure 35: September–November (SON) climatological mean of the zonal mass-weighted stream function (contours: $10^{11} \cdot \text{kg} \cdot \text{s}^{-1}$) computed with 5°S – 5°N averaged zonal wind for (a and b) ERA5 and MERRA2, (c–d) Atmosphereonly models (GA6 and GA7), and (e–f) coupled models (GC2 and GC3). Solid and dashed contours represent positive and negative values of mass-weighted stream functions respectively, separated with the zero value of mass-weighted stream (thicker contour). Contour intervals are 10 between positive contours and 4 between negative contours. The vertical lines are the zonal boundaries of the CA region.

and the width of the cell (Fig.35c–f) with the western edge of the cell located farther west in the models compared to reanalyses. Simulated LLWs transport moist air from a farther west position in the equatorial Atlantic (Fig.32c–f) in agreement with the farther west position of the western edge of the Congo basin cell (Fig.35c–f). Furthermore, the overestimated strength of the simulated Congo basin cell in the models is associated with strong simulated LLWs (Fig.32) over the Atlantic coastal area due to the strong ocean-land pressure contrast (Fig.33). As shown in the above section, this induces a strong moisture

divergence at the coastal area and, in turn, dry conditions. The misrepresentation in the intensity and width of the simulated Congo basin cell is therefore associated with the western CA dry bias through the overestimation of the simulated LLWs. The dryness of MetUM over the coastal region in CA is well known (Creese and Washington, 2016; James et al., 2018) and the present study underlines the persistence of this bias, although slightly reduced in recent versions of the model.

The misrepresentation of the Congo basin cell (Fig.35c-f) is also associated with the eastern CA wet bias. Known to play an important role in rainfall redistribution over CA via the zonal rainfall maximum position (Longandjo and Rouault, 2020), the width and the intensity of the Congo basin cell are respectively associated with the zonal position and the strength of the eastern CA rainfall peak (Longandjo and Rouault, 2020). Therefore, the overestimation in its simulated width and intensity (Fig.35c-f) is related to a larger advection of moisture from the farther west position in the equatorial Atlantic toward the eastern edge of the cell. This leads to a strong moisture convergence at the eastern edge of the cell and since this is the location of its rising branch, more convection and more rainfall are observed in comparison with the reanalyses. In addition, the depth of the cell appears to be higher in models. This is associated with the depth of the convection and the latter influences the biases. The height of the cell in models is therefore also associated with the wet bias.

Next we investigate how the topography at the Atlantic coastal area could affect rainfall. Figure 36 shows the vertical profile of zonal wind averaged between 10°S and 10°N with gray shape showing the high of the topography. In reanalysis (Fig.36a-c), and particularly in MERRA2, weak convection is found between 950hPa and 850hPa at 15°E likely due to orography near the coastal area. The topography blocks LLWs (moist air) coming from the Atlantic Ocean and forces upward motion and orographic rainfall. This phenomenon is not observed in models. At 15°E in models, convection tends to start at around 950hPa due to orography. But at 850hPa the convection is suppressed because as seen previously, the strength of LLWs is overestimated in models. Without the orographic rainfall at the coastal area, models depict dry biases.

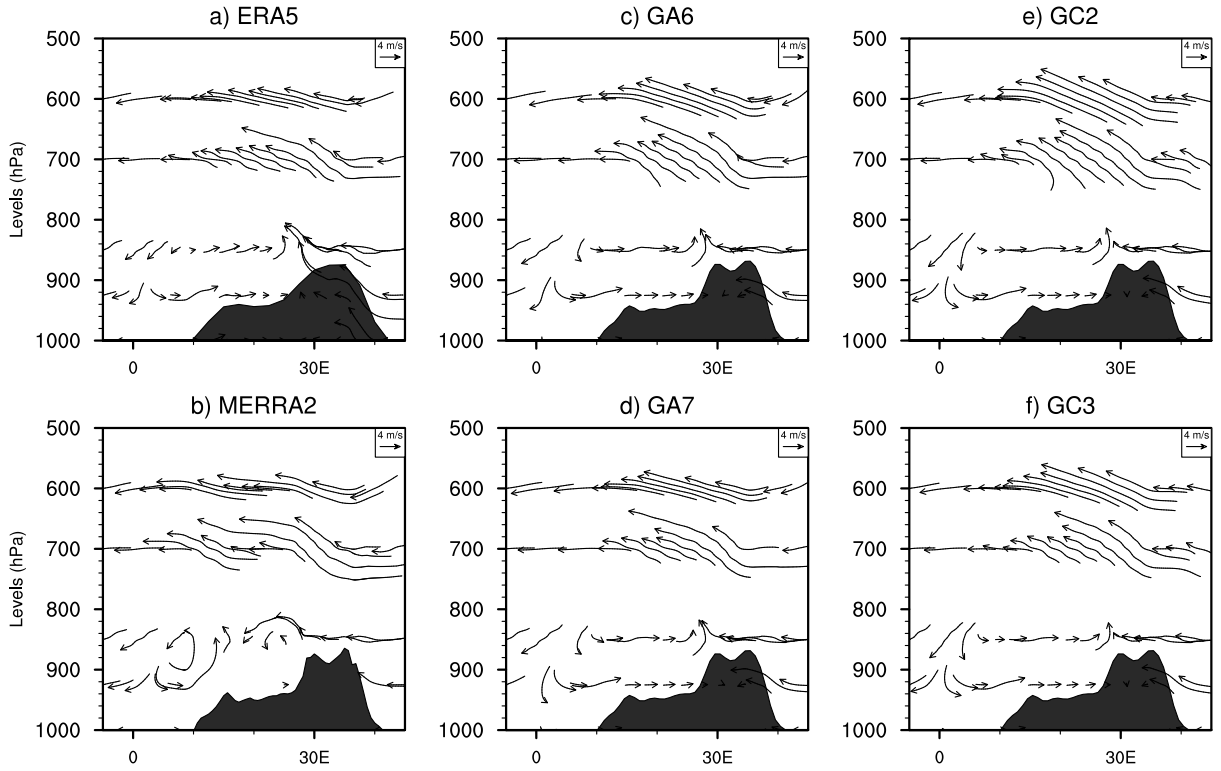


Figure 36: Vertical profile of zonal wind ($m.s^{-1}$: vectors) constructed with vertical velocity ($4.10^{-2}.Pa.s^{-1}$) and averaged between $10^{\circ}S$ and $10^{\circ}N$. Gray shade represents the orography in (a-b) each reanalysis, (c-d) atmosphere-only models and (e-f) coupled models.

3.3.3.2 Mid-tropospheric circulation

Known as the mid-tropospheric (700–600 hPa) easterly wind (with a speed equal to or greater than $6 m.s^{-1}$ (Nicholson and Grist, 2003; Kuete et al., 2020), the AEJ-N and AEJ-S are key regional circulation features over CA during the SON season. Previous studies have established that CA rainfall is strongly related to the advected moisture into the region with AEJ components playing an important role in controlling the mid-level moisture flux convergence (Nicholson and Grist, 2003; Jackson et al., 2009; Washington et al., 2013). Furthermore, Jackson et al. (2009) have identified a maximum in MCS activity in the region of that strong mid-level convergence.

Setting up by the surface temperature contrast between Congo and both Saharan Cook (1999) and Kalahari dry-lands (Kuete et al., 2020), we first investigate the link between the AEJ components and the mechanisms associated with their setup. Figure 37 shows AEJ components and the meridional potential temperature gradient at 850 hPa in both reanalyses and models. Although significant discrepancies could have been expected

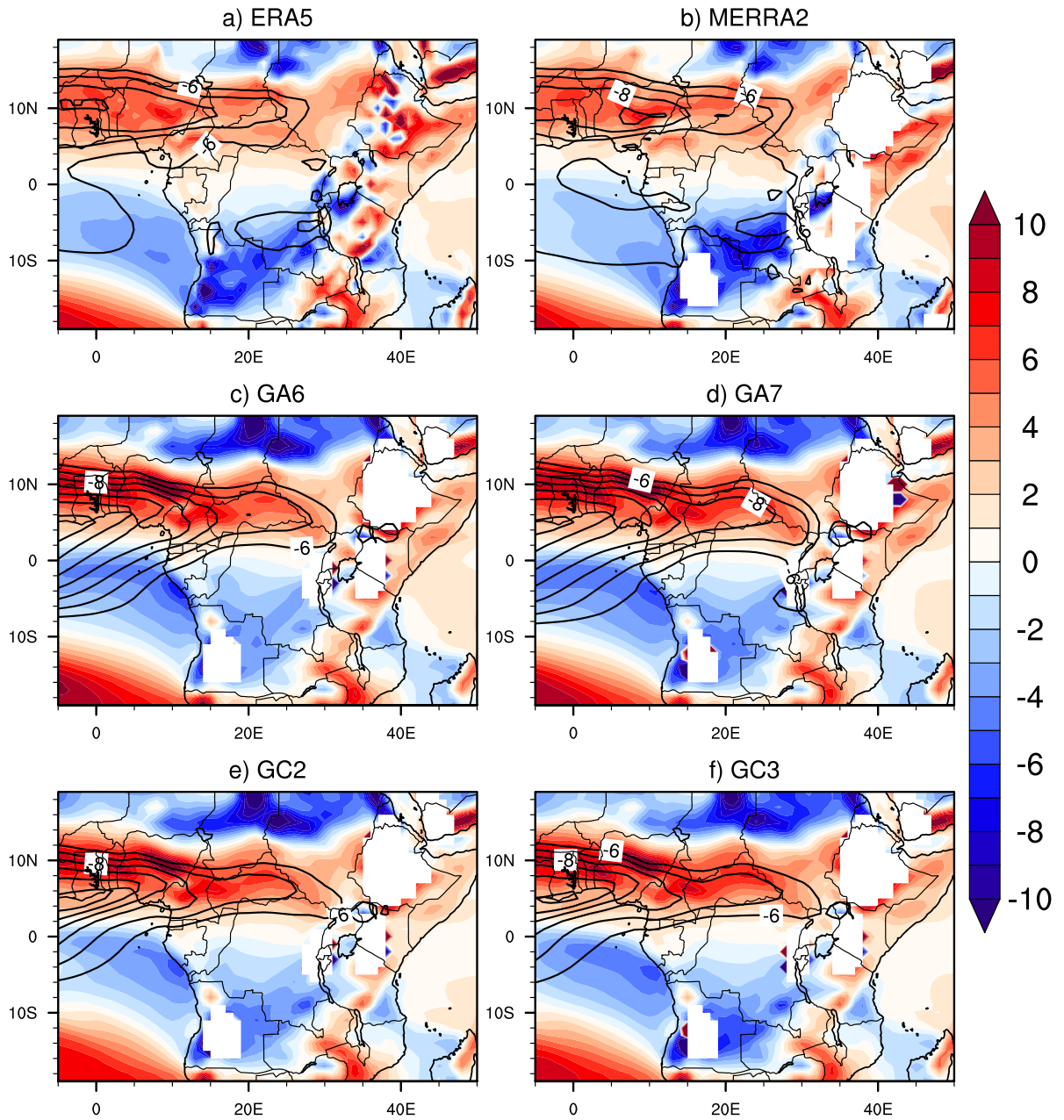


Figure 37: September–November long-term mean meridional potential temperature gradient ($10^6 \cdot K \cdot m^{-1}$; shaded) at 850 hPa and zonal easterly wind averaged between 700 and 600 hPa with speed $\geq 6 \text{ m} \cdot \text{s}^{-1}$ (contours) for (a–b) reanalysis, (cd) atmosphere-only models and (e–f) coupled models.

between different reanalysis products due to the paucity of upper-air observations in that region, it appears that the two reanalyses agree relatively well in the representation of the two AEJ's components (Fig.37a-b). Furthermore, the AEJ-N (AEJ-S) is associated with a strong positive (negative) meridional potential temperature gradient centred at around 10°N (10°S). Compared to reanalyses and according to the threshold of $6 \text{ m} \cdot \text{s}^{-1}$,

the intensity and the extent of the AEJ-N are both overestimated in the models (Fig.37c–f) and much more in the atmosphere-only formulation (Fig.37c–d) while its southern component is not detected in the two formulations of the model whatever the version (Fig.37c–f). This reflects an underestimation of the easterly wind in the region where the AEJ-S is supposed to be found. Errors in the simulated AEJ components are associated with a misrepresentation of the meridional potential temperature gradient. Compared to reanalyses, the overestimation (absence) of the AEJ-N (AEJ-S) is associated with a stronger (weaker) positive (negative) meridional potential temperature gradient centred at around 10°N (10°S). Therefore, the fact that the strength of both AEJ-N and AEJ-S biases are of the same magnitude in all versions of MetUM suggest that changes in land surface schemes across model versions have not significantly improved surface characteristics (e.g., temperature and soil moisture) contrast between Congo and both Saharan and Kalahari drylands.

To investigate how the wrong representation of the AEJ components contribute to the simulated wet bias over eastern CA, the jets are represented (contours) in Figure 38 with the vertical wind (vectors) and the net zonal moisture transport, computed as the difference between moisture flux across the western (20°E) and the eastern (30°E) boundary of the zonal extension of the wet bias. Positive values indicate moisture flux convergence and negative values moisture flux divergence. It appears in reanalyses (Fig.38a-b) that at mid-troposphere, jet components found at around 10°S and 10°E are associated with moisture flux divergence. This leads to moisture flux convergence and strong convection around the equator. In models (Fig.38c–f), the misrepresentation in the intensities of the AEJ's components is associated with biases in the net zonal moisture flux and convection. The overestimation (absence) of the AEJ-N (AEJ-S) is associated with a stronger mid-tropospheric net moisture flux divergence (convergence) favouring dry (wet) conditions. This is in line with Dezfuli and Nicholson (2013) who showed that, at interannual time scales, the variability of the strength of AEJ's components is opposed to that of the rainfall amount with abnormally strong (weak) jets associated with dry (wet) years. Then AEJ's components have opposite effects in the MetUM models. The overestimated AEJ-N strength tends to suppress convection while the absence of AEJ-S favours convection and in turn precipitation. These findings are similar to those of Creese and Washington (2018). Furthermore, biases in the strength of the AEJ's components

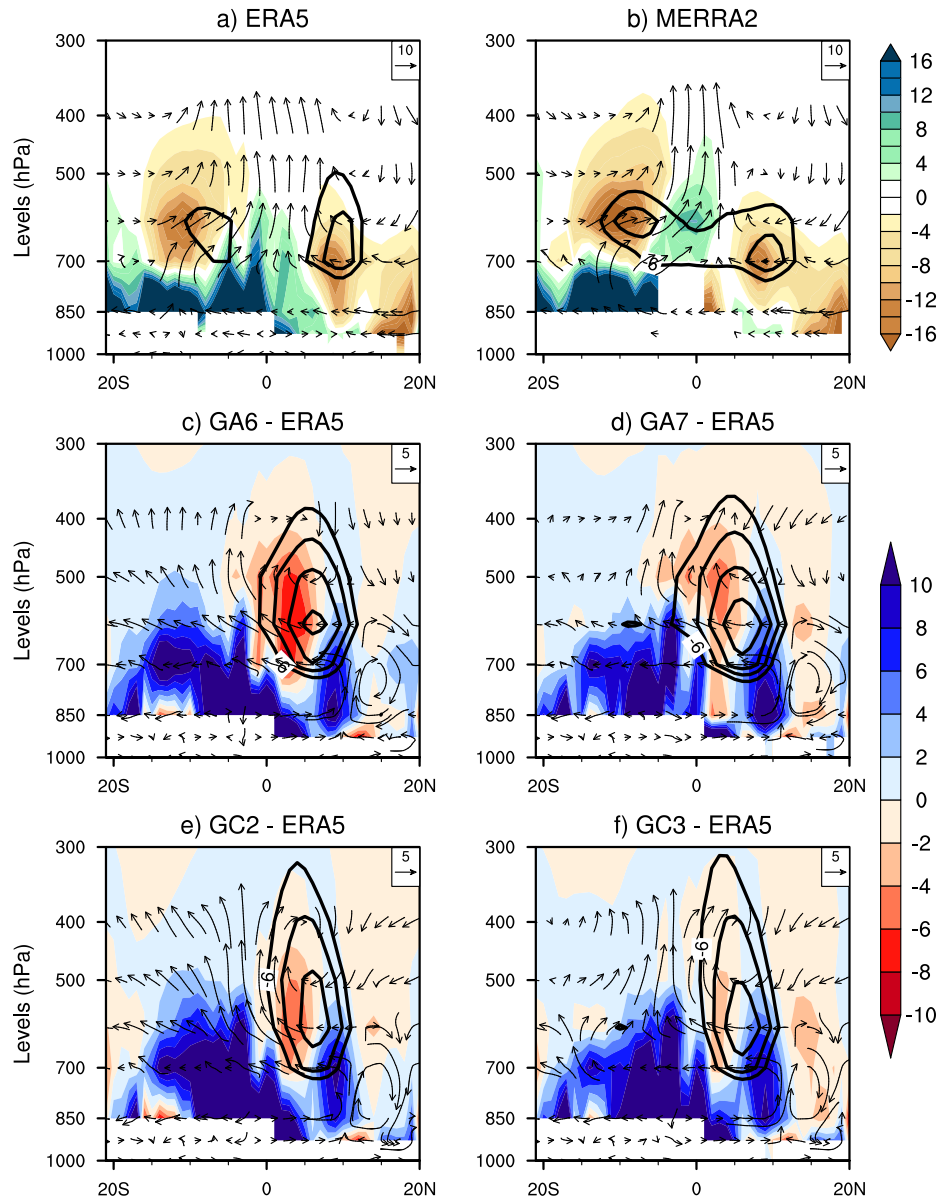


Figure 38: Latitude-height cross-section of September–November long term mean of (a and b) net zonal moisture flux (shaded: $\text{kg}\cdot\text{m}^{-1}\cdot\text{s}^{-1}$) calculated from west boundary (20°E) minus east boundary (30°E) and vertical wind (vectors: $4\cdot 10^{-2}\text{Pa}\cdot\text{s}^{-1}$) averaged between 20 and 30°E in reanalyses. (c–f) Same as in (a and b) minus ERA5 for atmosphere-only (c–d) and coupled (e–f) models. Solid contours (a–f) represent AEJ components ($U\text{ m}\cdot\text{s}^{-1}$) at 20°E in reanalyses, atmosphere-only and coupled models. $20\text{--}30^\circ\text{E}$ is the zonal extent of the wet bias in models.

shift the mid-tropospheric moisture flux convergence southward favouring more convection south of the equator (Fig.38c–f). This is in agreement with the wet bias which is more widespread south of the equator in the region (Fig.27f–i). In addition, the reason why the coupled models are wetter than their corresponding atmospheric formulations could

be due to the strength of their AEJ-N which is less strong than in atmospheric models. This is associated with less mid-tropospheric moisture flux divergence. Comparing the versions of the coupled (atmospheric) model with each other, it appears that, in the most recent version GC3 (GA7), the mid-tropospheric moisture flux divergence associated with the AEJ-N is less pronounced compared to the earlier model version (Fig.38e-f). This may explain why they are wetter than previous model versions.

Next we analyse the transverse ageostrophic circulation associated with AEJ components. Uccellini and Johnson (1979) developed a four-quadrant conceptual model of a “jet streak” (core region of maximum velocity) to describe the transverse circulations. The model states that, at the level of the jet, for a Northern (Southern) Hemisphere jet, divergence (convergence) is found in the right entrance region with convergence (divergence) in the left entrance region. There is ascent under region of upper-level divergence within the right (left) entrance of a northern (southern) hemisphere jet. Likewise, where the convergence overlies divergence, descent is found, namely, within the left (right) entrance of a northern (southern) hemisphere jet. This system is referred as the “transverse ageostrophic circulation” and the reverse happen in the exit region of the jet. The transverse circulations associated with a straight upper-level jet streak also couple with the winds at low levels to complete the circulations.

Figure 39 shows the vertical profile of long term mean SON wind divergence (shaded) and ageostrophic component of meridional wind (vectors) averaged between 20°E and 30°E. This is the entrance regions of the southern and northern components of AEJ, and the convergence area found around the equator at 700hPa is the left (right) entrance region of the AEJ-N (AEJ-S). The transverse ageostrophic circulations should exhibit at the left (right) entrance region of the AEJ-N (AEJ-S) a weak descending branch shared by the two transverse circulations. MERRA2 (Fig.39b) well represents the descending branch although ERA5 does not (Fig.39a). The absence of the descending component could explain why the models are wetter than reanalysis. However, more work is required to fully understand how transverse ageostrophic circulations associated to the two components of the AEJ could contribute to enhance or reduce rainfall over CA.

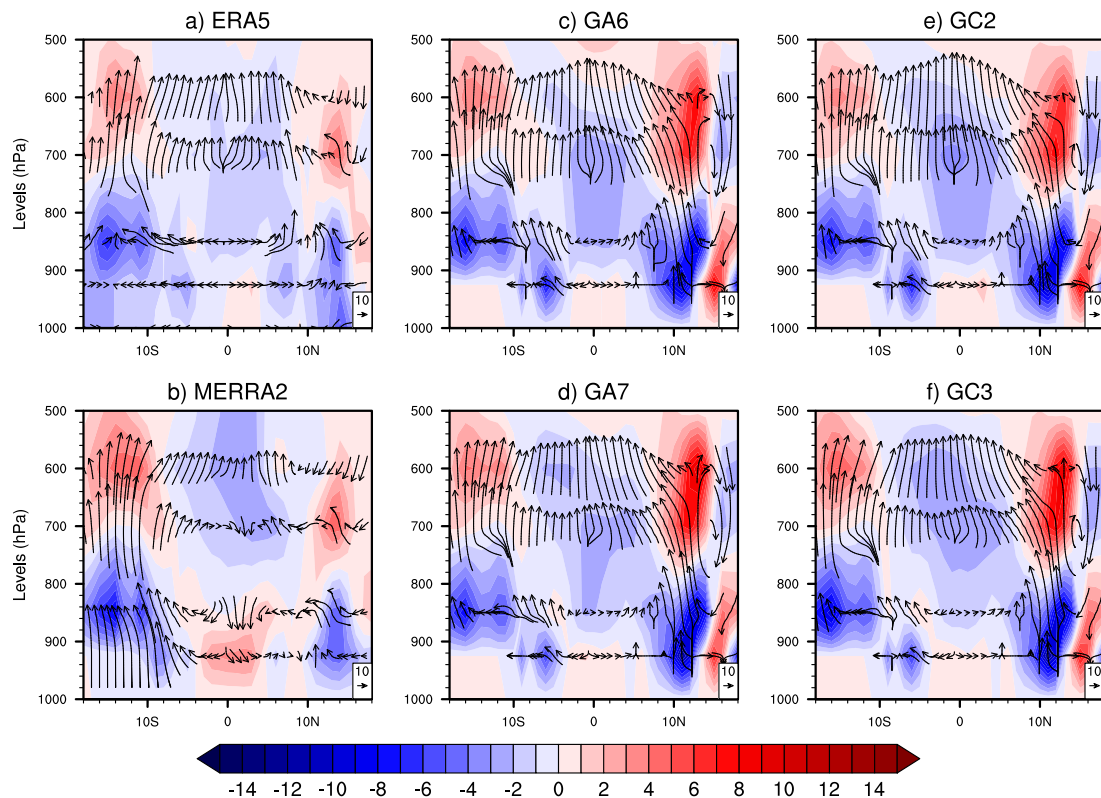


Figure 39: Vertical profile of long term mean September-November wind divergence ($10^{-6} \cdot s^{-1}$; shaded) and ageostrophic component of meridional wind ($m \cdot s^{-1}$; vectors) averaged between $15^{\circ} E$ and $25^{\circ} E$ for (a-b) reanalysis, (cd) atmosphere-only models and (e-f) coupled models. Around the Equator (between $1^{\circ} S$ and $1^{\circ} N$) the coriolis force used to calculate the meridional ageostrophic wind is replaced by $1^{\circ} S-1.5^{\circ} S$ and $1^{\circ} N-1.5^{\circ} N$ nearest values of coriolis force.

3.4 Conclusion

Based on analyses done in this chapter, it emerges that, although models capture relatively well the basic characteristics of rainfall over CA, most of them fail in terms of intensity with BCC-CSM overestimating in both versions while the GISS-E2 model underestimates due to failure in the simulation of moisture flux convergence over the region. To go deeper in the understanding of model bias, the focus was on the MetUM model and it was found that, during the SON season, the simulated western (eastern) CA dry (wet) bias is the result of unrealistic simulated atmospheric circulation in both large and regional scale.

General conclusion and outlooks

General conclusion

This study investigates processes leading to precipitation biases over Central Africa (CA) in Global climate Models (GCMs) taking part to the CMIP5 and CMIP6 projects. While some models (such as the BCC-CSM model) overestimate rainfall in both version other models (such as the GISS-E2 model) underestimate. The overestimation is associated with a surplus of low-level moisture flux convergence while the underestimation is likely due to a stronger mid-tropospheric moisture flux divergence associated with the overestimated strength in the simulated AEJ components.

To go deeper in the understanding of rainfall biases, analyses focused on the MetUM model during the main rainy season (September–November: SON). The model is currently a particular focus of model development over Africa as part of the Improving Model Processes for African Climate (IMPALA) programme. The versions of the MetUM which are considered in this study are those taking part to the CMIP5 and CMIP6 projects denoted respectively as GC2 and GC3 together with their associated atmosphere-only formulations GA6 and GA7. In all versions and formulations, the models depict a dipole bias over the region with a wet bias at the eastern CA and a dry bias over the coastal western CA (Fig.27f–i). The wet (dry) bias is stronger in the coupled (atmospheric) models and the exploration of remote and local climate processes is conducted to understand the models' biases.

At a large scale, differences between CGCM and AGCM are mainly due to the differences in SST which lead to bias in large-scale circulation and rainfall. Over the coastal western CA, the dry bias in the models is linked to the misrepresentation of the Atlantic-Congo zonal overturning cell with its overestimated sinking branch. This is associated with an increase in ocean-land pressure gradient between the equatorial eastern Atlantic Ocean (high pressure) and the Congo Basin (low pressure). The low-level zonal

moisture flux is therefore so strong as to dry the coastal region. The coupled models are less dry in that region compared to the atmosphere-only models because over the Gulf of Guinea, a warm SST bias is simulated in the coupled models and enhances evaporation that reduces the dry bias. Compared to older versions, the dry bias is reduced in the latest version of both coupled and atmospheric formulations of the model. This is linked to the weakening of the subsidence branch of the Atlantic-Congo zonal overturning cell. Over eastern CA, large-scale circulation from both the Atlantic and the Indian Oceans play a role in the eastern CA wet bias. From the Atlantic Ocean, the same large-scale circulation leading to a dry bias over the coastal western CA also contributes to enhanced rainfall over eastern CA. As the strength of low-level zonal moisture flux is overestimated, moisture from the Atlantic Ocean is advected further in the continent and contributes to enhanced rainfall over eastern CA. On the other hand, the subsidence branch of the Indian Ocean zonal overturning circulation is weakened by the anomalous mean state low-level easterly winds which are added to the Indian Ocean easterly winds during IOD years to increase the inflow of moisture from the Indian Ocean.

At the regional scale, the overestimated strength of the simulated Congo basin cell is associated with the western CA dry bias through the overestimation of the simulated LLWs. For the eastern CA wet bias, simulated AEJ components have opposite actions in the models. Due to a misrepresentation in the land-surface temperature, overestimated strength of the AEJ-N tends to suppress convection in the models while an underestimation of the AEJ-S intensity favours convection. Biases in the strength of the AEJ's components shift the mid-tropospheric moisture flux convergence southward favouring more convection south of the equator. In terms of differences between model versions, the mid-tropospheric moisture flux divergence associated with the AEJ-N is less pronounced in the latest model version. This explains why the latest version is wetter than the previous ones. Enhanced rainfall in eastern CA is also linked to the misrepresentation of the Congo basin cell. The overestimation in the simulated width and intensity of the cell is associated with a strong low-level moisture convergence over eastern CA which contributes to more precipitation.

Let us note that, the same biases pattern in the MetUM model were also reported on earlier versions of the model in James et al., 2018 and Hirons and Turne, 2018. Besides this, a similar west–east dipole pattern of rainfall biases over CA are highlighted in CMIP5

(Creese and Washington, 2018) and CORDEX models (Tamoffo et al., 2021) although the signs of the dipole are opposite in the MetUM model. This translates the fact that rainfall in these two subregions of CA is governed by different climate processes and models generally struggle to capture the corresponding features. In the MetUM model, although some differences exist between model versions, the present study has highlighted the persistent atmospheric circulation errors which lead to persistence in rainfall biases between different versions of the MetUM climate model over CA. Results from this work give direction to model developers to address those biases in the next versions of the model. This include among other things the improvement of the shared variability between rainfall over CA and SST and the revision of the land surface schemes across model versions to improved surface characteristics (e.g., temperature and soil moisture) contrast between Congo and both Saharan and Kalahari drylands.

Outlooks

As outlooks for a further study of Central Africa (CA) rainfall in General Circulation Models (GCMs) and associated mechanisms, it would be interesting to:

- Investigate on the projected rainfall over the region under different Global warming levels with CMIP6 models.
- Evaluate the plausibility of the changes using a process-based approach.

References

- Adebiyi, A.A., and P. Zuidema, 2016: The role of the southern african easterly jet in modifying the southeast atlantic aerosol and cloud environments. *Quarterly Journal of the Royal Meteorological Society*, **142**, 1574–1589.
- Aloysius, N.R., J. Sheffield, J.E. Sainers, H. Li, and E.F. Wood, 2016: Evaluation of historical and future simulations of precipitation and temperature in central africa from cmip5 climate models. *Journal of Geophysical Research: Atmospheres*, **121**, 130–152.
- Awange, J., V. Ferreira, E. Forootan, S. Andam-Akorful, N. Agutu, and X. He, 2016: Uncertainties in remotely sensed precipitation data over africa. *International Journal of Climatology*, **36**, 303–323.
- Baker, N.C., and P.C. Taylor, 2016: A framework for evaluating climate model performance metrics. *Journal of Climate*, **29**, 1773–1782.
- Balas, N., S.E. Nicholson, and D. Klotter, 2007: The relationship of rainfall variability in west central africa to sea-surface temperature fluctuations. *International Journal of Climatology*, **27**, 1335–1349.
- Beltrando, G., and P. Camberlin, 1993: Interannual variability of rainfall in the eastern horn of africa and indicators of atmospheric circulation. *International Journal of Climatology*, **13**, 533–546.
- Berckmans, J., T. Woollings, M.E. Demory, P.L. Vidale, and M. Roberts, 2013: Atmospheric blocking in a high resolution climate model: influences of mean state, orography and eddy forcing. *Atmospheric Science Letters*, **14**, 34–40.
- Black, E., J. Slingo, and K.R. Sperber, 2003: An observational study of the relationship between excessively strong short rains in coastal east africa and indian ocean sst. *Monthly Weather Review*, **131**, 74–94.
- Boer, G., and S. Lambert, 2001: Second-order space-time climate difference statistics.

- Climate Dynamics*, **17**, 213–218.
- Bracegirdle, T.J., E. Shuckburgh, J.B. Sallee, Z. Wang, A.J. Meijers, N. Bruneau, T. Phillips, and L.J. Wilcox, 2013: Assessment of surface winds over the atlantic, indian, and pacific ocean sectors of the southern ocean in cmip5 models: Historical bias, forcing response, and state dependence. *Journal of Geophysical Research: Atmospheres*, **118**, 547–562.
- Brubaker, K.L., D. Entekhabi, and P. Eagleson, 1993: Estimation of continental precipitation recycling. *Journal of Climate*, **6**, 1077–1089.
- Cook, K.H., 1999: Generation of the african easterly jet and its role in determining west african precipitation. *Journal of Climate*, **12**, 1165–1184.
- Cook, K.H., 2003: Role of continents in driving the hadley cells. *Journal of the atmospheric sciences*, **60**, 957–976.
- Cook, K.H., and E.K. Vizi, 2016: The congo basin walker circulation: dynamics and connections to precipitation. *Climate Dynamics*, **47**, 697–717.
- Creese, A., and R. Washington, 2016: Using qflux to constrain modeled congo basin rainfall in the cmip5 ensemble. *Journal of Geophysical Research: Atmospheres*, **121**, 13,415–13,442.
- Creese, A., and R. Washington, 2018: A process-based assessment of cmip5 rainfall in the congo basin: The september-november rainy season. *Journal of Climate*, **31**, 7417–7439.
- Crowhurst, D.M., S.J. Dadson, and R. Washington, 2020: Evaluation of evaporation climatology for the congo basin wet seasons in 11 global climate models. *Journal of Geophysical Research: Atmospheres*, **125**, e2019JD030619.
- Dezfuli, A., 2017: Climate of western and central equatorial africa. In: *Oxford Research Encyclopedia of Climate Science*.
- Dezfuli, A.K., and S.E. Nicholson, 2011: A note on long-term variations of the african easterly jet. *International Journal of Climatology*, **31**, 2049–2054.
- Dezfuli, A.K., and S.E. Nicholson, 2013: The relationship of rainfall variability in western equatorial africa to the tropical oceans and atmospheric circulation. part ii: The boreal autumn. *Journal of Climate*, **26**, 66–84.
- Diedhiou, A., S. Janicot, A. Viltard, P. De Felice, and H. Laurent, 1999: Easterly wave regimes and associated convection over west africa and tropical atlantic: Results

- from the ncep/ncar and ecmwf reanalyses. *Climate Dynamics*, **15**, 795–822.
- Dommo, A., N. Philippon, D.A. Vondou, G. Sèze, and R. Eastman, 2018: The june-september low cloud cover in western central africa: Mean spatial distribution and diurnal evolution, and associated atmospheric dynamics. *Journal of Climate*, **31**, 9585–9603.
- Donohoe, A., J. Marshall, D. Ferreira, and D. Mcgee, 2013: The relationship between itcz location and cross-equatorial atmospheric heat transport: From the seasonal cycle to the last glacial maximum. *Journal of Climate*, **26**, 3597–3618.
- Dyer, E.L.E., D.B.A. Jones, J. Nusbaumer, H. Li, O. Collins, G. Vettoretti, and D. Noone, 2017: Congo basin precipitation: Assessing seasonality, regional interactions, and sources of moisture. *Journal of Geophysical Research: Atmospheres*, **122**, 6882–6898.
- Edwards, P.N., 2011: History of climate modeling. *Wiley Interdisciplinary Reviews: Climate Change*, **2**, 128–139.
- Endo, S., and T. Tozuka, 2016: Two flavors of the indian ocean dipole. *Climate Dynamics*, **46**, 3371–3385.
- Eyring, V., S. Bony, G. Meehl, C. Senior, B. Stevens, R. Stouffer, and K. Taylor, 2016: Overview of the coupled model intercomparison project phase 6 (cmip6) experimental design and organisation. *Geoscientific Model Development Discussions*, **8**.
- Flato, G., J. Marotzke, B. Abiodun, P. Braconnot, S.C. Chou, W. Collins, P. Cox, F. Driouech, S. Emori, V. Eyring et al., 2013: Evaluation of climate models. In: *Climate change 2013: the physical science basis. Contribution of Working Group I to the Fifth Assessment Report of the Intergovernmental Panel on Climate Change*, pp. 741–866. Cambridge University Press.
- Fotso-Nguemo, T.C., R. Chamani, Z.D. Yepdo, D. Sonkoué, C.N. Matsaguim, D.A. Vondou, and R.S. Tanessong, 2018: Projected trends of extreme rainfall events from cmip5 models over central africa. *Atmospheric Science Letters*, **19**, e803.
- Funk, C., P. Peterson, M. Landsfeld, D. Pedreros, J. Verdin, S. Shukla, G. Husak, J. Rowland, L. Harrison, A. Hoell et al., 2015: The climate hazards infrared precipitation with stations? a new environmental record for monitoring extremes. *Scientific data*, **2**, 1–21.

- Gelaro, R., W. McCarty, M.J. Suárez, R. Todling, A. Molod, L. Takacs, C.A. Randles, A. Darmenov, M.G. Bosilovich, R. Reichle, K. Wargan, L. Coy, R. Cullather, C. Draper, S. Akella, V. Buchard, A. Conaty, A.M. da Silva, W. Gu, G.K. Kim, R. Koster, R. Lucchesi, D. Merkova, J.E. Nielsen, G. Partyka, S. Pawson, W. Putman, M. Rienecker, S.D. Schubert, M. Sienkiewicz, and B. Zhao, 2017: The modern-era retrospective analysis for research and applications, version 2 (merra-2). *Journal of Climate*, **30**, 5419–5454.
- Gleckler, P.J., K.E. Taylor, and C. Doutriaux, 2008: Performance metrics for climate models. *Journal of Geophysical Research: Atmospheres*, **113**.
- Goddard, L., and N.E. Graham, 1999: Importance of the indian ocean for simulating rainfall anomalies over eastern and southern africa. *Journal of Geophysical Research: Atmospheres*, **104**, 19099–19116.
- Guilyardi, E., A. Wittenberg, A. Fedorov, M. Collins, C. Wang, A. Capotondi, G.J. Van Oldenborgh, and T. Stockdale, 2009: Understanding el niño in ocean–atmosphere general circulation models: Progress and challenges. *Bulletin of the American Meteorological Society*, **90**, 325–340.
- Haensler, A., F. Saeed, and D. Jacob, 2013: Assessing the robustness of projected precipitation changes over central africa on the basis of a multitude of global and regional climate projections. *Climatic Change*, **121**, 349–363.
- Hall, N.M., G.N. Kiladis, and C.D. Thorncroft, 2006: Three-dimensional structure and dynamics of african easterly waves. part ii: Dynamical modes. *Journal of the Atmospheric Sciences*, **63**, 2231–2245.
- Haselow, L., R. Meissner, H. Rupp, and K. Miegel, 2019: Evaluation of precipitation measurements methods under field conditions during a summer season: A comparison of the standard rain gauge with a weighable lysimeter and a piezoelectric precipitation sensor. *Journal of Hydrology*, **575**, 537–543.
- Hastenrath, S., 1984: Interannual variability and annual cycle: Mechanisms of circulation and climate in the tropical atlantic sector. *Monthly Weather Review*, **112**, 1097–1107.
- Hastenrath, S., 2000: Zonal circulations over the equatorial indian ocean. *Journal of Climate*, **13**, 2746–2756.
- Hersbach, H., B. Bell, P. Berrisford, S. Hirahara, A. Horányi, J. Muñoz-Sabater,

- J. Nicolas, C. Peubey, R. Radu, D. Schepers et al., 2020: The era5 global reanalysis. *Quarterly Journal of the Royal Meteorological Society*, **146**, 1999–2049.
- Hirons, L., and A. Turner, 2018: The impact of indian ocean mean-state biases in climate models on the representation of the east african short rains. *Journal of Climate*, **31**, 6611–6631.
- Hirst, A.C., and S. Hastenrath, 1983: Atmosphere-ocean mechanisms of climate anomalies in the angola-tropical atlantic sector. *Journal of physical oceanography*, **13**, 1146–1157.
- Hsieh, J.S., and K.H. Cook, 2005: Generation of african easterly wave disturbances: Relationship to the african easterly jet. *Monthly weather review*, **133**, 1311–1327.
- Hua, W., L. Zhou, S.E. Nicholson, H. Chen, and M. Qin, 2019: Correction to: Assessing reanalysis data for understanding rainfall climatology and variability over central equatorial africa. *Climate Dynamics*, **53**, 5139–5139.
- Huffman, G.J., R.F. Adler, D.T. Bolvin, and G. Gu, 2009: Improving the global precipitation record: Gpcp version 2.1. *Geophysical Research Letters*, **36**.
- Hwang, Y.T., and D.M. Frierson, 2013: Link between the double-intertropical convergence zone problem and cloud biases over the southern ocean. *Proceedings of the National Academy of Sciences*, **110**, 4935–4940.
- IPCC, 2013: The physical science basis. *Contribution of working group I to the fifth assessment report of the intergovernmental panel on climate change*, **1535**, 2013.
- Jackson, B., S.E. Nicholson, and D. Klotter, 2009: Mesoscale convective systems over western equatorial africa and their relationship to large-scale circulation. *Monthly Weather Review*, **137**, 1272–1294.
- James, R., and R. Washington, 2013: Changes in african temperature and precipitation associated with degrees of global warming. *Climatic Change*, **117**, 859–872.
- James, R., R. Washington, B. Abiodun, G. Kay, J. Mutemi, W. Pokam, N. Hart, G. Artan, and C. Senior, 2018: Evaluating climate models with an african lens. *Bulletin of the American Meteorological Society*, **99**, 313–336.
- Jiang, J.H., H. Su, C. Zhai, V.S. Perun, A. Del Genio, L.S. Nazarenko, L.J. Donner, L. Horowitz, C. Seman, J. Cole et al., 2012: Evaluation of cloud and water vapor simulations in cmip5 climate models using nasa "a-train" satellite observations. *Journal of Geophysical Research: Atmospheres*, **117**.

- Jones, P.W., 1999: First-and second-order conservative remapping schemes for grids in spherical coordinates. *Monthly Weather Review*, **127**, 2204–2210.
- Jury, M.R., E. Matari, and M. Matitu, 2009: Equatorial african climate teleconnections. *Theoretical and Applied Climatology*, **95**, 407–416.
- Kim, D., K. Sperber, W. Stern, D. Waliser, I.S. Kang, E. Maloney, W. Wang, K. Weickmann, J. Benedict, M. Khairoutdinov et al., 2009: Application of mjo simulation diagnostics to climate models. *Journal of Climate*, **22**, 6413–6436.
- King, A.D., and L.J. Harrington, 2018: The inequality of climate change from 1.5 to 2°c of global warming. *Geophysical Research Letters*, **45**, 5030–5033.
- Koteswaram, P., 1958: The easterly jet stream in the tropics. *Tellus*, **10**, 43–57.
- Kuete, G., W. Pokam Mba, and R. Washington, 2020: African easterly jet south: Control, maintenance mechanisms and link with southern subtropical waves. *Climate Dynamics*, **54**, 1539–1552.
- Lin, R., T. Zhou, and Y. Qian, 2014: Evaluation of global monsoon precipitation changes based on five reanalysis datasets. *Journal of Climate*, **27**, 1271–1289.
- Longandjo, G.N.T., and M. Rouault, 2020: On the structure of the regional-scale circulation over central africa: seasonal evolution, variability, and mechanisms. *Journal of Climate*, **33**, 145–162.
- Maidment, R.I., D. Grimes, R.P. Allan, E. Tarnavsky, M. Stringer, T. Hewison, R. Roebeling, and E. Black, 2014: The 30 year tamsat african rainfall climatology and time series (tarcat) data set. *Journal of Geophysical Research: Atmospheres*, **119**, 10–619.
- Malhi, Y., S. Adu-Bredu, R.A. Asare, S.L. Lewis, and P. Mayaux, 2013: African rainforests: past, present and future. *Philosophical Transactions of the Royal Society B: Biological Sciences*, **368**, 20120312.
- Masson-Delmotte, V., 2018: *Global Warming of 1.5° C: An IPCC Special Report on the Impacts of Global Warming of 1.5° C Above Pre-industrial Levels and Related Global Greenhouse Gas Emission Pathways, in the Context of Strengthening the Global Response to the Threat of Climate Change, Sustainable Development, and Efforts to Eradicate Poverty*. World Meteorological Organization.
- Masson-Delmotte, V., P. Zhai, A. Pirani, S.L. Connors, C. Péan, S. Berger, N. Caud, Y. Chen, L. Goldfarb, M.I. Gomis et al., 2021: Climate change 2021: The physical

- science basis. contribution of working group i to the sixth assessment report of the intergovernmental panel on climate change. *IPCC: Geneva, Switzerland*.
- Matsuura, K., and C.J. Willmott, 2018: Terrestrial precipitation: 1900–2017 gridded monthly time series. *Electronic. Department of Geography, University of Delaware, Newark, DE*, **19716**.
- Meehl, G.A., G.J. Boer, C. Covey, M. Latif, and R.J. Stouffer, 1997: Intercomparison makes for a better climate model. *Eos, Transactions American Geophysical Union*, **78**, 445–451.
- Meehl, G.A., G.J. Boer, C. Covey, M. Latif, and R.J. Stouffer, 2000: The coupled model intercomparison project (cmip). *Bulletin of the American Meteorological Society*, **81**, 313–318.
- Meehl, G.A., C. Covey, T. Delworth, M. Latif, B. McAvaney, J.F. Mitchell, R.J. Stouffer, and K.E. Taylor, 2007: The wcrp cmip3 multimodel dataset: A new era in climate change research. *Bulletin of the American meteorological society*, **88**, 1383–1394.
- Meehl, G.A., C. Covey, B. McAvaney, M. Latif, and R.J. Stouffer, 2005: Overview of the coupled model intercomparison project. *Bulletin of the American Meteorological Society*, **86**, 89–93.
- Moihamette, F., W.M. Pokam, I. Diallo, and R. Washington, 2022: Extreme indian ocean dipole and rainfall variability over central africa. *International Journal of Climatology*, 1–18.
- Muller, C.J., L.E. Back, P.A. O’Gorman, and K.A. Emanuel, 2009: A model for the relationship between tropical precipitation and column water vapor. *Geophysical Research Letters*, **36**.
- Neupane, N., 2016: The congo basin zonal overturning circulation. *Advances in Atmospheric Sciences*, **33**, 767–782.
- Nicholson, S.E., and A.K. Dezfuli, 2013: The relationship of rainfall variability in western equatorial africa to the tropical oceans and atmospheric circulation. part i: The boreal spring. *Journal of Climate*, **26**, 45–65.
- Nicholson, S.E., and D. Entekhabi, 1986: The quasi-periodic behavior of rainfall variability in africa and its relationship to the southern oscillation. *Archives for meteorology, geophysics, and bioclimatology, Series A*, **34**, 311–348.
- Nicholson, S.E., and D. Entekhabi, 1987: Rainfall variability in equatorial and southern

- africa: Relationships with sea surface temperatures along the southwestern coast of africa. *Journal of Applied Meteorology and Climatology*, **26**, 561–578.
- Nicholson, S.E., and J.P. Grist, 2003: The seasonal evolution of the atmospheric circulation over west africa and equatorial africa. *Journal of Climate*, **16**, 1013–1030.
- Nikulin, G., C. Jones, F. Giorgi, G. Asrar, M. Büchner, R. Cerezo-Mota, O.B. Christensen, M. Déqué, J. Fernandez, A. Hänsler et al., 2012: Precipitation climatology in an ensemble of cordex-africa regional climate simulations. *Journal of Climate*, **25**, 6057–6078.
- Niznik, M.J., and B.R. Lintner, 2013: Circulation, moisture, and precipitation relationships along the south pacific convergence zone in reanalyses and cmip5 models. *Journal of climate*, **26**, 10174–10192.
- Nobre, P., and J. Shukla, 1996: Variations of sea surface temperature, wind stress, and rainfall over the tropical atlantic and south america. *Journal of climate*, **9**, 2464–2479.
- Ogalo, L.J., and J. JE, 1988: Teleconnection between seasonal rainfall over east africa and global sea surface temperature anomalies. *Journal of the Meteorological Society of Japan. Ser. II*, **66**, 807–822.
- Ogura, Y., and N.A. Phillips, 1962: Scale analysis of deep and shallow convection in the atmosphere. *J. atmos. Sci*, **19**, 173–179.
- Okumura, Y., and S.P. Xie, 2006: Some overlooked features of tropical atlantic climate leading to a new niño-like phenomenon. *Journal of climate*, **19**, 5859–5874.
- Oort, A.H., and J.J. Yienger, 1996: Observed interannual variability in the hadley circulation and its connection to enso. *Journal of Climate*, 2751–2767.
- Paradis, D., J. Lafore, J. Redelsperger, and V. Balaji, 1995: African easterly waves and convection. part i: Linear simulations. *Journal of Atmospheric Sciences*, **52**, 1657–1679.
- Peixoto, J.P., and A.H. Oort, 1992: Physics of climate.
- Pithan, F., T.G. Shepherd, G. Zappa, and I. Sandu, 2016: Climate model biases in jet streams, blocking and storm tracks resulting from missing orographic drag. *Geophysical Research Letters*, **43**, 7231–7240.
- Pokam, W.M., C.L. Bain, R.S. Chadwick, R. Graham, D.J. Sonwa, and F.M. Kamga,

- 2014: Identification of processes driving low-level westerlies in west equatorial africa. *Journal of Climate*, **27**, 4245–4262.
- Pokam, W.M., L.A.T. Djiotang, and F.K. Mkankam, 2012: Atmospheric water vapor transport and recycling in equatorial central africa through ncep/ncar reanalysis data. *Climate Dynamics*, **38**, 1715–1729.
- Ramon, J., L. Lledó, V. Torralba, A. Soret, and F.J. Doblas-Reyes, 2019: What global reanalysis best represents near-surface winds? *Quarterly Journal of the Royal Meteorological Society*, **145**, 3236–3251.
- Rayner, N.A., D.E. Parker, E.B. Horton, C.K. Folland, L.V. Alexander, D.P. Rowell, E.C. Kent, and A. Kaplan, 2003: Global analyses of sea surface temperature, sea ice, and night marine air temperature since the late nineteenth century. *Journal of Geophysical Research: Atmospheres*, **108**.
- Reichler, T., and J. Kim, 2008: How well do coupled models simulate today’s climate? *Bulletin of the American Meteorological Society*, **89**, 303–312.
- Saeed, F., A. Haensler, T. Weber, S. Hagemann, and D. Jacob, 2013: Representation of extreme precipitation events leading to opposite climate change signals over the congo basin. *Atmosphere*, **4**, 254–271.
- Saji, N., B. Goswami, P. Vinayachandran, and T. Yamagata, 1999: A dipole mode in the tropical indian ocean. *Nature*, **401**, 360.
- Sandjon, A.T., A. Nzeukou, and C. Tchawoua, 2012: Intraseasonal atmospheric variability and its interannual modulation in central africa. *Meteorology and Atmospheric Physics*, **117**, 167–179.
- Schott, F., J. Fischer, U. Garternicht, and D. Quadfasel, 1997: Summer monsoon response of the northern somali current, 1995. *Geophysical Research Letters*, **24**, 2565–2568.
- Schott, F.A., and J.P. McCreary Jr, 2001: The monsoon circulation of the indian ocean. *Progress in Oceanography*, **51**, 1–123.
- Shi, F., Z. Hao, and Q. Shao, 2014: The analysis of water vapor budget and its future change in the yellow-huai-hai region of china. *Journal of Geophysical Research: Atmospheres*, **119**, 10–702.
- Soldatenko, S., A. Bogomolov, and A. Ronzhin, 2021: Mathematical modelling of climate change and variability in the context of outdoor ergonomics. *Mathematics*, **9**, 2920.
- Sonkoué, D., D. Monkam, T.C. Fotso-Nguemo, Z.D. Yepdo, and D.A. Vondou, 2019:

- Evaluation and projected changes in daily rainfall characteristics over central africa based on a multi-model ensemble mean of cmip5 simulations. *Theoretical and Applied Climatology*, **137**, 2167–2186.
- Stachnik, J.P., and C. Schumacher, 2011: A comparison of the hadley circulation in modern reanalyses. *Journal of Geophysical Research: Atmospheres*, **116**.
- Tamoffo, A., 2020: *Implications of global warming levels of 1.5°C and 2.0°C in the Congo Basin: Assessment of RCA4 Regional Climate Model*. Ph. D. thesis, University of Yaounde I, Cameroun.
- Tamoffo, A.T., W. Moufouma-Okia, A. Dosio, R. James, W.M. Pokam, D.A. Vondou, T.C. Fotso-Nguemo, G.M. Guenang, P.H. Kamsu-Tamo, G. Nikulin, G.N. Longandjo, C.J. Lennard, J.P. Bell, R.R. Takong, A. Haensler, L.A.D. Tchotchou, and R. Nouayou, 2019: Process-oriented assessment of rca4 regional climate model projections over the congo basin under 1.5°C and 2°C global warming levels: influence of regional moisture fluxes. *Climate Dynamics*, **53**, 1911–1935.
- Tamoffo, A.T., D.A. Vondou, W.M. Pokam, A. Haensler, Z.D. Yepdo, T.C. Fotso-Nguemo, L.A.D. Tchotchou, and R. Nouayou, 2018: Daily characteristics of central african rainfall in the remo model. *Theoretical and Applied Climatology*, **137**, 2351–2368.
- Tanguay, M., A. Robert, and R. Laprise, 1990: A semi-implicit semi-lagrangian fully compressible regional forecast model. *Mon. Wea. Rev.*, **118**, 970–1.
- Tapp, M., and P. White, 1976: A non-hydrostatic mesoscale model. *Quarterly Journal of the Royal Meteorological Society*, **102**, 277–296.
- Taylor, K.E., 2001: Summarizing multiple aspects of model performance in a single diagram. *Journal of Geophysical Research: Atmospheres*, **106**, 7183–7192.
- Taylor, K.E., R.J. Stouffer, and G.A. Meehl, 2012: An overview of cmip5 and the experiment design. *Bulletin of the American Meteorological Society*, **93**, 485–498.
- Thorncroft, C., and M. Blackburn, 1999: Maintenance of the african easterly jet. *Quarterly Journal of the Royal Meteorological Society*, **125**, 763–786.
- Todd, M.C., and R. Washington, 2004: Climate variability in central equatorial africa: Influence from the atlantic sector. *Geophysical Research Letters*, **31**.
- Uccellini, L.W., and D.R. Johnson, 1979: The coupling of upper and lower tropospheric jet streaks and implications for the development of severe convective storms. *Monthly Weather Review*, **107**, 682–703.

- Ummenhofer, C.C., A. Sen Gupta, M.H. England, and C.J. Reason, 2009: Contributions of indian ocean sea surface temperatures to enhanced east african rainfall. *Journal of Climate*, **22**, 993–1013.
- Valík, A., R. Brázdil, P. Zahradníček, R. Tolasz, and R. Fiala, 2021: Precipitation measurements by manual and automatic rain gauges and their influence on homogeneity of long-term precipitation series. *International Journal of Climatology*, **41**, E2537–E2552.
- Van der Ent, R.J., H.H. Savenije, B. Schaefli, and S.C. Steele-Dunne, 2010: Origin and fate of atmospheric moisture over continents. *Water Resources Research*, **46**.
- van Niekerk, A., T.G. Shepherd, S.B. Vosper, and S. Webster, 2016: Sensitivity of resolved and parametrized surface drag to changes in resolution and parametrization. *Quarterly Journal of the Royal Meteorological Society*, **142**, 2300–2313.
- Vondou, D.A., and A. Haensler, 2017: Evaluation of simulations with the regional climate model remo over central africa and the effect of increased spatial resolution. *International Journal of Climatology*, **37**, 741–760.
- Walters, D., A.J. Baran, I. Boutle, M. Brooks, P. Earnshaw, J. Edwards, K. Furtado, P. Hill, A. Lock, J. Manners et al., 2019: The met office unified model global atmosphere 7.0/7.1 and jules global land 7.0 configurations. *Geoscientific Model Development*, **12**, 1909–1963.
- Washington, R., R. James, H. Pearce, W.M. Pokam, and W. Moufouma-Okia, 2013: Congo basin rainfall climatology: can we believe the climate models? *Phil. Trans. R. Soc. B*, **368**, 20120296.
- Watterson, I., J. Bathols, and C. Heady, 2014: What influences the skill of climate models over the continents? *Bulletin of the American Meteorological Society*, **95**, 689–700.
- Webster, P.J., 1983: Large scale dynamical processes in atmosphere.
- Whittleston, D., S.E. Nicholson, A. Schlosser, and D. Entekhabi, 2017: Climate models lack jet rainfall coupling over west africa. *Journal of Climate*, **30**, 4625–4632.
- Williams, K., D. Copesey, E. Blockley, A. Bodas-Salcedo, D. Calvert, R. Comer, P. Davis, T. Graham, H. Hewitt, R. Hill et al., 2018: The met office global coupled model 3.0 and 3.1 (gc3. 0 and gc3. 1) configurations. *Journal of Advances in Modeling Earth Systems*, **10**, 357–380.
- Wu, M.L.C., O. Reale, S.D. Schubert, M.J. Suarez, R.D. Koster, and P.J. Pegion, 2009:

- African easterly jet: Structure and maintenance. *Journal of Climate*, **22**, 4459–4480.
- Xie, S.P., and J.A. Carton, 2004: Tropical atlantic variability: Patterns, mechanisms, and impacts. *Earth's Climate: The Ocean-Atmosphere Interaction, Geophys. Monogr*, **147**, 121–142.
- Xu, L., S. Raman, and R. Madala, 1992: A review of non-hydrostatic numerical models for the atmosphere. In: *1st World Congress of Nonlinear Analysis Fire and Forest Meteorology. Nonlinear World, Walter de Gruyter, New York, Tampa, FL*.
- Yin, L., R. Fu, E. Shevliakova, and R.E. Dickinson, 2013: How well can cmip5 simulate precipitation and its controlling processes over tropical south america? *Climate Dynamics*, **41**, 3127–3143.
- Zheng, X., and E.A. Eltahir, 1998: The role of vegetation in the dynamics of west african monsoons. *Journal of Climate*, **11**, 2078–2096.
- Zhou, L., Y. Tian, R.B. Myneni, P. Ciais, S. Saatchi, Y.Y. Liu, S. Piao, H. Chen, E.F. Vermote, C. Song et al., 2014: Widespread decline of congo rainforest greenness in the past decade. *Nature*, **509**, 86–90.

List of publications

1. **Taguela, T. N.**, Pokam, W.M., Dyer, E., James, R. and Washington, R. (2022), **Low-level circulation over Central Equatorial Africa as simulated from CMIP5 to CMIP6 models**. *Climate Dynamics*, <https://doi.org/10.1007/s00382-022-06411-0> (**Impact Factor: 5.031**).
2. **Taguela, T. N.**, Pokam, W.M., and Washington, R. (2022), **Rainfall in uncoupled and coupled versions of the Met Office Unified Model over Central Africa: Investigation of processes during the September-November rainy season**. *International Journal of Climatology*, 1-21. <https://doi.org/10.1002/joc.7591> (**Impact Factor: 4.408**).
3. **Taguela, T. N.**, Vondou, D. A., Moufouma-Okia, W., Fotso-Nguemo, T. C., Pokam, W. M., Tanessong, R. S., et al (2020). **CORDEX multi-RCM hindcast over Central Africa: Evaluation within observational uncertainty**. *Journal of Geophysical Research: Atmospheres*, 125, e2019JD031607. <https://doi.org/10.1029/2019JD031607> (**Impact Factor: 5.217**).



Low-level circulation over Central Equatorial Africa as simulated from CMIP5 to CMIP6 models

Thierry N. Taguela¹ · Wilfried M. Pokam^{1,2} · Ellen Dyer³ · Rachel James⁴ · Richard Washington³

Received: 2 February 2022 / Accepted: 28 June 2022
© The Author(s) 2022

Abstract

We evaluate and compare the simulation of the main features (low-level westerlies (LLWs) and the Congo basin (CB) cell) of low-level circulation in Central Equatorial Africa (CEA) with eight climate models from Phase 6 of the Coupled Model Intercomparison Project (CMIP6) and the corresponding eight previous models from CMIP5. Results reveal that, although the main characteristics of the two features are reasonably well depicted by the models, they bear some biases. The strength of LLWs is generally overestimated in CMIP5 models. The overestimation is attributed to both divergent and rotational components of the total wind with the rotational component contributing the most in the overestimation. In CMIP6 models, thanks to a better performance in the simulation of both divergent and rotational circulation, LLWs are slightly less strong compared to the CMIP5 models. The improvement in the simulated divergent component is associated with a better representation of the near-surface pressure and/or temperature difference between the Central Africa landmass and the coastal Atlantic Ocean. Regarding the rotational circulation, and especially for HadGEM3-GC31-LL and BCC-CSM2-MR, a simulated higher 850 hPa pressure is associated with less pronounced negative vorticity and a better representation of the rotational circulation. Most CMIP5 models also overestimate the CB cell intensity and width in association with the simulated strength of LLWs. However, in CMIP6 models, the strength of key cell characteristics (intensity and width) are reduced compared to CMIP5 models. This depicts an improvement in the representation of the cell in CMIP6 models and this is associated with the improvement in the simulated LLWs.

Keywords Low-level westerlies · Congo basin cell · Temperature contrast · Pressure difference · Central Africa · CMIP5 · CMIP6

1 Introduction

Central equatorial Africa (CEA) (10° S–10° N; 10°–30° E) hosts the Congo basin (CB) whose important climatic role extends well beyond the African continent. The Basin is known as one of the three hot spots of major convective activity in the global tropics (Webster 1983), experiencing the highest lightning strike frequency of anywhere on the planet (Jackson et al. 2009) and receiving around 1500–2000 mm of rainfall per year (Dezfuli 2017). In addition, its rainforest stores incredible amounts of carbon, preventing it from being emitted into our atmosphere and fueling climate change. At the local scale, through evaporation, tropical forests and woodlands exchange vast amounts of water and energy with the atmosphere, controlling the seasonality of rainfall in the region (Crowhurst et al. 2020).

Despite its importance in the local and global climate systems, CEA remains a very understudied region compared

✉ Rachel James
rachel.james@bristol.ac.uk
Thierry N. Taguela
thierrytaguela@gmail.com

¹ Laboratory for Environmental Modelling and Atmospheric Physics, Department of Physics, University of Yaounde 1, Yaounde, Cameroon

² Department of Physics, Higher Teacher Training College, University of Yaounde 1, Yaounde, Cameroon

³ School of Geography and the Environment, University of Oxford, Oxford, UK

⁴ School of Geographical Sciences, University of Bristol, Bristol, UK

to other parts of Africa (Washington et al. 2013; Creese and Washington 2016). This is mainly due to a lack of observational data (Washington et al. 2013; Creese and Washington 2018). Although much remains to be done to cover the gap, several studies (Cook 1999; Nicholson and Grist 2003; Pokam et al. 2012, 2014; Nicholson and Dezfuli 2013; Dezfuli and Nicholson 2013; Cook and Vizzy 2016; Nicholson 2018; Longandjo and Rouault 2020; Kuete et al 2019) have used reanalysis data to highlight, describe and investigate the drivers of some important features of the atmospheric circulation in the region. Among them, elements of the low-level circulation play a crucial role because they are active year-round and their changes throughout the year strongly influence the climate in the region (Nicholson and Grist 2003; Pokam et al. 2014; Longandjo and Rouault 2020).

1.1 Key elements in the low-level circulation

The lower tropospheric circulation in CEA is mainly characterised by two components which are both established throughout the year: Low-level westerlies (LLWs: Nicholson and Grist 2003) and the Congo basin cell (CB cell: Longandjo and Rouault 2020).

LLWs are associated with the southeasterly trades on the northeastern flank of Saint Helena (South Atlantic) high. Due to the Coriolis force, the southeasterlies recurve and become westerlies when crossing the equator (Pokam et al. 2014). Nicholson and Grist (2003) suggested that the strength of equatorial westerlies is related to the sea level pressure associated with the South Atlantic High (SAH). However, in investigating the drivers of LLWs, Pokam et al. (2014) split the zonal wind into its divergent and rotational component and found that north of 6° N in CEA, LLWs are primarily a rotational flow forming part of the cyclonic circulation driven primarily by the heat low of the West African monsoon system. This northern arm of the LLW is well-developed from June to August. It weakens during September–November, disappears in the December–February season and originates in the March–May season. South of 6° N, the circulation is dominated by the divergent component and the seasonal variability of the LLW is controlled by the zonal land-sea thermal contrast near the equator. By advecting moisture from the Atlantic ocean to the CEA region, the strength of LLWs is related to rainfall variability in the region where wet years exhibit a distinct westerly wind during both wet seasons (Dezfuli and Nicholson 2013; Nicholson and Dezfuli 2013). This makes LLWs an essential circulation feature in CEA.

Many studies (Pokam et al. 2014; Cook and Vizzy 2016; Neupane 2016) have suggested the presence of a zonal shallow overturning cell over central Africa. The cell was finally highlighted by Longandjo and Rouault (2020) and they denoted it the Congo basin cell. It is a closed,

counterclockwise and shallow zonal overturning cell that is confined at the lower troposphere (between the surface and 800 hPa) and is active throughout the year. LLWs form the lower base of the cell and similar to LLWs, the Congo Basin cell intensity and width are driven by the near-surface temperature warming on both the central African landmass and the eastern equatorial Atlantic. The cell's maximum (minimum) intensity and width are registered in August/September (May). As shown by Longandjo and Rouault (2020) the eastern edge of the cell is associated with the Congo Air Boundary, a convergence zone where the low-level jets from the equatorial Atlantic, having crossed the central African landmass, meet the Indian monsoon system easterlies to form the ascending branch of the cell. It is a zone of maximum convection and precipitation in the region. The zonal rainfall maximum position in the region is then modulated by the width of the Congo basin cell.

Therefore, because LLWs contribute to modulate the amount of rainfall in CEA (Nicholson and Dezfuli 2013) while the CB cell plays a crucial role in rainfall redistribution over central Africa via the zonal rainfall maximum position (Longandjo and Rouault 2020), the ability of climate models to simulate their strength and drivers is important for advancing knowledge of the CEA climate.

1.2 State of evaluation

Climate models are tools used to investigate the response of climate to various forcings and for making climate projections (Creese and Washington 2016; Taguela et al. 2020). However, to assess confidence in projected outputs, models are evaluated on their ability to represent the past or present climate. In this line, the process-based evaluation method has been advocated (James et al. 2015, 2018; Rowell et al. 2015; Baumberger et al. 2017), because a better understanding of how models behave is fundamental to help determine how to improve them. In addition, it is also an important way to assess their adequacy for future projection. Although there is not much such study in CEA, there are growing efforts in that direction (Creese and Washington 2018; Tamoffo et al. 2019; Crowhurst et al. 2020; Tamoffo et al. 2021a, b).

For instance, regarding the LLWs in CEA, Tamoffo et al. (2021a, b) showed that rainfall in the regional climate model RCA4-v4 has been improved in CEA compared to its previous version (RCA4-v1) due to the stronger LLWs in the new version that advect sufficient moisture into the region and contribute to reduce the dry bias in the model. However, to the best of our knowledge, Creese and Washington 2018 is the only study that has investigated the LLWs in the hind-cast model output from the Coupled Model Intercomparison Project 5 (CMIP5) in CEA. This study assessed their impact on the simulated rainfall biases in the region during the SON (September–November) season. They found that wetter

models in the east of the region exhibit stronger westerly flow across the tropical eastern Atlantic, advecting a surplus of moisture in the region that contributes to an increase of rainfall. Since LLWs were not the focus of the study, they did not go deeply in their evaluation by investigating the origin of their biases. In addition, with the release of model datasets from the Coupled Model Intercomparison Project 6 (CMIP6), it will be interesting to assess how they represent LLWs and if there is an improvement compared to CMIP5 models. As far as the CB cell is concerned, it was recently highlighted and described by Longandjo and Rouault (2020) and has never been evaluated in any coupled climate models.

1.3 Aims

In light of the importance of these low-level circulation features in CEA (Sect. 1.1) and given the gap in the state of their evaluation in coupled climate models (Sect. 1.2), this paper aims to answer the following questions:

- How are the main features (LLWs and the CB cell) of low-level circulation in CEA represented in CMIP5 and CMIP6 models?
- Is there an improvement in CMIP6 compared to CMIP5 models?
- Do their drivers explain changes in models' behaviour?

The paper outline is as follows: Sect. 2 presents the data and methods used in this study. The LLWs and the CB cell are evaluated in CMIP5 and CMIP6 models in Sects. 3 and

4, respectively, while Sect. 5 summarizes our results and highlights the main conclusions.

2 Data and methods

Data used in this study are output from coupled general circulation models' (CGCMs) simulations taking part in the Coupled Model Intercomparison Project Phase 5 (CMIP5; Taylor et al. 2012) and 6 (CMIP6; Eyring et al. 2016). Only one ensemble member for each model is used: the r1i1p1 integration for CMIP5 and r1i1p1f1 for CMIP6 models. We analyse the monthly output of 16 climate models, 8 from CMIP5 and 8 from CMIP6 (see Table 1 for more details). To track any improvement, each CMIP6 model used is the new version of a corresponding CMIP5 model. For this study, model datasets cover a period from 1980–2005 to 1980–2010 for the CMIP5 and CMIP6 output respectively.

Three reanalysis datasets at monthly time scale from 1980 to 2010 are used to assess models output: MERRA2 (Gelaro et al. 2017) the updated version of MERRA, is a reanalysis dataset from the National Aeronautics and Space Administration (NASA). It is available on 72 sigma levels at a horizontal resolution of $0.5^\circ \times 0.625^\circ$; ERA-Interim (Dee et al. 2011) a reanalysis dataset produced with the ECMWF Integrated Forecast System (IFS Cycle 31r2) with a horizontal resolution of $0.75^\circ \times 0.75^\circ$ on 60 levels; ERA5 (Hersbach et al. 2020), the reanalysis dataset with the highest spatial resolution used in this study, is also produced by the European Centre for Medium-Range Weather Forecast (ECMWF) Integrated Forecast System (IFS Cycle 41r2) to

Table 1 Details of CMIP5 and CMIP6 models used in the study

Institute, Country	Model short name	Model name	Resolution (latitude \times longitude, vertical levels)	References
Beijing Climate Center, China Meteorological Administration (China)	BCC-CSM	CMIP5: BCC-CSM1.1-m	$1.125^\circ \times 1.12^\circ$, L26	Wu et al. (2014)
		CMIP6: BCC-CSM2-MR	$1.125^\circ \times 1.12^\circ$, L46	Wu et al. (2019)
Centre National de Recherches Météorologiques (France)	CNRM-CM	CMIP5: CNRM-CM5	$1.4^\circ \times 1.4^\circ$, L31	Volodire et al. (2013)
		CMIP6: CNRM-CM6-1	$1.4^\circ \times 1.4^\circ$, L91	Volodire et al. (2019)
NOAA Geophysical Fluid Dynamics Laboratory (USA)	GFDL-CM	CMIP5: GFDL-CM3	$2.0^\circ \times 2.5^\circ$, L48	Griffies et al. (2011)
		CMIP6: GFDL-CM4	$1.0^\circ \times 1.25^\circ$, L48	Held et al. (2019)
Met Office Hadley Centre (UK)	HadGEM	CMIP5: HadGEM2-CM3	$1.25^\circ \times 1.8^\circ$, L38	Collins et al. (2001)
		CMIP6: HadGEM3-GC31-LL	$1.25^\circ \times 1.8^\circ$, L38	Roberts (2017)
Atmosphere and Ocean Research Institute, The University of Tokyo (Japan)	MIROC	CMIP5: MIROC5	$1.4^\circ \times 1.4^\circ$, L40	Watanabe et al. (2010)
		CMIP6: MIROC6	$1.4^\circ \times 1.4^\circ$, L81	Tatebe et al. (2019)
NASA Goddard Institute for Space Studies (USA)	GISS-E2	CMIP5: GISS-E2-R	$2.5^\circ \times 2^\circ$, L29	Kim et al. (2012)
		CMIP6: GISS-E2-1-G	$2.5^\circ \times 2^\circ$, L40	Kelley et al. (2020)
Met Office Hadley Centre (UK)	UK	CMIP5: HadGEM2-ES	$1.25^\circ \times 1.8^\circ$, L38	Jones et al. (2011)
		CMIP6: UKESM1	$1.25^\circ \times 1.8^\circ$, L38	Sellar et al. (2019)
Meteorological Research Institute (Japan)	MRI	CMIP5: MRI-ESM1	$1.1^\circ \times 1.1^\circ$, L48	Adachi et al. (2013)
		CMIP6: MRI-ESM2-0	$1.1^\circ \times 1.1^\circ$, L48	Yukimoto et al. (2019)

Horizontal resolution (grids) and vertical levels are included

replace their ERA-Interim product. It has a spatial resolution of $0.25^\circ \times 0.25^\circ$ with 137 levels. Some variables used in our investigations are the horizontal wind vector (both zonal and meridional components) and the near surface temperature, pressure and geopotential height.

To evaluate the ability of models to represent LLWs over Central Equatorial Africa, the horizontal zonal wind is partitioned into divergent and rotational (non-divergent) components using the Helmholtz theorem as applied in Pokam et al. (2014). This is to assess the contribution of each component to the total zonal wind. Afterwards, we explore the processes that control each component to investigate mechanisms of the LLWs in CMIP5 and CMIP6 models. For bias calculation, datasets used in this study have been interpolated to a common grid of $1^\circ \times 1^\circ$ to easily compare models and reanalyses. Regarding the Congo basin cell, we use the zonal mass-weighted stream function, as computed in Longandjo and Rouault (2020) for its exploration. It satisfies the meridional mean continuity equation in spherical coordinates and is calculated at each pressure and longitude as a downward integrated zonal wind function. The zonal wind is first averaged between 5° N and 5° S before the zonal mass-weighted stream function is computed.

3 Low-level westerlies (LLWs)

The representation of the simulated LLWs together with the contribution of the divergent and rotational circulations to the total zonal wind are assessed in this section. The attention is also put on LLWs' drivers to understand their biases.

3.1 Mean seasonal climatology of the total circulation

With the core speed of the LLWs in CEA located along the coastal region between 10° and 15° E year-round (Pokam et al. 2014), the long term mean of the zonal wind is averaged in that longitude band in all the reanalyses, CMIP5 and CMIP6 models and represented in Figs. 1 and 2 for March–May (MAM) and September–November (SON) seasons, respectively. The focus is on the MAM and SON seasons because they are wet seasons that encompass the majority of mechanisms driving the region's climate system (Tamoffo et al. 2021b). It appears in reanalyses that, although the westerlies are weaker in MAM (Fig. 1a–c) than in SON (Fig. 2a–c) season, there is an agreement (even though not perfect) with the upper boundary of LLWs found around 850 hPa and the core speed located around 925 hPa in both seasons. Furthermore, in reanalyses, the MAM season depicts a distinct arm of westerly winds located north of 6° N which is strengthened (not shown here) in June–August (JJA) and weakened significantly in SON, to disappear (not

shown here) in December–February (DJF) as highlighted in Pokam et al. (2014). Although they bear some biases, the above basic features of LLWs are relatively well represented in models. In MAM, HadGEM2-CM3, BCC-CSM1.1-m and MIROC5 (GFDL-CM3, GISS-E2-R and MRI-ESM1) are CMIP5 models overestimating (underestimating) the upper boundary of LLWs found at around 800 hPa (900 hPa). However, this is slightly improved in CMIP6 models except in BCC-CSM2-MR and MIROC6. In addition to the overestimation of the upper boundary of LLWs in HadGEM2-CM3, the modelled westerlies are also extended further south in the SON season, with once more an improvement in its CMIP6 version. In the MAM season, most of the CMIP5 models fail to represent the arm of westerly winds located north of 6° N. There is no improvement observed in that feature in CMIP6 models. This could be due to the coarse resolution of both CMIP5 and CMIP6 models. However, the study will focus on the arm of westerly winds located south of 6° N because that arm is present year-round (Pokam et al. 2014). In both seasons, CMIP5 and CMIP6 models depict well the vertical location of the core speed of LLWs found at around 925 hPa as in reanalyses. Models' ability to represent the intensity and the spatial pattern of the core speed of LLWs at this level (925 hPa) is discussed next.

Figures 3 and 4 show for MAM and SON season respectively, the 925 hPa seasonal mean climatology of total circulation (vectors) and zonal wind (shading) speed from all the reanalyses (Figs. 3a–c and 4a–c). Biases relative to ERA5 are shown from CMIP5 and CMIP6 models (Figs. 3d–s and 4d–s). In both seasons, reanalyses depict an inflow of westerly winds in the study region through the western boundary with the inflow stronger in SON than in MAM season. The simulated biases of CMIP5 and CMIP6 models are similar in their spatial pattern but differ in intensity. In both seasons, the positive (negative) bias along the coastal region in HadGEM2-CM3, HadGEM2-ES, BCC-CSM1.1-m and MIROC5 (GFDL-CM3, GISS-E2-R and MRI-ESM1) denotes an excess (a deficient) in the intensity of westerly winds, much more pronounced in BCC-CSM1.1-m (GFDL-CM3). Although the sign of the biases is the same, an improvement in reducing the biases depicted in CMIP5 models is observed in their corresponding CMIP6 models in both seasons. However, in the MAM season, the CNRM-CM5 model and its corresponding CMIP6 version (CNRM-CM6-1) have an opposite bias in the simulated zonal wind along the coast. CNRM-CM5 overestimates while CNRM-CM6-1 underestimates.

3.2 Contribution from the divergent and rotational circulations

To focus on the westerly winds at the western boundary of the study region, the 925 hPa zonal wind and its divergent

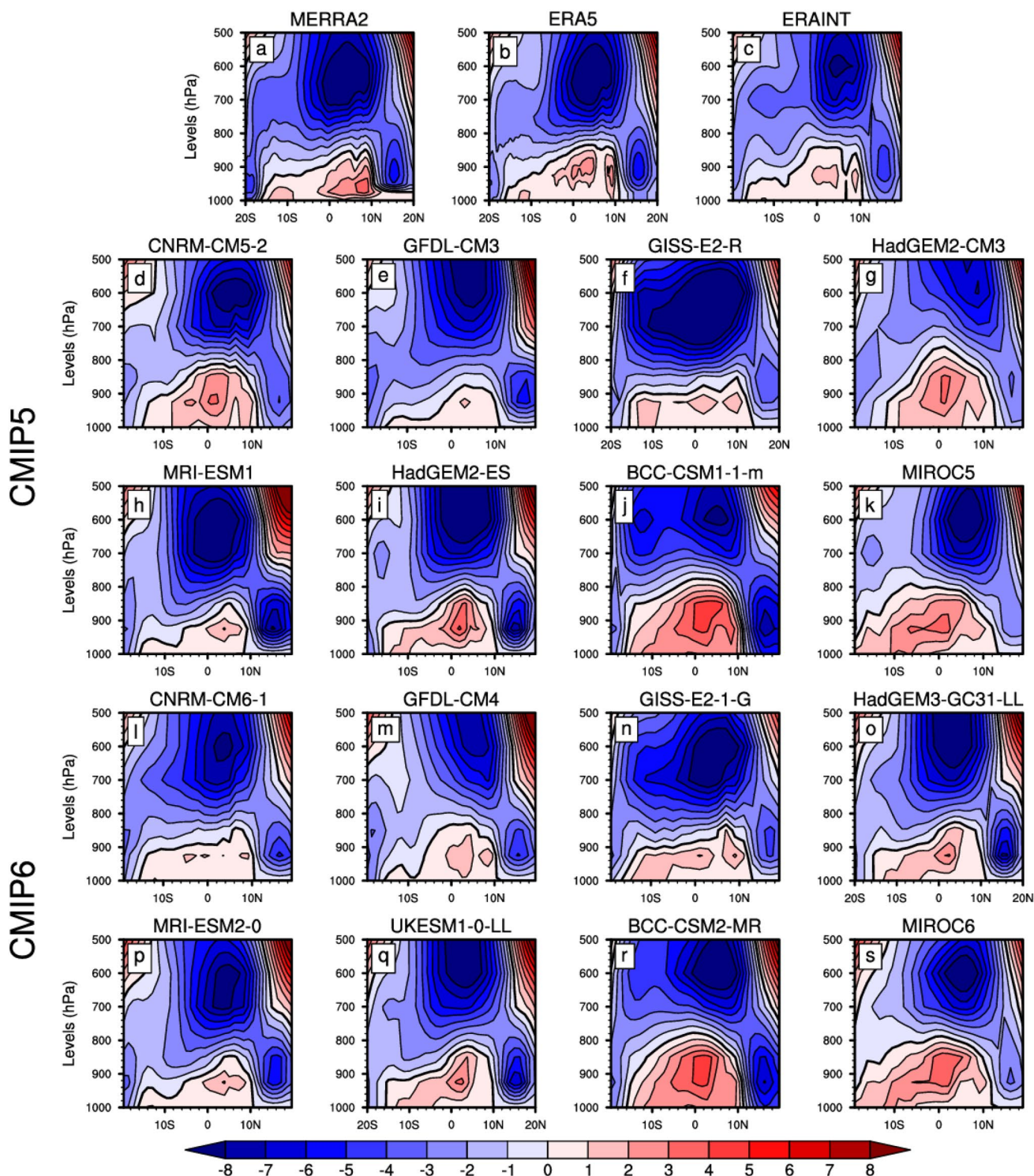


Fig. 1 March–May long term seasonal mean of zonal wind (m/s) averaged between 10° and 15° E for **a–c** reanalyses, **d–k** CMIP5 and **l–s** CMIP6 models. Positive values correspond to westerly winds and negative values to easterly winds

and rotational components are averaged between 10° S–5° N and 10°–15° E. Their annual cycles are then displayed in Fig. 5 for reanalyses, CMIP5 and CMIP6 models (Fig. 5a–f). This is done to assess the contribution of each

component to the total zonal wind and to determine to what extent they contribute to the models’ biases. Reanalyses agree well in the representation of the total zonal wind and its components. Throughout the year, the divergent

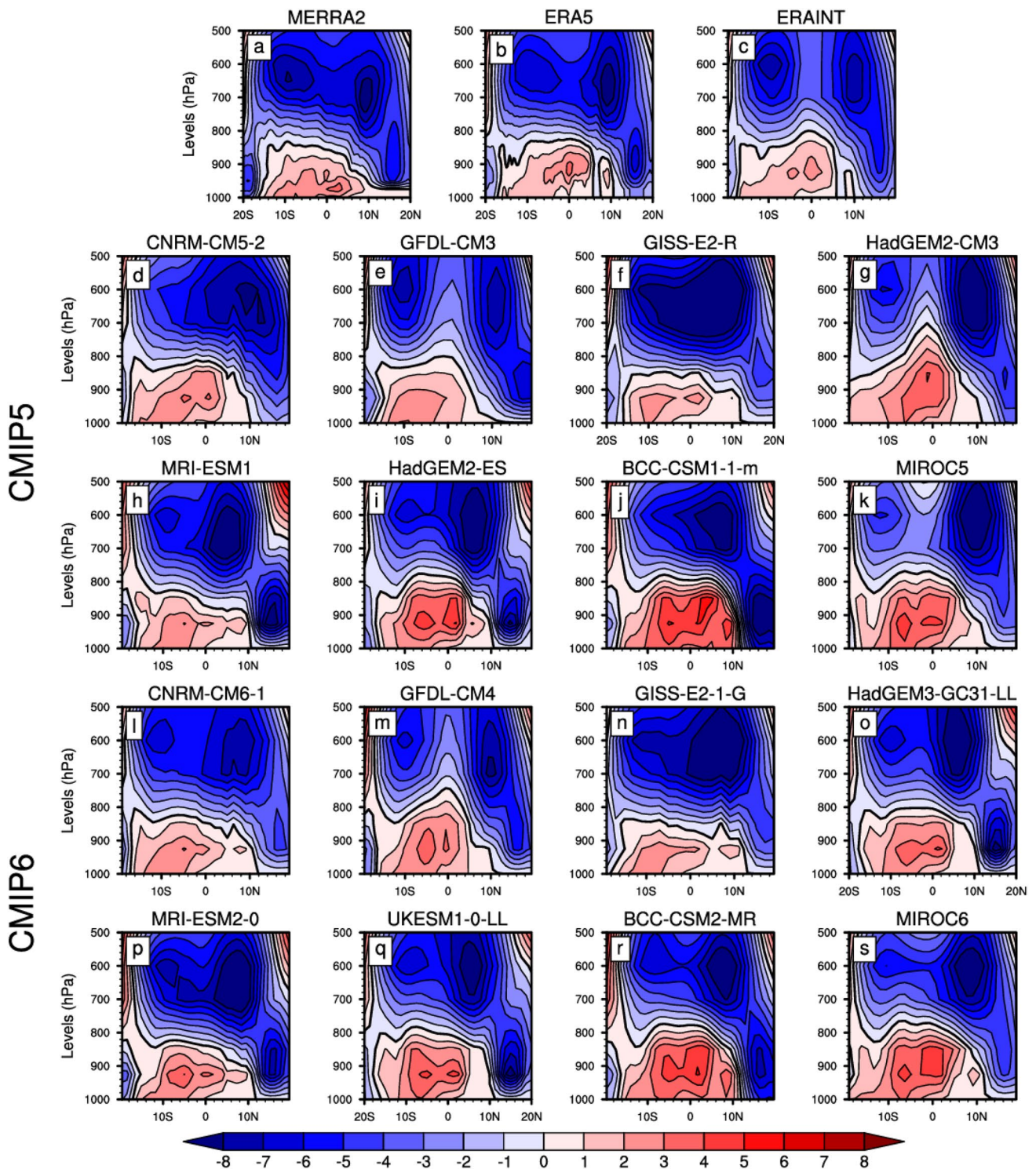


Fig. 2 Same as in Fig. 1, but for the September–November season

circulation (Fig. 5b and e) is a westerly wind (positive values) while the rotational circulation (Fig. 5c and f) is an easterly wind (negative values) in most months. The total zonal wind being also a westerly wind (positive values: Fig. 5a and d), it follows that it is mainly divergent in its

kinematic character. This is in line with the findings from Pokam et al. (2014). In addition, the reanalyses (Fig. 5a–f) show that, the total and divergent zonal wind peaks are found in February and August while for the rotational circulation, the peaks are found in May and November since

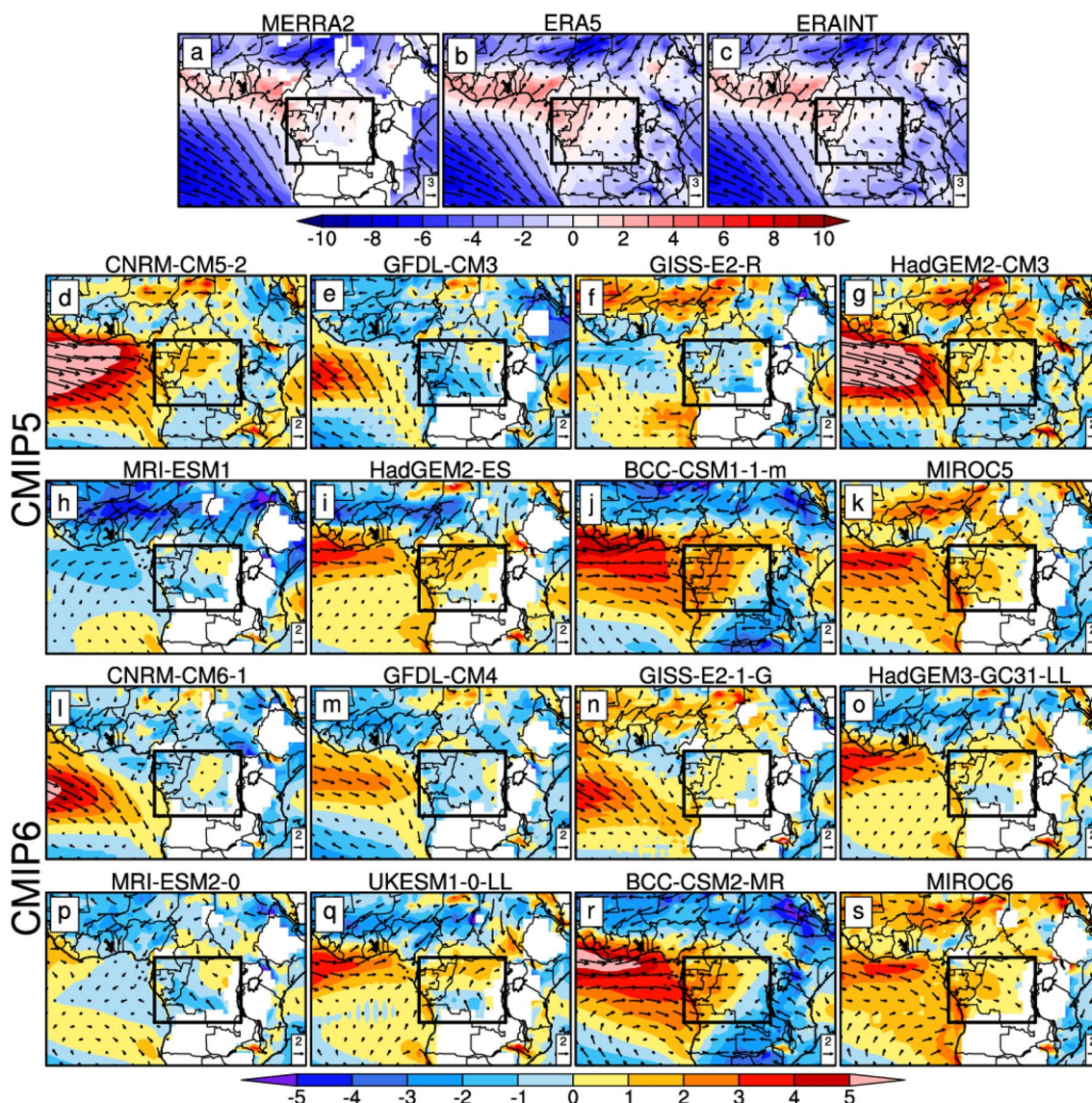


Fig. 3 Long term seasonal mean of March–May 925 hPa total wind (vectors: m/s) and zonal wind (shading: m/s) for **a–c** reanalyses, **d–k** CMIP5 models biases with respect to ERA5 and **l–s** CMIP6 models

biases with respect to ERA5. The black box is the study region, and the interest is on the inflow at the region’s western boundary

it is principally an easterly wind as highlighted above. Although the seasonality of the total zonal circulation and its components is reasonably captured by the CMIP5 and CMIP6 models, considerable differences in terms of intensity are depicted (Fig. 5a–f). Most of the CMIP5 models overestimate the strength of the total zonal circulation at the beginning and around the end of the year (Fig. 5a). Moreover, in addition to what emerges from Figs. 3 and 4, the BCC-CSM1.1-m model overestimates the total circulation not only in MAM and SON but over the whole year, in contrast with GFDL-CM3 which underestimates the westerly flow in most months (from February to September). Examining the wind components (Fig. 5b and c),

most models overestimate the westerly component of the rotational circulation throughout the year (Fig. 5c), making it a westerly flow that increases its contribution to the total wind. However, from one model to another, the positive or negative bias in the total zonal circulation (Fig. 5a) is generally attributed to the combined biases in both the divergent (Fig. 5b) and rotational (Fig. 5c) circulation. This is observed in the BCC-CSM1.1-m model that overestimates the total zonal wind as the result of the overestimation of both divergent and rotational components. On the other hand, the overestimated total zonal wind in the HadGEM2-CM3 model is only attributed to the rotational circulation in MAM and SON while from May to August,

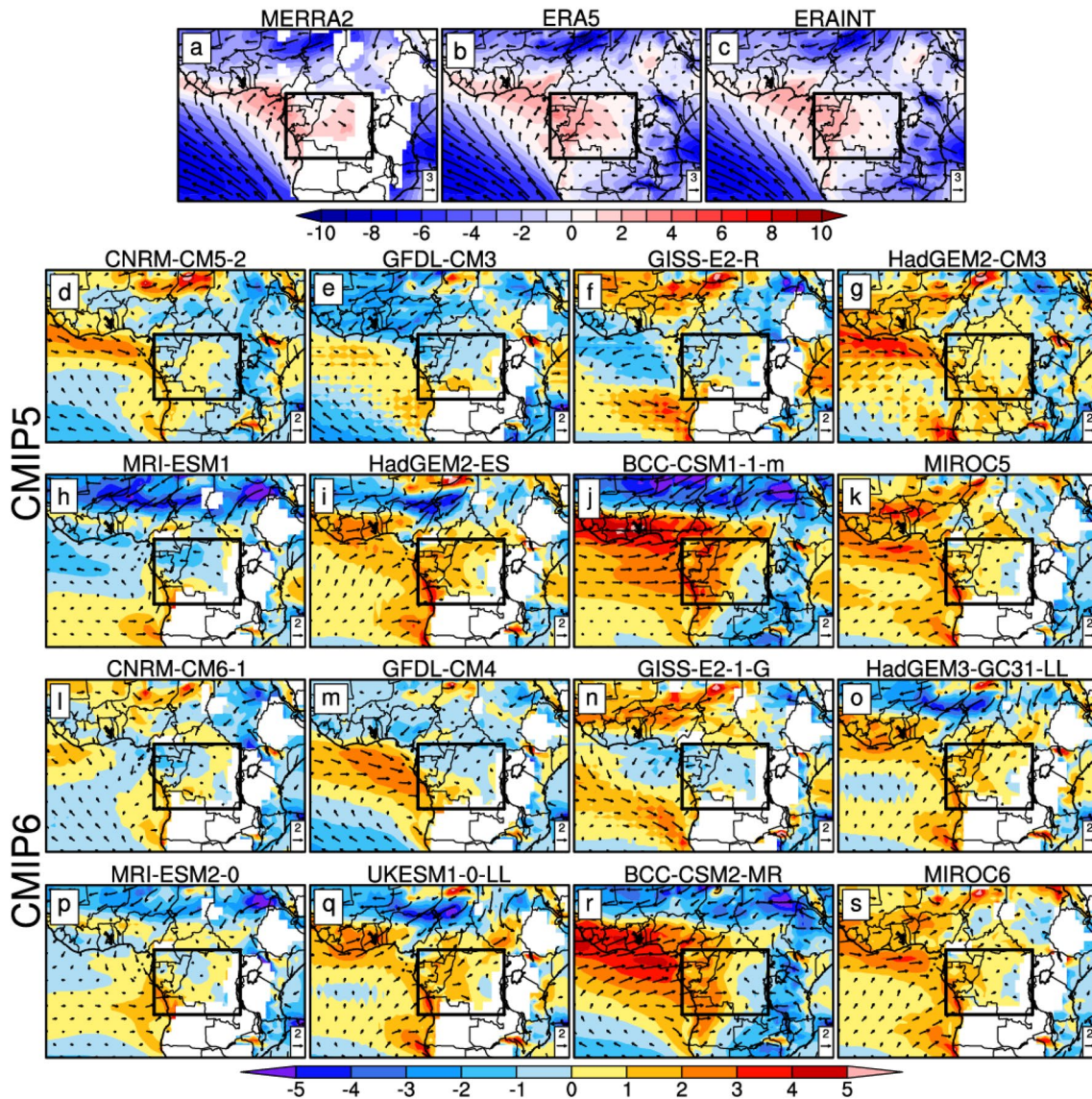


Fig. 4 Same as Fig. 3, but for the September–November season

the deficit of the total wind in the GFDL-CM3 model is mainly due to its underestimated divergent component.

Compared with reanalyses, the rotational circulation (Fig. 5f) in the CMIP6 models has led to a stronger underestimated total wind in GFDL-CM4 and MRI-ESM2-0 during June and May (Fig. 5d). However, in comparison with the CMIP5 models, smaller biases are generally observed in their corresponding CMIP6 models, highlighting the improvement in the total wind (Fig. 5d) which is the result of the improvement in both components (Fig. 5e and f). This is well observed in Fig. 5g–i displaying the annual cycle of the uncertainty ranges in total, divergent and rotational zonal wind from reanalyses, CMIP5 and

CMIP6 models. The uncertainty range here is the spread or the dispersion in a set of data. It is represented with a band and the smaller the bandwidth, the smaller the uncertainty and vice-versa. It appears that, compared to reanalyses, in most months, the spread of the total wind in CMIP6 models is slightly smaller than the one from CMIP5 models due to the improvement in both divergent (Fig. 5h) and rotational (Fig. 5i) circulation. However, in general, in both CMIP5 and CMIP6 models, the spread of the rotational component (Fig. 5i) is larger than the spread of the divergent (Fig. 5h) component. This highlights the fact that, in most months, the bias in the rotational circulation contributes most to the bias in the total zonal circulation.

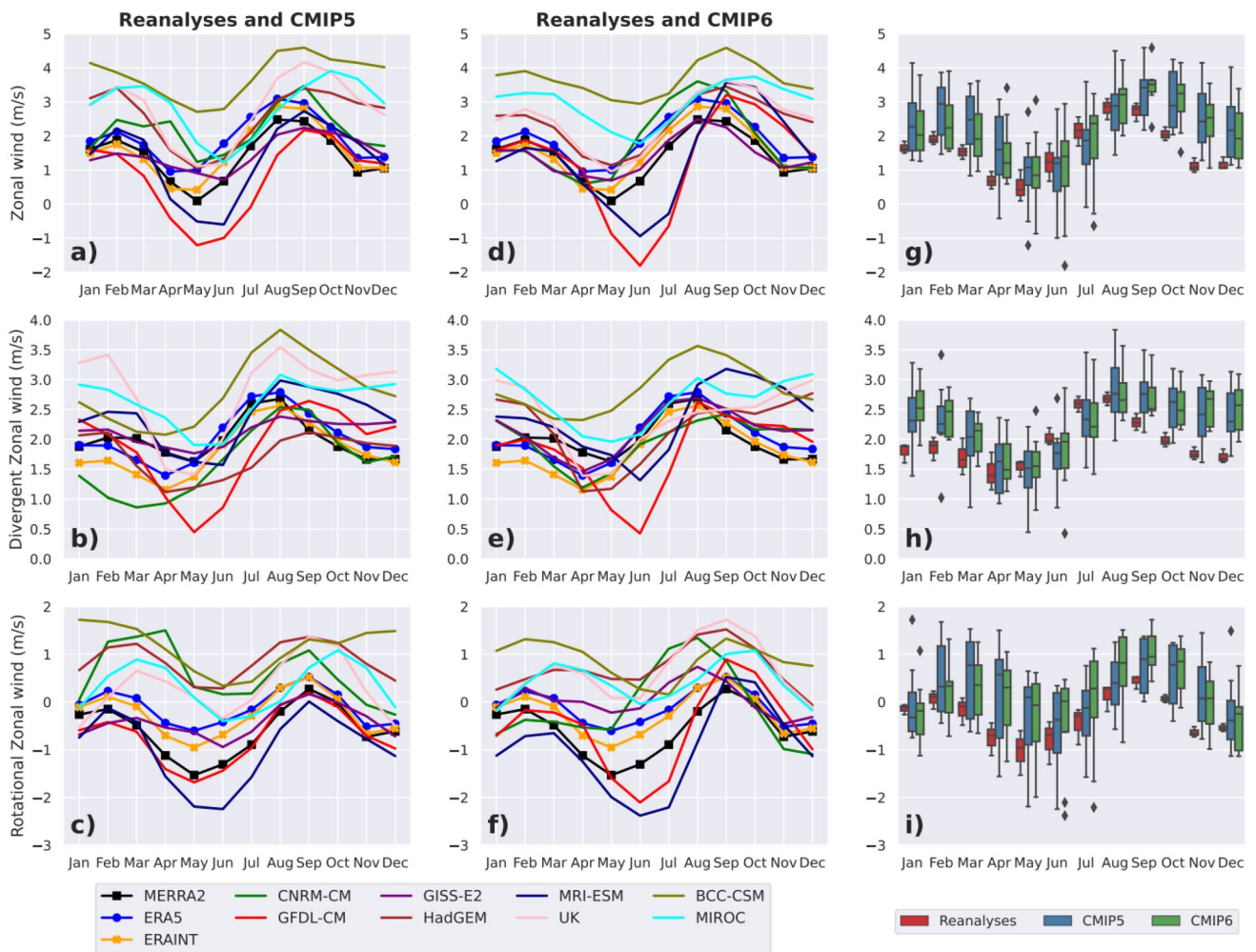


Fig. 5 Seasonal cycle of 925 hPa total, divergent and rotational zonal wind averaged between 10° S–5° N and 10°–15° E for **a–c** reanalyses and CIMP5 models, **d–f** reanalyses and CMIP6 models. **g–i** Uncer-

tainty ranges in total, divergent and rotational zonal wind from reanalyses (red), CMIP5 (blue) and CMIP6 (green) models. Note that westerly winds are positive while easterly are negative

3.3 Control mechanisms of LLWs

This section aims to understand simulated LLWs biases by exploring the processes that control the variability of the LLWs over CEA. As seen above, when decomposed into their two components, the LLWs biases are attributed to either the divergent or the rotational component or both. Therefore, investigating their drivers means looking at those of their two components. In addition, investigating whether drivers agree with the improvement in the simulation of LLWs from CMIP5 to CMIP6 models will add more confidence in the improvement and to the CMIP6 outputs.

Pokam et al. (2014) have shown that the divergent component of the LLWs in CEA is driven by the near-surface temperature difference between the Atlantic ocean and the Congo basin landmass. However, the area of the Atlantic ocean over which temperature variability is strongly associated with the coastal circulation variability is not clearly

defined and has always been taken arbitrarily (Cook and Vizy 2016; Neupane 2016; Longandjo and Rouault 2020). To identify that area, the near-surface temperature difference is calculated between western Central Africa (averaged in the black box in Fig. 6a) and each grid point over the Atlantic Ocean. The difference found for each grid point in the Atlantic ocean is correlated with the 925 hPa divergent wind averaged over the coastal area (between 10° S–5° N and 10°–15° E) and the correlation values obtained at each grid point are then displayed in Fig. 6 for reanalyses (Fig. 6a–c), CMIP5 (Fig. 6d–k) and CMIP6 (Fig. 6i–s) models. Let us note that, the computed correlation is based on the inter-annual variability. Except in ERA5, other reanalyses such as ERAINT and MERRA2 depict a positive correlation all over the Atlantic ocean (Fig. 6a–c). This means a high (low) temperature difference is associated with a strong (weak) divergent wind. The blue box (Fig. 6a) located at the east of the Atlantic ocean (between 10° S–0° and 0°–10° E) shows

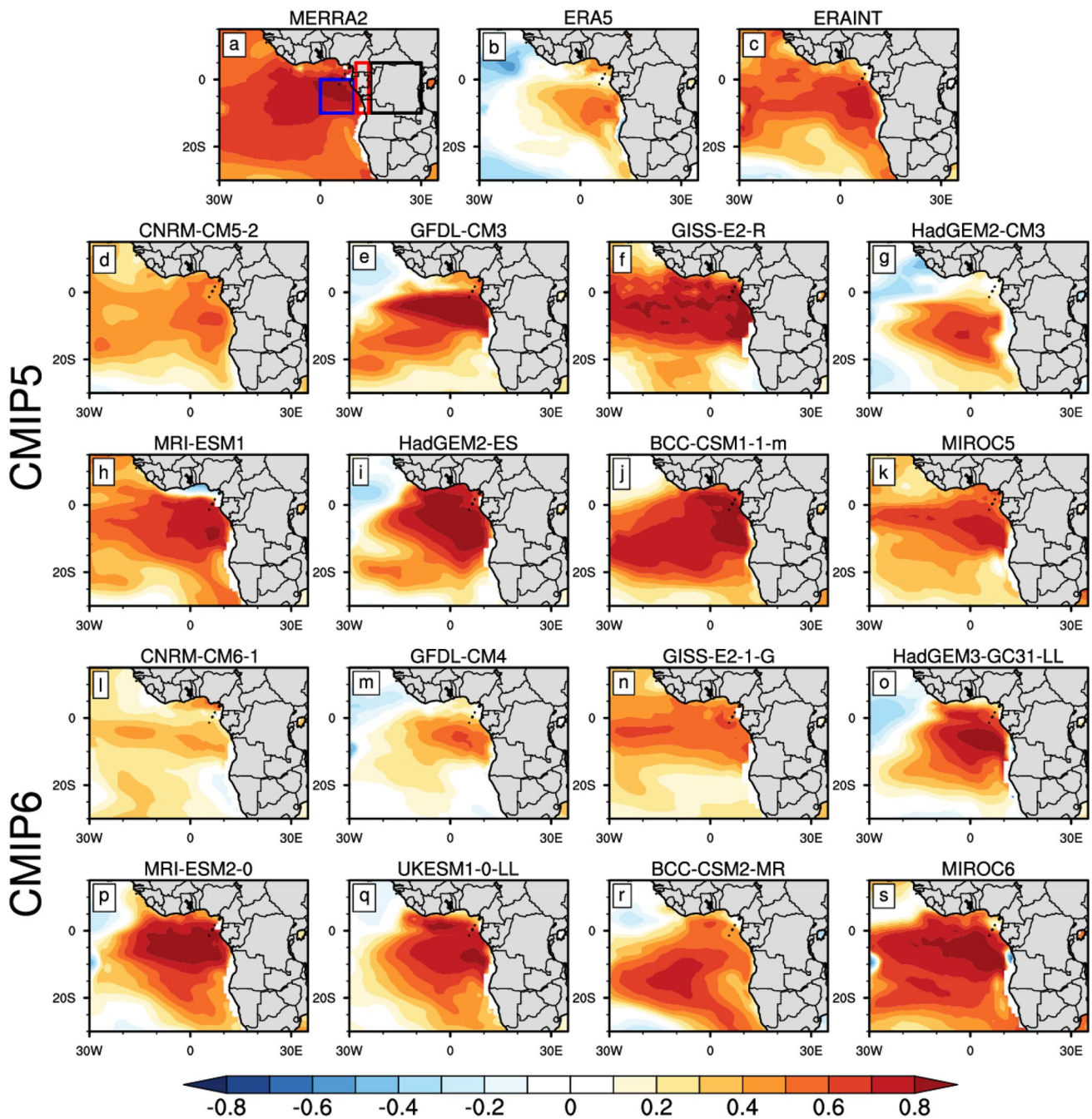


Fig. 6 Correlations of 925 hPa temperature difference between Central Africa (averaged in the black box) and each grid point temperature over the Atlantic Ocean, against the divergent wind, averaged between 10° S–5° N and 10°–15° E (red box) for **a–c** reanalyses, **d–k**

CMIP5 and **l–s** CMIP6 models. Long term annual mean data are used here and the blue box (**a**) shows the region of highest correlation in reanalyses

the region with the highest positive correlation based on all three reanalyses. All reanalyses agree relatively well with the location of that region (Fig. 6a–c) although the strength of the correlation is less in ERA5 (Fig. 6b). Both CMIP5 and CMIP6 models succeed in reproducing the positive correlation over the Atlantic ocean and the region of maximum correlation is also well detected by most models.

However, in CNRM-CM6-1 (Fig. 6l), GFDL-CM4 (Fig. 6m) and GISS-E2-1-G (Fig. 6n), the positive correlation is less strong compared to that depicted by their corresponding previous CMIP5 models (Fig. 6d–f). This feature suggests that the strength of the divergent wind is less related to the temperature difference between the Atlantic ocean and the Congo basin landmass in those models. In addition, in

HadGEM2-CM3 (Fig. 6g) and BCC-CSM2-MR (Fig. 6r), the region of maximum correlation is shifted a little southwestward in the Atlantic ocean.

Figure 7 is used to help further understand the divergent wind biases. It shows the annual cycle of temperature and pressure differences between the Central Africa landmass (black box in Fig. 6a) and the eastern Atlantic Ocean (blue box in Fig. 6a) from reanalyses, CMIP5 and CMIP6 models. It emerges that, throughout the year, the temperature (pressure) difference is positive (negative) because of higher (lower) temperatures (pressure) over the land than ocean. Reanalyses show two peaks found in February–March and July–August respectively. The two peaks are also observed in the seasonal cycle of the pressure difference and they coincide with the divergent wind component peaks (Fig. 5b). The second and stronger peak appears during the eastern equatorial Atlantic cold tongue (Cook and Vizy 2016; Neupane 2016). The later enhances the temperature difference between the cool SSTs and the warm continent and strengthen the divergent wind flow.

CMIP5 and CMIP6 models reasonably capture the main characteristic (the two peaks) of the annual cycle of both temperature and pressure differences, but they bear some biases. Most CMIP5 models underestimate the July–August peak of the temperature difference annual cycle (Fig. 7a). The underestimation is more pronounced in HadGEM and

is associated with an underestimation of the simulated pressure difference (Fig. 7b) which can explain why its simulated divergence wind is also underestimated (Fig. 5b). In BCC-CSM the overestimated divergent wind (Fig. 5b) is exclusively associated with the overestimation of the simulated pressure difference (Fig. 7b) as the temperature difference is within the range of reanalyses (Fig. 7a). Examining the corresponding CMIP6 models, GFDL-CM and MRI-ESM deteriorate in representing the annual cycle of both temperature and pressure difference as compared with their corresponding CMIP5 models, consistent with their simulated wind divergence. However, most CMIP6 models such as HadGEM and BCC-CSM do better (Fig. 7c and d) than their corresponding CMIP5 models (Fig. 7a and b). Figure 7e and f illustrate the improvement by showing the uncertainty ranges in thermal and pressure differences from reanalyses, CMIP5 and CMIP6 models. These results reveal that, the range of CMIP6 models remains larger than that of the reanalyses range but compared to CMIP5 the bandwidth of CMIP6 models is relatively small except in a few months such as June–July in the temperature difference annual cycle. However, from one month to another, the median CMIP6 model is generally closer to the median reanalysis. Overall, this shows that the improvement in the simulated divergent wind is associated with an improvement in the simulated drivers.

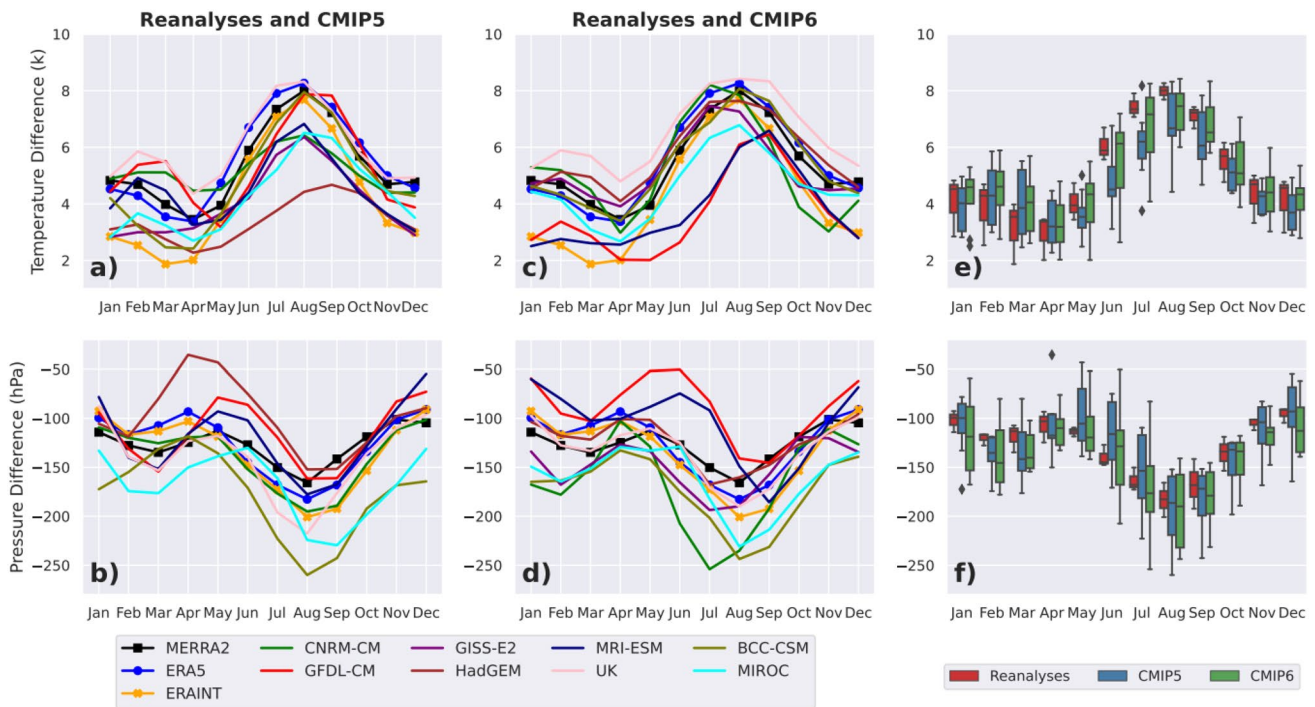


Fig. 7 Annual cycle of 925 hPa land–ocean thermal difference and the zonal pressure difference between the Central African landmass (10° S–5° N; 15°–30° E) and the coastal Atlantic Ocean (10° S–0°; 0°–10° E) for **a, b** reanalyses and CMIP5, **c, d** reanalyses and CMIP6

models. **e, f** Uncertainty ranges in land–ocean thermal and pressure differences from reanalyses (red), CMIP5 (blue) and CMIP6 (green) models

Figure 8 shows the spatial pattern of the long term annual mean 850 hPa relative vorticity (shading) and geopotential height (contours) for reanalyses, CMIP5 and CMIP6 models. Here, the focus on these variables (relative vorticity and geopotential height) at the 850 hPa pressure level is because at 925 hPa (where the core of the LLWs is found), many areas are blank due to high orography, making difficult any interpretation. In the reanalyses (Fig. 8a–c), at the western boundary of the study area (red box: Fig. 8a), the negative values of the relative vorticity associated with low-pressure values reflect a clockwise circulation corresponding to the rotational component of LLWs. These negative values of the relative vorticity are strengthened in most CMIP5 models in

line with the overestimation of their simulated LLWs rotational component all-year-round (Fig. 5c). The reinforcement of the negative values of relative vorticity is generally associated with a reinforcement of the simulated low pressure and this is particularly observed in HadGEM2-CM3 (Fig. 8g). By contrast, MRI-ESM1 (Fig. 8h) underestimates the strength of the negative vorticity found at the western boundary of the study region. This is consistent with the underestimated LLWs rotational component in that model (Fig. 5c). The CMIP6 models depict a similar pattern as their corresponding CMIP5 models with the negative values of the relative vorticity remaining pronounced with respect with reanalyses. However, although the improvement

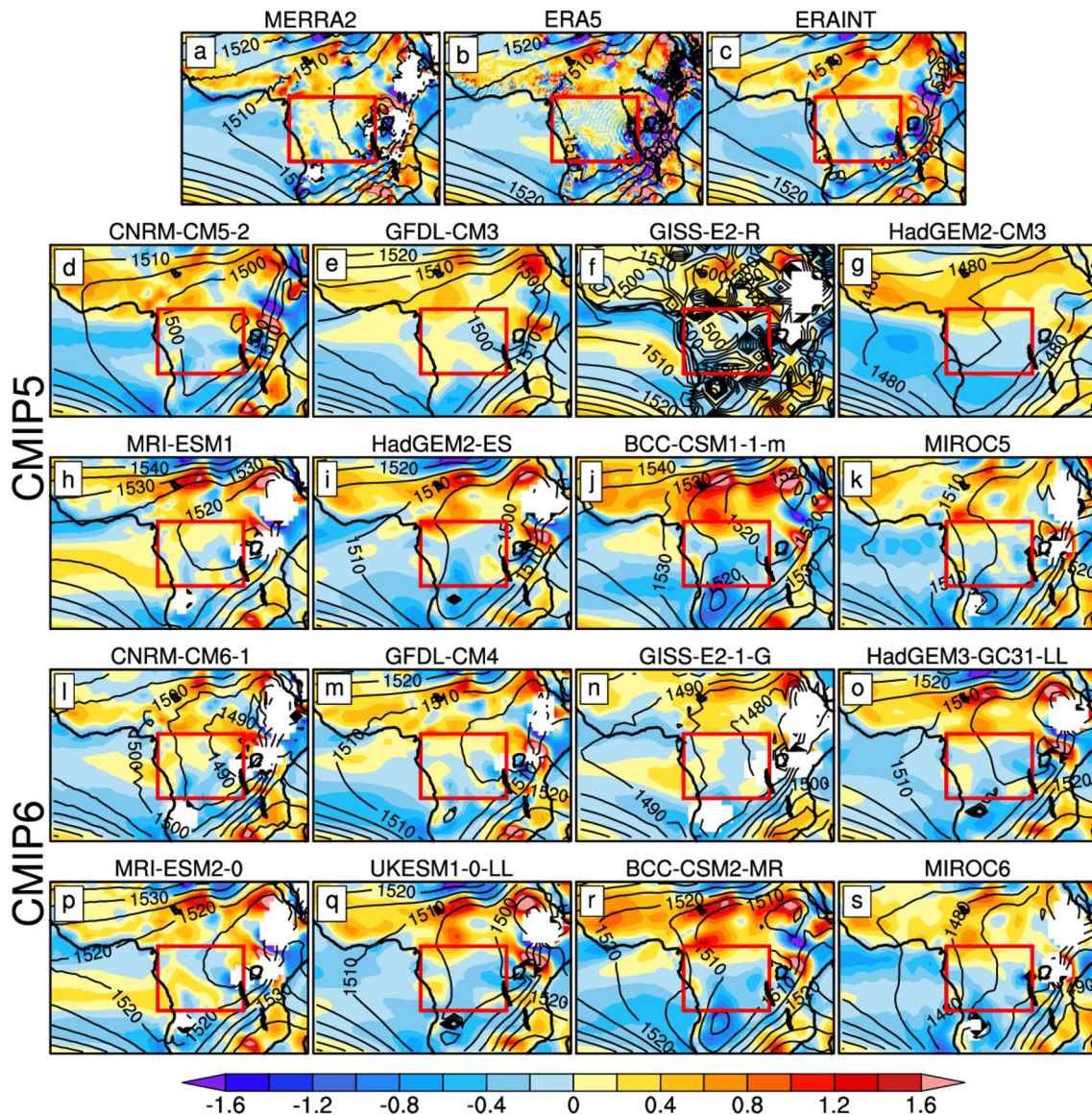


Fig. 8 Long term annual mean of 850 hPa relative vorticity (shading: 10^{-5} s^{-1}) and 850 hPa Geopotential height (contours: Pa) for **a–c** reanalyses, **d–k** CMIP5 and **l–s** CMIP6 models. The red box is the study

region, and the interest is on the value of the relative vorticity at the region's western boundary

in CMIP6 with respect to CMIP5 is not very obvious for all the models, an improvement is observed for some of them such as HadGEM3-GC31-LL and BCC-CSM2-MR. Furthermore, the improvement in the relative vorticity in HadGEM3-GC31-LL is associated with an improvement in the simulated pressure consistent with a better representation of the rotational circulation (Fig. 5f).

4 The Congo basin cell (CB cell)

In this section, we assess models' ability to represent the CB cell with the focus on the cell's key characteristics (intensity, width, western and eastern edge positions).

4.1 Mean seasonal climatology and link with LLWs

To investigate the Congo basin cell, Figs. 9 and 10 display the seasonal mean climatology of the mass-weighted stream-function (contours) for reanalyses, CMIP5 and CMIP6 models in MAM and SON seasons respectively. The zonal wind is also represented (shaded) in Figs. 9 and 10 to highlight the link between LLWs and the Congo basin cell. With the negative values of the mass-weighted stream-function depicting the Congo basin cell, it emerges from the figures that the three reanalyses agree relatively well in the intensity and the width of the cell in both seasons (Figs. 9a–c and 10a–c) although in MAM the cell looks wider in MERRA2 and ERA5 than ERAINT and its height is located around 800 hPa in MAM (Fig. 9a–c) but slightly higher in SON (Fig. 10a–c) season. In the MAM season (Fig. 9), CNRM-CM5, HadGEM2-CM3 and BCC-CSM1.1-m (GISS-E2-R and MRI-ESM1) are CMIP5 models that simulate a stronger and larger (weaker and narrower) cell compared to the reanalyses with the height of the cell exceeding 500 hPa in HadGEM2-CM3. To a certain extent, with this overestimated height, this could be assimilated to a large-scale circulation since there is an ongoing debate on whether the CB cell is distinct or not from the larger scale Central Africa Walker cell (Longandjo and Rouault 2020; Nicholson 2022). During the SON season, the cell remains stronger in HadGEM2-CM3 and BCC-CSM1.1-m but the width of the cell is less large in HadGEM2-CM3. Looking at the corresponding CMIP6 models, in terms of intensity, an improvement is particularly observed in CNRM-CM6-1 and HadGEM3-GC31-LL during the MAM season. Although BCC-CSM2-MR does not show a real improvement during the SON season, HadGEM3-GC31-LL shows an improvement in the cell's intensity, width and height while GFDL-CM4 depicts a stronger cell compared to its corresponding previous CMIP5 model (GFDL-CM3). However, we observe that compared to CMIP5 models, most of the corresponding CMIP6 models better represent the cell in both seasons.

It is also observed that the bias in the representation of the CB cell is generally associated with the bias in the strength of the simulated LLWs. In both seasons (Figs. 9 and 10) the overestimated (underestimated) Congo basin cell in models is associated with stronger (weaker) simulated LLWs. This highlights the fact that LLWs and the CB cell have the same drivers, consistent with findings from Longandjo and Rouault (2020). Therefore, in MAM and SON seasons, the improvement in the representation of the cell from CMIP5 to CMIP6 models is associated with the improvement in the representation of the simulated LLWs. Does the improvement extend throughout the year? We answer this question in the following section.

4.2 Annual cycle of the cell's key characteristics

Examining at the annual cycle of the cell in more detail, the models' ability to represent the seasonal evolution of the cell's key characteristics (intensity, width, western and eastern edge positions) is assessed in this section. Located between 925 and 850 hPa (Longandjo and Rouault 2020) the intensity of the cell is found by vertically averaging the mass-weighted stream function between 925 and 850 hPa and the minimum value found in the longitudinal band of the cell represents its intensity. The smaller that value, the stronger the cell because negative values of the mass-weighted stream functions are those depicting the cell. The western and eastern edges are located at the longitudes where the vertically (between 1000 and 850 hPa) averaged mass-weighted stream function is equal to zero or changes sign and the difference between the two edge longitudes indicates the width or zonal extent of the cell.

The seasonal cycle of these cell's key characteristics is represented in Fig. 11 for reanalyses, CMIP5 and CMIP6 models. The figure reveals that the seasonal evolution of the Congo basin cell is consistent in all three reanalyses with the maximum intensities found in February and August/September (Fig. 11a and e). Moreover, in agreement with findings from Longandjo and Rouault (2020), the second maximum is stronger than the first and throughout the year, the peaks of this bimodal signal are associated with the westernmost positions of the western edge (Fig. 11c and g) and the maximum width (Fig. 11b and f) of the cell. Although ERAINT does not agree with other reanalyses (MERRA2 and ERA5), the eastern edge position of the cell (Fig. 11d and h) has a low annual variability compared to the western edge position. CMIP5 models moderately capture the main features of the cell's key characteristics. However, most fail to simulate the bimodal signal of the evolution of the Congo basin cell's key characteristics, especially during the first half of the year. Although the second peak is reasonably well detected, most CMIP5 models fail to detect the first one, simulating it in April instead of February (Fig. 11a). In

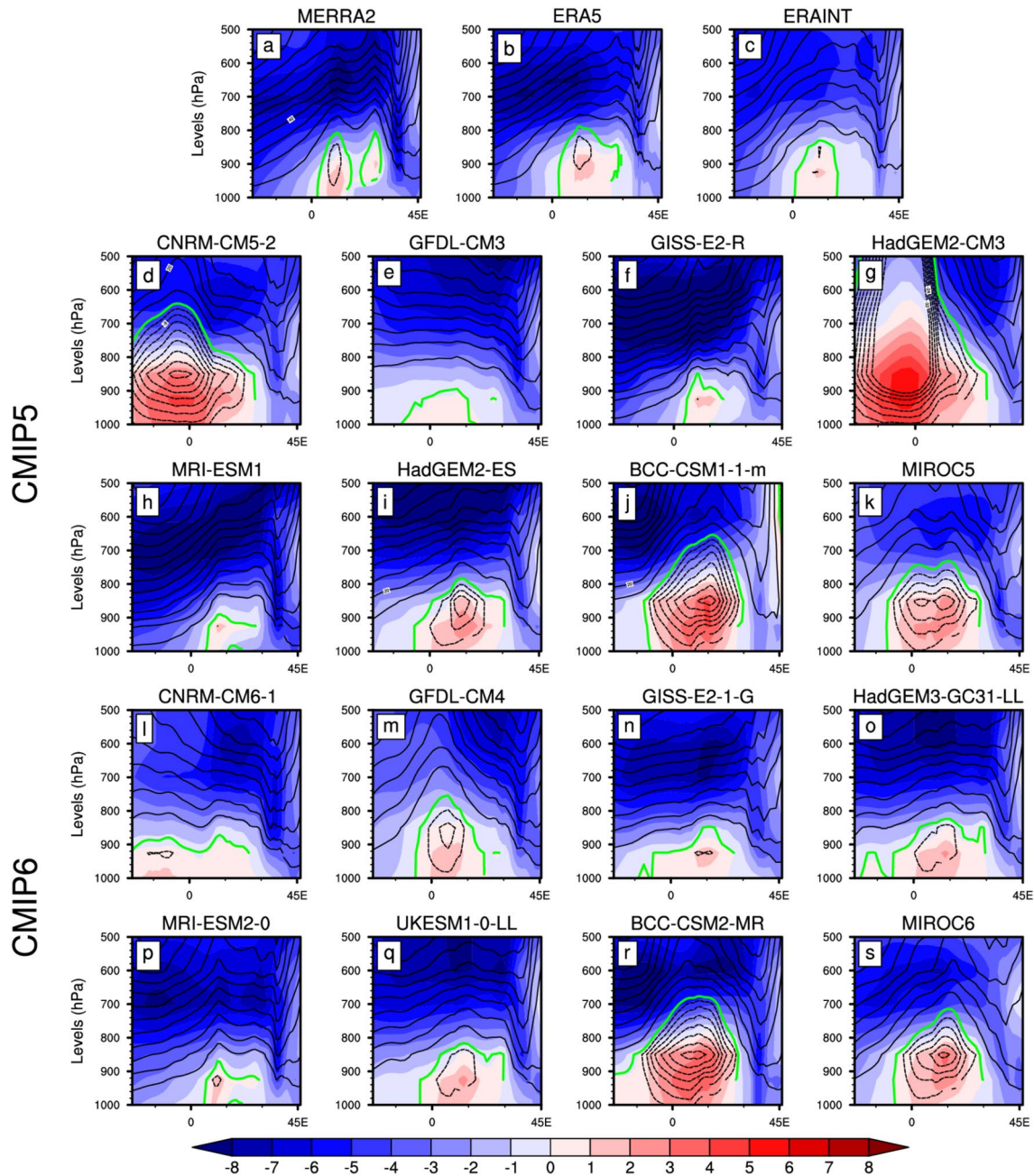


Fig. 9 March–May mean seasonal climatology of the zonal mass-weighted stream function (contours: $10^{11} \text{ kg s}^{-1}$) and the total zonal wind (shading: m/s) averaged between 5° S – 5° N for **a–c** reanalyses, **d–k** CMIP5 and **l–s** CMIP6 models. Solid black, green and dashed

black contours represent positive, zero and negative values of mass-weighted stream functions, respectively. Contour intervals are 10 between positive contours and 4 between negative contours

addition, especially in CNRM-CM and HadGEM (Fig. 11a), the simulated first peak found in April is stronger than the second (Fig. 11a) and is associated with a simulated larger cell (Fig. 11b) and a further west position of the simulated western edge (Fig. 11c). The simulated western edge longitude of the cell suggests that water vapour is transported from further afield in the Atlantic ocean toward central Africa inland. However, although the CMIP6 version of

BCC-CSM still overestimates the strength (Fig. 11e), the width (Fig. 11f) and the western edge position (Fig. 11g) of the cell throughout the year, CMIP6 models generally perform better in representing the seasonal cycle of the cell's key characteristics (Fig. 11e–h). This is well illustrated with the spread in CMIP6 models being smaller than that of CMIP5 models and their ensemble mean generally closer to reanalyses (Fig. 11i–k). The bandwidth of CMIP5 models

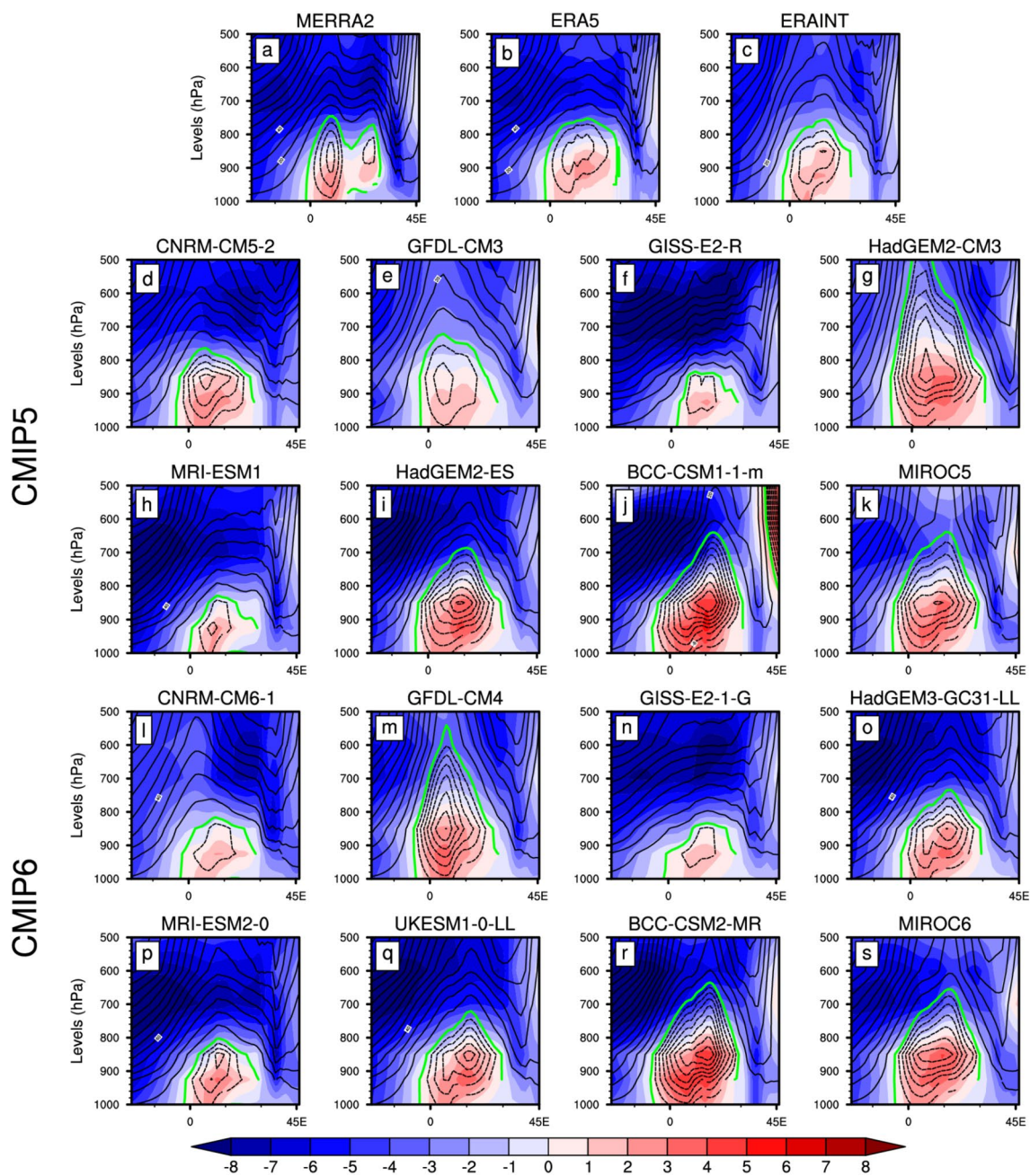


Fig. 10 Same as Fig. 9 but for the September–November season

is more important, showing a large range of disparity or dispersion compared to CMIP6 models.

5 Summary and conclusion

A recent study (Creese and Washington 2018) has highlighted the fact that rainfall bias in CMIP5 models over Central Equatorial Africa (CEA) is partly attributed to the misrepresentation of the important features of the atmospheric

low-level circulation in the region. However, the study did not go deeply in the understanding of the origin of the misrepresentation. Acting year-round, the key features of the lower circulation in CEA are the low-level westerlies (LLWs) and the Congo basin cell (CB) cell. With the release of CMIP6 models, in this paper, we compare the ability of eight CMIP6 climate models and the corresponding eight previous CMIP5 models to simulate the long term mean climatology and the seasonal cycle of these features. In addition, we explore their drivers to understand how these

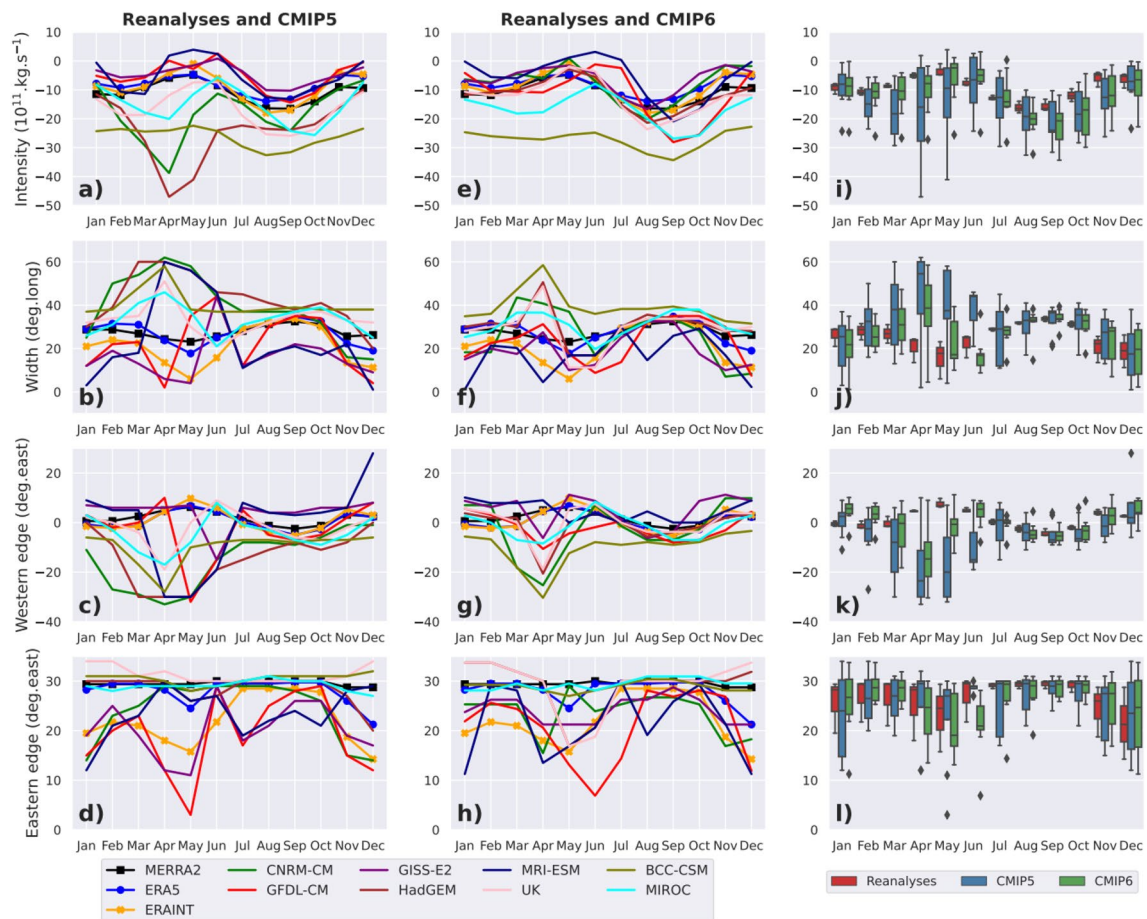


Fig. 11 Seasonal cycle on the Congo Basin cell intensity, width, western and eastern edge positions as depicted in **a–d** reanalyses and CMIP5 models, **e–h** reanalyses and CMIP6 models. **i–l** Uncertainty

ranges in CB cell intensity, width, western and eastern edge positions from reanalyses (red), CMIP5 (blue) and CMIP6 (green) models

features are represented in models and to explain changes in models' behaviour.

Although both CMIP5 and CMIP6 models perform well in simulating the main characteristics of LLWs such as the vertical location of the core speed found at around 925 hPa, and the two peaks in the seasonal cycle, most CMIP5 models overestimate the strength of LLWs by up to around 2 m/s in BCC-CSM1.1-m model. The overestimation is generally attributed to both divergent and rotational components of the total wind with the rotational component contributing the most in the overestimation. In CMIP6, although most models still overestimate LLWs strength, the intensity is slightly reduced compared to CMIP5 models. That improvement is the result of a better performance in both divergent and rotational circulation. The improvement in the simulated divergent component is associated with a better representation of the near-surface pressure and/or temperature difference between the Central Africa landmass and the coastal Atlantic Ocean. Regarding the rotational circulation, in a model such as HadGEM3-GC31-LL and BCC-CSM2-MR,

a simulated higher 850 hPa pressure is associated with less pronounced negative vorticity and a better representation of the rotational circulation (Fig. 5f).

For the CB cell, our results suggest that, its simulated biases are related to those of LLWs. In most CMIP5 models, the cell intensity and width are overestimated with the western edge generally found further west. These biases in the cell's key characteristics are associated with the overestimation of the simulated LLWs in CMIP5 models. However, although in CMIP6 models the cell key characteristics are still overestimated, the strength is reduced compared to CMIP5 models. This shows that CMIP6 models perform better in representing the cell and therefore, the improvement in the representation of the cell in CMIP6 models is associated with improvement in the representation of the simulated LLWs. We note that a small improvement in LLWs translates to a larger relative improvement in the CB cell.

Given the results we have highlighted in this study, compared to CMIP5 models, more confidence can be put in CMIP6 models although the spread is still relatively large.

However, to help better represent low level circulation features in the next generation of the coupled models, the land and ocean surface schemes could be advanced to resolve much better the surface characteristics which in turn can lead to an improvement of the simulated low-level circulation drivers (land–ocean thermal and pressure differences). In the meanwhile, the future work will investigate whether the improvement in the simulation of these low-level circulation features in CEA from CMIP5 to CMIP6 models has an impact like an improvement in the representation of rainfall in the region.

Acknowledgements The GCMs data used in this study were made available through the Earth System Grid Federation (ESGF) Peer-to-Peer system (<https://data.ceda.ac.uk/badc/cmip6/>). Reanalysis data used in this analysis were provided by the Copernicus Climate Change Service (<https://cds.climate.copernicus.eu/cdsapp#!home>; Hersbach et al. 2020), ECMWF (<https://ecmwf.int/en/forecasts/datasets/reanalysis-datasets/era-interim>) and NASA (<https://disc.sci.gsfc.nasa.gov/daac-bin/FTPSubset.pl>). This work has been funded by the UK Government's Foreign, Commonwealth and Development Office (FCDO). We acknowledge the World Climate Research Programme, which, through its Working Group on Coupled Modelling, coordinated and promoted CMIP6. We thank the climate modeling groups for producing and making available their model output, the Earth System Grid Federation (ESGF) for archiving the data and providing access, and the multiple funding agencies who support CMIP6 and ESGF. The first author thank the LaunchPAD team for the fruitful discussions.

Funding UK Government's Foreign, Commonwealth and Development Office (FCDO).

Data availability The GCM data used in this study were made available through the Earth System Grid Federation (ESGF) Peer-to-Peer system (<https://data.ceda.ac.uk/badc/cmip6/>). Reanalysis data used in this analysis were provided by the Copernicus Climate Change Service (<https://cds.climate.copernicus.eu/cdsapp#!home>; Hersbach et al. 2020), ECMWF (<https://ecmwf.int/en/forecasts/datasets/reanalysis-datasets/era-interim>) and NASA (<https://disc.sci.gsfc.nasa.gov/daac-bin/FTPSubset.pl>). The authors' code is available online (https://github.com/Priority-on-African-Diagnostics/LaunchPAD/tree/master/DIAGNOSTICS/Low_Level_Westerlies).

Declarations

Conflict of interest The authors declare that they have no conflicts of interest.

Ethics approval Not applicable.

Consent to participate Not applicable.

Consent to publication Not applicable.

Open Access This article is licensed under a Creative Commons Attribution 4.0 International License, which permits use, sharing, adaptation, distribution and reproduction in any medium or format, as long as you give appropriate credit to the original author(s) and the source, provide a link to the Creative Commons licence, and indicate if changes were made. The images or other third party material in this article are included in the article's Creative Commons licence, unless indicated

otherwise in a credit line to the material. If material is not included in the article's Creative Commons licence and your intended use is not permitted by statutory regulation or exceeds the permitted use, you will need to obtain permission directly from the copyright holder. To view a copy of this licence, visit <http://creativecommons.org/licenses/by/4.0/>.

References

- Adachi Y, Yukimoto S, Deushi M, Obata A, Nakano H, Tanaka TY et al (2013) Basic performance of a new earth system model of the Meteorological Research Institute (MRI-ESM1). *Pap Meteorol Geophys* 64:1–19. <https://doi.org/10.2467/mripapers.64.1>
- Baumberger C, Knutti R, Hadorn GH (2017) Building confidence in climate model projections: An analysis of inferences from fit. *Wiley Interdiscip Rev: Clim Change*. <https://doi.org/10.1002/wcc.454>
- Collins MSFB, Tett SFB, Cooper C (2001) The internal climate variability of HadCM3, a version of the Hadley Centre coupled model without flux adjustments. *Clim Dyn* 17(1):61–81. <https://doi.org/10.1007/s003820000094>
- Cook KH (1999) Generation of the African easterly jet and its role in determining West African precipitation. *J Clim* 12(5):1165–1184. [https://doi.org/10.1175/1520-0442\(1999\)0122.0.co;2](https://doi.org/10.1175/1520-0442(1999)0122.0.co;2)
- Cook KH, Vizy EK (2016) The Congo Basin Walker circulation: dynamics and connections to precipitation. *Clim Dyn* 47(3–4):697–717. <https://doi.org/10.1007/s00382-015-2864-y>
- Creese A, Washington R (2016) Using qflux to constrain modeled Congo Basin rainfall in the CMIP5 ensemble. *J Geophys Res: Atmos*. <https://doi.org/10.1002/2016jd025596>
- Creese A, Washington R (2018) A process-based assessment of CMIP5 rainfall in the Congo Basin: the September–November rainy season. *J Clim* 31(18):7417–7439. <https://doi.org/10.1175/jcli-d-17-0818.1>
- Crowhurst D, Dadson S, Peng J, Washington R (2020) Contrasting controls on Congo Basin evaporation at the two rainfall peaks. *Clim Dyn* 56(5–6):1609–1624. <https://doi.org/10.1007/s00382-020-05547-1>
- Dee DP, Uppala SM, Simmons AJ, Berrisford P, Poli P, Kobayashi S et al (2011) The ERA-Interim reanalysis: configuration and performance of the data assimilation system. *Q J R Meteorol Soc* 137(656):553–597. <https://doi.org/10.1002/qj.828>
- Dezfuli A (2017) Climate of western and central equatorial Africa. In: *Oxford research encyclopedia of climate science*, Oxford, pp 66. <https://doi.org/10.1093/acrefore/9780190228620.013.511>
- Dezfuli AK, Nicholson SE (2013) The relationship of rainfall variability in Western Equatorial Africa to the tropical oceans and atmospheric circulation. Part II: the boreal autumn. *J Clim* 26(1):66–84. <https://doi.org/10.1175/jcli-d-11-00686.1>
- Eyring V, Bony S, Meehl GA, Senior GA, Stevens B, Stouffer RJ, Taylor KE (2016) Overview of the Coupled Model Intercomparison Project Phase 6 (CMIP6) experimental design and organization. *Geosci Model Dev* 9:1937–1958. <https://doi.org/10.5194/gmd-9-1937-2016>
- Gelaro R, McCarty W, Suárez MJ, Todling R, Molod A, Takacs L et al (2017) The modern-era retrospective analysis for research and applications, version 2 (MERRA-2). *J Clim* 30(14):5419–5454. <https://doi.org/10.1175/jcli-d-16-0758.1>
- Griffies SM, Winton M, Donner LJ, Horowitz LW, Downes SM, Farneti R et al (2011) The GFDL CM3 coupled climate model: characteristics of the ocean and sea ice simulations. *J Clim* 24(13):3520–3544. <https://doi.org/10.1175/2011JCLI3964.1>

- Held IM, Guo H, Adcroft A, Dunne JP, Horowitz LW, Krasting J et al (2019) Structure and performance of GFDL's CM4. 0 climate model. *J Adv Model Earth Syst* 11(11):3691–3727. <https://doi.org/10.1029/2019MS001829>
- Hersbach H, Bell B, Berrisford P, Hirahara S, Horányi A, Muñoz-Sabater J et al (2020) The ERA5 global reanalysis. *Q J R Meteorol Soc* 146(730):1999–2049. <https://doi.org/10.1002/qj.3803>
- Jackson B, Nicholson SE, Klotter D (2009) Mesoscale convective systems over Western Equatorial Africa and their relationship to large-scale circulation. *Mon Weather Rev* 137(4):1272–1294. <https://doi.org/10.1175/2008mwr2525.1>
- James R, Washington R, Jones R (2015) Process-based assessment of an ensemble of climate projections for West Africa. *J Geophys Res: Atmos* 120(4):1221–1238. <https://doi.org/10.1002/2014jd022513>
- James R, Washington R, Abiodun B, Kay G, Mutemi J, Pokam W et al (2018) Evaluating climate models with an African lens. *Bull Am Meteor Soc* 99(2):313–336. <https://doi.org/10.1175/bams-d-16-0090.1>
- Jones C, Hughes JK, Bellouin N, Hardiman SC, Jones GS, Knight J et al (2011) The HadGEM2-ES implementation of CMIP5 centennial simulations. *Geoscientific Model Dev* 4(3):543–570. <https://doi.org/10.5194/gmd-4-543-2011>
- Kelley M, Schmidt GA, Nazarenko LS, Bauer SE, Ruedy R, Russell GL et al (2020) GISS-E2. 1: configurations and climatology. *J Adv Model Earth Syst* 12(8):e2019MS002025. <https://doi.org/10.1029/2019MS002025>
- Kim D, Sobel AH, Del Genio AD, Chen Y, Camargo SJ, Yao MS et al (2012) The tropical subseasonal variability simulated in the NASA GISS general circulation model. *J Clim* 25(13):4641–4659. <https://doi.org/10.1175/JCLI-D-11-00447.1>
- Kuete G, Mba WP, Washington R (2019) African Easterly Jet South: control, maintenance mechanisms and link with Southern subtropical waves. *Clim Dyn* 54(3–4):1539–1552. <https://doi.org/10.1007/s00382-019-05072-w>
- Longandjo GT, Rouault M (2020) On the structure of the regional-scale circulation over Central Africa: seasonal evolution, variability, and mechanisms. *J Clim* 33(1):145–162. <https://doi.org/10.1175/jcli-d-19-0176.1>
- Neupane N (2016) The Congo Basin zonal overturning circulation. *Adv Atmos Sci* 33:767–782. <https://doi.org/10.1007/s00376-015-5190-8>
- Nicholson SE (2018) The ITCZ and the seasonal cycle over equatorial Africa. *Bull Am Meteor Soc* 99(2):337–348. <https://doi.org/10.1175/bams-d-16-0287.1>
- Nicholson SE (2021) The rainfall and convective regime over equatorial Africa, with emphasis on the Congo Basin. In: Alsdorf D, Tshimanga R, Moukandi G (eds) Congo basin hydrology, climate and biogeochemistry: a foundation for the future. American Geophysical Union, Washington DC, pp 25–48
- Nicholson SE, Dezfuli AK (2013) The relationship of rainfall variability in Western Equatorial Africa to the tropical oceans and atmospheric circulation. Part I: the Boreal Spring. *J Clim* 26(1):45–65. <https://doi.org/10.1175/jcli-d-11-00653.1>
- Nicholson SE, Grist JP (2003) The seasonal evolution of the atmospheric circulation over West Africa and Equatorial Africa. *J Clim* 16(7):1013–1030. [https://doi.org/10.1175/1520-0442\(2003\)0162.0.co;2](https://doi.org/10.1175/1520-0442(2003)0162.0.co;2)
- Pokam WM, Djiotang LA, Mkankam FK (2012) Atmospheric water vapor transport and recycling in Equatorial Central Africa through NCEP/NCAR reanalysis data. *Clim Dyn* 38(9–10):1715–1729. <https://doi.org/10.1007/s00382-011-1242-7>
- Pokam WM, Bain CL, Chadwick RS, Graham R, Sonwa DJ, Kamga FM (2014) Identification of processes driving low-level Westerlies in West Equatorial Africa. *J Clim* 27(11):4245–4262. <https://doi.org/10.1175/jcli-d-13-00490.1>
- Roberts M (2017) MOHC HadGEM3-GC31-LL model output prepared for CMIP6 HighResMIP. Earth Syst Grid Fed. <https://doi.org/10.22033/ESGF/CMIP6.1901>
- Rowell DP, Booth BB, Nicholson SE, Good P (2015) Reconciling past and future rainfall trends over East Africa. *J Clim* 28(24):9768–9788. <https://doi.org/10.1175/jcli-d-15-0140.1>
- Sellar AA, Jones CG, Mulcahy JP, Tang Y, Yool A, Wiltshire A et al (2019) UKESM1: Description and evaluation of the UK earth system model. *J Adv Model Earth Syst* 11(12):4513–4558. <https://doi.org/10.1029/2019MS001739>
- Taguela TN, Vondou DA, Moufouma-Okia W, Fotso-Nguemo TC, Pokam WM, Tanessong RS et al (2020) CORDEX multi-RCM hindcast over Central Africa: evaluation within observational uncertainty. *J Geophys Res: Atmos*. <https://doi.org/10.1029/2019jd031607>
- Tamoffo AT, Moufouma-Okia W, Dosio A, James R, Pokam WM, Vondou DA et al (2019) Process-oriented assessment of RCA4 regional climate model projections over the Congo Basin under 1.5°C and 2°C global warming levels: Influence of regional moisture fluxes. *Clim Dyn* 53(3–4):1911–1935. <https://doi.org/10.1007/s00382-019-04751-y>
- Tamoffo AT, Nikulin G, Vondou DA, Dosio A, Nouayou R, Wu M, Igri PM (2021a) Process-based assessment of the impact of reduced turbulent mixing on Congo Basin precipitation in the RCA4 Regional Climate Model. *Clim Dyn* 56(5–6):1951–1965. <https://doi.org/10.1007/s00382-020-05571-1>
- Tamoffo AT, Amekudzi LK, Weber T, Vondou DA, Yamba EI, Jacob D (2021b) Mechanisms of rainfall biases in two CORDEX-CORE regional climate models at rainfall peaks over Central Equatorial Africa. *J Clim* 35(2):639–668. <https://doi.org/10.1175/JCLI-D-21-0487.1>
- Tatebe H, Ogura T, Nitta T, Komuro Y, Oguchi K, Takemura T et al (2019) Description and basic evaluation of simulated mean state, internal variability, and climate sensitivity in MIROC6. *Geoscientific Model Dev* 12(7):2727–2765. <https://doi.org/10.5194/gmd-12-2727-2019>
- Taylor KE, Stouffer RJ, Meehl GA (2012) An overview of CMIP5 and the experiment design. *Bull Am Meteorol Soc* 93:485–498. <https://doi.org/10.1175/BAMS-D-11-00094.1>
- Voldoire A, Sanchez-Gomez E, Salas y Méliá D, Decharme B, Casou C, Sénési S, et al (2013) The CNRM-CM5. 1 global climate model: description and basic evaluation. *Clim Dyn* 40(9):2091–2121. <https://doi.org/10.1007/s00382-011-1259-y>
- Voldoire A, Saint-Martin D, Sénési S, Decharme B, Alias A, Chevalier M et al (2019) Evaluation of CMIP6 deck experiments with CNRM-CM6-1. *J Adv Model Earth Syst* 11(7):2177–2213. <https://doi.org/10.1029/2019MS001683>
- Washington R, James R, Pearce H, Pokam WM, Moufouma-Okia W (2013) Congo Basin rainfall climatology: can we believe the climate models? *Philos Trans R Soc B: Biol Sci* 368(1625):20120296. <https://doi.org/10.1098/rstb.2012.0296>
- Webster PJ (1983) Large-scale structure of the tropical atmosphere. In: Hoskins BJ, Pearce RP (eds) Large-scale dynamical processes in the atmosphere. Academic Press, Cambridge, pp 235–275
- Wu T, Song L, Li W, Wang Z, Zhang H, Xin X et al (2014) An overview of BCC climate system model development and application for climate change studies. *J Meteorol Res* 28(1):34–56. <https://doi.org/10.1007/s13351-014-3041-7>
- Wu T, Lu Y, Fang Y, Xin X, Li L, Li W et al (2019) The Beijing climate center climate system model (BCCCSM): the main progress from CMIP5 to CMIP6. *Geoscientific Model Dev* 12(4):1573–1600. <https://doi.org/10.5194/gmd-12-1573-2019>
- Watanabe M, Suzuki T, O'ishi R, Komuro Y, Watanabe S, Emori S, et al (2010) Improved climate simulation by MIROC5: mean states, variability, and climate sensitivity. *J Clim* 23(23):6312–6335. <https://doi.org/10.1175/2010JCLI3679.1>

Yukimoto S, Kawai H, Koshiro T, Oshima N, Yoshida K, Urakawa S et al (2019) The meteorological research institute earth system model version 2.0, MRI-ESM2. 0: description and basic evaluation of the physical component. *J Meteorol Soc Jpn Ser II*. <https://doi.org/10.2151/jmsj.2019-051>

Publisher's Note Springer Nature remains neutral with regard to jurisdictional claims in published maps and institutional affiliations.

RESEARCH ARTICLE

Rainfall in uncoupled and coupled versions of the Met Office Unified Model over Central Africa: Investigation of processes during the September–November rainy season

Thierry N. Taguela¹  | Wilfried M. Pokam^{1,2}  | Richard Washington³ 

¹Laboratory for Environmental Modelling and Atmospheric Physics (LEMAP), Department of Physics, University of Yaounde 1, Yaounde, Cameroon

²Department of Physics, Higher Teacher Training College, University of Yaounde 1, Yaounde, Cameroon

³School of Geography and the Environment, University of Oxford, Oxford, UK

Correspondence

Thierry N. Taguela, Laboratory for Environmental Modelling and Atmospheric Physics, Department of Physics, University of Yaounde 1, Yaounde, Cameroon.
Email: thierrytaguela@gmail.com

Funding information

Natural Environment Research Council (NERC), Grant/Award Numbers: NE/M017206/1, NE/M020207/1

Abstract

Although climate models are important for making projections of future climate, little attention has been devoted to model simulation of the complex climate of Central Africa (CA). This study investigates rainfall biases through processes in three versions of the Met Office Unified Model over CA with both coupled and atmosphere-only formulations for each version. The study shows that the models depict a wet (dry) bias over the eastern (coastal western) CA in the September–November season with the wet (dry) bias stronger in coupled (atmosphere-only) models. Here, we explore potential regional to large-scale causes of these biases. Results reveal that the overestimation of the simulated sinking branch of the Atlantic–Congo zonal overturning cell is associated with a strong near-surface temperature and pressure gradient between CA and the eastern Atlantic Ocean. This leads to strong low-level westerlies (LLWs) which dry the coastal western CA and strengthen the intensity of the Congo basin cell. Over eastern CA, the wet bias is partially due to the misrepresentation in the strength of both African easterly jet components that shift the mid-tropospheric moisture flux convergence southward favouring more convection south of the equator. Furthermore, the overestimation in the simulated width and intensity of the Congo basin cell is associated with a strong low-level moisture convergence over eastern CA which contributes to more precipitation. Remote contributions to the wet bias come from both the Atlantic and the Indian Oceans. The simulated Atlantic–Congo zonal overturning circulation dries the coast through its overestimated lower branch (LLWs) which moves further into the continent and advects more moisture to the eastern CA. In the meantime, during positive Indian Ocean Dipole years, the advected moisture from the Indian Ocean to the CA region is overestimated in models, much more in coupled models and contributes to the eastern CA wet bias.

KEYWORDS

African easterly jet, Atlantic–Congo zonal overturning cell, Central Africa, Congo basin cell, Indian Ocean dipole, MetUM, rainfall bias

1 | INTRODUCTION

Central Africa (CA) encompasses the Congo River basin and rainforest which are respectively the world's second largest river basin and rainforest next to those of the Amazon. The role of the Congo Basin in the Earth climate system is undisputed (Washington *et al.*, 2013). However, the climate of the region, compared to other regions of the World, has remained critically understudied (Hua *et al.*, 2019). This creates a gap in the understanding of the global climate system and complicates the analysis of its representation in climate models. Based on the urgent need for action to tackle climate change, the Paris agreement has called to limit global warming to well below 2°C above pre-industrial levels and is pursuing efforts to limit the temperature increase to 1.5°C (Masson-Delmotte, 2018). According to King and Harrington (2018), for a 0.5°C global warming, equatorial regions, and especially CA, will experience the largest changes in local climate compared to extratropical areas. This underlines the need for accurate projection of the future climate over the region to efficiently build mitigation and adaptation plans to reduce the potential impact on CA countries where livelihoods mainly depend on climate and especially rain-fed agriculture (Fotso-Nguemo *et al.*, 2018). Since general circulation models (GCMs) are crucial to developing climate projections (Creese and Washington, 2016), it becomes urgent to better evaluate hindcasts to identify the strengths, diagnose the deficiencies and thereby improve these vital tools.

The CA rainfall pattern follows a bimodal distribution with peaks in the March–April–May (MAM) and September–October–November (SON) rainy seasons, with higher amounts occurring during the SON season on average (Jackson *et al.*, 2009). Roughly 70% of rainfall variability in this region is the result of mesoscale convective systems (MCSs: Nesbitt *et al.*, 2006; Hartman, 2021) initiated in the lee of the high terrain of the Great Rift Valley (Jackson *et al.*, 2009). In addition, rainfall is driven by features such as the African easterly jet (AEJ: Nicholson and Grist, 2003; Kuete *et al.*, 2019), low-level westerlies (LLWs: Pokam *et al.*, 2014) and the Congo basin Walker like circulation (Cook and Vizu, 2015). However, in the region, climate models generally fail to represent these drivers leading to rainfall biases.

Several studies have assessed models over CA (James and Washington, 2012; Nikulin *et al.*, 2012; Haensler *et al.*, 2013; Saeed *et al.*, 2013; Washington *et al.*, 2013; Aloysius *et al.*, 2016; Vondou and Haensler, 2017; Fotso-Nguemo *et al.*, 2018; Sonkoué *et al.*, 2018; Tamoffo *et al.*, 2019a; Taguela *et al.*, 2020). However, Almazroui *et al.* (2020) and Zhu and Yang (2020) have noted a lack of model improvement in the new generation of climate

models. Early studies on climate model analysis were mostly restricted to statistical evaluation. However, scalar metrics in climate model evaluation give information on the degree to which the model is far from the observation but do not yield the reason behind biases. The identification of misrepresentation of physical processes underlying model biases may help to explain why models fail and enable efforts to improve them (James *et al.*, 2018).

Recent studies have started to apply a process-based approach to evaluate climate models on their capacity to reproduce important processes driven rainfall variability over the study region. Findings from Creese and Washington (2018) show that, over the Atlantic Ocean, models combining larger and more equator-ward sea surface temperature (SST) bias, higher evaporation and higher local convection have a wet bias in the western CA. They also found that the underestimation of the simulated strength of the northern component of the African easterly jet (AEJ-N) leads to wet bias over eastern CA while an overestimation of the AEJ-N strength may suppress convection and lead to a dry precipitation bias. Furthermore, they have concluded that the overestimation of the simulated Indian Ocean overturning cell may also contribute to an overestimation of both subsidence over the western Indian Ocean and convection over the eastern CA. Tamoffo *et al.* (2019b) found that overestimation of the strength of the simulated AEJ components favours mid-level moisture divergence which dries mid-tropospheric layers over CA and in turn induces a dry precipitation bias. It has also been established (Washington *et al.*, 2013; Creese and Washington, 2016) that there is a strong relationship between simulated rainfall and moisture flux convergence over CA. For that reason, simulated moisture transport is a good candidate for understanding precipitation bias. The findings from Pokam *et al.* (2014) show that LLWs from the eastern Atlantic Ocean are an important source of moisture over CA. However, as demonstrated by James *et al.* (2018), an overestimation of the strength of the simulated LLWs in models leads to a dry precipitation bias over the coastal region in CA. It clearly appears from these studies that rainfall biases could be reduced by improving the simulated SST, both wind convergence and divergence, moisture transport and/or Walker type circulations. Such studies are useful for model development because they provide reasons for model errors by tracing processes that are not well simulated. Therefore, they provide direction to model developers to improve the next generation of climate models.

This study aims to continue efforts on the process-based evaluation of models over CA. It has been established that CA rainfall is modulated by both regional climate circulation (Nicholson and Grist, 2003; Jackson *et al.*, 2009; Pokam *et al.*, 2011, 2014; Longandjo and Rouault, 2019) and the large-scale response of the atmosphere to tropical SST variations (Dezfuli and Nicholson, 2013; Nicholson

and Dezfuli, 2013; Dezfuli *et al.*, 2015; Hua *et al.*, 2016; Dyer *et al.*, 2017; Hua *et al.*, 2017). Therefore, in this study, the investigation of simulated rainfall bias will emphasize both regional and large-scale features already identified as key contributors to climate variability over the region. The focus of the paper is on the Met Office Unified Model (MetUM) which is currently a particular focus of model development over Africa as part of the Improving Model Processes for African Climate (IMPALA) programme. Several versions of the MetUM are considered in this study, including both coupled global climate model (CGCM) and atmosphere-only (AGCM) formulations of each model version. We investigate the influence of the atmosphere–ocean coupling by highlighting differences and similarities between the coupled and atmosphere-only models over CA. We also compare different versions of the coupled and atmosphere-only model with each other to identify and, where possible, explain changes from one version to another. In parallel, the persistence of errors between the model's versions is emphasized. This is particularly important to establish as such errors will require a concerted effort to address in order to improve the next versions of the model.

This work is organized as follows. In Section 2, we present details of the MetUM. Observational and reanalyses data are also presented in Section 2 together with the methods used to assess the model outputs. Section 3 shows the pattern of the MetUM rainfall climatology in the main rainy season (September–November: SON) in the region. We show how rainfall biases in MetUM over CA can be explained or understood through the exploration of remote and local processes in Sections 4 and 5 respectively. Section 6 gives a summary and concluding remarks.

2 | DATA AND METHODS

The MetUM is the global modelling system developed and used at the Met Office in the United Kingdom (UK). Three versions of the model are evaluated in this study, including three Global Coupled models GC2 (Williams *et al.*, 2015), GC3 (Williams *et al.*, 2018) and GC4 together with their corresponding atmosphere-only formulations GA6 (Walters *et al.*, 2017), GA7 (Walters *et al.*, 2019) and GA8 respectively. They were all run at a grid spacing of 0.833° longitude \times 0.555° latitude. Monthly outputs are used for this study. The atmosphere-only versions, GA6 and GA7 have 27 years (from 1982 to 2008) of simulations while GA8 has 20 years (from 1989 to 2008). For coupled models, 35 years (1981 to 2015 for GC2 and GC4; 2080 to 2114 for GC3) of simulations are used. Let us note that GC3 is a free-running simulation and years do not correspond to observations. Therefore the selected output

period (2080 to 2114) corresponds to hindcasts and not the projections. GA6/GC2, GA7/GC3 and GA8/GC4 are the three latest versions of MetUM with GA8/GC4 being the most recent version released. The most noteworthy modifications in GA7/GC3 compared with GA6/GC2 are to the physical parameterization including a new modal aerosol scheme, an improved treatment of gaseous absorption in the radiation scheme, revisions to the numerics of the convection scheme, introduction of multi-layer sea ice and the introduction of a seamless stochastic physics package in the atmospheric model (Williams *et al.*, 2018; Walters *et al.*, 2019). Although published details of GA8/GC4 is as yet still forthcoming, in terms of changes in GA8/GC4 compared to GA7/GC3, a routine basket of parametrization changes (among many others) are as below: increased detrained cloud, time-smoothed convective increments, Convective cloud tuning for GA8 and the most notable of which is the introduction of prognostic based convective entrainment rate. However, let us note that, relative to GC3, there are no science changes to the ocean model in GC4.

Several reference datasets, both observations and reanalyses, are used to evaluate models outputs. They are also at a monthly time scale resolution covering the period 1981 to 2015 (35 years). The observed rainfall used in this study is from the following sources: the Global Precipitation Climatology Project (GPCP version 3.1: Huffman *et al.*, 2020) available on a 0.5° grid and derived from gauge and satellite measurements with a less use of rain gauges over the study region translated by a weak relative weighting of gauges in the data (not shown here); precipitation from The University of Delaware with a spatial resolution of 0.5° derived from gauge measurements (UDEL version 5.01: Matsuura and Willmott, 2015) and the Climate Hazards group Infrared Precipitation with Stations (CHIRPS: Funk *et al.*, 2015) at 0.05° grid spacing. The satellite estimates and observed SSTs is from HadISST version 1 (Rayner, 2003) with a spatial resolution of 1° . The reanalyses data are used here for the assessment of the dynamical aspects of the atmosphere (such as convection, subsidence, moisture transport and wind convergence). This is a widespread practice for the region of interest (Todd and Washington, 2004; Balas *et al.*, 2007; Jury *et al.*, 2008; Jackson *et al.*, 2009; Pokam *et al.*, 2011, 2014; Sandjon *et al.*, 2012; Dezfuli and Nicholson, 2013; Nicholson and Dezfuli, 2013; Cook and Vizey, 2015; Dommo *et al.*, 2018). Owing to the large variation in precipitation estimates from satellite and reanalyses datasets (Washington *et al.*, 2013; Creese and Washington, 2016; James *et al.*, 2018), two reanalyses are used in this study to evaluate the models. These are ERA5 reanalysis with a grid resolution of $0.25^\circ \times 0.25^\circ$ (Hersbach *et al.*, 2020) produced by the European Centre

for Medium-Range Weather Forecast Integrated Forecast System (IFS Cycle 41r2) and a 0.5° latitude by 0.625° longitude grid resolution MERRA2 (Gelaro *et al.*, 2017) provided by the National Aeronautics and Space Administration, United States (US).

To keep uniformity between datasets in terms of spatial resolution and enable comparison, all data used in this study are remapped onto a $1^\circ \times 1^\circ$ spatial grid. Data sets with higher resolution than $1^\circ \times 1^\circ$ are remapped using the first-order conservative remapping method (Jones, 1999) while coarser-resolution datasets are bilinearly interpolated (Nikulin *et al.*, 2012). At the local or regional scale, the zonal mass-weighted stream function as computed in Longandjo and Rouault (2019) is used to explore the Congo basin cell. It satisfies the meridional mean continuity equation in spherical coordinates and is calculated at each pressure and longitude as a function of the downward integrated zonal wind. The large-scale forcing such as the influence of Indian Ocean SST on CA rainfall is investigated through the Indian Ocean Dipole (IOD). Also called Dipole Mode Index (Saji *et al.*, 1999), the IOD index is defined as the SST difference between the western equatorial ocean (10°S – 10°N , 50° – 70°E) and the southeastern ocean (10°S – 0°N , 90° – 110°E).

3 | SEPTEMBER–NOVEMBER RAINFALL CLIMATOLOGY

Here, we present the spatial pattern of the mean September–November rainfall climatology over CA depicted by three observations (GPCP: Figure 1a, UDEL: Figure 1b and CHIRPS: Figure 1c) and two reanalyses (ERA5: Figure 1d and MERRA2: Figure 1e). The models' (coupled models and their corresponding atmosphere-only version) biases with respect to GPCP are shown in Figure 1f–k. Three observational data sets of precipitation provide a perspective on precipitation uncertainty. The choice of GPCP in bias calculation is due to its availability over oceans. The CA domain used in this study is 9° – 29°E , 12°S – 6°N (box, Figure 1a) but Figure 1 covers a larger area including surrounding oceans to provide an overview of the spatial distribution of rainfall biases around CA and to detect possible links with CA rainfall biases.

Observations agree well with the spatial distribution of mean SON rainfall over CA (Figure 1a–c). Two areas of maximum rainfall are located in the northwestern and northeastern parts of CA (Figure 1a–c) although both are higher in CHIRPS (Figure 1c). At the centre of the region, UDEL and CHIRPS show a rainfall maximum that is higher in UDEL and does not appear in GPCP. This highlights uncertainties between observations. According to

Maidment *et al.* (2014), in regions where the gauge network is sparse and unevenly distributed, conversion from point to area averages may be subject to large representativeness errors. This is the case over the Congo Basin where very few gauges exist (Washington *et al.*, 2013). In general, the reanalyses (Figure 1d,e) struggle to capture both the spatial pattern and the intensity of rainfall over CA. For instance, the northwestern and the northeastern rainfall maxima are overestimated in the two reanalyses and this is more pronounced in MERRA2 compared to ERA5. In addition, the spatial extent of rainfall maxima in MERRA2 is too large. The disagreement among the reanalyses is likely due to differences in forecast models, data assimilation schemes and available observations (e.g., radiosonde, aircraft and satellite data) (Lin *et al.*, 2014). However, compared to MERRA2 (Figure 1e), ERA5 (Figure 1d) is closest to the mean observed rainfall climatology (GPCP: Figure 1a). Therefore, in dynamical analyses, ERA5 will be considered as the principal reference among reanalyses.

All versions of the MetUM in both coupled and atmosphere-only formulation depict a dipole bias over CA in SON season (Figure 1f–k) with a wet bias (dry bias) over the eastern (western) CA. The dipole pattern is consistent across the model versions whichever observation is taken as reference (not shown). The wet bias is noticeably larger in coupled models while in atmosphere-only formulations, the dry bias in the western CA is most pronounced. Furthermore, from the older (GA6/GC2) to the recent (GA8/GC4) version in both atmosphere-only and coupled models, the eastern CA wet bias strengthens while the coastal western CA dry bias weakens. This suggests that newer versions of MetUM are wetter over the entire CA compared to previous ones although remaining dry over the coastal region compared to GPCP. Over the Indian Ocean, a wet bias is evident in the central equatorial basin in atmosphere-only models (Figure 1f–h) while in coupled models (Figure 1i–k) the structure of the bias is a dipole with the predominance of dry (wet) bias in the southeastern (western) equatorial Indian Ocean. Let us notice that, the wet bias found in the equatorial Indian Ocean in both atmosphere-only and coupled formulations is much improved in the latest version of the model (GA8/GC4). The improvement could be due to the important convection changes made in GA8/GC4. However, unlike in atmosphere-only models, in coupled models, the Indian Ocean wet bias extends to the east of the African continent to link with the wet bias over eastern CA. The hypothesis here is that a large-scale circulation associated with the Indian Ocean contributes to the eastern CA wet bias in coupled models and may help to explain why they are wetter than their atmosphere-only versions. It should be noted that the wet bias over eastern

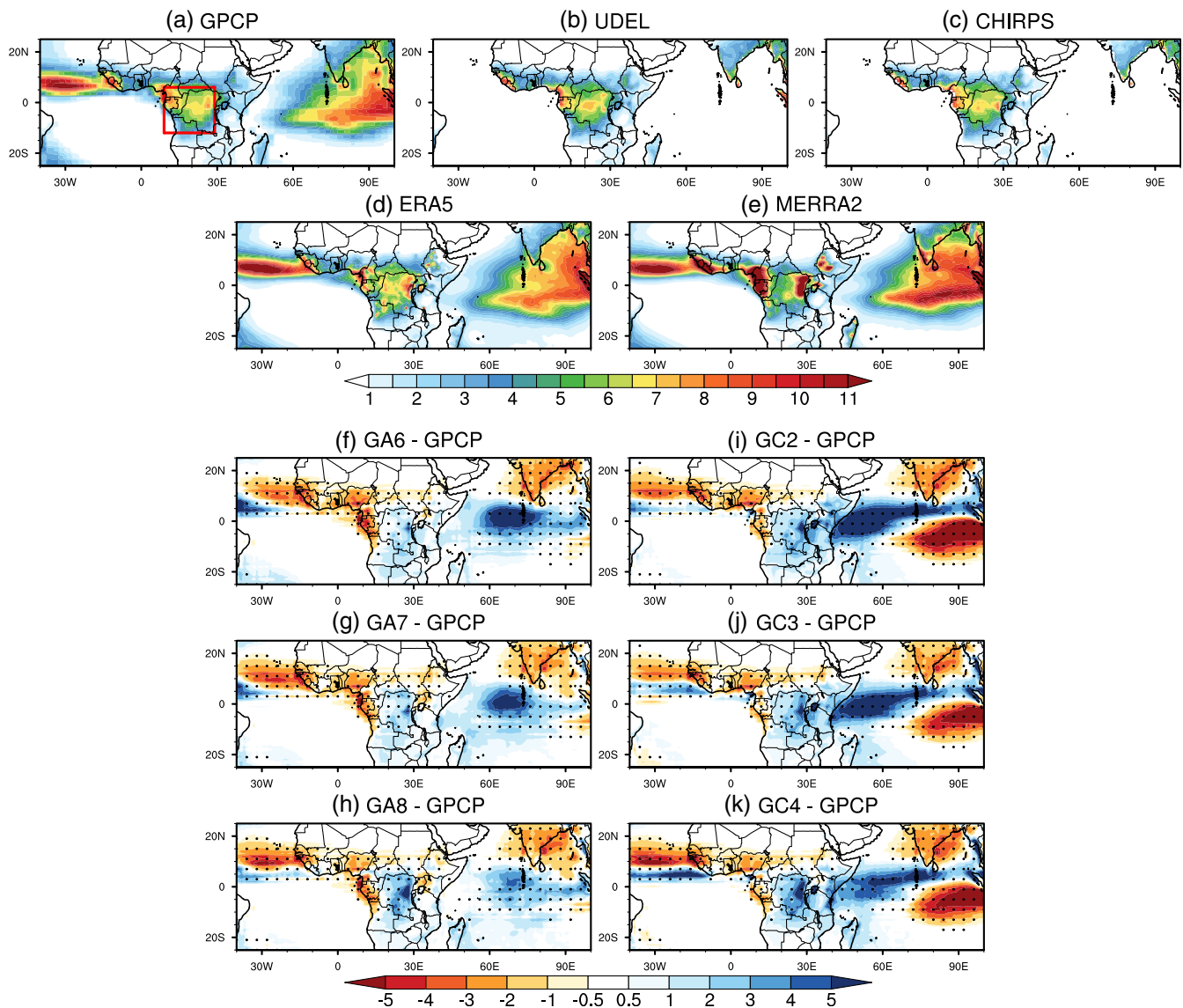


FIGURE 1 September–November spatial rainfall (mm day^{-1}) climatology for (a–e) GPCP, UDEL, CHIRPS, ERA5 and MERRA2 absolute values (1981–2015), (f–h) atmosphere-only and (i–k) coupled models biases with respect to GPCP. The box in (a) indicates the Central Africa domain used in this study and superimposed dots in (f–k) indicate the areas where the differences are statistically significant at the 95% confidence level using the *t*-test [Colour figure can be viewed at wileyonlinelibrary.com]

CA increases in recent versions of the MetUM while over the western Indian Ocean it decreases. This shows that the contribution to the eastern CA wet bias is not limited to the Indian Ocean. As far as the dry bias over the coastal western CA is concerned, in both coupled and atmosphere-only formulations, the bias is not a localized bias too. It extends to the southern coast of Western Africa and could also be the result of the Atlantic Ocean large-scale circulation. Therefore, to understand the models' biases, analyses will first focus on the remote or large-scale drivers such as the atmospheric response to the simulated SST over the Atlantic and Indian Oceans.

4 | UNDERSTANDING THE MODELS' BIASES: LINKS TO REMOTE FORCING AND LARGE-SCALE CIRCULATION

4.1 | Rainfall and SST teleconnection in MetUM

Dezfuli and Nicholson (2013) have highlighted the relationship between rainfall in CA subregions and SST. Their findings reveal that the boreal autumn (October–December) rainfall over eastern (western) CA shows a large spread of positive correlation with SST over the

equatorial Indian Ocean (Benguela coast and the equatorial Atlantic Ocean). Similar findings are shown in Figure 2a (Figure 3a) where observed SON rainfall from GPCP is averaged over eastern (western) CA and correlated with observed SON SST from HadISST for the period 1981–2015.

However, in Figure 2a (Figure 3a), the highest positive correlation is found south of Madagascar (southwest of South Africa in the Atlantic Ocean). Figure 2b–g (Figure 3b–g) show biases of correlations computed as in Figure 2a (Figure 3a) for each model with respect to Figure 2a

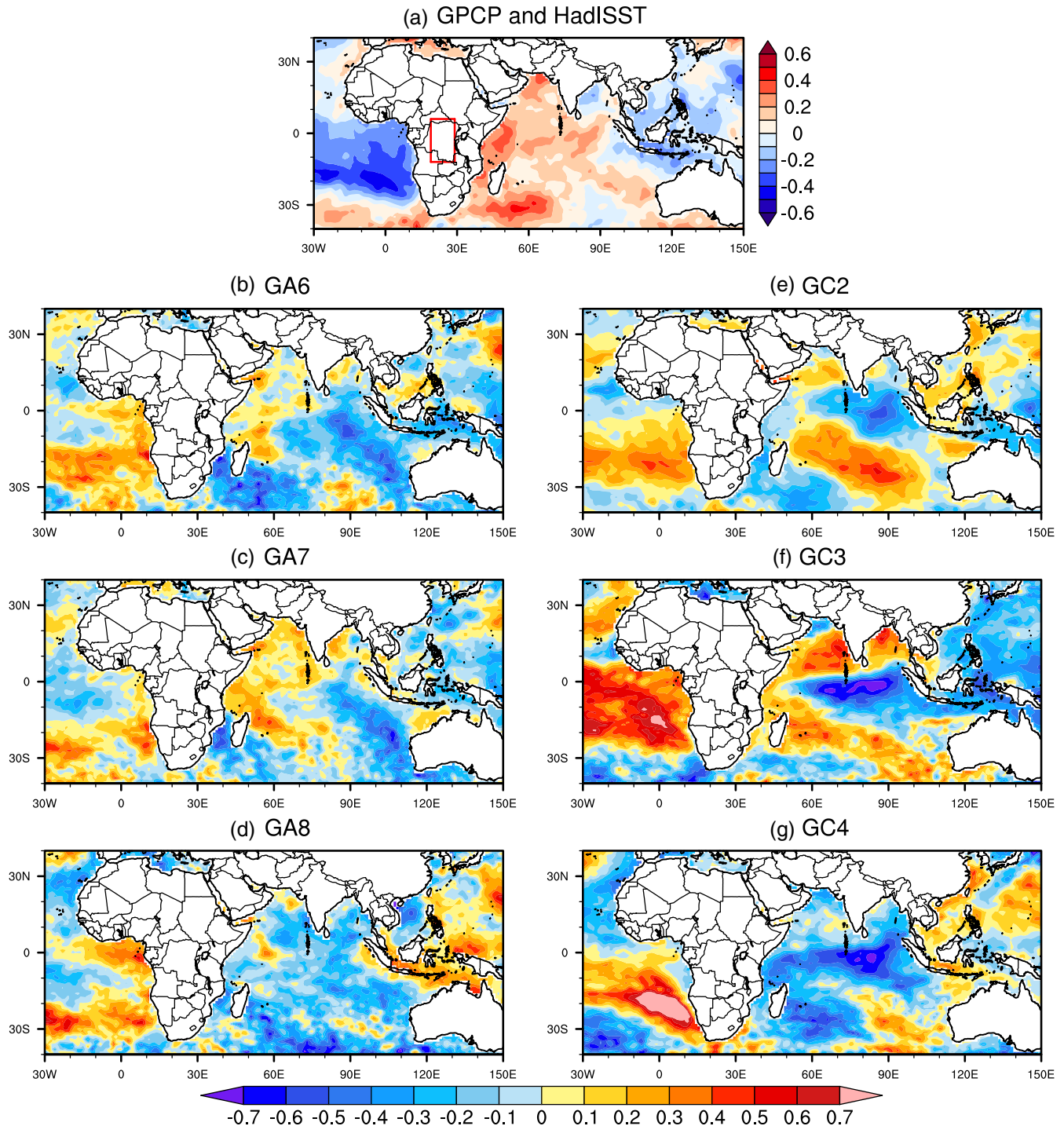


FIGURE 2 (a) Correlations of observed SON rainfall from GPCP, averaged over eastern Central Africa (the box: 12°S – 6°N , 19 – 29°E), against observed SON SST from HadISST for the period 1981–2015. (b–g) biases of correlations computed as in (a) for each model with respect to (a). We have used 27 years of GA6 and GA7 and 20 years of GA8 while 35 years of GC2, GC3 and GC4 were used [Colour figure can be viewed at wileyonlinelibrary.com]

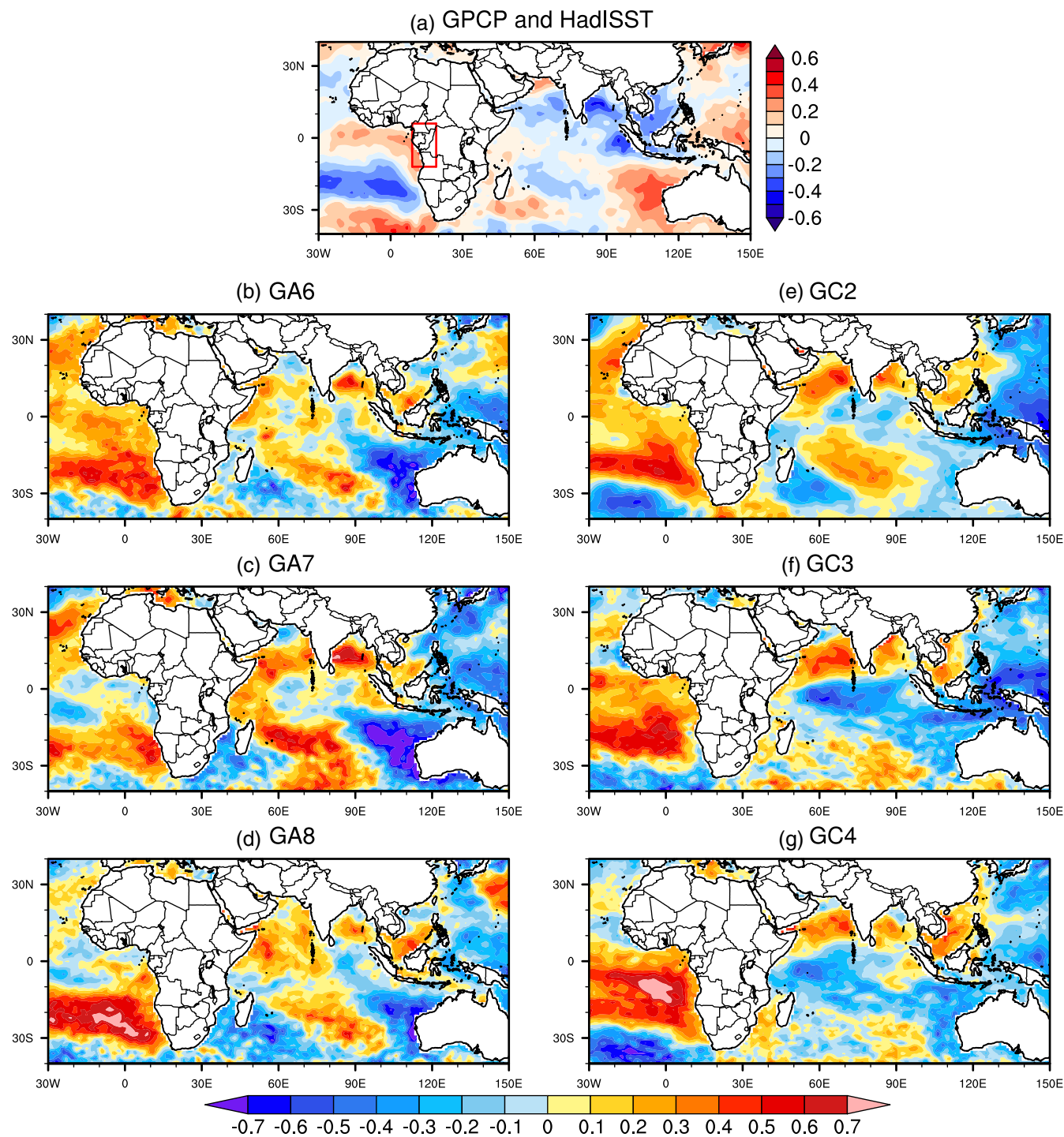


FIGURE 3 (a) Correlations of observed SON rainfall from GPCP, averaged over western Central Africa (the box: 12°S–6°N, 9–19°E), against observed SON SST from HadISST, for the period 1981–2015. (b–g) biases of correlations computed as in (a) for each model with respect to (a). We have used 27 years of GA6 and GA7 and 20 years of GA8 while 35 years of GC2, GC3 and GC4 were used [Colour figure can be viewed at wileyonlinelibrary.com]

(Figure 3a). The eastern (western) CA area over which rainfall is averaged represents the area of the wet (dry) bias.

In general, the models struggle to capture the basic features of the teleconnection such as the areas of positive and negative correlation between CA rainfall and

SST. In Figure 2b–g, between 0 and 30°S, models generally depict a position correlation bias over the Atlantic Ocean, stronger in coupled than in atmospheric models. This shows that the relationship between the eastern CA rainfall and SST over the Atlantic Ocean is stronger in

models than in observations and the strength of the relationship is more pronounced in coupled models. In the Indian Ocean, a dipole pattern of correlation bias is observed with positive and negative biases in the western and eastern Indian Ocean respectively (although the structure is not well observed in GC2). In addition, the western positive (eastern negative) correlation bias extends southeasterly (westward) in the coupled models. The dipole pattern breaks down considerably in GA8 (Figure 2d) and GC4 (Figure 2g) with the spreading of negative correlations biases all over the Indian Ocean basin. This translates to a weak relationship between eastern CA rainfall and SST variation in the latest version of the model and could be attributed to the fact that changes between GA7/GC3 and GA8/GC4 were focused on convection with the ocean remaining unchanged. For the relationship between the simulated western CA rainfall and SST (Figure 3b–g), over the Atlantic Ocean, models depict a positive correlation bias stronger than that in Figure 2b–g showing that the western CA rainfall is more associated with the Atlantic Ocean SST variability than the eastern CA rainfall. Furthermore, this positive correlation bias is stronger in coupled (Figure 3e–g) than in atmosphere-only (Figure 3b–d) formulations. In the Indian Ocean basin, west of Australia a negative correlation bias stronger in AGCM than in CGCM is

observed and extends westward along the equatorial region in all CGCM (Figure 3e–g). In sum, in both AGCMs and CGCMs, the deficiencies in the representation of the shared variability between CA rainfall and SST compared to observation are noticed and CGCMs seem to be not superior to AGCMs in this regard. This suggests biases in simulated mechanisms linking Indian and Atlantic Oceans to CA rainfall in both AGCMs and CGCMs.

4.2 | The tropical large-scale circulation

To investigate possible links between the large-scale circulation and precipitation biases, an overview of the zonal circulation along the equator is shown in Figure 4. It represents the longitude-height cross-section of vertical wind and the streamlines constructed from the divergent component of the zonal wind and the vertical wind averaged between 5°S and 5°N . The Atlantic-Congo zonal overturning cell is found between 5°W and 25°E in reanalyses (Figure 4a,b). The cell is described in Longandjo and Rouault (2019) as being a non-closed cell at the base when we assume that the zonal circulation is not thermally driven by the divergent component of the zonal wind. However, its simulated subsiding branch is more

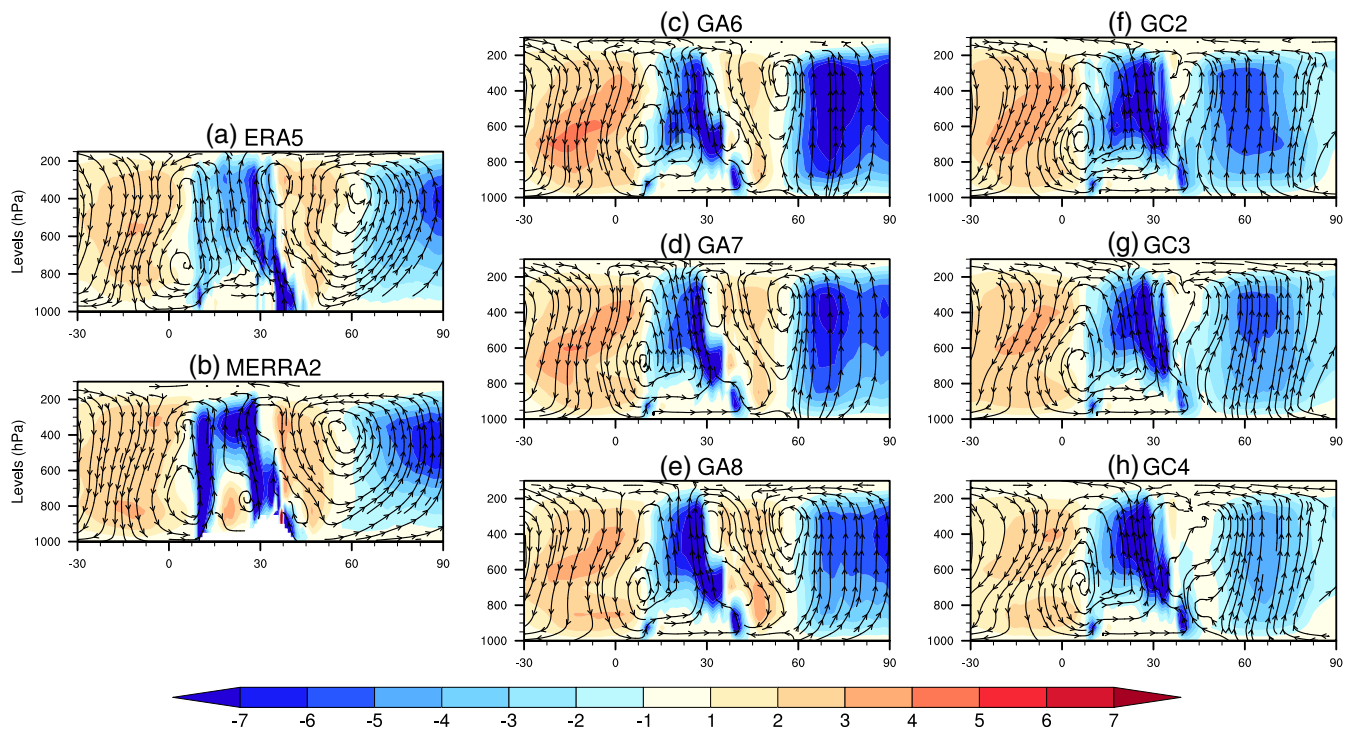


FIGURE 4 Longitude-height cross-section of the September–November mean climatology of vertical wind ($10^{-2} \text{ Pa s}^{-1}$: Shaded) and streamline constructed from the divergent component of the zonal wind (m s^{-1}) and the vertical wind ($10^{-3} \text{ Pa s}^{-1}$) averaged between 5°S and 5°N for (a and b) reanalyses, (c–e) atmosphere-only models and (f–h) coupled models [Colour figure can be viewed at wileyonlinelibrary.com]

intense in the models (Figure 4c–h), particularly in atmospheric versions (Figure 4c–e). Furthermore, the downward branch of the Indian Ocean zonal overturning circulation is almost absent in the three versions of the coupled model (Figure 4f–h). SST biases may help understand this and how rainfall is affected.

The SON climatological SST from HadISST (Figure 5a) and CGCMs SST biases with respect to HadISST (Figure 5e–g) are represented in Figure 5. Given that the AGCMs are prescribed with HadISST, AGCMs SST biases with respect to HadISST are zero and therefore are not represented (Figure 5b–d). Then, it is plausible that the strong subsidence over the Gulf of Guinea (Figure 4) may be attributed to the lack of ocean–atmosphere coupling in the case of the AGCMs. It is also plausible that this response could derive from the anomalously strong upward motion located between 60°E and 90°E over the equatorial Indian Ocean (Figure 4c–h). However, in the coupled models, though the convection over the equatorial Indian Ocean is still pronounced and even more zonally extensive, compared to atmospheric models, a weakening of the subsidence in the Gulf of Guinea is observed (Figure 4f–h). This is associated with the warm SST biases depicted over the Gulf of Guinea (Figure 5e–g). Although the strength of the downward branch is less pronounced in the coupled models than in the atmospheric models, it remains stronger than in the reanalyses. Over the western Indian Ocean, coupled models also depict a warm SST bias inhibiting the subsidence branch of the overturning circulation there.

4.2.1 | The western CA dry bias along the coast

Low-level atmospheric circulation with its associated moisture transport from the Atlantic Ocean is known to be primarily driven by the surface temperature difference between the Atlantic Ocean and the Congo basin landmass (Pokam *et al.*, 2014). In this section, in addition to the surface temperature difference, we explore the contribution of the anomalously strong simulated subsidence over the Gulf of Guinea (Figure 4) on low-level moisture transport off the Atlantic Ocean to CA to understand the western CA dry bias.

Figure 6 shows the September–November climatological 850 hPa geopotential height (shaded) and moisture transport (vectors) from reanalyses (Figure 6a,b) and the models' biases with respect to MERRA2 (Figure 6c–h). In reanalyses (Figure 6a,b) and around the equator (between 5°S and 5°N), the geopotential height decreases progressively eastward from the Atlantic Ocean (Gulf of Guinea) to the continent. This shows a contrast of surface pressure between the ocean and the continent with high

(low) pressure over the ocean (continent) bound up with the sinking (rising) branch of the Atlantic-Congo zonal overturning cell. The simulated 850 hPa geopotential height biases (Figure 6c–h) show differences in the models with GA6, GC2 and GC3 depicting in general negative biases while GA7, GA8 and GC4 depict positive biases. However, despite the differences, in all versions and formulations of the model, the zonal transect of surface pressure exhibits a decrease from the Atlantic Ocean to the continent, stronger in models than in the reanalyses (Figure 7a). This is particularly well observed in GA7 (Figure 6d), GA8 (Figure 6e) and GC4 (Figure 6h) with a higher pressure bias over the ocean and a lower pressure bias over the continent related to the strong simulated sinking branch of the Atlantic-Congo zonal overturning cell (Figure 4). In addition, the stronger simulated land-ocean thermal difference between the Central African landmass and the coastal Atlantic Ocean (Figure 7b) is in agreement with the simulated strength of the zonal surface pressure decrease from the Atlantic Ocean to the continent (Figure 7a). This has an impact on low-level moisture transport.

In reanalyses and over the Atlantic Ocean (Figure 6a,b), moisture transport is predominantly easterly and northeasterly north of the equator and southeasterly south of the equator. However, the strength of the subsidence branch of the Atlantic-Congo zonal overturning cell in the models (Figure 4c–h) is associated with higher pressure over the Gulf of Guinea (Figure 6c–h). This enhances the pressure gradient between the Atlantic Ocean and the Coastal area which increases moisture transport as indicated by the westerly and southwesterly biases over southern West Africa and along the coastal region of CA (Figure 6c–h). The strong moisture transport in the models results in the dry bias at the western CA coast. Therefore, the stronger dry bias in atmospheric models over western CA as compared to coupled models is associated with the more pronounced overestimated subsidence over the Gulf of Guinea. Furthermore, although in the most recent version of both coupled and atmospheric models (GC4/GA8) the strength of the downward branch of the Atlantic-Congo zonal overturning circulation is still overestimated with respect to ERA5, an improvement in the strength is observed compared to older versions (Figure 4). Its weakening in GC4/GA8 is in agreement with the reduced dry bias over western CA compared to older versions (GC2/GA6, GC3/GA7).

4.2.2 | The eastern CA wet bias

Simulated large-scale circulations over both the Atlantic Ocean and the Indian ocean may contribute to the overestimation of rainfall over the eastern CA in the models. In terms of the contribution from the Atlantic Ocean, as

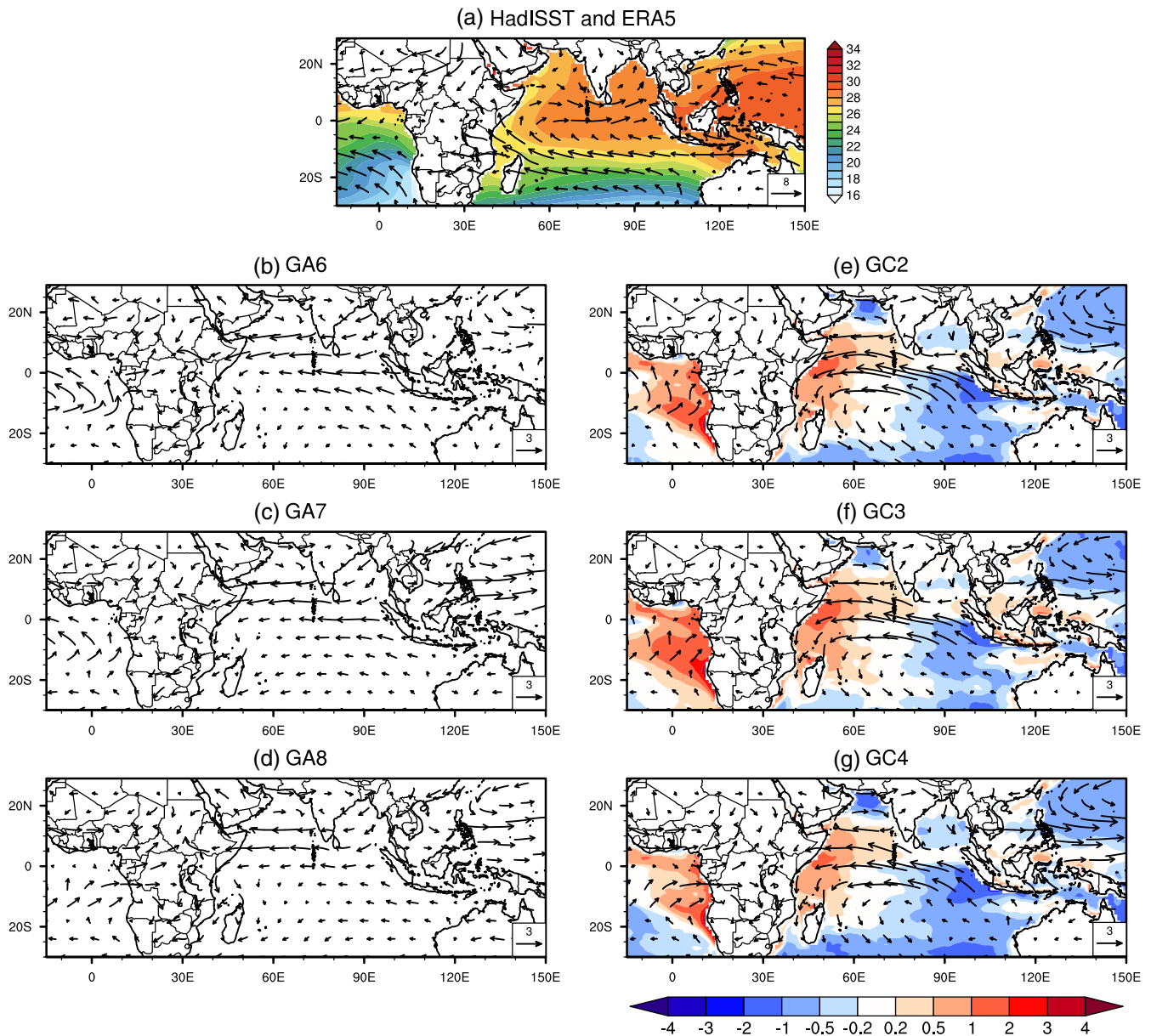


FIGURE 5 September–November climatology of (a) absolute values of SST ($^{\circ}\text{C}$: Shaded) from HadISST and 850 hPa wind (m s^{-1} : Vectors) from ERA5; (b–d) AGCMs 850 hPa wind (m s^{-1} : Vectors) biases with respect to ERA5; (e–g) CGCMs SST ($^{\circ}\text{C}$: Shaded) and 850 hPa wind (m s^{-1} : Vectors) biases with respect to HadISST and ERA5 respectively [Colour figure can be viewed at wileyonlinelibrary.com]

shown in the previous sections, the strength of the simulated subsidence over the Gulf of Guinea is overestimated (Figure 4) and associated with a high ocean–land pressure gradient which strengthens the moisture transport from the Atlantic Ocean to CA (Figure 6). The strength of the moisture transport is then sufficiently strong to dry out the coast and wet the eastern CA. Moisture entering through the western boundary of the CA region is then overestimated in both coupled and atmospheric models. In addition, in all versions of the coupled model, warmer SST in the Gulf of Guinea (Figure 5e–g) is likely to enhance evaporation and therefore, more moisture is

available to be advected toward eastern CA. This can explain why eastern CA is wetter in coupled models than in atmospheric models.

To understand the misrepresentation of the Indian Ocean large-scale circulation (Figure 4) and how this could affect CA rainfall, mean SON SST and low-level (850 hPa) wind are explored over the Indian Ocean in Figure 5. Maximum SST are found over the equatorial Indian Ocean (Figure 5a) with warmer SST in the eastern sector of the ocean compared to the western sector. This leads to a prevalence of westerly winds which form the lower branch of the Indian Ocean zonal overturning

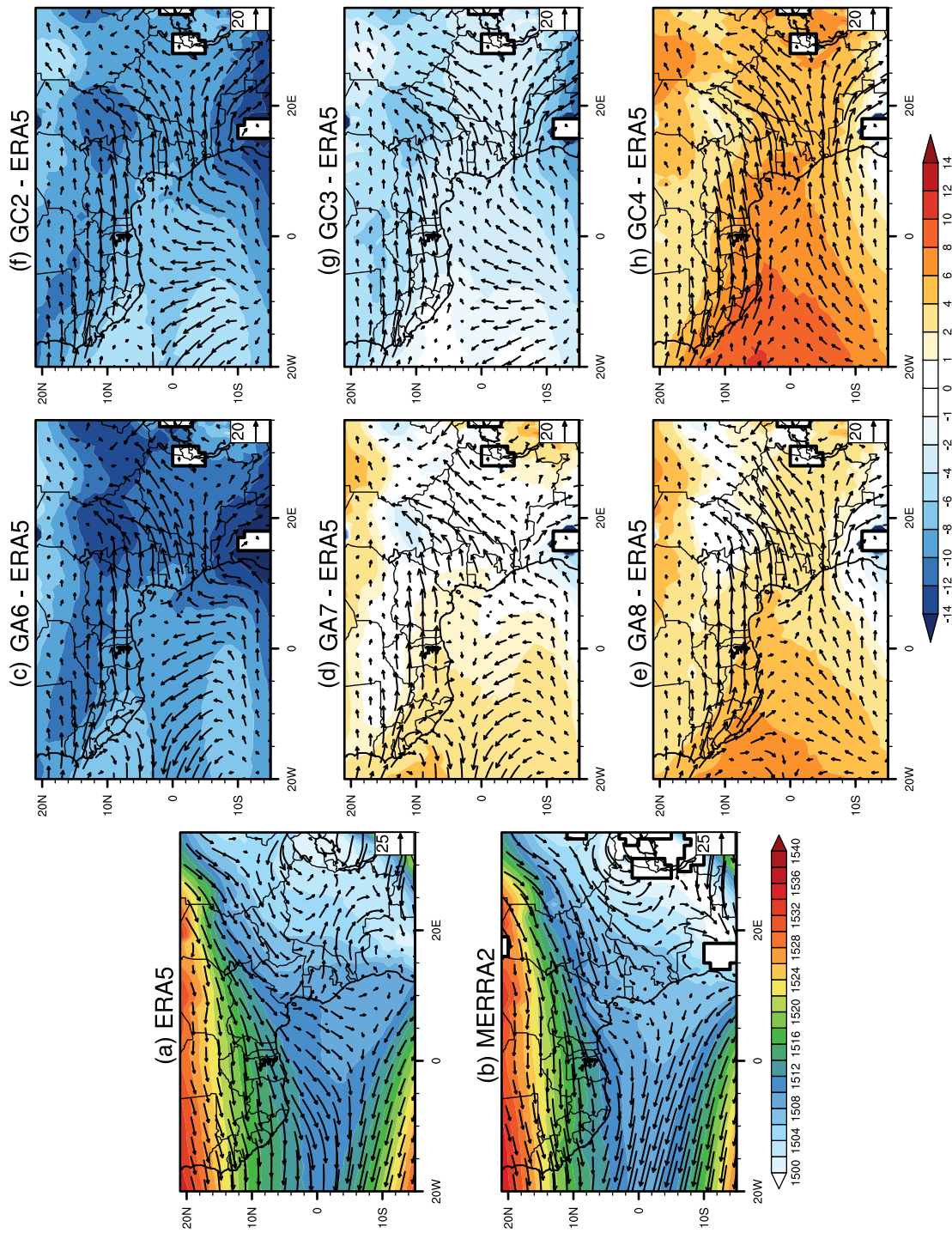


FIGURE 6 September–November climatological 850 hPa geopotential height (m: Shaded) and moisture transport ($\text{g kg}^{-1} \text{m s}^{-1}$; Vectors). (a and b) Absolute values of ERA5 and MERRA2 respectively. (c–h) Models geopotential height and moisture transport with respect to ERA5 [Colour figure can be viewed at wileyonlinelibrary.com]

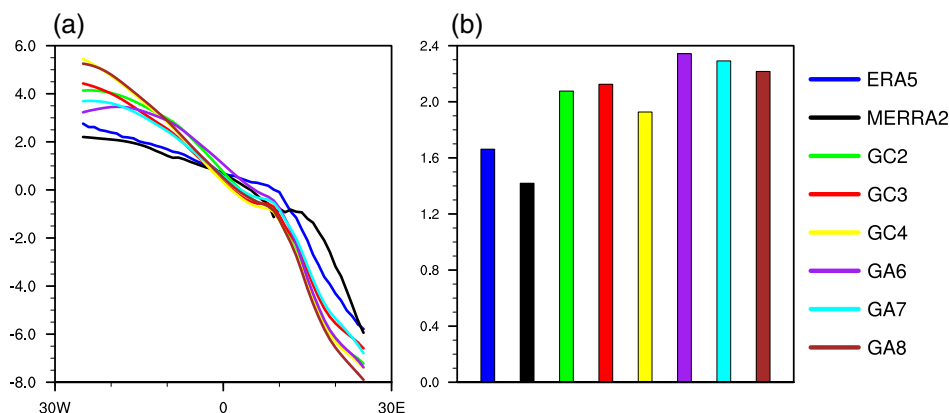


FIGURE 7 a) September–November meridional average (5°S – 5°N) of 850 hPa geopotential height (m) minus spatial mean (5°S – 5°N ; 25°W – 25°E) of 850 hPa geopotential height for reanalyses, coupled and atmosphereonly models. (b) 850 hPa land-ocean thermal difference between the Central African landmass (5°S – 5°N ; 15° – 29°E) and the coastal Atlantic Ocean (5°S – 5°N ; 5°W – 5°E) for reanalyses, coupled and atmosphere-only models [Colour figure can be viewed at wileyonlinelibrary.com]

circulation (Figure 5a). With regard to the coupled models, they depict a mean SST bias in the Indian Ocean with the pattern of the positive IOD with a warm (cold) bias over the western (southeastern) Indian Ocean (Figure 5e–g). This is similar to the findings from Hirons and Turner (2018). In agreement with the dipole pattern of correlation over the Indian Ocean (Figure 2b–g), the simulated 850 hPa equatorial winds in the Indian Ocean exhibit easterly anomalies which are more pronounced in CGCMs than in AGCMs (Figure 5b–g). The easterly anomalies result in weaker westerly winds in AGCM and anomalous easterly winds in CGCM (not shown here). Therefore, the easterly anomalies present in the atmospheric models are intensified in the coupled models due to the positive IOD pattern in the mean state of their SST biases (Figure 5e–g). Indeed, in the coupled models, the positive IOD pattern weakens the downward branch of the Indian Ocean East–West overturning circulation (Figure 4) and strengthens the existing easterly anomalies at the surface (Figure 5). The easterly anomalies are likely to be associated with an anomalous moisture advection from the Indian Ocean to the continent.

To assess the effect of the positive IOD-like pattern on the advected moisture from the Indian Ocean, an examination of the strongest positive IOD years compared to the mean state in both the reanalyses and the models is performed. A composite of years with the strongest positive IOD pattern is constructed following Hirons and Turner (2018). For each dataset, the IOD index is calculated for each year in the SON season and years are ranked from the lowest to the highest value of their IOD index. The top 20% of years is then chosen to build the composite and the number of years in the composite depends on the length of each data. Therefore, 7 years are used for the composite in the reanalyses and the

coupled models, 5 in GA6 and GA7 and 4 in GA8. The SON climatological mean of the vertical integrated zonal moisture flux (shading) and total moisture flux (vectors) is subtracted from the mean of the years corresponding to the composite to form the composite anomaly which is represented in Figure 8 for each dataset. The two reanalyses agree with an inflow of moisture through the eastern boundary of the CA region (Figure 8a,b). In agreement with findings from Moihamette *et al.*, 2022, this highlights the fact that during positive IOD years, easterly winds advect more moisture from the Indian Ocean to CA and contribute to rainfall in the region. Although the moisture is drawn from a much broader area across the IO basin in the reanalyses (Figure 8a,b) compared with a narrower channel of moisture in the models (Figure 8c–h), the inflow of moisture from the Indian Ocean at the eastern boundary of the rectangular box is stronger and extends further west in models. The westward extension is more pronounced in the coupled than in the atmosphere-only models (Figure 8c–h). In the atmosphere-only models, the mean state easterly winds anomalies (Figure 5b–d) is added to the easterly wind due to a positive IOD pattern in the composite to advect more moisture from the Indian Ocean to the CA region as shown in Figure 8c–e. In the coupled models, the anomalous mean state easterly winds from the atmosphere-only models are reinforced by the positive IOD pattern in the mean state SST biases (Figure 5e–g). This is added to the easterlies of the positive IOD years to advect more moisture from the Indian Ocean to the CA region (Figure 8f–h) compared to the atmosphere-only models. As a result in the MetUM models, biases in large-scale circulation over the Indian Ocean contribute to the wet conditions over eastern CA, in line with the spatial distribution of simulated rainfall biases (Figure 1i–k).

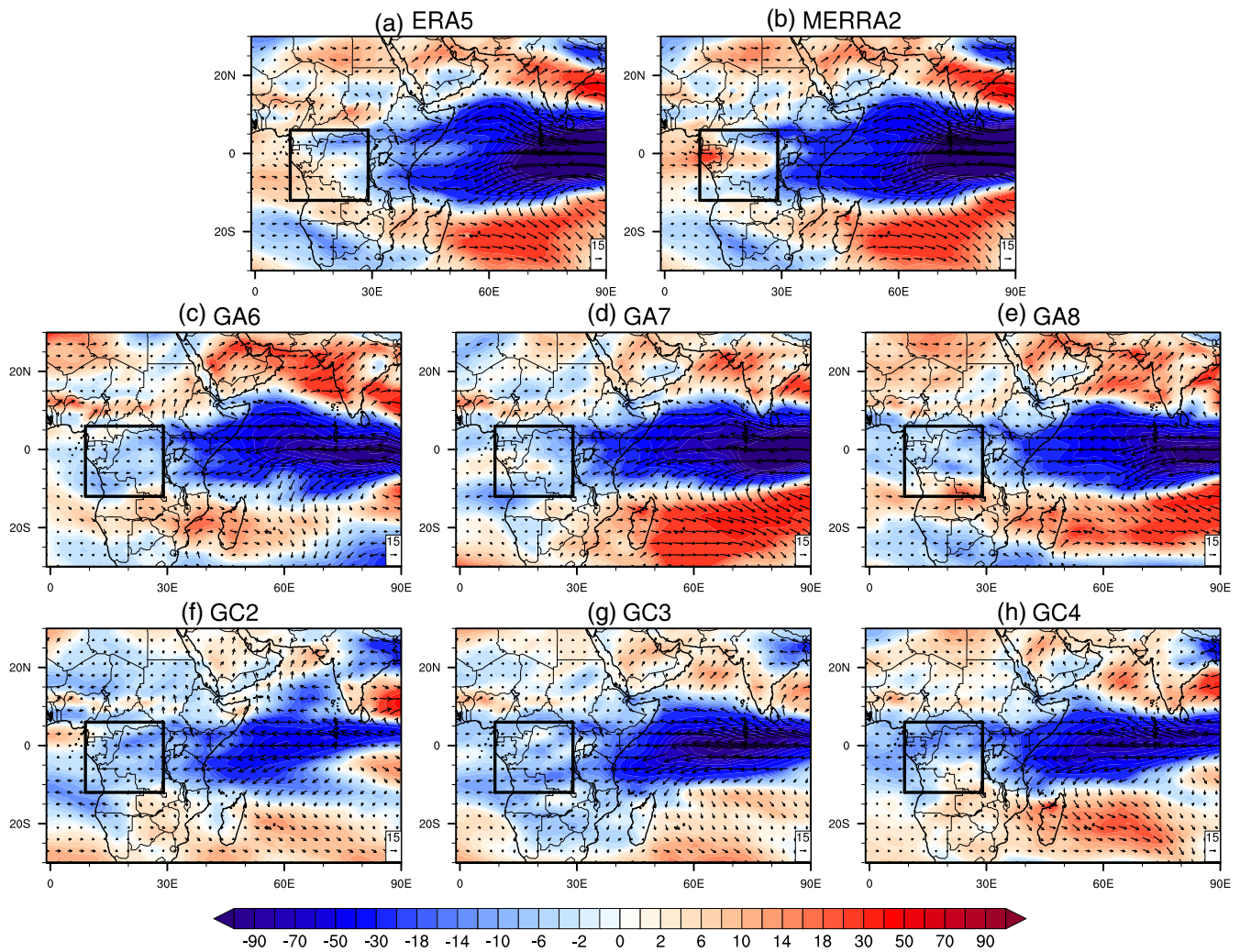


FIGURE 8 Composite anomaly of SON vertical integrated (1,000–100 hPa) zonal moisture transport ($\text{kg m}^{-1} \text{s}^{-1}$; Shading) and total moisture transport ($\text{kg m}^{-1} \text{s}^{-1}$; Vectors) for positive IOD years. The strongest positive IOD years minus the mean state in (a and b) each reanalysis, (c–e) atmosphere-only models and (f–h) coupled models. The box in (a–h) indicates the Central Africa domain used in this study [Colour figure can be viewed at wileyonlinelibrary.com]

These results show that large-scale circulations from both the Atlantic and the Indian Oceans have a role in the overestimation of the simulated rainfall over eastern CA. However, simulated key regional features may also contribute to overestimating or underestimating simulated rainfall over the region.

5 | UNDERSTANDING THE MODELS' BIASES: A REGIONAL APPROACH

Past studies (Nicholson and Grist, 2003; Jackson *et al.*, 2009; Dezfuli and Nicholson, 2013; Kuete *et al.*, 2019; Longandjo and Rouault, 2019) have shown that there are dominant features of the local circulation such as the two components of the African Easterly Jet (AEJ-S and AEJ-N)

and the Congo basin cell that play an important role in rainfall variability over CA. In this section, these features are investigated in association with the wet and dry biases over eastern and western CA respectively.

5.1 | The western CA dry bias along the coast

Longandjo and Rouault (2019) highlights the existence of a lower tropospheric, closed, counterclockwise and shallow zonal overturning cell over CA namely the Congo basin cell discernible throughout the year. The Congo basin cell intensity and width are driven by the near-surface temperature warming on both the central African landmass and the eastern equatorial Atlantic, leading to LLWs which form the lower branch of the cell. Therefore,

the width of the cell is linked to the strength of LLWs. The stronger the LLWs, the larger the Congo basin cell.

Figure 9 shows the zonal mass-weighted stream function with the zonal wind averaged over the latitudinal band 5°N – 5°S before computing the zonal mass-weighted stream function. Negative values of the mass-weighted stream function (dashed red contours) depict the Congo basin cell. It appears that the models overestimate the intensity and the width of the cell (Figure 9c–h) with the western edge of the cell located farther west in the models

compared to reanalyses. Simulated LLWs transport moist air from a farther west position in the equatorial Atlantic (Figure 6c–h) in agreement with the farther west position of the western edge of the Congo basin cell (Figure 9c–h). Furthermore, the overestimated strength of the simulated Congo basin cell in the models is associated with strong simulated LLWs (Figure 6) over the Atlantic coastal area due to the strong ocean-land pressure contrast (Figure 7). As shown in Section 4.2.1, this induces a strong moisture divergence at the coastal area and, in turn, dry conditions.

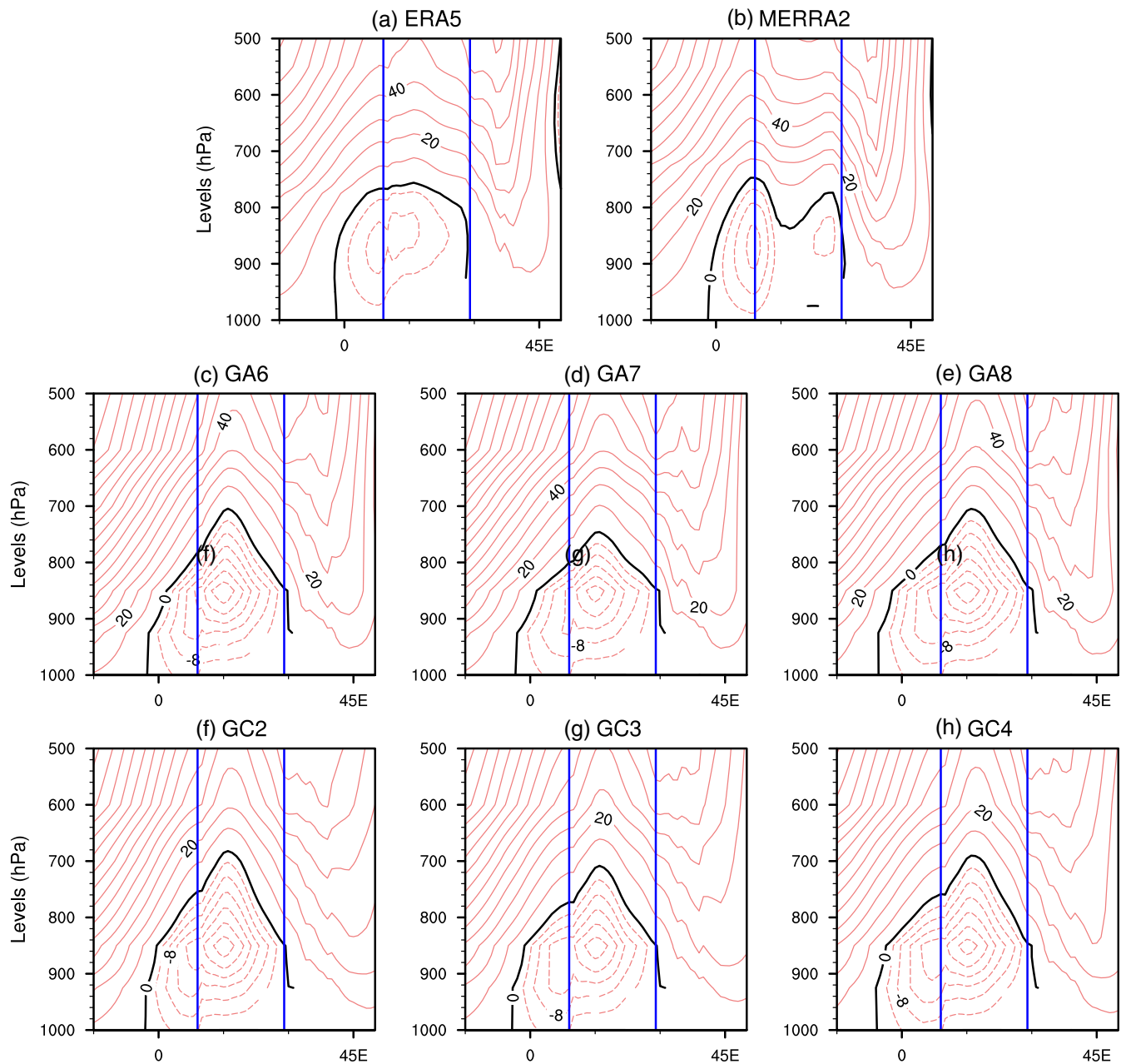


FIGURE 9 September–November climatological mean of the zonal mass-weighted stream function (contours: $10^{11} \text{ kg s}^{-1}$) computed with 5°S – 5°N averaged zonal wind for (a and b) ERA5 and MERRA2, (c–e) Atmosphereonly models (GA6, GA7 and GA8), and (f–h) coupled models (GC2, GC3 and GC4). Solid and dashed contours represent positive and negative values of mass-weighted stream functions respectively, separated with the zero value of mass-weighted stream (thicker contour). Contour intervals are 10 between positive contours and 4 between negative contours. The vertical lines are the zonal boundaries of the Central Africa region [Colour figure can be viewed at wileyonlinelibrary.com]

The misrepresentation in the intensity and width of the simulated Congo basin cell is therefore associated with the western CA dry bias through the overestimation of the simulated LLWs. The dryness of MetUM over the coastal region in CA is well known (Creese and Washington, 2016; James *et al.*, 2018) and the present study underlines the persistence of this bias, although slightly reduced in recent versions of the model.

5.2 | The eastern CA wet bias

The misrepresentation of the Congo basin cell (Figure 9c–h) is also associated with the eastern CA wet bias. Known to play an important role in rainfall redistribution

over CA via the zonal rainfall maximum position (Longandjo and Rouault, 2019), the width and the intensity of the Congo basin cell are respectively associated with the zonal position and the strength of the eastern CA rainfall peak (Longandjo and Rouault, 2019). Therefore, the overestimation in its simulated width and intensity (Figure 9c–h) is related to a larger advection of moisture from the farther west position in the equatorial Atlantic toward the eastern edge of the cell. This leads to a strong moisture convergence at the eastern edge of the cell and since this is the location of its rising branch, more convection and more rainfall are observed in comparison with the reanalyses. In addition, the depth of the cell appears to be higher in models. This is associated with the depth of the convection and the latter influences

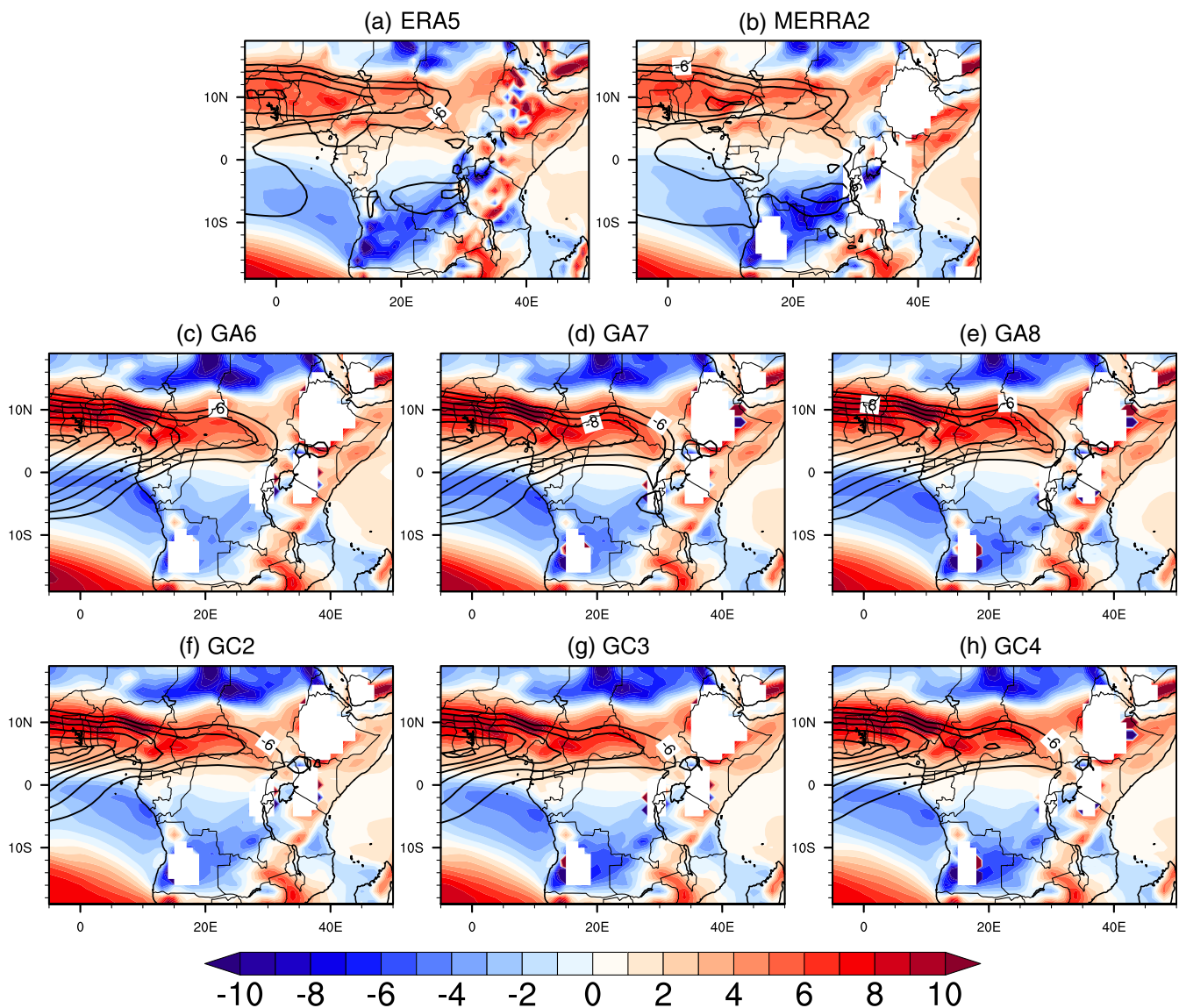


FIGURE 10 September–November long-term mean meridional potential temperature gradient (10^{-6} K m^{-1} ; shaded) at 850 hPa and zonal easterly wind averaged between 700 and 600 hPa with speed $\geq 6 \text{ m s}^{-1}$ (contours) for (a and b) each reanalysis, (c–e) atmosphere-only models and (f–h) coupled models [Colour figure can be viewed at wileyonlinelibrary.com]

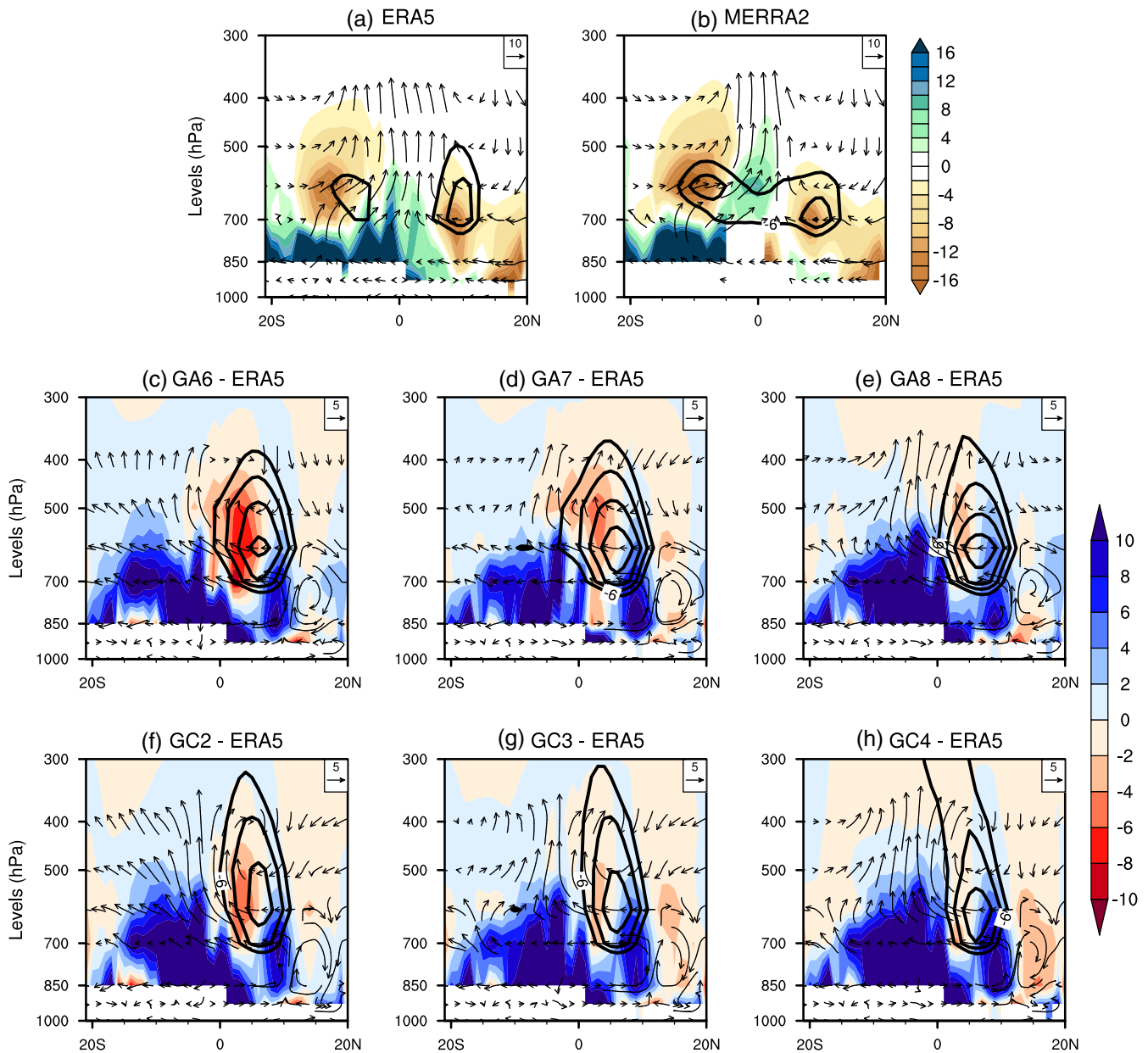


FIGURE 11 Latitude-height cross-section of September–November long term mean of (a and b) net zonal moisture flux (shaded: $\text{kg m}^{-1} \text{s}^{-1}$) calculated from west boundary (19°E) minus east boundary (29°E) and vertical wind (vectors: $4.10^{-2} \text{ Pa s}^{-1}$) averaged between 19 and 29°E in reanalyses. (c–h) Same as in (a and b) minus ERA5 for atmosphere-only (c–e) and coupled (f–h) models. Solid contours (a–h) represent AEJ components (U m s^{-1}) at 19°E in reanalyses, atmosphere-only and coupled models. 19 – 29°E is the zonal extent of the wet bias in models [Colour figure can be viewed at wileyonlinelibrary.com]

the biases. The height of the cell in models is therefore also associated with the wet bias.

Next, we analyse the contribution of the AEJ components to the eastern CA wet bias. Known as the mid-tropospheric (700–600 hPa) easterly wind (with a speed equal to or greater than 6 m s^{-1} (Nicholson and Grist, 2003; Kuete *et al.*, 2019), the AEJ-N and AEJ-S are key regional circulation features over CA during the SON season. Previous studies have established that CA rainfall is strongly related to the advected moisture into the region

with AEJ components playing an important role in controlling the mid-level moisture flux convergence (Nicholson and Grist, 2003; Jackson *et al.*, 2009; Washington *et al.*, 2013). Furthermore, Jackson *et al.* (2009) have identified a maximum in MCS activity in the region of that strong mid-level convergence.

Setting up by the surface temperature contrast between Congo and both Saharan (Cook, 1999) and Kalahari drylands (Kuete *et al.*, 2019), we first investigate the link between the AEJ components and the mechanisms

associated with their setup. Figure 10 shows AEJ components and the meridional potential temperature gradient at 850 hPa in both reanalyses and models. Although significant discrepancies could have been expected between different reanalysis products due to the paucity of upper-air observations in that region, it appears that the two reanalyses agree relatively well in the representation of the two AEJ's components (Figure 10a,b). Furthermore, the AEJ-N (AEJ-S) is associated with a strong positive (negative) meridional potential temperature gradient centred at around 10° N (10° S). Compared to reanalyses and according to the threshold of 6 m s^{-1} , the intensity and the extent of the AEJ-N are both overestimated in the models (Figure 10c–h) and much more in the atmosphere-only formulation (Figure 10c–e) while its southern component is not detected in the two formulations of the model whatever the version (Figure 10c–h). This reflects an underestimation of the easterly wind in the region where the AEJ-S is supposed to be found. Errors in the simulated AEJ components are associated with a misrepresentation of the meridional potential temperature gradient. Compared to reanalyses, the overestimation (absence) of the AEJ-N (AEJ-S) is associated with a stronger (weaker) positive (negative) meridional potential temperature gradient centred at around 10° N (10° S). Therefore, the fact that the strength of both AEJ-N and AEJ-S biases are of the same magnitude in all versions of MetUM suggest that changes in land surface schemes across model versions have not significantly improved surface characteristics (e.g., temperature and soil moisture) contrast between Congo and both Saharan and Kalahari drylands.

To investigate how the wrong representation of the AEJ components contribute to the simulated wet bias over eastern CA, the jets are represented (contours) in Figure 11 with the vertical wind (vectors) and the net zonal moisture transport, computed as the difference between moisture flux across the western (19° E) and the eastern (29° E) boundary of the zonal extension of the wet bias. Positive values indicate moisture flux convergence and negative values moisture flux divergence. It appears in reanalyses (Figure 11a,b) that at mid-troposphere, jet components found at around 10° S and 10° E are associated with moisture flux divergence. This leads to moisture flux convergence and strong convection around the equator. In models (Figure 11c–h), the misrepresentation in the intensities of the AEJ's components is associated with biases in the net zonal moisture flux and convection. The overestimation (absence) of the AEJ-N (AEJ-S) is associated with a stronger mid-tropospheric net moisture flux divergence (convergence) favouring dry (wet) conditions. This is in line with Dezfuli and Nicholson (2013) who showed that, at interannual time scales, the variability of the strength of AEJ's components is opposed to that

of the rainfall amount with abnormally strong (weak) jets associated with dry (wet) years. Then AEJ's components have opposite effects in the MetUM models. The overestimated AEJ-N strength tends to suppress convection while the absence of AEJ-S favours convection and in turn precipitation. These findings are similar to those of Creese and Washington (2018). Furthermore, biases in the strength of the AEJ's components shift the mid-tropospheric moisture flux convergence southward favouring more convection south of the equator (Figure 11c–h). This is in agreement with the wet bias which is more widespread south of the equator in the region (Figure 1f–k). In addition, the reason why the coupled models are wetter than their corresponding atmospheric formulations could be due to the strength of their AEJ-N which is less strong than in atmospheric models. This is associated with less mid-tropospheric moisture flux divergence. Comparing the versions of the coupled (atmospheric) model with each other, it appears that, in the most recent version GC4 (GA8), the mid-tropospheric moisture flux divergence associated with the AEJ-N is less pronounced compared to earlier model versions (Figure 11e,h). This may explain why they are wetter than previous model versions.

6 | SUMMARY AND CONCLUSIONS

This study investigates processes leading to precipitation biases over CA in different versions of the MetUM model (atmosphere–ocean coupled and atmosphere-only formulations) during the main rainy season (September–November: SON). In all versions and formulations, the models depict a dipole bias over the region with a wet bias at the eastern CA and a dry bias over the coastal western CA (Figure 1f–k). The wet (dry) bias is stronger in the coupled (atmospheric) models and the exploration of remote and local climate processes is conducted to understand the models' biases.

At a large scale, differences between CGCM and AGCM are mainly due to the differences in SST which lead to bias in large-scale circulation and rainfall. Over the coastal western CA, the dry bias in the models is linked to the misrepresentation of the Atlantic-Congo zonal overturning cell with its overestimated sinking branch. This is associated with an increase in ocean-land pressure gradient between the equatorial eastern Atlantic Ocean (high pressure) and the Congo Basin (low pressure). The low-level zonal moisture flux is therefore so strong as to dry the coastal region. The coupled models are less dry in that region compared to the atmosphere-only models because over the Gulf of Guinea, a warm SST bias is simulated in the coupled models and enhances

evaporation that reduces the dry bias. Compared to older versions, the dry bias is reduced in the latest version of both coupled and atmospheric formulations of the model. This is linked to the weakening of the subsidence branch of the Atlantic-Congo zonal overturning cell. Over eastern CA, large-scale circulation from both the Atlantic and the Indian Oceans play a role in the eastern CA wet bias. From the Atlantic Ocean, the same large-scale circulation leading to a dry bias over the coastal western CA also contributes to enhanced rainfall over eastern CA. As the strength of low-level zonal moisture flux is overestimated, moisture from the Atlantic Ocean is advected further in the continent and contributes to enhanced rainfall over eastern CA. On the other hand, the subsidence branch of the Indian Ocean zonal overturning circulation is weakened by the anomalous mean state low-level easterly winds which are added to the Indian Ocean easterly winds during IOD years to increase the inflow of moisture from the Indian Ocean.

At the regional scale, the overestimated strength of the simulated Congo basin cell is associated with the western CA dry bias through the overestimation of the simulated LLWs. For the eastern CA wet bias, simulated AEJ components have opposite actions in the models. Due to a misrepresentation in the land-surface temperature, overestimated strength of the AEJ-N tends to suppress convection in the models while an underestimation of the AEJ-S intensity favours convection. Biases in the strength of the AEJ's components shift the mid-tropospheric moisture flux convergence southward favouring more convection south of the equator. In terms of differences between model versions, the mid-tropospheric moisture flux divergence associated with the AEJ-N is less pronounced in the latest model version. This explains why the latest version is wetter than the previous ones. Enhanced rainfall in eastern CA is also linked to the misrepresentation of the Congo basin cell. The overestimation in the simulated width and intensity of the cell is associated with a strong low-level moisture convergence over eastern CA which contributes to more precipitation.

Let us note that, the same biases pattern in the MetUM model were also reported on earlier versions of the model in James *et al.*, 2018 and Hirons and Turne, 2018. Besides this, a similar west-east dipole pattern of rainfall biases over CA are highlighted in CMIP5 (Creese and Washington, 2018) and CORDEX models (Tamoffo *et al.*, 2021) although the signs of the dipole are opposite in the MetUM model. This translates the fact that rainfall in these two subregions of CA is governed by different climate processes and models generally struggle to capture the corresponding features. In the MetUM model, although some differences exist between model versions, the present study has highlighted the persistent atmospheric circulation

errors which lead to persistence in rainfall biases between different versions of the MetUM climate model over CA. Results from this work give direction to model developers to address those biases in the next versions of the model. This include among other things the improvement of the shared variability between rainfall over CA and SST and the revision of the land surface schemes across model versions to improved surface characteristics (e.g., temperature and soil moisture) contrast between Congo and both Saharan and Kalahari drylands.


ACKNOWLEDGEMENTS

This work has been partly supported by the Natural Environment Research Council (NERC)-Department for International Development (DFID)-funded Improving Model Processes for African Climate (IMPALA) project (Grant NE/M017206/1) and UMFULA (Grant NE/M020207/1), as part of the Future Climate for Africa (FCFA) program. The authors would like to acknowledge the UK Met Office and all the reanalyses data providers for making available all data used in this study. The helpful input of Rachel James, Neil Hart, Vondou Derbetini, Giresse Kuete and Alain Tamoffo was also really appreciated. The authors thank the two anonymous reviewers and the editor whose comments helped improve and clarify this manuscript.

AUTHOR CONTRIBUTIONS

Thierry N. Taguela: Conceptualization; formal analysis; investigation; methodology; software; validation; writing – original draft; writing – review and editing. **Wilfried M. Pokam:** Methodology; project administration; resources; supervision; validation; writing – original draft; writing – review and editing. **Richard Washington:** Conceptualization; funding acquisition; methodology; project administration; supervision; validation; writing – review and editing.

ORCID

Thierry N. Taguela  <https://orcid.org/0000-0001-8140-125X>

Wilfried M. Pokam  <https://orcid.org/0000-0002-1993-5098>

Richard Washington  <https://orcid.org/0000-0003-2521-4614>

REFERENCES

- Almazroui, M., Saeed, F., Saeed, S., Islam, M.N., Ismail, M., Klutse, N.A. and Siddiqui, M.H. (2020) Projected change in temperature and precipitation over Africa from CMIP6. *Earth Systems and Environment*, 4(3), 455–475. <https://doi.org/10.1007/s41748-020-00161-x>.
- Aloysius, N.R., Sheffield, J., Saiers, J.E., Li, H. and Wood, E.F. (2016) Evaluation of historical and future simulations of

- precipitation and temperature in Central Africa from CMIP5 climate models. *Journal of Geophysical Research: Atmospheres*, 121(1), 130–152. <https://doi.org/10.1002/2015jd023656>.
- Balas, N., Nicholson, S.E. and Klotter, D. (2007) The relationship of rainfall variability in west Central Africa to sea-surface temperature fluctuations. *International Journal of Climatology*, 27(10), 1335–1349. <https://doi.org/10.1002/joc.1456>.
- Cook, K.H. (1999) Generation of the African easterly jet and its role in determining west African precipitation. *Journal of Climate*, 12(5), 1165–1184. [https://doi.org/10.1175/1520-0442\(1999\)0122.0.co;2](https://doi.org/10.1175/1520-0442(1999)0122.0.co;2).
- Cook, K.H. and Vizi, E.K. (2015) The Congo Basin Walker circulation: dynamics and connections to precipitation. *Climate Dynamics*, 47(3–4), 697–717. <https://doi.org/10.1007/s00382-015-2864-y>.
- Creese, A. and Washington, R. (2016) Using qlflux to constrain modeled Congo Basin rainfall in the CMIP5 ensemble. *Journal of Geophysical Research: Atmospheres*, 121(22), 13,415–13,442. <https://doi.org/10.1002/2016jd025596>.
- Creese, A. and Washington, R. (2018) A process-based assessment of CMIP5 rainfall in The Congo Basin: the September–November rainy season. *Journal of Climate*, 31(18), 7417–7439. <https://doi.org/10.1175/jcli-d-17-0818.1>.
- Dezfuli, A.K. and Nicholson, S.E. (2013) The relationship of rainfall variability in Western equatorial Africa to the tropical oceans and atmospheric circulation. Part II: the boreal autumn. *Journal of Climate*, 26(1), 66–84. <https://doi.org/10.1175/jcli-d-11-00686.1>.
- Dezfuli, A.K., Zaitchik, B.F. and Gnanadesikan, A. (2015) Regional atmospheric circulation and rainfall variability in south equatorial Africa. *Journal of Climate*, 28(2), 809–818. <https://doi.org/10.1175/jcli-d-14-00333.1>.
- Dommo, A., Philippon, N., Vondou, D.A., Sèze, G. and Eastman, R. (2018) The June–September low cloud cover in Western Central Africa: mean spatial distribution and diurnal evolution, and associated atmospheric dynamics. *Journal of Climate*, 31(23), 9585–9603. <https://doi.org/10.1175/jcli-d-17-0082.1>.
- Dyer, E.L., Jones, D.B., Nusbaumer, J., Li, H., Collins, O., Vettoretti, G. and Noone, D. (2017) Congo Basin precipitation: assessing seasonality, regional interactions, and sources of moisture. *Journal of Geophysical Research: Atmospheres*, 122(13), 6882–6898. <https://doi.org/10.1002/2016jd026240>.
- Fotso-Nguemo, T.C., Chamani, R., Yepdo, Z.D., Sonkoué, D., Matsaguim, C.N., Vondou, D.A. and Tanessong, R.S. (2018) Projected trends of extreme rainfall events from CMIP5 models over Central Africa. *Atmospheric Science Letters*, 19(2), 1–8. <https://doi.org/10.1002/asl.803>.
- Funk, C., Peterson, P., Landsfeld, M., Pedreros, D., Verdin, J., Shukla, S., Husak, G., Rowland, J., Harrison, L., Hoell, A. and Michaelsen, J. (2015) The climate hazards infrared precipitation with stations—a new environmental record for monitoring extremes. *Scientific Data*, 2(1), 150066. <https://doi.org/10.1038/sdata.2015.66>.
- Gelaro, R., McCarty, W., Suárez, M.J., Todling, R., Molod, A., Takacs, L., Randles, C., Darmenov, A., Bosilovich, M.G., Reichle, R., Wargan, K., Coy, L., Cullather, R., Draper, C., Akella, S., Buchard, V., Conaty, A., da Silva, A., Gu, W., Kim, G.K., Koster, R., Lucchesi, R., Merkova, D., Nielsen, J.E., Partyka, G., Pawson, S., Putman, W., Rienecker, M., Schubert, S.D., Sienkiewicz, M. and Zhao, B. (2017) The modern-era retrospective analysis for research and applications, version 2 (MERRA-2). *Journal of Climate*, 30(14), 5419–5454. <https://doi.org/10.1175/jcli-d-16-0758.1>.
- Haensler, A., Saeed, F. and Jacob, D. (2013) Assessing the robustness of projected precipitation changes over Central Africa on the basis of a multitude of global and regional climate projections. *Climatic Change*, 121(2), 349–363. <https://doi.org/10.1007/s10584-013-0863-8>.
- Hartman, A.T. (2021) Tracking mesoscale convective systems in central equatorial Africa. *International Journal of Climatology*, 41(1), 469–482. <https://doi.org/10.1002/joc.6632>.
- Hersbach, H., Bell, B., Berrisford, P., Hirahara, S., Horányi, A., Muñoz-Sabater, J., Nicolas, J., Peubey, C., Radu, R., Schepers, D., Simmons, A., Soci, C., Abdalla, S., Abellan, X., Balsamo, G., Bechtold, P., Biavati, G., Bidlot, J., Bonavita, M., Chiara, G., Dahlgren, P., Dee, D., Diamantakis, M., Dragani, R., Flemming, J., Forbes, R., Fuentes, M., Geer, A., Haimberger, L., Healy, S., Hogan, R.J., Hólm, E., Janisková, M., Keeley, S., Laloyaux, P., Lopez, P., Lupu, Cristina, Radnoti, G., Rosnay, P., Rozum, I., Vamborg, F., Villaume, S. and Thépaut, J.-N. (2020) The ERA5 global reanalysis. *Quarterly Journal of the Royal Meteorological Society*, 146(730), 1999–2049. <https://doi.org/10.1002/qj.3803>.
- Hirons, L. and Turner, A. (2018) The impact of Indian Ocean mean-state biases in climate models on the representation of the east African short rains. *Journal of Climate*, 31(16), 6611–6631. <https://doi.org/10.1175/jcli-d-17-0804.1>.
- Hua, W., Zhou, L., Chen, H., Nicholson, S.E., Jiang, Y. and Raghavendra, A. (2017) Understanding the central equatorial African long-term drought using AMIP-type simulations. *Climate Dynamics*, 50(3–4), 1115–1128. <https://doi.org/10.1007/s00382-017-3665-2>.
- Hua, W., Zhou, L., Chen, H., Nicholson, S.E., Raghavendra, A. and Jiang, Y. (2016) Possible causes of the central equatorial African long-term drought. *Environmental Research Letters*, 11(12), 124002. <https://doi.org/10.1088/1748-9326/11/12/124002>.
- Hua, W., Zhou, L., Nicholson, S.E., Chen, H. and Qin, M. (2019) Correction to: assessing reanalysis data for understanding rainfall climatology and variability over central equatorial Africa. *Climate Dynamics*, 53(7–8), 5139. <https://doi.org/10.1007/s00382-019-04918-7>.
- Huffman, G.J., Behrangi, A., Bolvin, D.T. and Nelkin, E.J. (2020) In: Huffman, G.J., Behrangi, A., Bolvin, D.T. and Nelkin, E.J. (Eds.) *GPCP Version 3.1 Satellite-Gauge (SG) Combined Precipitation Data Set*. Greenbelt, MD: NASA GES DISC. <https://doi.org/10.5067/DBVUO4KQHXTK>.
- Jackson, B., Nicholson, S.E. and Klotter, D. (2009) Mesoscale convective systems over Western equatorial Africa and their relationship to large-scale circulation. *Monthly Weather Review*, 137(4), 1272–1294. <https://doi.org/10.1175/2008mwr2525.1>.
- James, R. and Washington, R. (2012) Changes in African temperature and precipitation associated with degrees of global warming. *Climatic Change*, 117(4), 859–872. <https://doi.org/10.1007/s10584-012-0581-7>.
- James, R., Washington, R., Abiodun, B., Kay, G., Mutemi, J., Pokam, W., Hart, N., Artan, G. and Senior, C. (2018) Evaluating Climate Models with an African Lens. *Bulletin of the American Meteorological Society*, 99(2), 313–336. <https://doi.org/10.1175/bams-d-16-0090.1>

- Jones, P.W. (1999) First and second order conservative remapping schemes for grids in spherical coordinates. *Monthly Weather Review*, 127, 2204–2210. <https://doi.org/10.1175/1520-0493>.
- Jury, M.R., Matari, E. and Matitu, M. (2008) Equatorial African climate teleconnections. *Theoretical and Applied Climatology*, 95(3–4), 407–416. <https://doi.org/10.1007/s00704-008-0018-4>.
- King, A.D. and Harrington, L.J. (2018) The inequality of climate change from 1.5 to 2°C of global warming. *Geophysical Research Letters*, 45(10), 5030–5033. <https://doi.org/10.1029/2018gl078430>.
- Kuete, G., Mba, W.P. and Washington, R. (2019) African easterly jet south: control, maintenance mechanisms and link with southern subtropical waves. *Climate Dynamics*, 54(3–4), 1539–1552. <https://doi.org/10.1007/s00382-019-05072-w>.
- Lin, R., Zhou, T. and Qian, Y. (2014) Evaluation of global monsoon precipitation changes based on five reanalysis datasets. *Journal of Climate*, 27(3), 1271–1289. <https://doi.org/10.1175/jcli-d-13-00215.1>.
- Longandjo, G.T. and Rouault, M. (2019) On the structure of the regional-scale circulation over Central Africa: seasonal evolution, variability, and mechanisms. *Journal of Climate*, 33(1), 145–162. <https://doi.org/10.1175/jcli-d-19-0176.1>.
- Maidment, R.I., Grimes, D., Allan, R.P., Tarnavsky, E., Stringer, M., Hewison, T., Roebeling, R. and Black, E. (2014) The 30 year TAMSAT african rainfall climatology and time series (TARCAT) data set. *Journal of Geophysical Research: Atmospheres*, 119(18), 10619–10644. <https://doi.org/10.1002/2014jd021927>
- Matsuura, K. and Willmott, C.J. (2015) *Terrestrial Precipitation: 1900–2017 Gridded Monthly Time Series*. Newark, DE: University of Delaware Department of Geography. http://climate.geog.udel.edu/~climate/html_pages/Global2017/README_GlobalTsP2017.html.
- Moihamette, F., Pokam, W.M., Diallo, I. and Washington, R. (2022) Extreme Indian Ocean dipole and rainfall variability over Central Africa. *International Journal of Climatology*, 1–18. <https://doi.org/10.1002/joc.7531>.
- Masson-Delmotte, V., Zhai, P., Pörtner, H.O., Roberts, D., Skea, J., Shukla, P., Pirani, A., Moufouma-Okia, W., Péan, C., Pidcock, R., Connors, S., Matthews, J.B.R., Chen, Y., Zhou, X., Gomis, M.I., Lonnoy, E., Maycock, T., Tignor, M. & Waterfield, T. (2018) Global warming of 1.5° c. an ipcc special report on the impacts of global warming of 1.5° c above pre-industrial levels and related global greenhouse gas emission pathways, in the context of strengthening the global response to the threat of climate change, sustainable development, and efforts to eradicate poverty. <https://www.ipcc.ch/sr15/>.
- Nesbitt, S.W., Cifelli, R. and Rutledge, S.A. (2006) Storm morphology and rainfall characteristics of TRMM precipitation features. *Monthly Weather Review*, 134, 2702–2721. <https://doi.org/10.1175/MWR3200.1>.
- Nicholson, S.E. and Dezfuli, A.K. (2013) The relationship of rainfall variability in Western equatorial Africa to the tropical oceans and atmospheric circulation. Part I: the boreal spring. *Journal of Climate*, 26(1), 45–65. <https://doi.org/10.1175/jcli-d-11-00653.1>.
- Nicholson, S.E. and Grist, J.P. (2003) The seasonal evolution of the atmospheric circulation over West Africa and equatorial Africa. *Journal of Climate*, 16(7), 1013–1030. [https://doi.org/10.1175/1520-0442\(2003\)0162.0.co;2](https://doi.org/10.1175/1520-0442(2003)0162.0.co;2).
- Nikulin, G., Jones, C., Giorgi, F., Asrar, G., Büchner, M., Cerezo-Mota, R., Christensen, O. B., Déqué, M., Fernandez, J., Hänsler, A., van Meijgaard, E., Samuelsson, P., Sylla, M.B. and Sushama, L. (2012) Precipitation climatology in an ensemble of CORDEX-Africa Regional climate simulations. *Journal of Climate*, 25(18), 6057–6078. <https://doi.org/10.1175/jcli-d-11-00375.1>
- Pokam, W.M., Bain, C.L., Chadwick, R.S., Graham, R., Sonwa, D.J. and Kamga, F.M. (2014) Identification of processes driving low-level westerlies in west equatorial Africa. *Journal of Climate*, 27(11), 4245–4262. <https://doi.org/10.1175/jcli-d-13-00490.1>.
- Pokam, W.M., Djotang, L.A. and Mkankam, F.K. (2011) Atmospheric water vapor transport and recycling in equatorial Central Africa through NCEP/NCAR reanalysis data. *Climate Dynamics*, 38(9–10), 1715–1729. <https://doi.org/10.1007/s00382-011-1242-7>.
- Rayner, N.A. (2003) Global analyses of sea surface temperature, sea ice, and night marine air temperature since the late nineteenth century. *Journal of Geophysical Research*, 108(D14), 4407. <https://doi.org/10.1029/2002jd002670>.
- Saeed, F., Haensler, A., Weber, T., Hagemann, S. and Jacob, D. (2013) Representation of extreme precipitation events leading to opposite climate change signals over The Congo Basin. *Atmosphere*, 4(3), 254–271. <https://doi.org/10.3390/atmos4030254>.
- Saji, N.H., Goswami, B.N., Vinayachandran, P.N. and Yamagata, T. (1999) A dipole mode in the tropical Indian Ocean. *Nature*, 401(6751), 360–363. <https://doi.org/10.1038/43854>.
- Sandjon, A.T., Nzeukou, A. and Tchawoua, C. (2012) Intraseasonal atmospheric variability and its interannual modulation in Central Africa. *Meteorology and Atmospheric Physics*, 117(3–4), 167–179. <https://doi.org/10.1007/s00703-012-0196-6>.
- Sonkoué, D., Monkam, D., Fotso-Nguemo, T.C., Yepdo, Z.D. and Vondou, D.A. (2018) Evaluation and projected changes in daily rainfall characteristics over Central Africa based on a multi-model ensemble mean of CMIP5 simulations. *Theoretical and Applied Climatology*, 137(3–4), 2167–2186. <https://doi.org/10.1007/s00704-018-2729-5>.
- Taguela, T.N., Vondou, D.A., Moufouma-Okia, W., Fotso-Nguemo, T.C., Pokam, W.M., Tanessong, R.S., Yepdo, Z.D., Haensler, A., Longandjo, G.N., Bell, J.P., Takong, R.R. and Djotang Tchotchou, L.A. (2020) CORDEX multi-RCM hindcast over central Africa: evaluation within observational uncertainty. *Journal of Geophysical Research: Atmospheres*, 125(5), 1–12. <https://doi.org/10.1029/2019jd031607>
- Tamoffo, A.T., Amekudzi, L.K., Weber, T., Vondou, D.A., Yamba, E.I. and Jacob, D. (2021) Mechanisms of rainfall biases in two CORDEX-CORE regional climate models at rainfall peaks over central equatorial Africa. *Journal of Climate*, 1–69, 639–668. <https://doi.org/10.1175/JCLI-D-21-0487.1>.
- Tamoffo, A.T., Moufouma-Okia, W., Dosio, A., James, R., Pokam, W. M., Vondou, D.A., Fotso-Nguemo, T.C., Guenang, G.M., Kamsu-Tamo, P.H., Nikulin, G., Longandjo, G.-N., Lennard, C.J., Bell, J.-P., Takong, R.R., Haensler, A., Tchotchou, L.A.D., Nouayou and R. (2019b) Process-oriented assessment of RCA4 regional climate model projections over the Congo Basin under 1.5°C and 2°C global warming levels: influence of regional moisture fluxes. *Climate Dynamics*, 53(3–4), 1911–1935. <https://doi.org/10.1007/s00382-019-04751-y>
- Tamoffo, A.T., Vondou, D.A., Pokam, W.M., Haensler, A., Yepdo, Z.D., Fotso-Nguemo, T.C., Tchotchou, L.A.D. and Nouayou, R. (2019a)

- Daily characteristics of Central African rainfall in the REMO model. *Theoretical and Applied Climatology*, 137(3-4), 2351–2368. <https://doi.org/10.1007/s00704-018-2745-5>
- Todd, M.C. and Washington, R. (2004) Climate variability in central equatorial Africa: influence from the Atlantic sector. *Geophysical Research Letters*, 31(23), 1–4. <https://doi.org/10.1029/2004gl020975>.
- Vondou, D.A. and Haensler, A. (2017) Evaluation of simulations with the regional climate model REMO over Central Africa and the effect of increased spatial resolution. *International Journal of Climatology*, 37, 741–760. <https://doi.org/10.1002/joc.5035>.
- Walters, D., Baran, A.J., Boutle, I., Brooks, M., Earnshaw, P., Edwards, J., Furtado, K., Hill, P., Lock, A., Manners, J., Morcrette, C., Mulcahy, J., Sanchez, C., Smith, C., Stratton, R., Tennant, W., Tomassini, L., Van Weverberg, K., Vosper, S., Willett, M., Browse, J., Bushell, A., Carslaw, K., Dalvi, M., Essery, R., Gedney, N., Hardiman, S., Johnson, B., Johnson, C., Jones, A., Jones, C., Mann, G., Milton, S., Rumbold, H., Sellar, A., Ujiie, M., Whittall, M., Williams, K. and Zerroukat, M. (2019) The met office unified model global atmosphere 7.0/7.1 and JULES global land 7.0 configurations. *Geoscientific Model Development*, 12(5), 1909–1963. <https://doi.org/10.5194/gmd-12-1909-2019>
- Walters, D., Boutle, I., Brooks, M., Melvin, T., Stratton, R., Vosper, S., Wells, H., Williams, K., Wood, N., Allen, T., Bushell, A., Copsey, D., Earnshaw, P., Edwards, J., Gross, M., Hardiman, S., Harris, C., Heming, J., Klingaman, N., Levine, R., Manners, J., Martin, G., Milton, S., Mittermaier, M., Morcrette, C., Riddick, T., Roberts, M., Sanchez, C., Selwood, P., Stirling, A., Smith, C., Suri, D., Tennant, W., Vidale, P.L., Wilkinson, J., Willett, M., Woolnough, S. and Xavier, P. (2017) The met office unified model global atmosphere 6.0/6.1 and JULES global land 6.0/6.1 configurations. *Geoscientific Model Development*, 10(4), 1487–1520. <https://doi.org/10.5194/gmd-10-1487-2017>
- Washington, R., James, R., Pearce, H., Pokam, W.M. and Moufouma-Okia, W. (2013) Congo Basin rainfall climatology: can we believe the climate models? *Philosophical Transactions of the Royal Society B: Biological Sciences*, 368(1625), 20120296. <https://doi.org/10.1098/rstb.2012.0296>.
- Williams, K.D., Copsey, D., Blockley, E.W., Bodas-Salcedo, A., Calvert, D., Comer, R., Davis, P., Graham, T., Hewitt, H.T., Hill, R., Hyder, P., Ineson, S., Johns, T.C., Keen, A.B., Lee, R. W., Megann, A., Milton, S.F., Rae, J.G.L., Roberts, M.J., Scaife, A.A., Schiemann, R., Storkey, D., Thorpe, L., Watterson, I.G., Walters, D.N., West, A., Wood, R.A., Woollings, T. and Xavier, P.K. (2018) The met office global coupled model 3.0 and 3.1 (GC3.0 and GC3.1) configurations. *Journal of Advances in Modeling Earth Systems*, 10(2), 357–380. <https://doi.org/10.1002/2017ms001115>
- Williams, K.D., Harris, C.M., Bodas-Salcedo, A., Camp, J., Comer, R.E., Copsey, D., Fereday, D., Graham, T., Hill, R., Hinton, T., Hyder, P., Ineson, S., Masato, G., Milton, S.F., Roberts, M.J., Rowell, D.P., Sanchez, C., Shelly, A., Sinha, B., Walters, D.N., West, A., Woollings, T. and Xavier, P.K. (2015) The met office global coupled model 2.0 (GC2) configuration. *Geoscientific Model Development*, 8(5), 1509–1524. <https://doi.org/10.5194/gmd-8-1509-2015>
- Zhu, Y. and Yang, S. (2020) Interdecadal and interannual evolution characteristics of the global surface precipitation anomaly shown by CMIP5 and CMIP6 models. *International Journal of Climatology*, 41, 1–19. <https://doi.org/10.1002/joc.6756>.

How to cite this article: Taguela, T. N., Pokam, W. M., & Washington, R. (2022). Rainfall in uncoupled and coupled versions of the Met Office Unified Model over Central Africa: Investigation of processes during the September–November rainy season. *International Journal of Climatology*, 1–21. <https://doi.org/10.1002/joc.7591>

CORDEX Multi-RCM Hindcast Over Central Africa: Evaluation Within Observational Uncertainty

Key Points:

- Most RCMs along with their ensemble mean generally fall in the range of observational uncertainty
- The ensemble mean of models is generally found within the observational range when most models are there as well
- The ensemble mean of models does not generally outperform individual RCMs realization as it is reported in several previous studies

Supporting Information:

- Supporting Information S1

Correspondence to:

T. N. Taguela,
thierrytaguela@gmail.com

Citation:

Taguela, T. N., Vondou, D. A., Moufouma-Okia, W., Fotso-Nguemo, T. C., Pokam, W. M., Tanessong, R. S., et al. (2020). CORDEX multi-RCM hindcast over Central Africa: Evaluation within observational uncertainty. *Journal of Geophysical Research: Atmospheres*, 125, e2019JD031607. <https://doi.org/10.1029/2019JD031607>

Received 23 SEP 2019

Accepted 15 FEB 2020

Accepted article online 18 FEB 2020

Thierry N. Taguela^{1,2}, Derbetini A. Vondou^{1,2}, Wilfran Moufouma-Okia³, Thierry C. Fotso-Nguemo^{1,4}, Wilfried M. Pokam^{1,2,5}, Roméo S. Tanessong^{1,6}, Zéphirin D. Yepdo^{1,4}, Andreas Haensler⁷, Georges N. Longandjo⁸, Jean P. Bell⁹, Roland R. Takong⁸, and Lucie A. Djiotang Tchotchou¹

¹Laboratory for Environmental Modelling and Atmospheric Physics, Department of Physics, University of Yaounde 1, Yaounde, Cameroon, ²Laboratoire Mixte International "Dynamique des écosystèmes continentaux d'Afrique Centrale en contexte de changements globaux" (LMI DYCOFAC), Institut de Recherche pour le Développement, Yaoundé, Cameroun, ³Climate and Water Department, World Meteorological Organization, Geneva, Switzerland, ⁴Climate Change Research Laboratory (CCRL), National Institute of Cartography, Yaounde, Cameroon, ⁵Department of Physics, Higher Teacher Training College, University of Yaounde 1, Yaounde, Cameroon, ⁶School of Wood, Water and Natural Resources, Faculty of Agronomy and Agricultural Sciences, University of Dschang, Ebolowa, Cameroon, ⁷Institute of Hydrology, Faculty of Environment and Natural Resources, University Freiburg, Freiburg im Breisgau, Germany, ⁸Department of Oceanography, University of Cape Town, Cape Town, South Africa, ⁹Department of Physics, Faculty of Science, University of Douala, Douala, Cameroon

Abstract This paper investigates the performance of 10 Regional Climate Models (RCMs) hindcasts from the Coordinated Regional Climate Downscaling Experiments (CORDEX) over Central Africa, covering the period 1998–2008 and performed over a common model grid spacing 0.44° (~50 km). Multiple observational data sets are used to evaluate model performances over four targeted subregions. Throughout the work, a measure of observational uncertainty is made and we discuss whether or not the models are found within or outside the range of observational uncertainty. Results indicate that RCMs generally capture rainfall and temperature basic features, though important biases exist and vary for models and seasons. Dry (wet) biases are common features over the Congo basin (northern and southern part of the domain). In terms of precipitation and temperature in both seasonal and annual scale, most RCMs along with their ensemble mean generally fall in the range of observational uncertainty. Furthermore, most RCMs show a good spread of grid points where the added value of RCMs is found although the added value in temperature is not as great as with precipitation. UC-WRF is among models adding less value on ERAINT and this could explain why whatever the time scale of variability, UC-WRF outputs are generally out from the observational uncertainty. The multimodel ensemble mean is generally found within observational range when most models are there as well. This highlights the fact that the ensemble mean, built from the equal treatment of RCMs, does not generally outperform individual RCMs realization as it is reported in several previous studies.

1. Introduction

Many of the observed climate changes and impact since the 1950s are unprecedented and can be confidently attributed to anthropogenic emissions (Hansen & Stone, 2016). However, there is little research connecting precipitation changes in Central Africa (CA) to impacts in natural, managed, and human systems. The reliable detection and attribution of changes in climate and their effects, is fundamental to understanding the scientific basis of climate change and in enabling decision makers to manage climate risks. The fifth assessment report (AR5) of the Intergovernmental Panel on Climate Change (IPCC) reviews the scientific, technical, and socioeconomic information relevant to understanding the scientific basis of risk of human-induced climate change, its potential impacts, and options for adaptation and mitigation (Pachauri et al., 2014). AR5 focuses on four major climatic zones across Africa including Sahara, Western Africa, Eastern Africa, and Southern Africa, and concludes that multiple biophysical, political, and socioeconomic stresses interact to increase the region's susceptibility and constrain its adaptive capacity (Christensen et al., 2013). Evidence of warming has increased over land regions across Africa, consistent with anthropogenic climate change (Creese et al., 2019; Fotso-Nguemo et al., 2016; Pokam et al., 2018; Tamoffo et al., 2018).